AD_____

Award Number DAMD17-94-J-4424

TITLE: Single-Pulse Dual-Energy Mammography Using a Binary Screen Coupled to Dual CCD Cameras

PRINCIPAL INVESTIGATOR: John M. Boone, Ph.D.

CONTRACTING ORGANIZATION: University of California
                          Office of Research
                          Davis, California 95616-8671

REPORT DATE: August 1999

TYPE OF REPORT: Final

PREPARED FOR: U.S. Army Medical Research and Materiel Command
               Fort Detrick, Maryland 21702-5012

DISTRIBUTION STATEMENT: Approved for Public Release;
                        Distribution Unlimited

The views, opinions and/or findings contained in this report are those of the author(s) and should not be construed as an official Department of the Army position, policy or decision unless so designated by other documentation.

20000417 119

REPORT DOCUMENTATION PAGE

Form Approved
OMB No. 0704-0188

Public reporting burden for this collection of information is estimated to average 1 hour per response, including the time for reviewing instructions, searching existing data sources, gathering and maintaining the data needed, and completing and reviewing the collection of information. Send comments regarding this burden estimate or any other aspect of this collection of information, including suggestions for reducing this burden, to Washington Headquarters Services, Directorate for Information Operations and Reports, 1215 Jefferson Davis Highway, Suite 1204, Arlington, VA 22202-4302, and to the Office of Management and Budget, Paperwork Reduction Project (0704-0188), Washington, DC 20503.

1. AGENCY USE ONLY *(Leave blank)*	2. REPORT DATE August 1999	3. REPORT TYPE AND DATES COVERED Final (15 Jul 94 - 14 July 99)

4. TITLE AND SUBTITLE
Single-Pulse Dual-Energy Mammography Using a Binary Screen Coupled to Dual CCD Cameras

5. FUNDING NUMBERS
DAMD17-94-J-4424

6. AUTHOR(S)
John M. Boone, Ph.D.

7. PERFORMING ORGANIZATION NAME(S) AND ADDRESS(ES)
University of California Office of Research
Davis, California 95616-8671

8. PERFORMING ORGANIZATION REPORT NUMBER

9. SPONSORING / MONITORING AGENCY NAME(S) AND ADDRESS(ES)
U.S. Army Medical Research and Materiel Command
Fort Detrick, Maryland 21702-5012

10. SPONSORING / MONITORING AGENCY REPORT NUMBER

11. SUPPLEMENTARY NOTES

12a. DISTRIBUTION / AVAILABILITY STATEMENT
Approved for Public Release; Distribution Unlimited

12b. DISTRIBUTION CODE

13. ABSTRACT *(Maximum 200 words)*

Mammographic screening for breast cancer currently represents a women's best chance for surviving breast cancer. Nevertheless, for women with dense breasts, mammography by itself may not be as efficient as other imaging strategies. Dual energy mammography is a technique in which the complicated structure of the normal, dense breast can be eliminated mathematically in the image, thereby highlighting the remaining microcalcification structures that may be present and are early tell-tale signs of possible breast cancer. This grant focussed on optimizing (maximizing image quality while minimizing radiation dose) the dual energy mammography technique using computer simulation and "Monte Carlo" techniques. In addition, a dual energy mammography system was built and its performance was measured. The research identified the best x-ray spectra that should be used for dual energy mammography acquisition. The research also indicated that single pulse, dual detector dual energy acquisition should be avoided, and rather dual x-ray pulse (switched kVp) approaches using a single detector should be used. Several databases were produced by this effort. These tools, which include a comprehensive attenuation coefficient library, four spectral models, and tables for generating breast dose, should be useful for other investigators seeking to further improve the sensitivity of mammography screening.

14. SUBJECT TERMS
Breast Cancer

15. NUMBER OF PAGES
285

16. PRICE CODE

17. SECURITY CLASSIFICATION OF REPORT Unclassified	18. SECURITY CLASSIFICATION OF THIS PAGE Unclassified	19. SECURITY CLASSIFICATION OF ABSTRACT Unclassified	20. LIMITATION OF ABSTRACT Unlimited

NSN 7540-01-280-5500

Standard Form 298 (Rev. 2-89)
Prescribed by ANSI Std. Z39-18 298-102

USAPPC V1.00

FOREWORD

Opinions, interpretations, conclusions and recommendations are those of the author and are not necessarily endorsed by the U.S. Army.

_____ Where copyrighted material is quoted, permission has been obtained to use such material.

_____ Where material from documents designated for limited distribution is quoted, permission has been obtained to use the material.

__√__ Citations of commercial organizations and trade names in this report do not constitute an official Department of Army endorsement or approval of the products or services of these organizations.

_____ In conducting research using animals, the investigator(s) adhered to the "Guide for the Care and Use of Laboratory Animals," prepared by the Committee on Care and use of Laboratory Animals of the Institute of Laboratory Resources, national Research Council (NIH Publication No. 86-23, Revised 1985).

__√__ For the protection of human subjects, the investigator(s) adhered to policies of applicable Federal Law 45 CFR 46.

_____ In conducting research utilizing recombinant DNA technology, the investigator(s) adhered to current guidelines promulgated by the National Institutes of Health.

_____ In the conduct of research utilizing recombinant DNA, the investigator(s) adhered to the NIH Guidelines for Research Involving Recombinant DNA Molecules.

_____ In the conduct of research involving hazardous organisms, the investigator(s) adhered to the CDC-NIH Guide for Biosafety in Microbiological and Biomedical Laboratories.

July 21, 1999

PI - Signature   Date

Page 2

TABLE OF CONTENTS

DAMD17-94-J-4424

SINGLE-PULSE DUAL-ENERGY MAMMOGRAPHY USING A BINARY SCREEN COUPLED TO DUAL CCD CAMERAS

INTRODUCTION

Breast cancer is a national epidemic affecting one in every eight women in the United States. Until preventive agents and/or a cure is found, the best chance that a women has to survive breast cancer is through early detection. X-ray mammography remains the diagnostic test which has the highest chance of identifying breast cancer at its earliest stage, a stage where the medical prognosis is still excellent.

X-ray mammography has received a great deal of attention through-out the 1980's and 1990's, a period of time where the awareness of breast screening has increased steadily. Throughout this period, the technology used for mammography has enjoyed steadily increasing sophistication and performance. In 1980, xeromammography was the imaging modality of choice for breast screening, and xeromammography was touted at that time in part because it could be used with non-dedicated equipment. However, over the past twenty years there has been increased specialization in mammography equipment, and at the present time dedicated mammography x-ray machines, sporting molybdenum and rhodium anodes, coupled with screen-film mammographic cassettes, represents the state of the art in screening mammography.

Digital x-ray mammography systems have been developed over the past several years, and several manufacturers have applied for and await approval by the Food and Drug Administration, which is necessary for these digital systems to be used routinely for clinical screening of breast cancer. Once these systems become widely available, the scientific imaging community which has been studying this technology for several years generally expects an increased level of breast cancer detection performance. With digital imaging systems, the image data becomes easily available for computer processing and manipulation, and this in itself may prove to be one of the biggest advantages of digital mammography.

The current project exploits the digital nature of digital mammography equipment for use in a dual energy imaging post processing technique designed to increase the detection of microcalcifications which frequently accompany a small breast cancer soft tissue lesion. The presence of microcalcifications occurs in perhaps 40% of all early breast cancers. Although not all microcalcifications are associated with cancer, these structures nevertheless can be considered as markers which allow the detection of breast cancer much sooner than if no microcalcifications had been present. The reason that microcalcifications lend themselves to early detection is that calcium has a markedly different atomic number (Z=20) than the other constituents of breast tissue (hydrogen, oxygen, carbon, nitrogen, $Z_{effective} \approx 7.6$). At the x-ray energies used in mammography, materials with higher atomic numbers produce image contrast with a Z^3 dependency, and so the ability to visualize calcium-containing lesions increases over soft tissue lesions by a factor of about $(13/7.6)^3 = 4.9$.

Dual energy mammography is a technique aimed at further enhancing the detectability of microcalcifications in the breast, as a way of improving the early detection of breast cancer. In the following, we report our efforts to advance the state of the art of dual energy mammography towards the goal of early breast cancer detection.

BODY

SoW Task 1

Task 1 of this grant involves computer simulation procedures. We took a very fundamental approach to computer simulation, in the attempt to assure that the computer simulation results were meaningful and accurate. In the pursuit of being thorough, we started at a very basic level and developed our own source of x-ray attenuation coefficients, and a spectral model covering the mammographic energy range (20 to 40 kVp) with three anode materials (W, Mo, and Rh), and covering the general diagnostic energy range with a tungsten anode from 30 to 140 kVp.

In our first step towards the computer simulations, we sought to develop a set of attenuation coefficients that would allow maximum flexibility in terms of defining simulated test objects (out of any material) at any practical x-ray energy. This project is described in detail in the accompanying paper entitled "Comparison of x-ray cross sections for diagnostic and therapeutic medical physics", Paper #2 in the appendix.

The general diagnostic spectral model was reported ("An accurate method for computer-generating tungsten anode x-ray spectra from 30 to 140 kV") in *Medical Physics*, and is included in the appendix as Paper #5. Figure 1 illustrates the concept used for producing the modeled x-ray spectra. Measured x-ray spectra from an unfiltered tungsten general diagnostic x-ray system are shown in Figure 1(a), with spectra at 40, 50, 70, 80, …140 kVp. Each spectra is normalized to that produced by 1 mAs. The data aligned with the vertical lines (marked A, B and C) are re-plotted in Figure 1(b) as the solid circles, and the solid lines connecting the data points were interpolated using polynomials of the form:

$$\Phi = c_0 + c_1 \ x + c_2 \ x^2 + c_3 \ x^3 + c_4 \ x^4$$

A set of polynomial coefficients (c_0-c_4) for each of 140 different energies (1 to 140 keV, by 1 keV intervals) was produced. These coefficients can be used to calculate (quite accurately) any tungsten anode x-ray spectrum ranging from 40 kVp to 140 kVp.

The model for mammography spectra was also reported in *Medical Physics* ("Molybdenum, rhodium, and tungsten anode spectral models using interpolating polynomials with application to mammography") and is included in the appendix as Paper #6. The technique used to model unfiltered molybdenum, rhodium, and tungsten anode x-ray spectra in the range of 18 to 42 kVp is identical to that described previously (in Figure 1) for general diagnostic x-ray spectra. Examples of molybdenum spectra produced by the model are shown in Figure 2, rhodium spectra are shown in Figure 3, and mammography energy range tungsten x-ray spectra (using a thin beryllium window x-ray tube) are illustrated in Figure 4. Each spectrum is normalized to 1000 mR.

In our pursuit of accurate x-ray spectrum modeling and measurement, we also become involved in a collaboration with Dr. Richard Deslattes at NIST, evaluating an x-ray spectrometer he developed under a different Army BCRP grant (DAMD-17-94MM4539). We evaluated the potential of that diffraction-based spectrometer to produce accurate measured spectra, and in the process we developed a set of calibrations for the Deslattes spectrometer as reported in "Mammography spectrum measurement using an x-ray diffraction device", included as Paper #9 in the appendix.

A very important step in developing a basic set of simulation tools required that we use Monte Carlo methods to calculate the average normalized glandular dose (DgN) for a wide variety of x-ray spectra. The existing DgN values [1-3] are tabulated for a set of clinical mammography x-ray spectra using Mo and Rh anode targets. For dual energy mammography, clearly tungsten target data are needed for the high energy beam, and therefore the PI set out on (what turned out to be) a lengthy Monte Carlo evaluation of DgN values for arbitrary x-ray spectra and monoenergetic x-ray beams ranging from 1 keV to 120 keV. The geometry used in the Monte Carlo study is illustrated in Figure 5, with the breast parenchyma encapsulated in a layer of skin, as shown. The results of our Monte Carlo investigation were compared with the data of others. The data of Dance[3] is compared in Figure 6, and the correlation between the data from Wu Tucker and Barnes[1] (the data principally used in the United States) and our data is shown in Figure 7. As seen in Figures 6 and 7, the results from our Monte Carlo studies compares very well with the DgN values of others. Further details are contained in Paper #11 in the appendix entitled "Monte Carlo assessment of glandular breast dose for monoenergetic and high-energy polyenergetic x-ray beams", which is *in press* in the October 1999 issue of *Radiology*. The Editor of Radiology, Dr. Anthony Proto, has decided to feature this article in the form of an invited editorial, written by Dr. Carolyn Kimme-Smith. The commentary will accompany the article in the October 1999 issue of *Radiology*. After verifying the validity of the Monte Carlo techniques, we then extended the reported DgN values to high energy polyenergetic x-ray spectra. Figure 8 shows DgN values for 0% glandular breasts (that is, 100% adipose) from 40 to 120 kVp, and Figure 9 shows the DgN values for 100% glandular breasts. In addition to the polyenergetic results, monoenergetic results were also computed and these data are shown in Figure 10 (0% glandular breast) and Figure 11 (100% glandular breast). Combining the data by linear interpolation methods allows the computation of DgN values for any intermediate degree of breast glandularity.

We also set out to validate our Monte Carlo (MC) technique against metrics other than the DgN. These results are as of yet unpublished (manuscript in preparation). Figure 12 illustrates depth-dose curves comparing our MC code against the data produced by another MC package sold by Oak Ridge National Laboratory called TART98. Good agreement is seen in Figure 12. The fraction of absorbed energy for a breast is compared in Figure 13, again with excellent agreement. Figure 14 illustrates a comparison of the scatter lateral distribution data of Chan, et al. [4-6] at 100 keV, and results for 40 keV are shown in Figure 15. The geometry of the simulation is illustrated as an inset in Figure 15. Depth dose results are compared with Chan, et al.[4-6] in Figure 16 with good agreement. Chan[4-6] also computed the number of interactions per exit scatter photon, and

we altered our code to compute this parameter for comparison in Figure 17. Reasonable agreement is seen. Klein[7] reported measured scatter exit angle data (not MC generated), and we modified our code to make this comparison seen in Figure 18. Excellent agreement is seen. The DgN data of Wu, et al.[1] discussed above is also compared graphically in Figure 19. (Figure 7 showed these data plotted against each other).

We have also made our own scatter to primary ratio measurements using a flat panel digital detector system discussed later, with the intention of using these physical measurements to further verify our MC code. The measurement technique was reported at the 1999 American Association of Physicists in Medicine meeting in Nashville, by Dr. Virgil Cooper, a post-doc working in the PI's laboratory under partial support from this grant. His poster presentation of that work ("Scatter-to-primary measurements in mammography using edge spread functions") is included as Paper #15 in the appendix. Preliminary comparisons between the measured data and those produced by our MC code are shown in Figure 20, with reasonable agreement.

SoW Task 1.2: The most efficient x-ray spectrum will be identified for single energy mammography

The description of our work in Task 1.2 and 1.1 is reversed for a more concise presentation of results.

What defines the "most efficient" x-ray spectrum is one that maximizes both the contrast and signal to noise ratio (SNR) in the image, using the least glandular dose to the breast. A Figure of Merit (FOM), therefore, can be expressed as:

$$FOM = \frac{contrast \times SNR}{\sqrt{dose}}$$

The benefit of taking the square root of the dose is that the FOM becomes independent of the number of x-ray photons used, eliminating exposure level as a parameter in the optimization. This FOM was used in concert with Monte Carlo calculations for single energy (conventional) mammography. For the dual energy mammography detector system (described more completely below), the thickness of the detector needs to be thin enough to deliver good spatial resolution but thick enough to have reasonable absorption at the higher energy, and thus we modeled a 60 mg/cm^2 Gd$_2$O$_2$S detector. The FOM is shown in Figure 21(top) for a 3 mm soft tissue lesion, for a 4 cm thick breast and from 20 kV to 40 kV. Optimization occurs where the FOM is at a maximum for each breast thickness. The data for a 50% glandular breast are shown. The dotted lines also show the results for an ideal detector system (one that absorbs all energy incident upon it). In mammography, we want to maximize the contrast to both soft tissue lesions and to microcalcifications, different tasks. The results of the FOM analysis for a 50 μm microcalcification lesion is illustrated in Figure 21 (bottom). Fortunately, the optimal Mo-Mo (anode-filter combination) kVp's for both the soft tissue and calcium based lesions are very similar at each breast thickness. These results made use of a 5:1 grid, typical of that used in clinical mammography. Figure 22 illustrates a comparison

between Mo-Mo x-ray spectra (solid lines) and Rh-Rh spectra (dotted lines). Not surprisingly, the Mo-Mo spectra proved most efficient for 2 and 4 cm breasts, while the Rh-Rh spectra proved more efficient for the 6 and 8 cm thick breasts. The optimization results shown in Figure 21 and 22 are consistent with the clinical practice of mammography.

Beyond the scope of this grant, we aim to study the relative contribution of contrast versus SNR in the numerator of the FOM indicated above. For example, let's redefine the FOM mentioned above as:

$$FOM' = \frac{contrast^{\alpha} \times SNR^{\beta}}{\sqrt{dose}}$$

It is necessary to assign $\beta=1$ to maintain the exposure independence of the FOM, as mentioned above. Since screen-film mammography is well known to be a *contrast limited* detector system, one would think for this modality that an emphasis on delivering contrast might be appropriate, for example making $\alpha > 1$ emphasizing contrast and deemphasizing SNR. For digital mammography systems, where contrast can be arbitrarily enhanced by windowing and leveling (and other post-processing techniques), the images are thought to be *noise limited*. It may be appropriate therefore to assign $\alpha < 1$ to emphasize SNR. These issues can be evaluated using computer simulated lesions, modeling each detector system (using the H&D curve of film versus the linear, wide dynamic range response of a digital system) in a computer observer ROC analysis[8].

SoW Task 1.1: The most efficient x-ray spectrum will be identified for dual energy imaging

While it is possible to optimize the acquisition of the low energy image and the high energy image simultaneously (as we have in the past [9]), we feel that dual energy mammography will never be the *only* technique used for mammographic screening, but will serve as an adjunct to conventional single energy mammography. This being the case, the low energy image needs to be of equal quality to a standard mammogram, and thus the results for the single energy imaging optimization presented above (for Task 1.2) remain valid for the low energy image used in dual energy mammography.

To optimize the high energy image of the dual energy pair, it is clear that what we want to do is *minimize* the contrast of the target object (a microcalcification in this case), as opposed to maximizing it as with the low energy image optimization. By doing so, the dual energy signal will be maximized. This can be done by redefining the FOM as:

$$FOM = \frac{\left(\dfrac{SNR}{contrast}\right)}{\sqrt{dose}}$$

Using the general diagnostic spectral model (tungsten anode), and filtering the x-ray spectra using added filtration (1.5 mm Al and 2.0 mm Cu), the above FOM was computed for a 50 μm microcalcification and the results are shown in Figure 23. Well defined maxima are seen at each breast thickness, in all cases occurring at 95 kVp. Examples of the heavily filtered x-ray beams are shown in Figure 24 (80 and 100 kVp beams are shown). The optimization studies performed here for both the single and dual energy mammography are planned for publication in a paper soon to be written up. When completely and accepted for publication, these manuscripts will be submitted to the Command as an addendum to this report.

SoW Task 1.3: Identify the best screen parameters (thickness and phosphor ratio) for the proposed imaging system.

As reported below, the dual energy mammography system evolved from a single x-ray pulse, dual detector system as originally envisioned, to a dual x-ray pulse, single detector system. In the process, we also abandoned the binary phosphor concept and thus the need to optimize the phosphor ratio was eliminated. Whereas the screen thickness is an important parameter in a sandwich detector design (because it plays a role in hardening the beam for the second detector, thus affecting the energy separation between the low and high energy beams), it is not in a two pulse single detector design (energy separation is achieved by switching the kV and perhaps adding filtration with the higher kVp beam). Because of the change in design of the dual energy imaging system (discussed below), optimization of the screen thickness and phosphor ratio became unnecessary. However, we did perform a general evaluation of the potential of different x-ray phosphors to serve in digital mammography (and radiography), focussing on the role that x-ray fluorescence plays in reducing the detection efficiency of the imaging system. This investigation led to Paper #10 in the appendix, "A Monte Carlo study of the x-ray fluorescence in x-ray detectors". In this study, we evaluated seven different x-ray phosphors (Gd_2O_2S, CsI, Se, BaFBr, $YTaO_4$, $CaWO_4$, and ThO_2) using Monte Carlo techniques, and quantified how the x-ray fluorescence (characteristic radiation produced in the x-ray detector) affects the signal to noise ratio in each type of phosphor. These data are illustrated in Figure 25 (Gd_2O_2S and CsI), Figure 26 (Se and BaFBr), Figure 27 ($YTaO_4$ and $CaWO_4$) and in Figure 28 (ThO_2).

Figure 29 illustrates the fraction of the total energy absorbed in the detector that is reabsorbed "scatter" (from Rayleigh, Compton, and x-ray fluorescence), as a function of incident x-ray energy. The results for five different detector thicknesses are shown. Just above the K-edge of the phosphor (Gd: 50 keV K-edge), about 10% of the energy detected in the phosphor (i.e. the radiographic signal) is due to x-ray fluorescence. Depending on the spatial distribution, this reabsorbed signal energy will be realized as either actual signal (if the reabsorption occurs within a distance smaller than the resolution cell) or as correlated noise (if the reabsorption occurs beyond the resolution cell). Figure 30 illustrates the radial spread of energy in a Gd_2O_2S intensifying screen as a function of screen thickness. Note that the ordinate axis is logarithmic, indicating that a very small amount of x-ray scatter and characteristic re-absorption occurs. In addition, the range of the reabsorbed energy is relative short. The quantum detection efficiency as

a function of x-ray energy for Gd_2O_2S, CsI, and BaFBr is shown in Figure 31. Most physicists view the k-edge of a phosphor as an opportunity where improved absorption can be achieved by appropriate spectra shaping. However, it is the *energy* absorbed in the detector that generates the signal, not merely the detection of an incident photon itself. When x-ray fluorescence is considered (x-ray fluorescence is the re-emission of energy as a characteristic radiation photon, that generally escapes detection) as shown in Figure 32 for three common detectors, the loss of the characteristic x-ray energy tends to mitigate the value of the k-edge in terms of improving the detector absorption characteristics.

SoW Task 1.4: Find the most efficient anti-scatter grid for the proposed system.

Software was written for numerically computing the efficiency of primary and scatter rejection of an anti-scatter grid[10-12]. Various characteristics of grids can be observed. Figure 33 illustrates the grid transmission as a function of incident scatter angle for grids with different interspace materials. Results for aluminum, carbon fiber (CF), and air interspace materials are shown. Figure 33(top) shows the results for 25 keV x-ray photons, and Figure 33(bottom) shows the data for 40 keV x-rays. A 5:1 grid ratio was used for the data in this figure. Figure 34 illustrates the effect of grid ratio on the grid transmission versus angle, and as expected higher grid ratios deliver better scatter rejection. Data for carbon fiber (top) and aluminum (bottom) interspace grids are shown. The influence of x-ray energy on the grid transmission is seen in Figure 35.

Using the FOM analysis as discussed above for the optimization of the low energy (conventional) mammogram, the influence of the anti-scatter grid was evaluated and is shown in Figure 36. Air-interspace grids deliver better FOM values out to a grid ratio of 9:1, since air interspaces do not increase the primary attenuation with increased grid thickness (i.e. grid ratio). Carbon fiber interspaced grids track closely with the air-core grids, however some loss in the FOM is seen at higher grid ratios due to the slight increase in primary attenuation (which affects the SNR in the FOM). For aluminum-core grids, a marked reduction in the FOM values is seen as the grid ratio increases from 1 to 9, indicating that aluminum is not compatible with the x-ray energies used in mammography.

SoW Task 2

SoW Task 2.1: In consultation with mechanical engineer, design and build the mechanical aspects of the dual-camera imaging system.

In our initial discussions with the mechanical engineer consultant on this proposal, Mr. Roger Malcolm, we expressed our interest in building a mechanical assembly for the dual energy mammography system which was flexible enough to allow a series of changes as the project developed. After much discussion back and forth between the PI and the Mr. Malcolm, we decided to fabricate a series of struts which could be combined with our

optical tables in a very flexible manner. The struts were designed to have holes every 2.5 cm, which is consistent with the hole patterns of the optical tables used for the project. The design of the struts is illustrated in Figure 37.

The strut support system was then successfully built by the mechanical engineer's firm, and a number of struts of various lengths (30 cm [1'], 60 cm [2'], 90 cm [3'], 120 cm [4'], and 240 cm [8']) were delivered to the PI's laboratory. They were used as the mechanical support for the dual energy mammography system, discussed in the next section. In the four years that we have been using the struts, we have found them to be exceptionally useful as an experimental tool.

SoW Task 2.2: Install the optical and electronic components to the completed housing, and develop automatic alignment techniques for the two images.

The design of the single-pulse, dual-energy mammography system based on the binary screen system[13] was originally pursued as described in the funded grant proposal. The binary screen is an intensifying screen in which two phosphors with different K-edges (for example, Y_2O_2S, K=19 keV, and Gd_2O_2S, K=50 keV) are mixed. Each phosphor is designed to emit different wavelengths of visible light. Using two cameras, each optically filtered to accept only the light from one of the phosphors, a two channel imaging system can be constructed. For example, if the yttrium based phosphor emitted in the green (Y_2O_2S:Tb), and the gadolinium based phosphor (Gd_2O_2S:Eu) emitted in the red, the red-filtered camera (filtered so only red light would *pass* and be imaged) would produce the high x-ray energy image while the green-filtered image would receive only the emission from the yttrium phosphor (low K-edge) and would therefore produce the low x-ray energy image.

The grant was written in 1993, and at that time it was thought that charged coupled device (CCD) cameras were the best solution for building the prototype dual energy digital mammography system necessary for this project. After receiving funding for this project, we sought to develop a dual energy mammography system in which the detective quantum efficiency (DQE(f)) was maximized. However, the literature having to do with lens coupling calculations was a bit confusing, and the post-doctoral fellow supported under this grant (Dr. Tong Yu) with solid optical physics training background studied this in depth, and produced a paper entitled "Lens coupling efficiency: derivation and application under differing geometrical assumptions" (paper 4 in the appendix). Simultaneous with this work, we evaluated the potential of scintillating fiber optic plates to act as the x-ray-to-light converter for the dual energy system, resulting in a paper entitled "Scintillating fiber optic screens: A comparison of MTF, light conversion efficiency, and emission angle with Gd_2O_2S:Tb screens" (paper 3 in the appendix).

After the analytical and experimental work which resulted in papers 3 and 4, we realized that for a reasonably-sized field of view imaging system, that our DQE(f) was going to be severely limited by the available light quanta reaching the camera. The chip on the CCD cameras that we purchased was approximately 2 cm on a side. To achieve a field of view

of 5 cm with our F/1.2 lens (the lowest F number that we could afford for this project, each lens ~ $550), the light collection efficiency was calculated (see Figure 5 of Paper 4) to be less than 5%. For the binary phosphor to work, colored filters need to be imposed between the screen and the CCD camera to eliminate the wavelengths emitted from the other phosphor, but of course any color filter transmits only a fraction of the light incident upon it, even in its transmission band. It was thought that reducing the light collection efficiency below 5% would have a devastating effect on the DQE(f). Realizing this, early on in the research we shifted our design from the binary screen concept to the sandwich detector system illustrated in Figure 38.

The sandwich dual energy imaging system was build, and a photograph of it is shown in Figure 39. Two high resolution (2k × 2k) Kodak-chip CCD cameras were purchased from Princeton Instruments, and mounted in the designed configuration as shown in the photograph. The cameras were mounted on computer controlled moving stages, and a fair amount of effort was expended developing the software interfacing the motion control, the camera acquisition, and the alignment of the low energy (produced by the first phosphor shown on the left in Figure 38 and by CCD #1) and the high energy (produced by the phosphor on the right and CCD #2) images. The alignment between the two images was matched to the extent possible mechanically, and further alignment was performed in software. The alignment algorithm made use of a fiducial template (an x-ray image of a brass plate with holes drilled out in a rectalinear pattern was used), and was capable of correcting for differences between translation (horizontal and vertical), rotation, and magnification of the two images. In addition, a warping algorithm was developed and incorporated into the alignment procedure to accommodate the slight spherical distortion imposed by the lenses. The warping algorithm, developed under this project, was successfully employed for an unrelated project and resulted in a publication "Angiographic film subtraction using a laser digitizer and computer processing" (paper #8 in the appendix). A simple diagram of how the alignment algorithm worked is shown in Figure 40.

At the time we were developing the dual energy mammography system, the PI's colleague Dr. Tony Seibert (partially supported on this grant) was working on an unrelated project with Dr. Robert Alvarez, the person credited with initially developing dual energy techniques in the late 1970's with Dr. Albert McCovsky at Stanford University. Drs. Seibert and Alvarez were developing a dual-pulse, dual-detector (using computed radiography imaging plates) dual-energy technique for chest radiography[14,15]. Because Drs. Boone and Seibert share the same x-ray research laboratory, the Seibert/Alvarez dual energy project for chest radiography was developed on the same x-ray generator and x-ray tube that was used for this project. The Seibert/Alvarez project resulted in the development of a rapid kV switching interface to the x-ray generator, which allowed switching the kV from 50 to 120 kV in less than 30 ms. Thus, in addition to migrating towards a sandwich detector for the dual energy mammography system, we began thinking that better dual energy performance could be obtained if we incorporated the sandwich detector with a dual-pulse technique. Thus, the front detector in the sandwich would be used to image a low-kV pulse of x-rays, and milliseconds thereafter the rear detector would be used to image a high-kV pulse.

SoW Task 3.1: Measure the MTF of the system after optimizing alignment.

In measuring the MTF of the dual energy imaging system, it was our first opportunity to get fundamentally involved measuring the MTF of optical systems. This led us to develop a new technique for measuring optical MTFs, and this resulted in a paper "Sinusoidal modulation analysis for optical system MTF measurements", paper #1 in the appendix. (This is described slightly out of the actual temporal order for continuity in the description; the optical MTF based on sine wave filters was actually Dr. Yu's first project in the lab).

We measured the MTF of the sandwiched dual-energy system, for both the front ("reflection mode") CCD camera (CCD #1 in Figure 38), and for the back ("transmission mode") CCD camera (CCD #2 in Figure 38). In addition, we studied the influence of intensifying screens of different thickness (the Min-R was a 34 mg/cm^2 Gd$_2$O$_2$S screen, the Lanex was a 60 mg/cm^2 Gd$_2$O$_2$S screen). The MTF curves are shown in Figure 41. While it was recognized that the limiting spatial resolution seen in this figure is about 8 cycles/mm for the Min-R screen and about 6 cycles/mm for the Lanex screen was lower than that required for clinical mammography, for the prototype system these system MTF curves were thought to be adequate to show proof of principle. (At the present time, however, one commercial vendor is seeking FDA approval for a digital mammography system which has a 5 cycle/mm limiting spatial resolution.)

SoW Task 3.2: Measure the DQE(f) of the system, and estimate the dose efficiency using the proposed Figure of Merit (FOM).

Noise power spectrum measurements were made using both screen types (Lanex and Min-R) in both sandwich positions (front, reflection mode and back, transmission mode), and these are shown in Figure 42. To compute the detective quantum efficiency (DQE(f)), the MTF(f) and NPS(f) measurements are combined with the known photon fluence (Q):

$$DQE(f) = \frac{k[MTF(f)]^2}{Q \; NPS(f)}$$

In the calculation of DQE(f), the photon fluence Q is needed, and a proceedings paper was produced which gives tables for determining the relative fluence based on the kV and half value layer of the x-ray beam (paper #14 in the appendix). The DQE(f) curves for the front and back detector components of the dual energy mammography system are shown in Figure 43.

The zero-frequency DQE values are partially representative of the quantum detection performance of the digital detector system. For the front Min-R screen, about 25%

quantum efficiency was achieved, while for the thicker Lanex screen a very respectable 45% quantum efficiency was achieved in the front, reflective position. However, for the back transmission detector, 17% efficiency was measured with the Lanex screen and 13% quantum efficiency was measured for the Min-R screen. Furthermore, because of the large amount of x-ray scatter reaching the back detector from the front detector and copper filter, we suspect that the measured DQE values are inflated. This is because the scattered photons increase the number of detected quanta (improving SNR and reducing NPS(f)), but they are not accounted for in the value of Q (since a methodology for incorporating scatter into the calculation of the DQE(f) has not been developed). However, for example if the scatter to primary $\approx$ 1, the value of Q should be doubled, reducing the DQE(f) by a factor of two. Consequently, we suspect that the actual DQEs of the back detector in the sandwich detector design are much lower than the 13% and 17% measured. While dual energy techniques based on sandwich detector design have been around for a decade or more[16-18], our experiments were focusing on dual energy *mammography*. Because of the heightened importance of dose efficiency in mammography, we were quite intent on developing a dual energy mammography system with excellent dose efficiency (i.e. good quantum detection efficiency and good DQE(f)). In hindsight it was obvious, but in attempting to apply the analytical tool of the DQE(f) to dual energy mammography, we realized the following: Whenever x-ray photons are passed through the breast, and then filtered (by the front intensifying screen and copper filter) prior to being detected by the rear detector, the quantum detection efficiency (and therefore the detective quantum efficiency – DQE(f)) will always suffer. We realized that the sandwich detector design for mammography will never achieve adequate dose efficiency for a clinically acceptable examination.

By the time we had designed and built the dual energy detector system discussed above, it was 1996, and exciting things were happening in the field in terms of digital detector technology. Specifically, amorphous silicon thin film transistor (*a*-Si TFT) imaging plates ("flat panel imagers") were becoming a reality. The PI was approached in February of 1997 by a manufacturer (Varian Imaging Products, Palo Alto, CA) of a *a*-Si TFT imager (with a 18 cm × 24 cm field of view, and 127 µm pixels) to assess the performance of the detector system. The PI entered into a funded research relationship with Varian, and has had the flat panel imaging system in his laboratory now for almost two years[19]. Although the pixel size is a bit larger than that desired for digital mammography, for the proof of principal aspects of the current dual energy research the ~4 cycles/mm limiting spatial resolution of the flat panel detector (see Figure 44) was considered adequate. The DQE was measured at 50 kV, with a mean exposure to the plate of 21 mR, and is shown in Figure 45. The DQE(f) at f=0 is seen to be about 25%. At higher exposure levels, the DQE improves as the system electronic noise becomes a smaller fraction of the signal.

With the flat panel detector in the laboratory, in addition to the rapid switching x-ray generator, we felt that we had an exceptional tool for studying *dual-pulse single detector* dual energy mammography, contrary to the title of the grant eluding to *single pulse dual detector* imaging. Thus, over the course of the research, we evolved substantially and

concluded that for a dual energy mammography technique with maximum dose efficiency, the switched kV, single detector approach was best.

SoW Task 3.3:Digitize film images and compare contrast and SNR to digital images.

This task was inter-related with the small clinical trail which was designed to image about 50 women using both conventional mammography and the dual energy imaging system. Because Task 5 was officially eliminated from the Statement of Work (see details below), the source of comparison images was never realized.

SOW TASK 4

SoW Task 4.1: Investigate the potential of neural networks to perform noise suppression and dual energy subtraction in a single pass.

The PI engaged in an evaluation of neural network techniques designed to perform dual energy subtraction. This project was conducted using computer simulation techniques. The optimal x-ray spectra as identified previously were used, and the optimal x-ray spectra for the 4 cm 50% glandular breast are illustrated in Figure 46. Over a range of calcium thicknesses from 0 to 3 mm, and over breast thicknesses from 3 to 5 cm, dual energy images were calculated. The low energy image, $I_L(x,y)$, was calculated using:

$$I_L(x,y) = \int_E \Phi_L(E) \; E \; e^{-\mu(E)t(x,y) - \xi(E)z(x,y)} \; f(E) \; dE$$

The low energy spectrum is represented by $\Phi_L(E)$, and the detector efficiency is represented by $f(E)$. The detector was considered to be a 60 mg/cm^2 Gd$_2$O$_2$S screen. The tissue attenuation coefficient is represented by $\mu(e)$, unit density calcium by $\xi(E)$, and the tissue and calcium thickness are $t(x,y)$ and $z(x,y)$, respectively. The high energy images were calculated using:

$$I_H(x,y) = \int_E \Phi_H(E) \; E \; e^{-\mu(E)t(x,y) - \xi(E)z(x,y)} \; f(E) \; dE$$

with the same definitions as above, except the subscript H refers to high energy. Flat field images were acquired (in simulation) for both the high $[I_{H,0}(x,y)]$ and low $[I_{L,0}(x,y)]$ energy x-ray spectra:

$$I_{H,0}(x,y) = \int_E \Phi_H(E) \quad E \; f(E) \; dE$$

$$I_{L,0}(x,y) = \int_E \Phi_L(E) \quad E \; f(E) \; dE$$

Letting $I'_L(x,y) = \text{Ln}\{ I_{L,0}(x,y) \div I_L(x,y) \}$ and $I'_H(x,y) = \text{Ln}\{ I_{H,0}(x,y) \div I_H(x,y) \}$, dual energy images were computed using linear decomposition by:

$$DE(x,y) = I'_L(x,y) - R\ I'_H(x,y)$$

The value of R is selected on an ad hoc basis to deliver the best tisssue subtraction. A value of 0.23 was used for the work presented here. The spectra $\Phi_L(E)$ and $\Phi_H(E)$ are illustrated in Figure 46. Tissue inhomogeneity was computed using software which generated hundreds of randomly placed spherical tissue blobs, and the maximum thickness of the inhomogeneous region was 2 cm (average thickness = 1 cm), and this was added to a 3 cm homogeneous slab, for an average total breast thickness of 4 cm. Various calcium based test objects were used in the study.

The neural network was a feed forward backpropagation network[20], with two input nodes (the data from the low and high image pixels), five hidden nodes were used, and one output node (the dual energy computed pixel value). The output of the neural network ranges from 0 to 1, and so images were re-scaled making use of the full 8 bit dynamic range of the display devices (monitor and laser film). Using a 400 pixel data set, the performance of the neural network was tested on data sets of un-logged data, with the results shown in Figure 47. Poor tissue cancellation resulted in this situation. The neural network performed much better when the logarithm was pre-calculated, as seen in Figure 48. This figure shows the results with no noise added, but is equivalent to the noisy data sets tested as well. The performance of standard linear decomposition is shown in Figure 49.

The simulated images are shown in Figure 50 for low exposure levels (LE=50 mR, HE=12.5 mR), and images for different exposure levels are illustrated in Figure 51 (80 mR/20 mR) and Figure 52 (2000 mR/1000 mR). On each image, 25 very subtle square calcifications were placed (only a few are visible on the photos). The images give a subjective impression concerning the performance of the neural network versus linear decomposition algorithms for reconstructing the dual energy images. To quantify the performance of the two algorithms, a set of images ranging in exposure levels (low energy exposures given, high energy exposure was half of this) from 12.5 mR up to 3200 mR. The detail SNR of 10 x 10 pixel calcium lesions of differing thicknesses were computed on all images using both algorithms, and the resulting SNRs are plotted in Figure 53. Whereas the neural network produced comparable SNR images at low exposure levels, the linear decomposition algorithm performed better at higher exposure levels (at high SNR).

While we have not abandoned completely the hopes of developing a robust neural network based dual energy algorithm, the results of our studies as represented in Figure 53 seem to indicate that neural networks do not perform as well as conventional approaches. Because this was a negative result, we did not pursue publishing it.

SoW Task 4.2:Develop image display software for the dual energy images, including algorithms for identifying calcifications on the dual energy images, and investigate the use of using color techniques for overlaying the microcalcifications onto the image.

This task is basically a segmentation study. It was hoped that the dual energy images would demonstrate calcifications with sufficient SNR that segmentation (that is, having the computer easily identify which pixels corresponded to calcifications) could be accomplished in a robust (here meaning with little human intervention) manner. While a simulated source of dual energy images was demonstrated above in Task 4.1, it was felt that segmentation software for images with computer generated texture would not necessarily be representative of that optimized for actual breast images. The acquisition of actual breast images was the goal of Task 5, but this aspect of the grant was officially eliminated as part of this grant (see below). Consequently, the development of the segmentation software was not possible given our lack of a clinical data set of dual energy images.

A project was initiated to produce a breast phantom which would be accurate in terms of its composition for use in dual energy mammography studies. A variety of common materials available at the grocery store were studied for their suitability as glandular or adipose breast constituents. Some of the items studies included salami, bologna, cheese, mayonnaise, water, various plastics, etc. It was found that gelatin was an excellent substitute for glandular tissue, and we experimented with various concentrations of gelatin to achieve the 1.04 density as reported by Hammerstein[21] for breast glandular tissue. Lard (pork fat is called *lard*, beef fat is called *tallow*) was found to be an excellent substitute for adipose tissue, with a measured density of 0.93, identical to Hammerstein's measurements for breast adipose tissue. A 50%/50% mixture of lard and gelatin was mixed and placed into a plastic mold which has the approximate shape of a 4 cm compressed breast. The plastic is very similar to the skin layer as reported by Hammerstein. The phantom was imaged using 50 kV and 120 kV x-ray spectra with the flat panel detector system. A picture of the setup is shown in Figure 54. The low energy, high energy, and dual energy subtracted (linear decomposition) images are shown in Figure 55. A profile through the image data (at the line shown on the dual energy image illustrated in Figure 55) is shown for the three images in Figure 56. The dual energy subtraction acts to reduce a great deal of the structure noise due to the tissue inhomogeneity, as expected.

SoW Task 5

Task 5 involved a pre-clinical trial involving approximately 50 patients. The study section review of the original proposal recommended that this component of the project be deleted. Given the 27% cut in requested funding that associated the award of this grant, the PI wrote the Command and received permission to delete Task 5 from the Statement of Work for this grant. The letter documenting this change is included in the Appendix.

KEY RESEARCH ACCOMPLISHMENTS

ACCOMPLISHMENTS

Our principal accomplishment was the realization that single pulse dual detector mammography is a bad idea, because of the poor DQE of the back detector. Basically, single x-ray pulse dual energy techniques make use of a broad x-ray spectrum incident upon the breast, and achieve energy separation based on either k-edge effects (the binary screen design) or x-ray filtration effects (the sandwich detector design). Neither of these techniques are as dose efficient as simply exposing the breast to two different x-ray beams in a dual x-ray pulse approach. The compression used in modern mammography acts to immobilize the breast, and thus a rapid sequence dual x-ray exposure technique is possible assuming that a detector exists with rapid readout as well. We have demonstrated the ability to switch our constant potential x-ray generator between 50 kV and 120 kV in as little as 30 milliseconds. However, the readout time of the flat panel imager at 127 μm resolution requires about 5 seconds. By binning 2 × 2 pixels together in the readout, 33 millisecond readout is possible (fluoroscopic mode), but the limiting spatial resolution of the 254 μm pixels becomes unacceptable low (Nyquist = 2 cycles/mm) for mammography. Rotating or translating two flat panel imagers may be a solution to this problem, however we remained focussed in the physics problem, not the engineering details.

In the process of studying the problem of dual energy mammography, we accomplished several other things related to mammography in general. The spectral models developed under the funding provided by this grant are probably the most accurate computer generated spectral models available (since they really just interpolate measured x-ray spectra, the gold standard), and we have distributed them on the world wide web to make them widely accessible. The PI has received E-mail inquiries from all over the world concerning these models.

The calculation of DgN values for all possible x-ray spectra, including those ranging up to 120 keV, will make it possible for others (and for us to continue) to study the possibility of using alternate x-ray spectra for mammography. We feel that this is extremely important in an era where digital mammography systems are soon to become a clinical reality. It is widely thought that alternate anode materials will be useful for digital mammography, for example the Fischer scanning slot mammography system pushes tube loading characteristics of the x-ray tube, and tungsten anodes will probably be required for such a system. Tungsten is a better x-ray tube anode material than molybdenum (used in conventional screen-film mammography) because it is more efficient ($\varepsilon \propto Z^2$) and has better heat loading properties (very high melting point of 3300 °C). Our compilation of DgN values for various non-standard anode-filter combinations, along with the more general monoenergetic DgN values will be useful for optimizing the x-ray spectrum used for digital mammography. The DgN values were reported for breast compositions ranging from 0% to 100% glandular, and for breast thicknesses

ranging from 2 to 12 cm, thus extending the data available to the small group of women with compressed breast thicknesses above 8 cm.

The optimal x-ray spectra for dual energy mammography have been identified, however we have not had a chance to complete the manuscript reporting this work yet. Once the manuscript is completed, submitted, and published, we will submit it to the Command as an addendum to this report.

Dual energy *radiography* is designed to use two energies to separate two different materials, tissue versus bone. By extension, dual energy mammography as originally envisioned in this grant was designed to separate tissue versus microcalcifications. However, over the course of study it has become clear that for dense breasts (the one's where dual energy techniques would be potentially useful for), the breast is composed of two different tissue types (adipose and glandular), each slightly different in terms of effective atomic number. Thus, dual energy subtraction is limited in terms of its ability to completely subtract the soft tissue structure. The dual energy image seen in Figure 55 demonstrates this. While this is a potential limitation for improving the detectability of microcalcifications (since tissue structure noise remains in the subtracted image), the PI has become recently interested in the analysis of breast density (Paper #7 in the appendix entitled "A breast density index for digital mammograms based on radiologist's ranking"). For a physical characterization of breast density at the original baseline screening, it may be useful to use dual energy mammographic techniques to evaluate the breast density characteristics of a women's breast, so decisions concerning subsequent screening modalities might be made. For example, women with dense breasts may be screening using some combination of MRI, digital mammography, ultrasound, dual energy mammography, and conventional mammography, depending on the density of her breasts.

WHAT WE FAILED TO ACCOMPLISH

The optimal x-ray spectra for a 4 cm 50% glandular breast (for example) are a 25 kVp Mo-Mo spectrum for the low energy x-ray beam, and a 95 kVp copper-filtered tungsten spectrum for the high energy x-ray beam (Figure 46). While we do have a Mo-Mo x-ray system (GE 600T) and a tungsten anode high kVp system (Toshiba CPG) in the research laboratory, they are two different systems. In our more recent studies using the flat panel detector for breast phantom work (i.e. Figure 54), it was not experimentally feasible to make the two acquisitions without significantly perturbing the alignment of the breast phantom. Thus, it was not possible to demonstrate *experimentally* the performance of dual energy mammography using the optimal x-ray spectra, and we were forced to compromise in our production of dual energy data for this grant by using the 50 kVp setting (lowest kVp possible on this system) on the Toshiba generator for the low-kVp x-ray beam. The half value layer of the 50 kVp Toshiba spectrum was over 2.0 mm of aluminum, much higher than the approximately 0.31 mm HVL of the 25 kVp Mo-Mo spectrum. Because of this limitation, we emphasized the computer simulation aspects of the proposal. Nevertheless, once the x-ray system is reinstalled in the PI's new laboratory (a move occurred across the street here recently), we intend to try mounting

the flat panel detector and the breast phantom holder on a computer controlled sliding platform, allowing accurate translation between the central beams of the two x-ray systems.

REPORTABLE OUTCOMES

PEER-REVIEWED PUBLICATIONS WHICH ACKNOWLEDGE GRANT DAMD17-94-J-4424

1. JM Boone, Tong Yu, J.A. Seibert, Sinusoidal modulation analysis for optical system MTF measurements, Med. Phys 23, 1955-1963, 1996
2. JM Boone and AE Chavez, Comparison of x-ray cross sections for diagnostic and therapeutic medical physics, Med. Phys 23, 1997-2005, 1996
3. T Yu, JM Sabol, JA Seibert, and JM Boone, Scintillating fiber optic screens: A comparison of MTF, light conversion efficiency, and emission angle with $Gd_2O_2S:Tb$ screens, Med. Phys. 24, 279-285, 1997
4. T Yu and JM Boone, Lens coupling efficiency: derivation and application under differing geometrical assumptions, Med. Phys. 24;565-570, 1997
5. JM Boone and JA Seibert, An accurate method for computer-generating tunsten anode x-ray spectra from 30 kV to 140 kV, Medical Physics 24;1661-1670, 1997.
6. JM Boone, TR Fewell, and RJ Jennings, Molybdenum, rhodium, and tungsten anode spectral models using interpolating polynomials with application to mammography, Medical Physics 24;1863-1874, 1997.
7. JM Boone, KK Lindfors, CS Beatty and JA Seibert, "A breast density index for digital mammograms based on radiologists' ranking", Journal of Digital Imaging 11: 101-115, 1998
8. JM Boone , NM Corrigan, ST Hecht, and DP Link, "Angiographic film subtraction using a laser digitizer and computer processing", Journal of Digital Imaging, 11: 159-167 (1998)
9. JM Boone, T Yu, and JA Seibert, "Mammographic spectrum measurement using an x-ray diffraction device", Physics in Medicine and Biology 43: 2569-2582 (1998)
10. JM Boone, JA Seibert, JM Sabol, and M Tecotzky, "A Monte Carlo study of x-ray fluorescence in x-ray detectors", Medical Physics 26, 905-916 (1999)
11. JM Boone, "Monte Carlo assessment of glandular breast dose for monoenergetic and high-energy polyenergetic x-ray beams", Radiology, in press

PROCEEDINGS PAPERS WHICH ACKNOWLEDGE GRANT DAMD17-94-J-4424

12. T Yu, JM Sabol, JA Seibert, and JM Boone, J Duryea and JA Seibert, Imaging consideration for scintillating fiber optic screens, Proc SPIE 3032: 137-141, 1997
13. T Yu and JM Boone, A diffraction spectrometer for spectral analysis of mammographic x-ray sources, SPIE 3336: 58-64, 1998
14. JM Boone, Spectral modeling and compilation of quantum fluence in radiography and mammography, SPIE 3336: 592-601, 1998

INFORMATICS – DATABASES WHICH WERE GENERATED BY GRANT DAMD17-94-J-4424

Four widely available databases were produced by this grant:

1. As part of the publication of our scientific efforts, the attenuation coefficients (from paper #2) are maintained on the world wide web by the American Institute of Physics, the publisher of the journal *Medical Physics*. http://www.aip.org/epaps/epaps.html. These data, which includes source code, allows the calculation of mass attenuation coefficients and mass energy attenuation coefficients for elements Z=1 through Z=100, over an energy range from 1 keV to 50 MeV.

2. The software for the general diagnostic spectral model (reported as Paper #5) is also available on the web at: http://www.aip.org/epaps/epaps.html. This software (including source code) allows the computation of general diagnostic x-ray spectra from 30 kVp to 140 kVp.

3. The software for the mammographic x-ray spectral models (reported as Paper #6) is available at the AIP website, http://www.aip.org/epaps/epaps.html. This software enables the calculation of mammography energy x-ray spectra from 18 kVp to 42 kVp, for molybdenum, rhodium, and tungsten anode targets. Subsequent mathematical filtering of the beam can be performed using the attenuation coefficients provided in Database #1, listed above.

4. A fourth source of information important for breast imaging will be distributed via E-mail by the PI, once the *in press* Radiology report (Paper #11) is published in October 1999. The publisher of Radiology does not support a website, so the PI will make available the data files corresponding to the DgN calculations to any interested party making an E-mail request (as mentioned in the paper).

CONCLUSIONS

We have produced a series of computer simulation tools which are useful in the area of optimizing the image quality and radiation dose efficiency of radiographic and mammographic procedures. These tools were specifically designed for use in optimizing dual energy mammography, and using them we were able to identify the most efficient x-ray spectra for dual energy mammography. These software tools (listed in the reportable outcomes section) include attenuation coefficients, four x-ray spectral models, and information necessary for evaluating the radiation dose to the breast for arbitrary incident x-ray spectra. These tools should continue to be useful for investigators studying dual energy mammography.

A sandwich design dual energy mammography system was designed, constructed, and tested. The system was capable of using single pulse dual detector or dual pulse dual detector acquisition strategies. After the evaluation of the results of these measurements, we have identified with confidence that the dual x-ray pulse (i.e. switched kV) method of dual energy acquisition is a mandatory requirement for dual energy mammography, because of the exceptional dose concerns of this examination. Conversely, we have found that sandwiched detector systems for dual energy mammography are not appropriate because of the exceptional amount of radiation that is wasted such a design.

One of the limitations identified by this work is that the two x-ray spectra required for kV-switched dual energy mammography (a Mo-Mo ~25 kVp beam and a W-Cu 95 kVp beam) need to be produced by two fundamentally different x-ray tube/generator systems. It is of course necessary to have the source (the focal spot) of both x-ray beams at the same location in space, to achieve two images without parallax errors. Thus, future research concerning dual energy mammography should include an evaluation of the feasibility of producing the high and low energy x-ray spectra from a single x-ray system.

"So What?"

The research funded under this grant has led to the following knowledge:

The search for a dual energy mammography technology should focus on a dual pulse (switched kVp) approach, using either one or two solid state detectors. Depending upon breast thickness and composition, the low energy beam should employ either Mo or Rh target material, while the high energy beam should be produced with a tungsten target.

The software tools mentioned above will continue to be useful for scientists working in optimizing screen-film, digital, and dual energy mammography.

BIBLIOGRAPHY

PEER-REVIEWED PUBLICATIONS WHICH ACKNOWLEDGE GRANT DAMD17-94-J-4424

1. JM Boone, Tong Yu, J.A. Seibert, Sinusoidal modulation analysis for optical system MTF measurements, Med. Phys 23, 1955-1963, 1996

2. JM Boone and AE Chavez, Comparison of x-ray cross sections for diagnostic and therapeutic medical physics, Med. Phys 23, 1997-2005, 1996

3. T Yu, JM Sabol, JA Seibert, and JM Boone, Scintillating fiber optic screens: A comparison of MTF, light conversion efficiency, and emission angle with Gd_2O_2S:Tb screens, Med. Phys. 24, 279-285, 1997

4. T Yu and JM Boone, Lens coupling efficiency: derivation and application under differing geometrical assumptions, Med. Phys. 24;565-570, 1997

5. JM Boone and JA Seibert, An accurate method for computer-generating tunsten anode x-ray spectra from 30 kV to 140 kV, Medical Physics 24;1661-1670, 1997.

6. JM Boone, TR Fewell, and RJ Jennings, Molybdenum, rhodium, and tungsten anode spectral models using interpolating polynomials with application to mammography, Medical Physics 24;1863-1874, 1997.

7. JM Boone, KK Lindfors, CS Beatty and JA Seibert, "A breast density index for digital mammograms based on radiologists' ranking", Journal of Digital Imaging 11: 101-115, 1998

8. JM Boone , NM Corrigan, ST Hecht, and DP Link, "Angiographic film subtraction using a laser digitizer and computer processing", Journal of Digital Imaging, 11: 159-167 (1998)

9. JM Boone, T Yu, and JA Seibert, "Mammographic spectrum measurement using an x-ray diffraction device", Physics in Medicine and Biology 43: 2569-2582 (1998)

10. JM Boone, JA Seibert, JM Sabol, and M Tecotzky, "A Monte Carlo study of x-ray fluorescence in x-ray detectors", Medical Physics 26, 905-916 (1999)

11. JM Boone, "Monte Carlo assessment of glandular breast dose for monoenergetic and high-energy polyenergetic x-ray beams", Radiology, in press

PROCEEDINGS PAPERS WHICH ACKNOWLEDGE GRANT DAMD17-94-J-4424

12. T Yu, JM Sabol, JA Seibert, and JM Boone, J Duryea and JA Seibert, Imaging consideration for scintillating fiber optic screens, Proc SPIE 3032: 137-141, 1997

13. T Yu and JM Boone, A diffraction spectrometer for spectral analysis of mammographic x-ray sources, SPIE 3336: 58-64, 1998

14. JM Boone, Spectral modeling and compilation of quantum fluence in radiography and mammography, SPIE 3336: 592-601, 1998

PERSONNEL SUPPORTED ON THIS PROJECT

Personnel who received salary support from this grant

John M. Boone, Ph.D.
Karen K. Lindfors, M.D.
J. Anthony Seibert, Ph.D.
Andres E. Chavez, M.S.
Tong Yu, Ph.D.
Virgil N. Cooper, III, Ph.D.

REFERENCES

1. X. Wu, G. T. Barnes, and D. M. Tucker, "Spectral dependence of glandular tissue dose in screen-film mammography.", Radiology **179,** 143-148 (1991)

2. X. Wu, E. L. Gingold, G. T. Barnes, and D. M. Tucker, "Normalized average glandular dose in molybdenum target-rhodium filter and rhodium target-rhodium filter mammography.", Radiology **193,** 83-89 (1994)

3. D. R. Dance, "Monte Carlo calculation of conversion factors for the estimation of mean glandular breast dose.", Phys.Med.Biol. **35,** 1211-1219 (1990)

4. H. P. Chan and K. Doi, "The validity of Monte Carlo simulation in studies of scattered radiation in diagnostic radiology.", Phys.Med.Biol. **28,** 109-129 (1983)

5. H. P. Chan and K. Doi, "Radiation dose in diagnostic radiology: Monte Carlo simulation studies.", Med.Phys. **11,** 480-490 (1984)

6. H. P. Chan and K. Doi, "Physical characteristics of scattered radiation in diagnostic radiology: Monte Carlo simulation studies.", Med.Phys. **12,** 152-165 (1985)

7. D. J. Klein, H. P. Chan, E. P. Muntz, K. Doi, K. Lee, P. Chopelas, H. Bernstein, and J. Lee, "Experimental and theoretical energy and angular dependencies of scattered radiation in the mammography energy range.", Med.Phys. **10,** 664-668 (1983)

8. J. M. Boone, "Color mammography. Image generation and receiver operating characteristic.", Invest.Radiol. **26,** 521-527 (1991)

9. J. M. Boone, G. S. Shaber, and M. Tecotzky, "Dual-energy mammography: a detector analysis.", Med.Phys. **17,** 665-675 (1990)

10. J. M. Boone and J. A. Seibert, "A comparison of mono- and poly-energetic x-ray beam performance for radiographic and fluoroscopic imaging.", Med.Phys. **21,** 1853-1863 (1994)

11. D. R. Dance, J. Persliden, and G. A. Carlsson, "Calculation of dose and contrast for two mammographic grids.", Phys.Med.Biol. **37,** 235-248 (1992)

12. H. P. Chan, K. L. Lam, and Y. Z. Wu, "Studies of performance of antiscatter grids in digital radiography: effect on signal-to-noise ratio.", Med.Phys. **17,** 655-664 (1990)

13. J. M. Boone, M. Tecotzky, and G. M. Alexander, "Binary screen detector system for single-pulse dual-energy radiography.", Radiology **183,** 863-870 (1992)

14. J.A. Seibert, T. Poage, and R. Alvarez, Implementation of an active detector for dual energy radiography (abstract). . Med.Phys. 25, A154. 1999. (abstract)

15. R. E. Alvarez, "Active energy selective image detector for dual-energy computed radiography.", Med.Phys. **23,** 1739-1748 (1996)

16. R. A. Sones and G. T. Barnes, "Noise correlations in images acquired simultaneously with a dual- energy sandwich detector.", Med.Phys. **16,** 858-861 (1989)

17. T. Asaga, S. Chiyasu, S. Mastuda, H. Mastuura, H. Kato, M. Ishida, and T. Komaki, "Breast imaging: dual-energy projection radiography with digital radiography.", Radiology **164,** 869-870 (1987)

18. J. T. Ho, R. A. Kruger, and J. A. Sorenson, "Comparison of dual and single exposure techniques in dual-energy chest radiography.", Med.Phys. **16,** 202-208 (1989)

19. J. M. Boone and J.A. Seibert DQE analysis of an amorphous silicon thin film transistor x-ray system for fluoroscopic imaging. Med.Phys. 25, A147. 7-1-1999. (abstract)

20. J. M. Boone, V. G. Sigillito, and G. S. Shaber, "Neural networks in radiology: an introduction and evaluation in a signal detection task.", Med.Phys. **17,** 234-241 (1990)

21. G. R. Hammerstein, D. W. Miller, D. R. White, M. E. Masterson, H. Q. Woodard, and J. S. Laughlin, "Absorbed radiation dose in mammography.", Radiology **130,** 485-491 (1979)

Appendix 1:

Letter concerning Statement of Work Task 5 follows this page

GRANT AGREEMENT

GRANT NO: DAMD17-94-J-4424 Modification P80001	EFFECTIVE DATE See Grants Officer Signature Date Below	GRANT AMOUNT $584,437.00	Page 1 of 1 D. Laspe 301-619-7147

PROJECT TITLE: Single-Pulse Dual-Energy Mammography Using a Binary Screen Coupled to
Dual CCD Cameras

CFDA 12.420

PERFORMANCE PERIOD: 15 July 1994 - 14 August 1998 (Research ends 14 July 1998)	PRINCIPAL INVESTIGATOR: Dr. John M. Boone
AWARDED AND ADMINISTERED BY: U.S. Army Medical Research Acquisition Activity ATTN: MCMR-AAA- A 820 Chandler St. Fort Detrick Maryland 21702-5014	**PAYMENTS WILL BE MADE BY:** EFT:T Army Vendor Pay 1-888-478-5636 DFAS-SA/FPA 500 McCullough Avenue San Antonio, TX 78215-2100
AWARDED TO: Regents of the University of California Office of Research 410 Mrak Hall University of California, Davis Davis, CA 95616-8671	**REMIT PAYMENT TO:** Regents of the University of California Office of Research 410 Mrak Hall University of California, Davis Davis, CA 95616-8671

ACCOUNTING AND APPROPRIATION DATA: NO CHANGE

SCOPE OF WORK:

The following change is made in the schedule of this grant:

  Task 5, which involves the use of human subjects, is deleted from the grant statement of work.

TOTAL AMOUNT OF AWARD: $584,437 (See payment schedule for Disbursement Schedule)
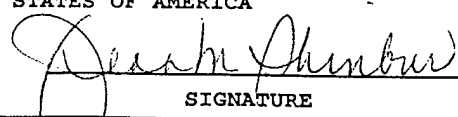
RECIPIENT	GRANTS OFFICER
ACCEPTED BY: _____ SIGNATURE	UNITED STATES OF AMERICA _____ SIGNATURE

NAME AND TITLE	DATE	NAME AND TITLE	DATE
Kevin M. Smith Vice Chancellor for Research	JAN 1 4 1998	JEAN M. SHINBUR GRANTS OFFICER	30 Jan '98

USAMRAA FORM 25-R-E, MAR 97 (Previous editions are obsolete)

FIGURE CAPTIONS

Figure 1
A series of measured x-ray spectra are illustrated in 1a. The data along each vertical line (marked A, B, and C) is re-plotted in the lower figure (1b) as a function of kVp. In the lower figure, the solid circles indicate the measured data and the connecting lines represent polynomial fits to that data. The spectral model is built up of such polynomial fits, spanning all 140 energies (up to 140 kVp) for this general diagnostic tungsten anode spectral model. So, for example, to compute the spectral fluece at 40 keV (Curve A) at 75 kVp, the polynomial equation at that keV is solved for. By computing polynomials at each energy in the spectrum for the specified kVp, any arbitrary x-ray spectrum from 40 to 140 kVp can be generated.

Figure 2
An example of four molybdenum anode spectra is shown. Each spectrum is normalized to 1 Roentgen.

Figure 3
Four spectra produced by the rhodium spectral model are illustrated.

Figure 4
Using measured spectral data from a thin beryllium window x-ray tube, a tungsten anode spectral model was produced in the mammographic energy range (18 KVP-42 kVp). The four spectra seen in this spectra were filtered with 50 micrometers of palladium.

Figure 5
The geometry incorporated in the Monte Carlo assessment of normalized glandular dose is illustrated.

Figure 6
A comparison between the DgN values of Dance are compared to the results produced by our Monte Carlo simulations. Good agreement is seen.

Figure 7
The DgN values of Wu, Tucker and Barnes are plotted as a function of the corresponding DgN values produced by our Monte Carlo model. Excellent correlation between the two data sets is demonstrated for the three breast compositions shown.

Figure 8

DgN values are shown for breast thicknesses ranging from 2 cm to 12 cm for polychromatic tungsten anode x-ray spectra. These data are for a 0% glandular breast composition.

FIGURE 9
The DgN values are shown for a 100% glandular breast for a polyenergetic tungsten anode x-ray spectra.

Figure 10
DgN values for zero percent glandular breast are shown for monoenergetic x-ray energy spanning from 10 – 115 keV, for 0% glandular breast.

Figure 11
Monoenergetic DgN values are shown for the 100% glandular breast.

Figure 12
The energy deposited as a function of depth into tissue is shown on this figure, comparing the calculated results using the Tart 98 software and our own Monte Carlo results. The Tart 98 results are plotted as lines, and the results from our Monte Carlo studies are shown as individual data points. Excellent agreement is seen.

Figure 13
The fractional energy absorbed (fraction of incident photon energy) is shown plotted as a function of energy for 100% glandular and 0% glandular (100% adipose) breasts. Results are compared between the Tart 98 package and our Monte Carlo code, and excellent agreement is seen.

Figure 14
The relative intensity of lateral scattering is compared with the work of Chan, and good agreement is seen. These data are for 100 keV monoenergetic x-ray photons.

Figure 15
The lateral scattering data of Chan at 40 keV are compared with our results, and again good agreement is seen. The geometry used in this simulation is illustrated as the inset on this figure.

Figure 16
Depth dose data from Chan and from our work are compared with good agreement.

Figure 17
The number of interactions per exit scatter photon was compared for four phantom thicknesses with the work of Chan and good agreement is seen.

Figure 18

The angular distribution of scatter radiation is shown. The measured data from Klein is compared with the Monte Carlo results produced in our laboratory. Excellent agreement is seen.

Figure 19
DgN values from three different sources (see key) are compared for three breast thicknesses and for kVps running from 23 to 35 kVp.

Figure 20
Scatter to primary ratios (SPR) are shown compared in this figure. The beam-stop data were measured in our laboratory, and the Monte Carlo data were computed in our laboratory. In this preliminary comparison, reasonable agreement is seen.

Figure 21
The figure of merit (FOM) is seen plotted as a function of kVp for a 3 mm soft tissue lesion (upper plot) and for a 50 micrometer microcalcification (lower plot). Arrows indicate the maximum in each curve corresponding to the optimal kVp for each breast thickness and each target.

Figure 22
The figure of merit is compared for Mo-Mo spectra and Rh-Rh spectra. The Mo-Mo spectra produce the higher FOMs for the 2 and 4 cm breast thicknesses, while the rhodium anode spectra produced the highest FOMs for the 6 and 8 cm breasts.

Figure 23
The figure of merit was modified as discussed in the text to minimize target contrast. Here, the target was a 50 micrometer mark of calcification. FOMs were computed from 50 – 140 kVp, and maximal FOMs (corresponding to *minimum* contrast with best noise and dose characteristics) occurred at 95 kVp for breast thicknesses from 2 – 8 cm.

Figure 24
X-ray spectra produced by the general diagnostic spectral model were heavily filtered (1.5 mm aluminum and 2 mm copper), and used in the FOM analysis for the high energy x-ray beam. The 80 kVp and 100 kVp x-ray spectra are illustrated here.

Figure 25
Using Monte Carlo methodology, the amount of secondary radiation detected in an intensifying screen was computed. The secondary radiation included both x-ray scatter (Rayleigh and Compton) and reabsorbed x-ray fluorescence. This figure shows the secondary to primary ratio (S/P) of energy absorbed in the detector as a function of polyenergetic kVp of a tungsten anode spectrum. Each of the five lines corresponds to a different screen thickness, as illustrated on the top figure. The results for gadolinium oxysulfide (top) and CsI (bottom) are shown. Most of the secondary radiation is reabsorbed x-ray fluorescence (as opposed to x-ray scatter), and therefore a large increase in the S/P ratio is seen above the K-edge of the phosphor.

Figure 26
The S/P ratios are demonstrated for Se (top) and for BaFBr (bottom) x-ray detectors. Because of the unique characteristics of selenium, different thicknesses were used in the simulation and these are illustrated in the top figure. The thicknesses for the BaFBr screen are as shown in Figure 25.

Figure 27
The S/P ratios are seen for $YTaO_4$ (top) and $CaWO_4$ (bottom) x-ray intensifying screens. As before, the S/P ratio increases markedly above the principal K-edge of the phosphor. Thicknesses are as shown for Gd_2O_2S in Figure 25.

Figure 28
The S/P ratio is seen for a hypothetical thorium oxide intensifying screen. The low S/P ratio is due to the very high K-edge (110 keV) of thorium. Thicknesses are as in Figure 25.

Figure 29
The amount of reabsorbed scatter energy deposition is plotted as a function of energy for five different screen thicknesses for the Ge_2O_2S phosphor. For realistic screen thicknesses, reabsorbed scatter represents approximately 10 percent of the entire signal just above the k-edge of the phosphor.

Figure 30
The lateral spread of energy deposition is illustrated for phosphors of differing thickness. These plots are similar to the point spread functions attributable to scatter and x-ray fluorescence. However, they are integrated over 2π. Notice that the ordinate is a logarithmic scale.

Figure 31
The quantum detection efficiency is illustrated as a function of energy for three x-ray phosphors commonly used in radiology. A large increase in photon absorption is observed at the principal K-edge of each phosphor.

Figure 32
The energy absorption is shown as a function of energy for the same three phosphors illustrated in the last figure. Due to the reemission of x-ray fluorescent photons, the increased energy absorption at the K-edge does not reflect the improvement demonstrated by photon absorption.

Figure 33
The grid transmission as a function of scatter angle is illustrated in this figure for 25 keV x-rays (top) and 40 keV x-rays (bottom). The three curves on each plot correspond to the grid interspace materials aluminum, carbon fiber (CF), and air.

Figure 34
The grid transmission as a function of angle is illustrated for different grid ratios, for the carbon fiber interspace grid (top) and for an aluminum interspace grid (bottom).

Figure 35
Grid transmission is illustrated as a function of energy for the carbon fiber (top) and aluminum (bottom) interspaced grids.

Figure 36
The figure of merit (maximizing contrast) was plotted as a function of grid ratio for four different energies and three different interspace materials, as indicated.

Figure 37
The design of the strut system used in the mechanical construction of the dual energy system is shown.

Figure 38
The system designed for single pulse, dual energy acquisition using a sandwiched detector is illustrated in this diagram.

Figure 39
A picture of the system diagramed in the last figure is shown. The two CCD cameras are seen in the foreground. Computer-controlled stepping motors were used to mechanically align the high and the low energy x-ray images. The breast phantom would be positioned against the entrant window, seen (with tape) towards the left of this figure. The light tight shroud was removed for this photograph.

Figure 40
The functionality of the alignment algorithm is diagramed in this figure.

Figure 41
The MTF values for both transmission and reflection mode imaging are shown. MTFs were measured using both Min-R and Lanex intensifying screens.

Figure 42
The noise power spectra are illustrated in this figure.

Figure 43
The detective quantum efficiency (DQE) of the dual energy dual detector sandwiched system are illustrated in this figure.

Figure 44
The MTF of the flat panel imaging plate is illustrated.

Figure 45
The DQE of the flat panel imaging system is shown.

Figure 46
The optimal dual energy spectra for a 4 cm breast (50% glandular) is shown. Each spectrum is normalized to 1 R exposure

Figure 47
The results of a neural network solution for dual energy image data, where logarithm was not computed on the image data. Poor tissue cancellation, as represented by the poor correction between actual and calculated calcium thickness, was observed.

Figure 48
When the neural network operated on previously logged data, excellent tissue cancellation was observed. This training set made use of 400 data points (pairs of pixel data), and 5 hidden nodes in the neural network were used.

Figure 49
Standard linear decomposition dual energy subtraction methods result in good performance, but residual due to non-linearities is seen as a broadening of the data towards small and large calcium thicknesses.

Figure 50
Four simulated images are seen, with the high energy (acquired) and low energy (acquired), and the linear decomposition dual energy (DE) image and neural network dual energy (DE) images shown as indicated in the key. Details of the simulations are given in the text. These images made use of 50 mR entrance exposure for the low energy image, and 12.5 mR for the high energy image.

Figure 51
These images made use of 80 mR entrance exposure for the low energy image, and 20 mR for the high energy image.

Figure 52
These images made use of 2000 mR entrance exposure for the low energy image, and 1000 mR for the high energy image.

Figure 53
The signal to noise ratio (SNR) is plotted as a function of exposure levels for three different lesion thicknesses. The linear decomposition results are shown as the solid lines, and the neural network results are shown as the dotted lines. At low SNR, the neural network technique appears to perform equivalently to the standard linear decomposition approach. At higher SNRs, however, the linear decomposition technique outperforms the neural network decomposition method.

Figure 54
The 50% adipose, 50% glandular breast phantom comprised of lard and gelatin is seen positioned in front of the flat panel detector system in the PI's laboratory.

Figure 55
The low energy, high energy, and dual energy subtracted images of the 50%/50% mammography phantom are illustrated. A calcium containing ramp and step wedge was also imaged simultaneously.

Figure 56
One line of the data from the three images shown in the previous figure is plotted in this figure. The position of the line is indicated on the dual energy image in Figure 55. Whereas the gray scale fluctuates in the acquired (low and high energy) images, the dual energy subtracted image shows reduced fluctuation due to the tissue subtractoin. The peaks corresponding to the two calcifications are visible (indicated by vertical lines). The remaining fluctuation in the dual energy subtracted image is a result of some noise, but is thought to be primarily due to the imperfect tissue cancellation resulting from the different tissue types in the image (adipose and glandular tissue, as represented by lard and gelatin in the phantom).

APPENDIX 2: FIGURES 1 THRU 56
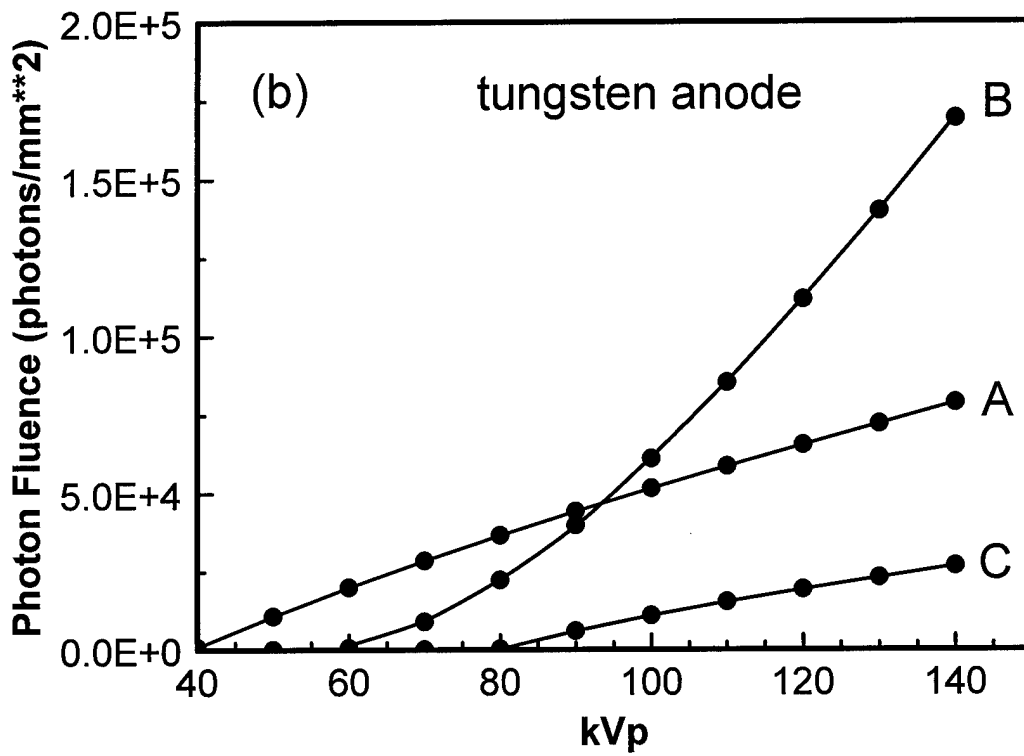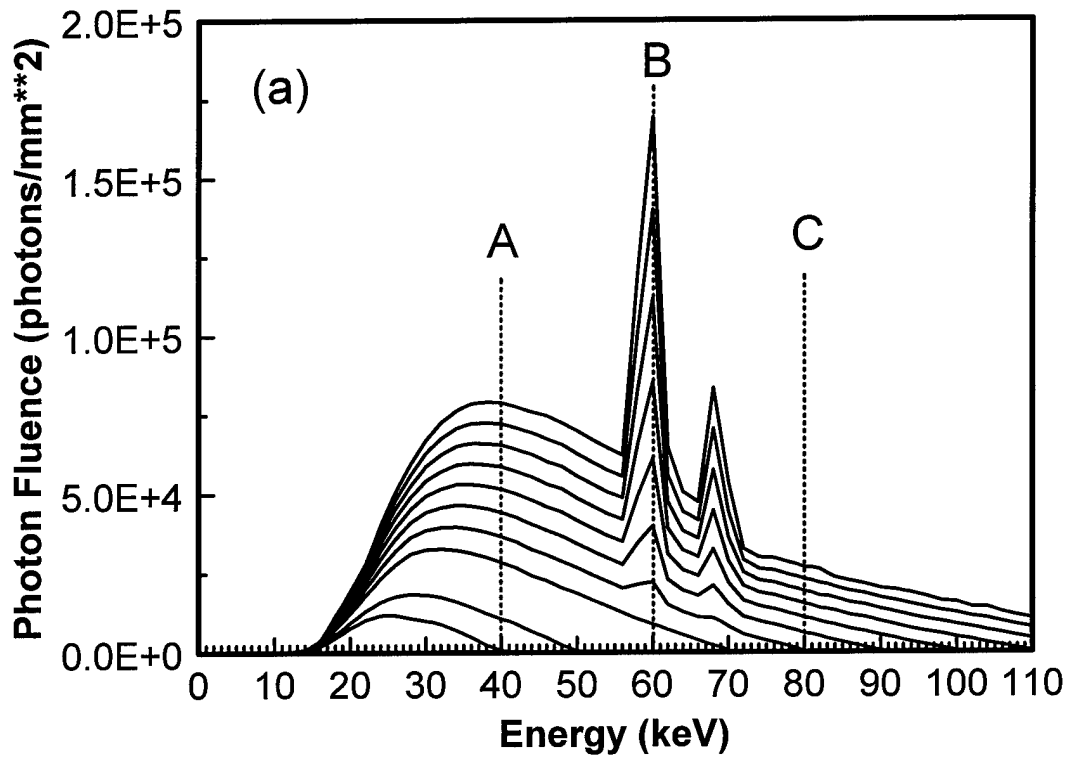
Figure 1
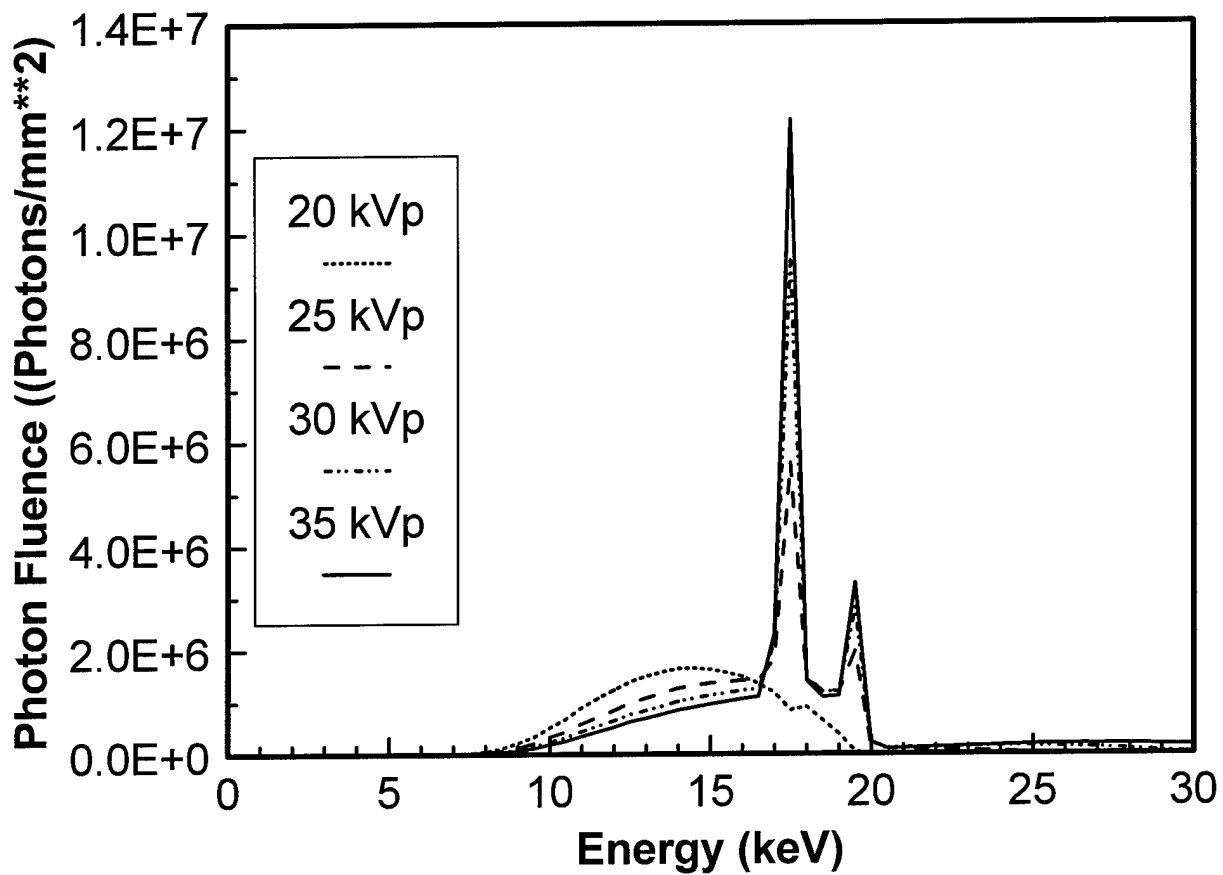
Molybdenum Spectral Model
Moly Filtration Added

Figure 2
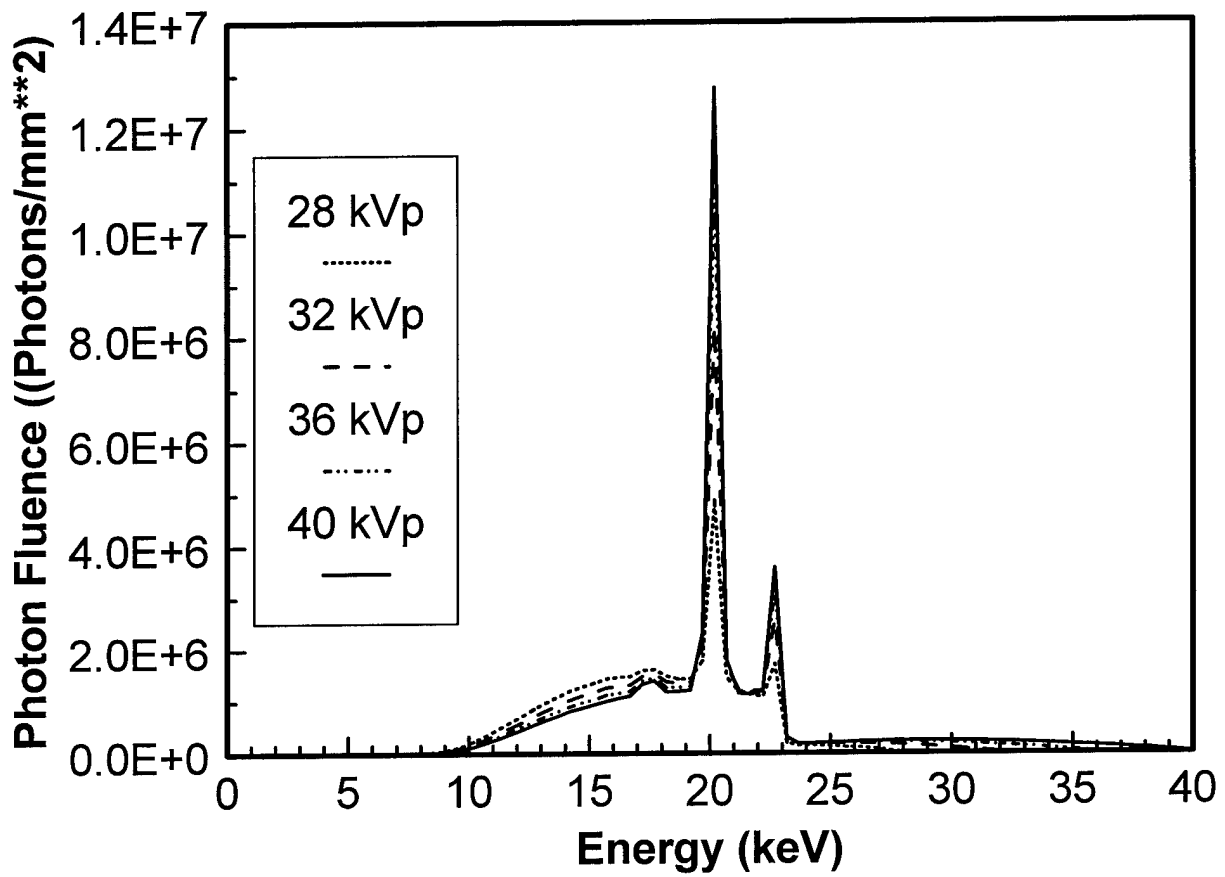
Rhodium Spectral Model
Rhodium Filtration Added

Figure 3
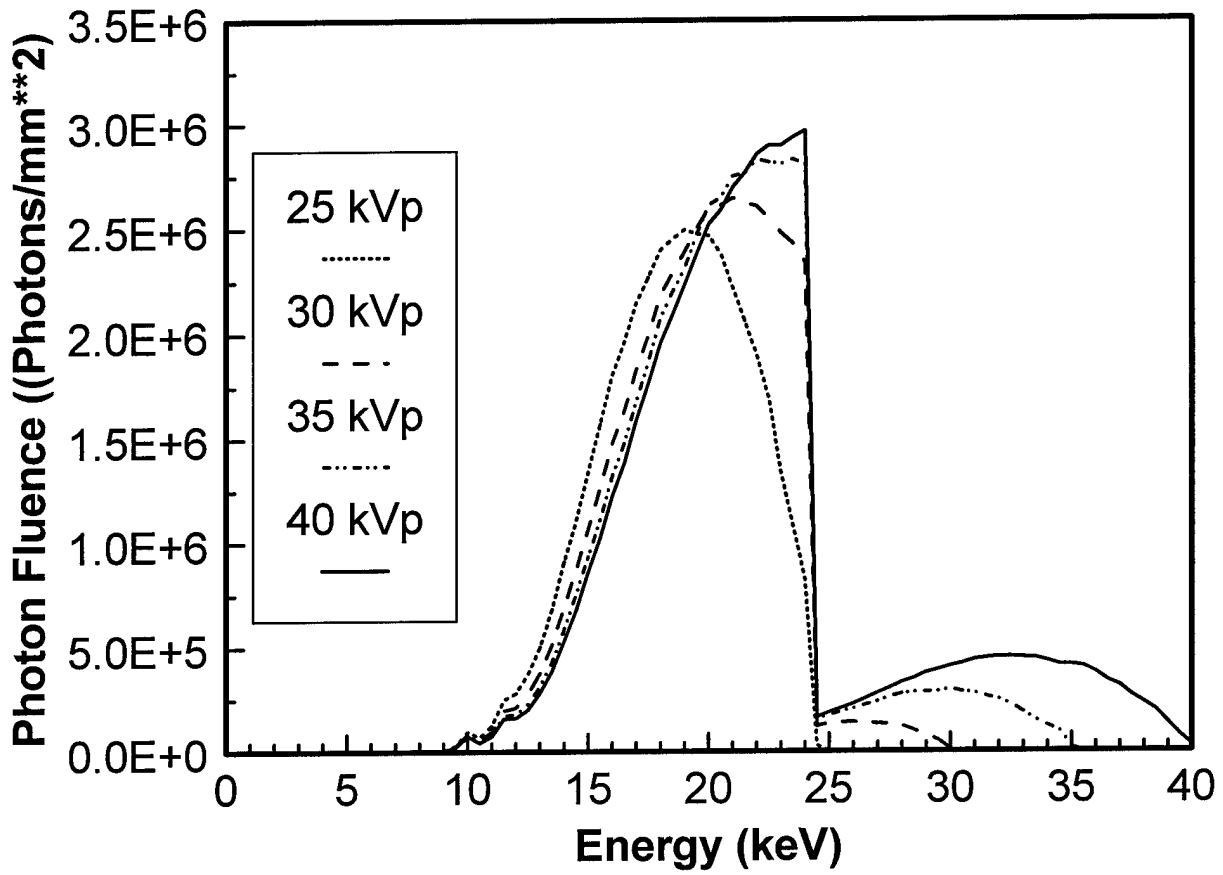
Tungsten Spectral Model
Paladium Filtration Added

Figure 4

Radiation Field

$T_{skin} = R_1 - R_2$

R_2

R_1

Top View

X-ray Source
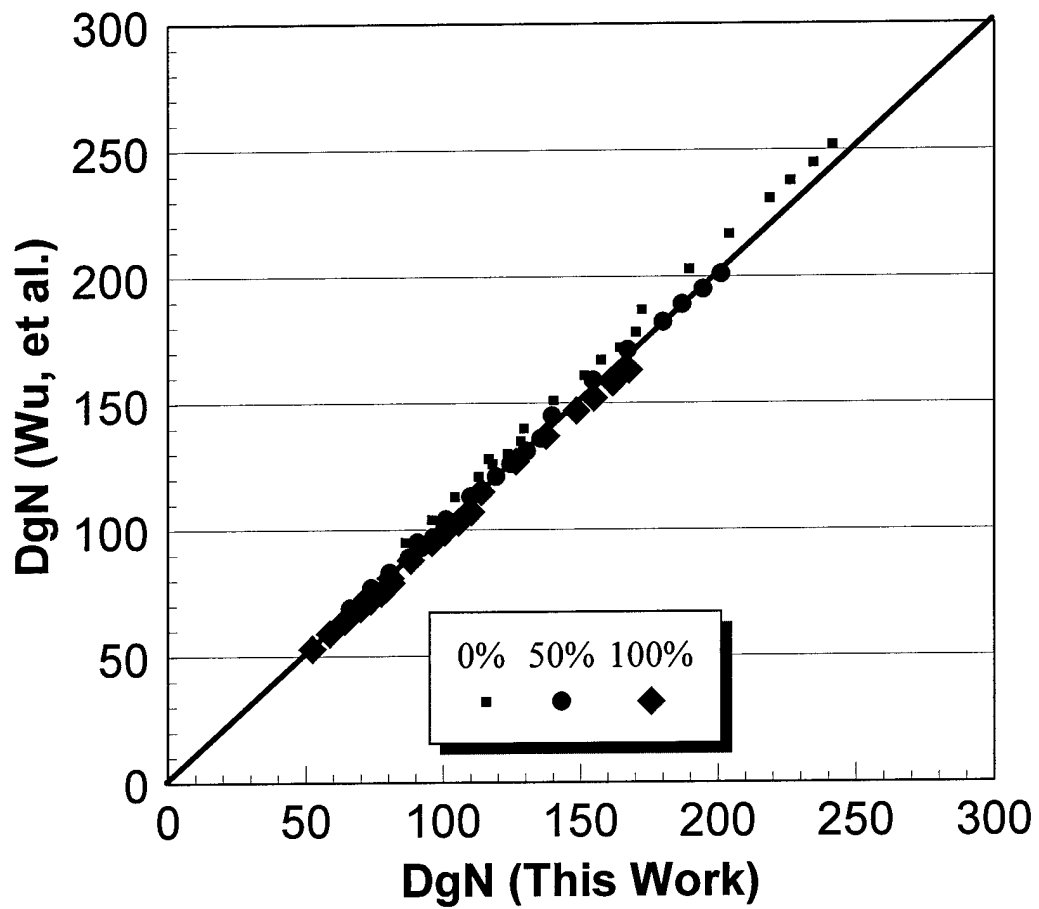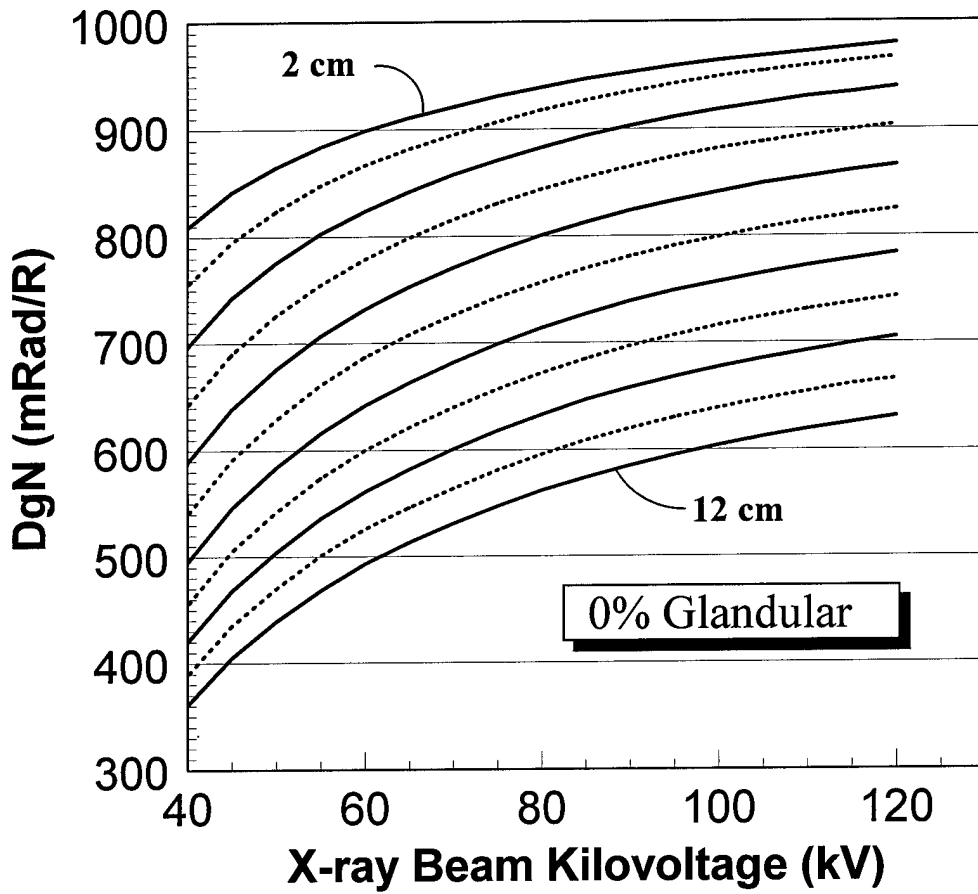
SID

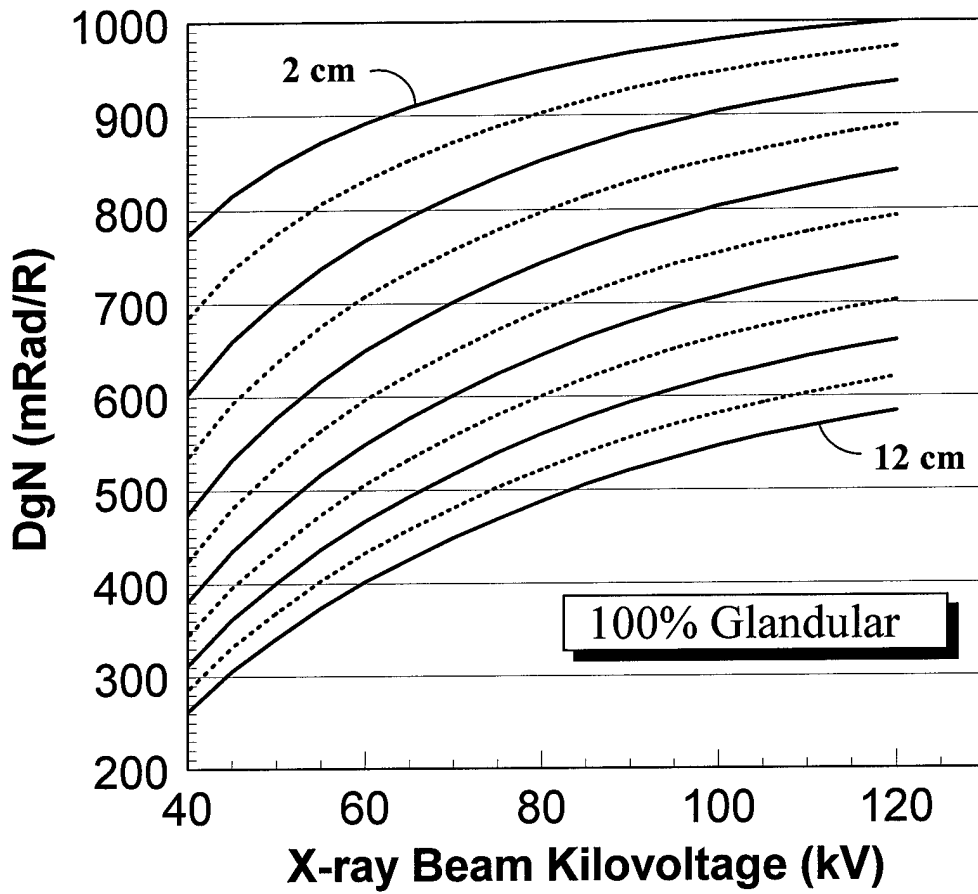T_{skin}

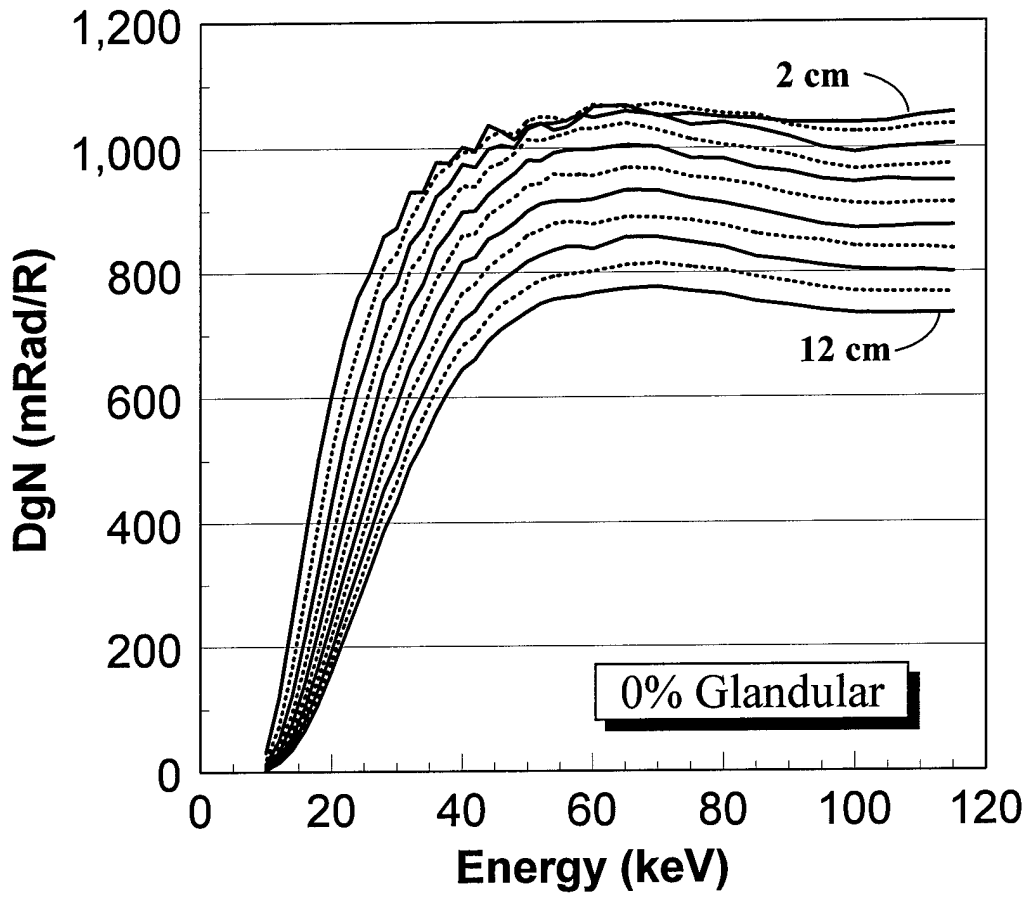T_{skin}

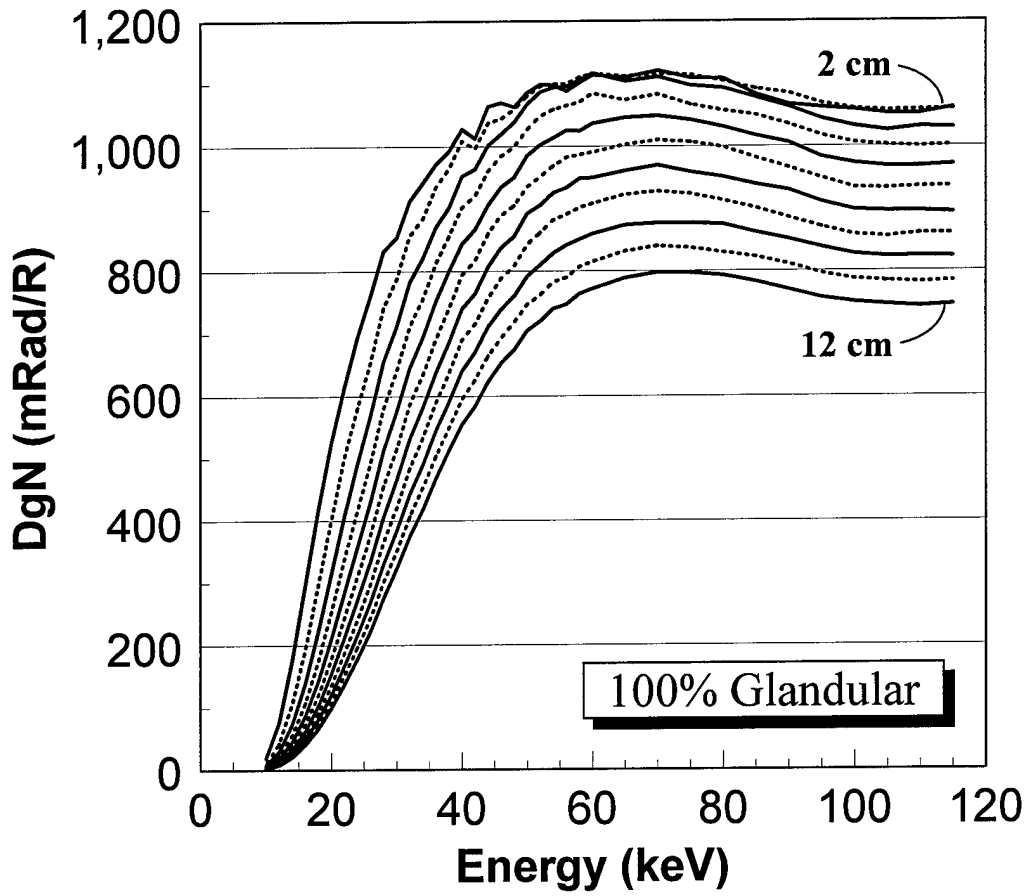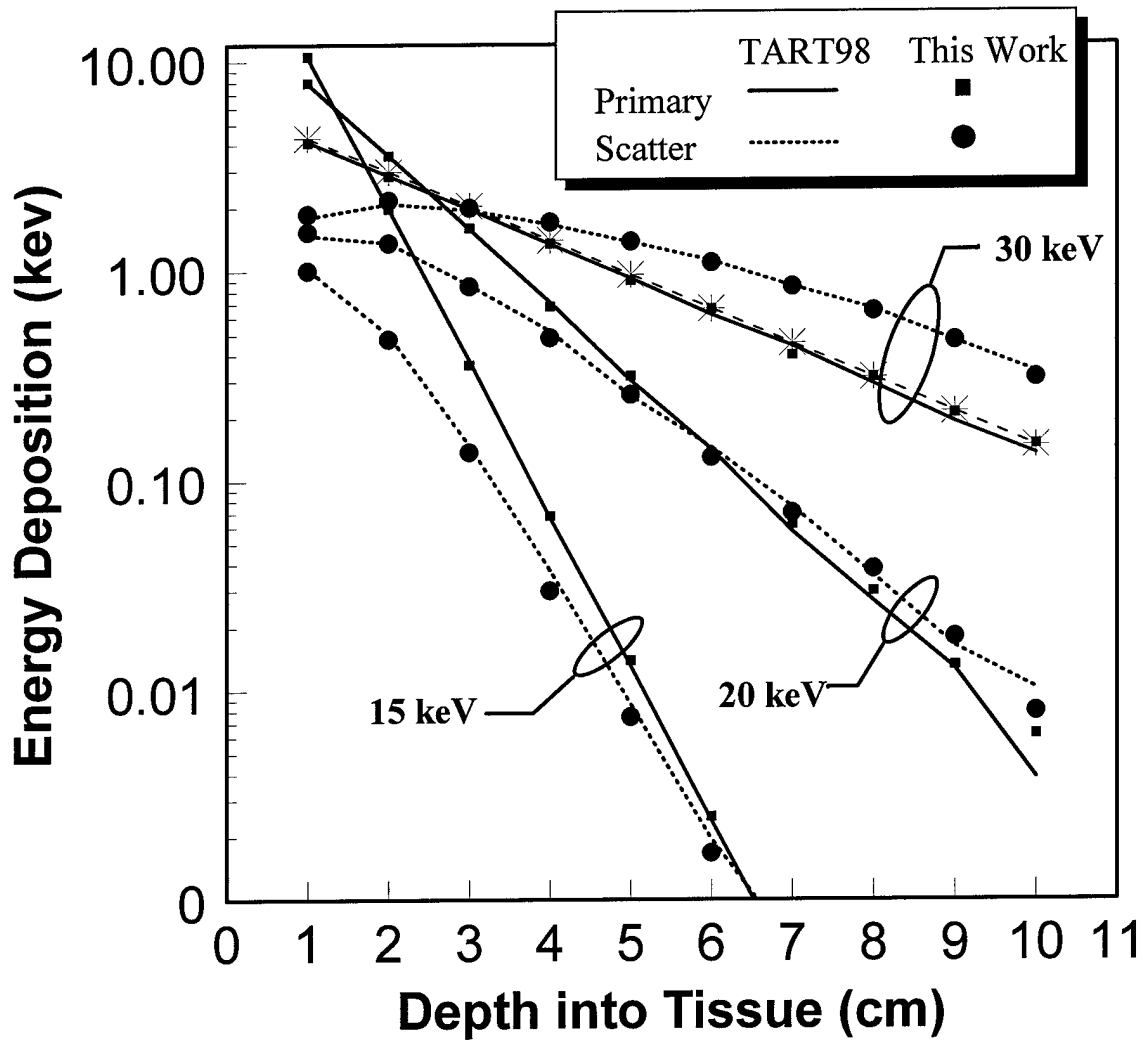T

Skin

Breast Tissue

Side View
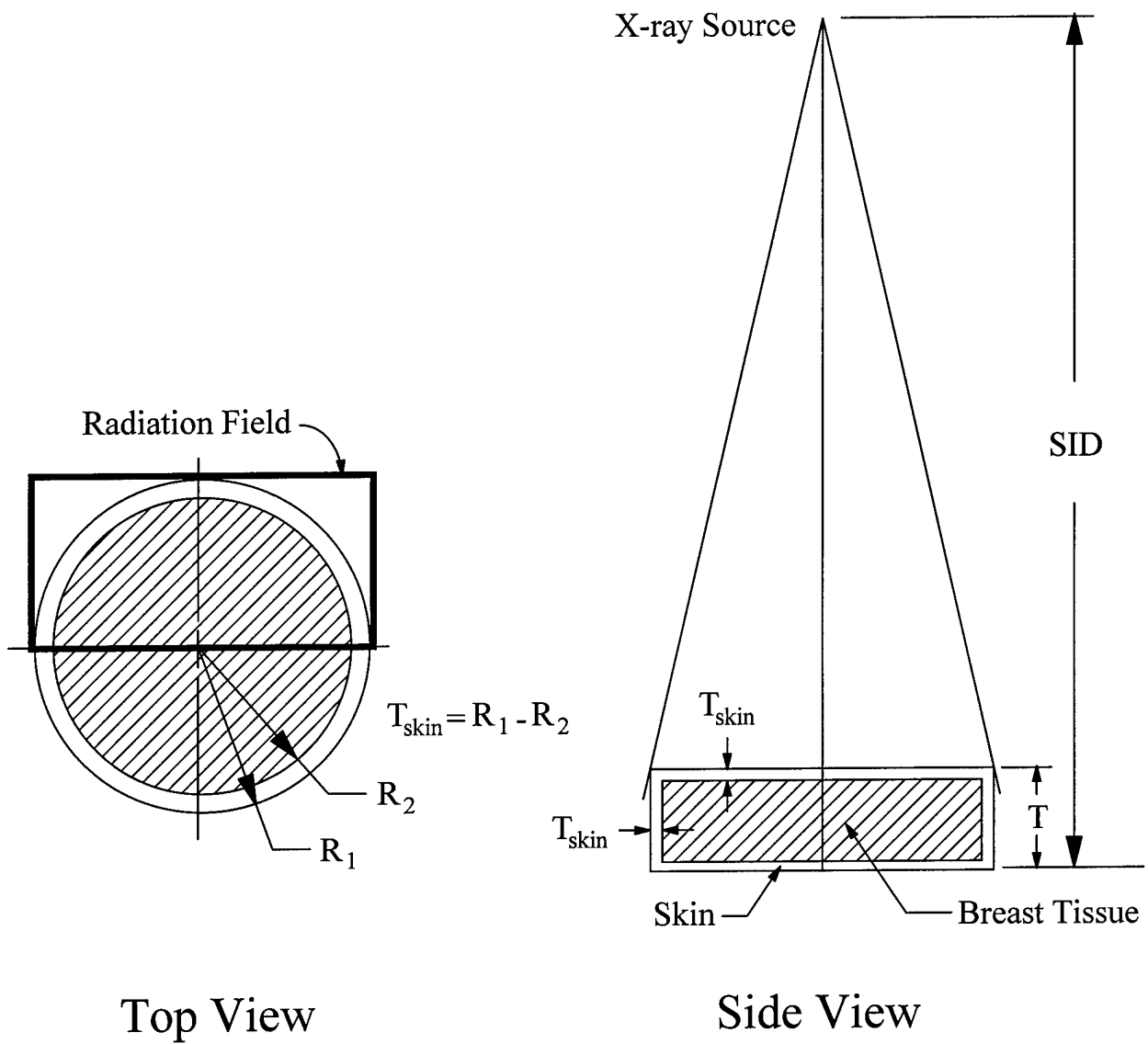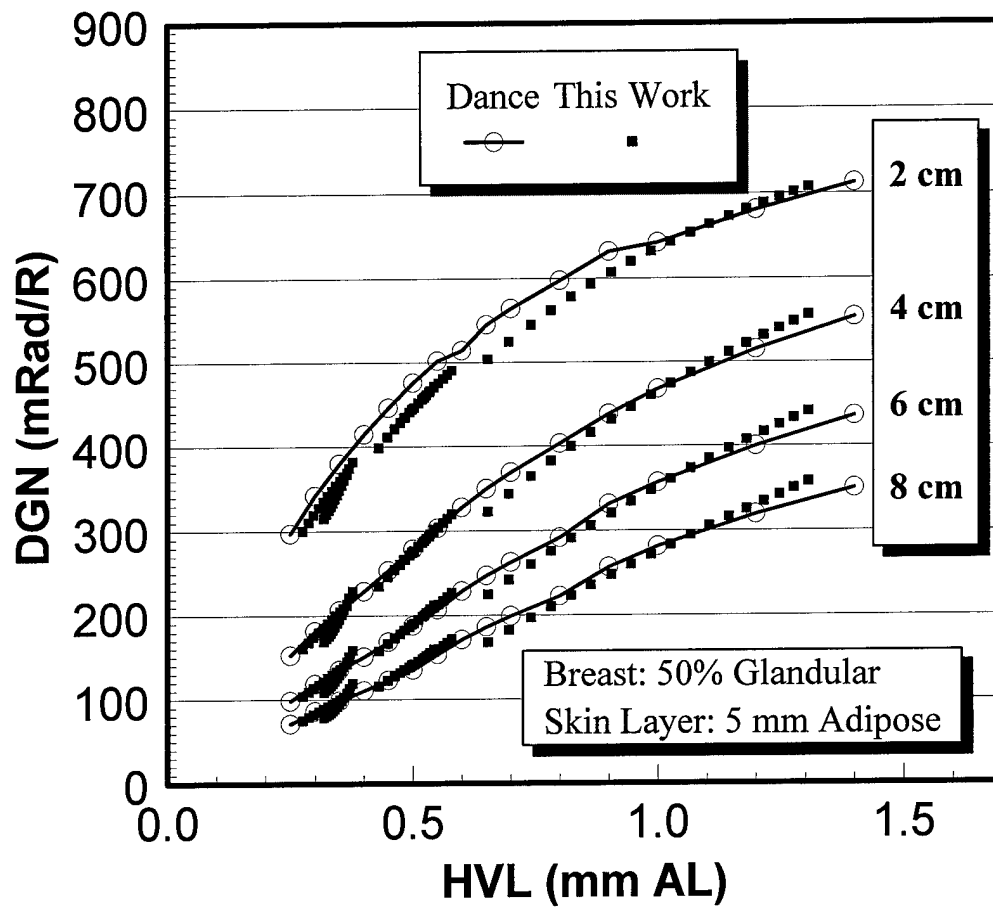
Figure 5

Figure 6

Figure 7
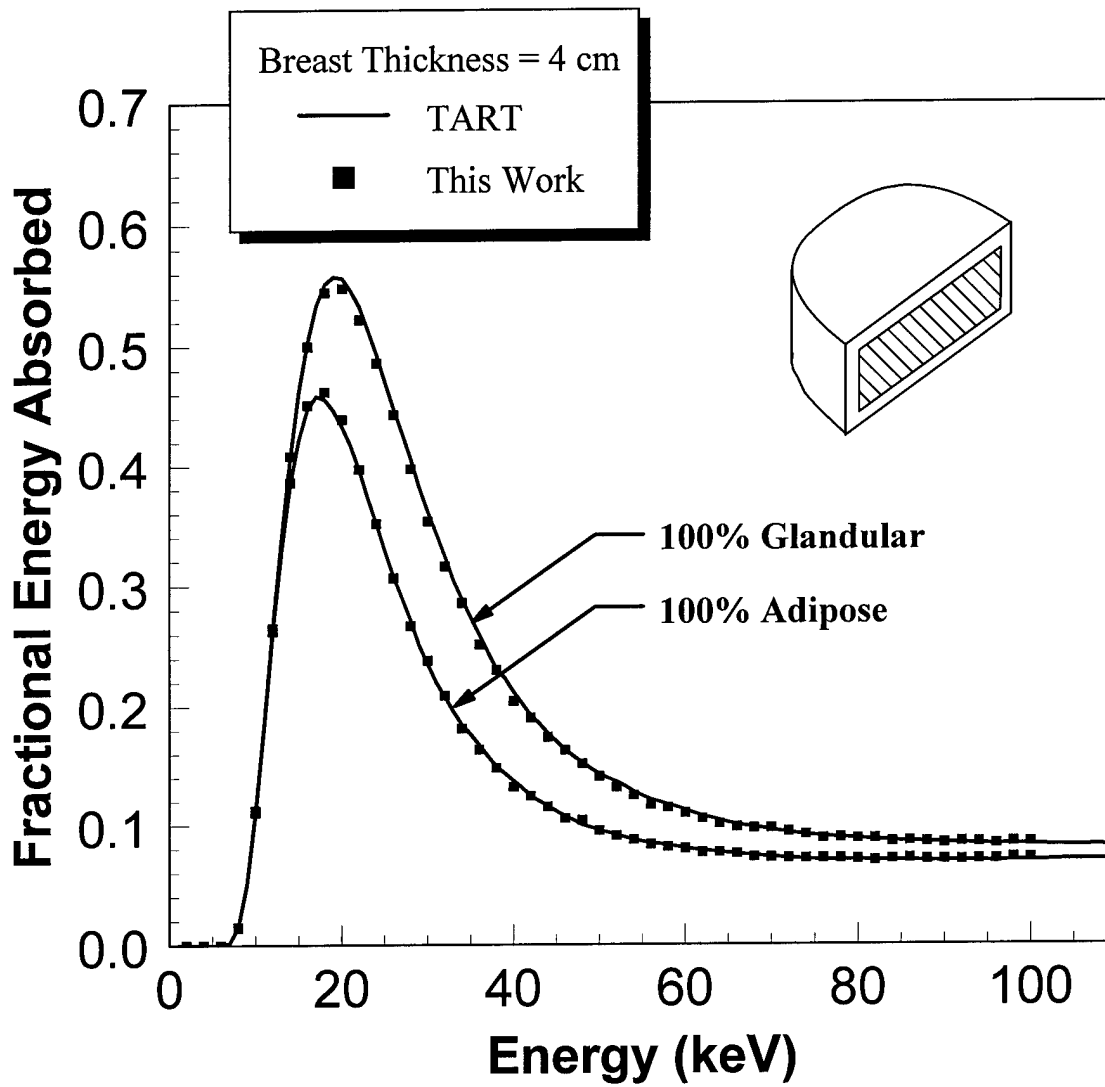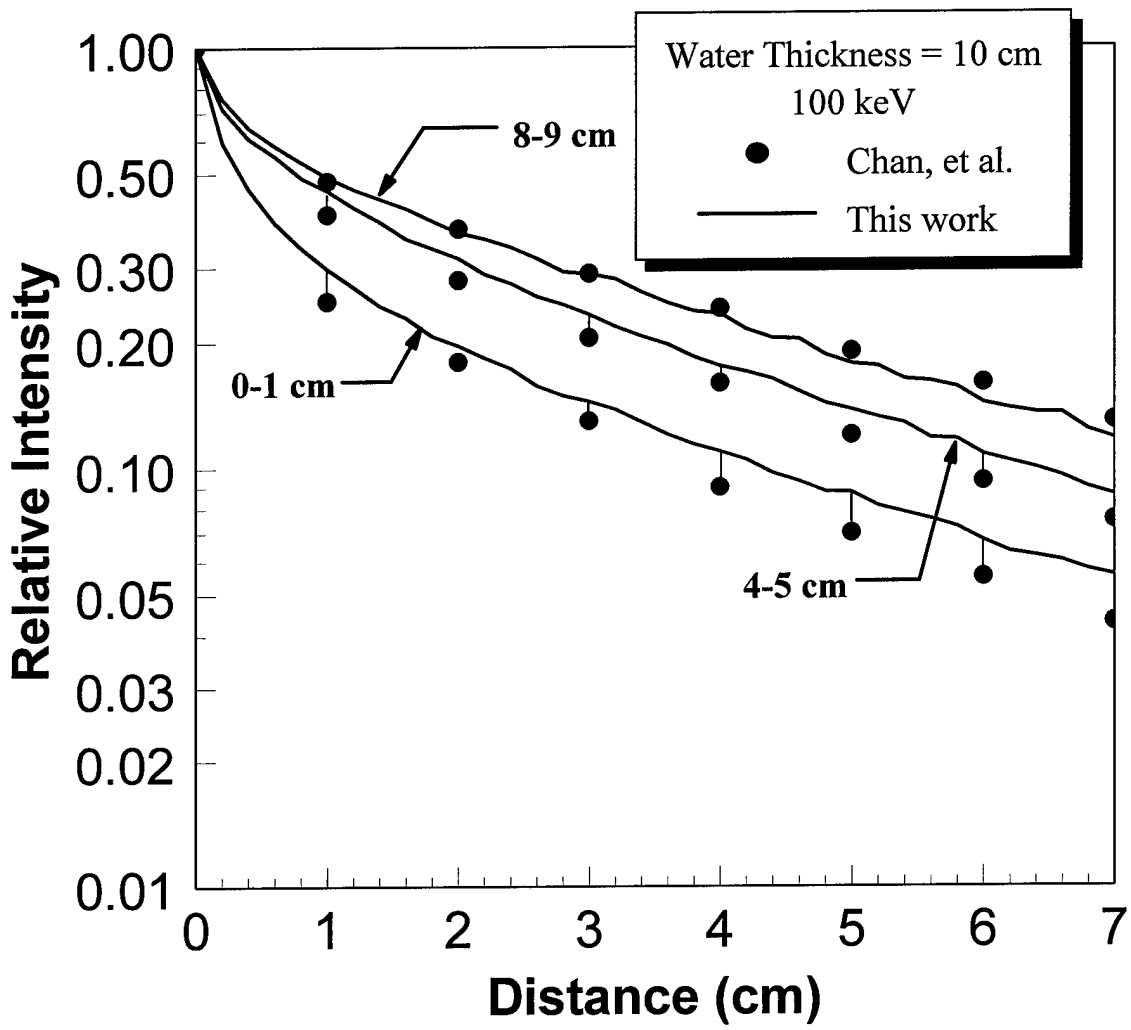
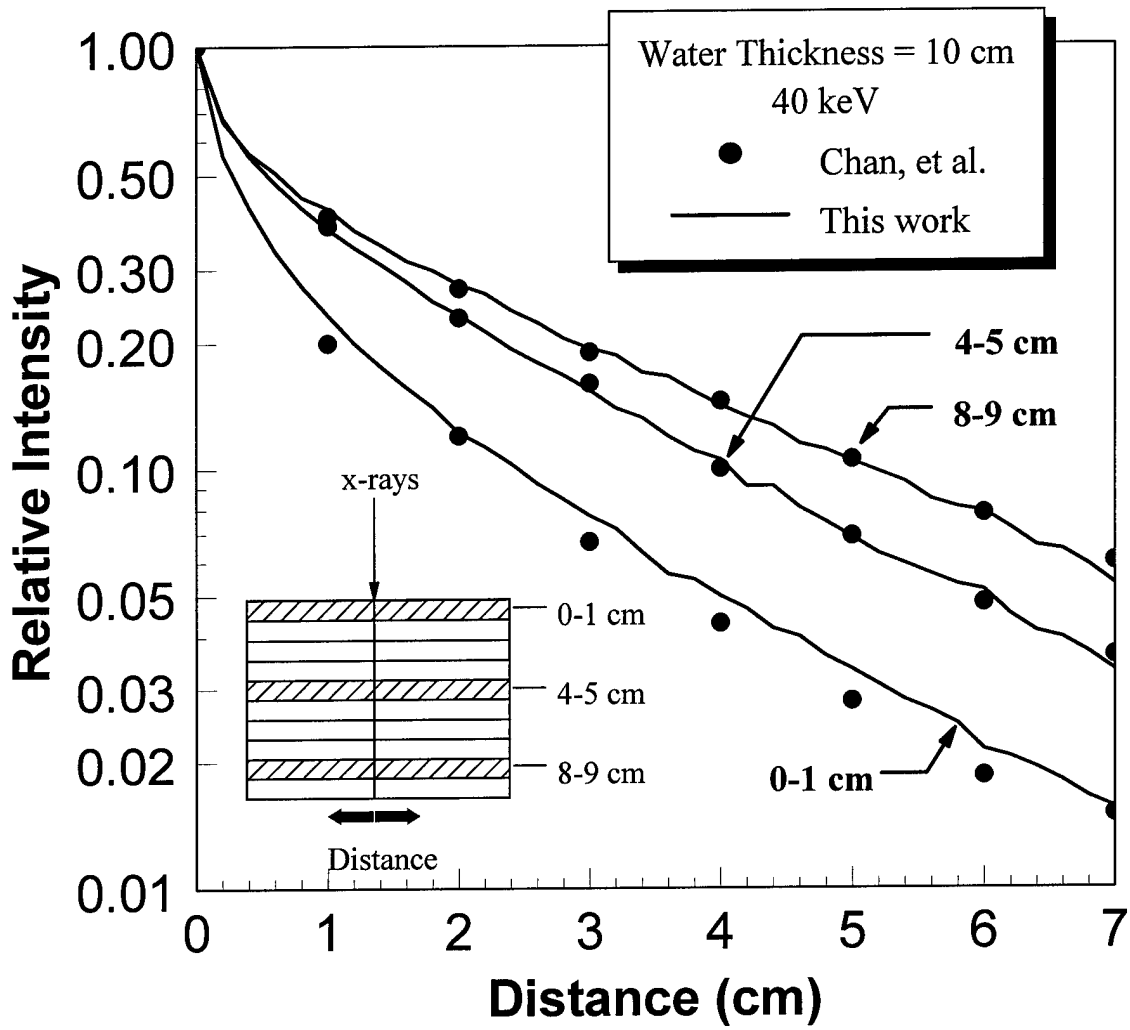Figure 8

Figure 9
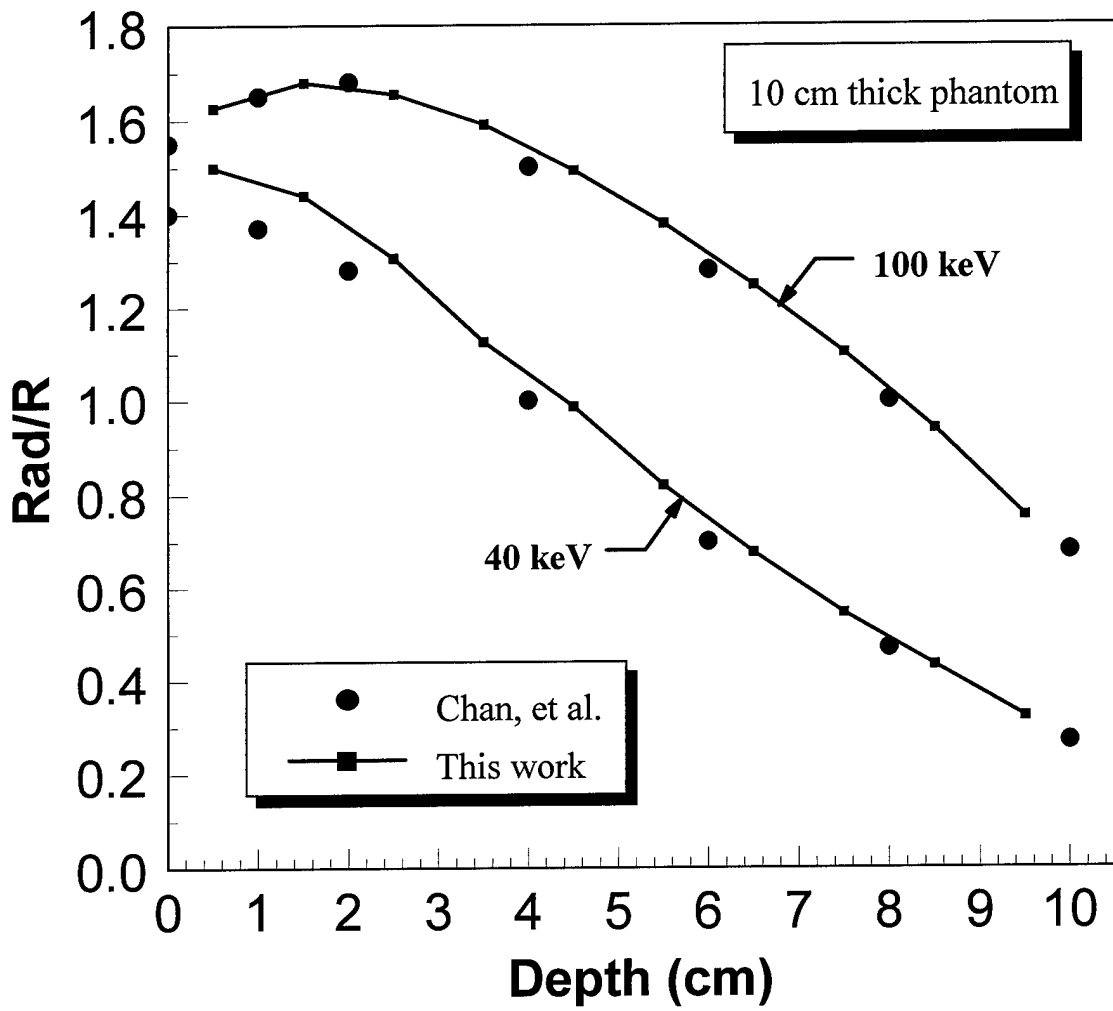
Figure 10

100% Glandular
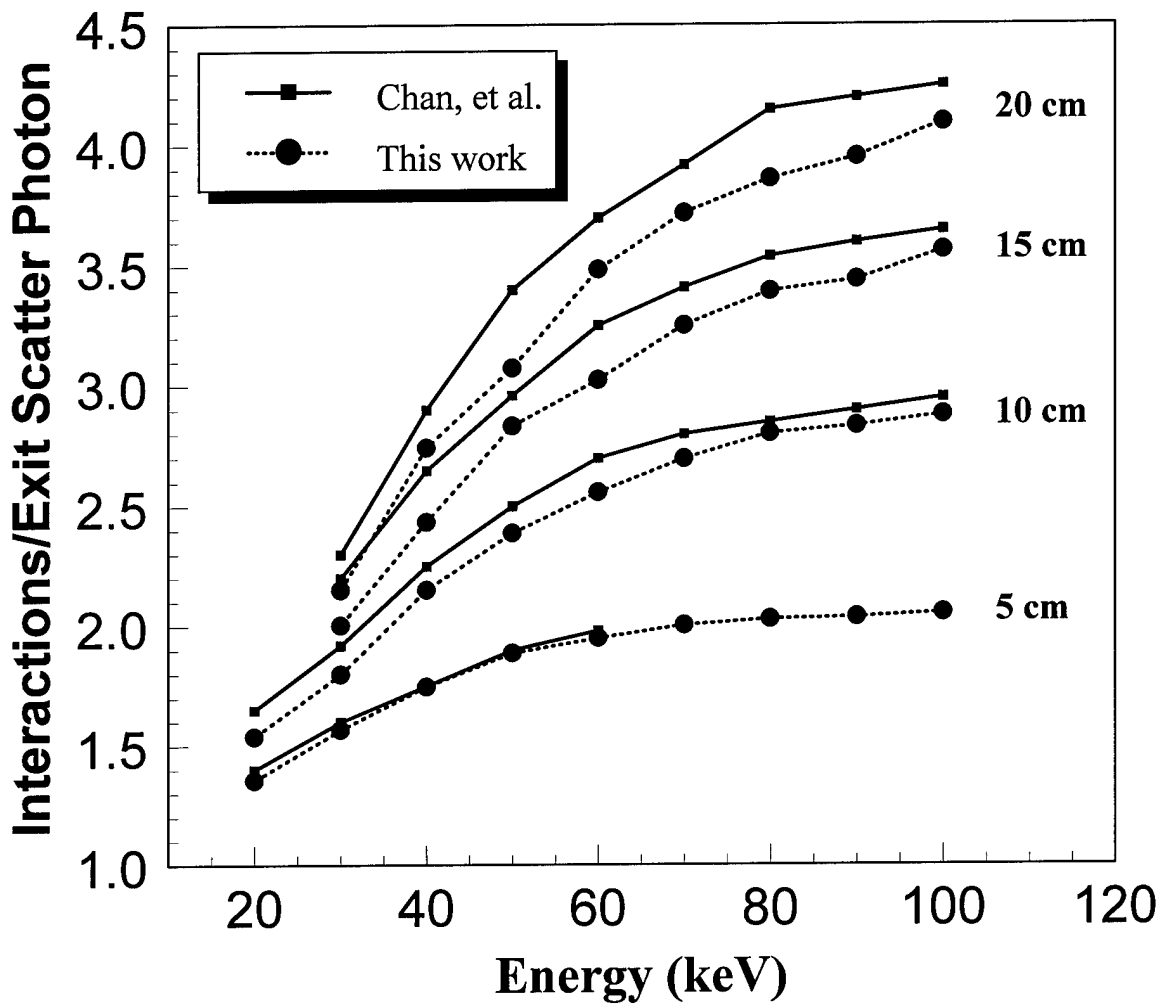
Figure 11

Figure 12

Figure 13

Figure 14

Figure 15

Figure 16

Figure 17
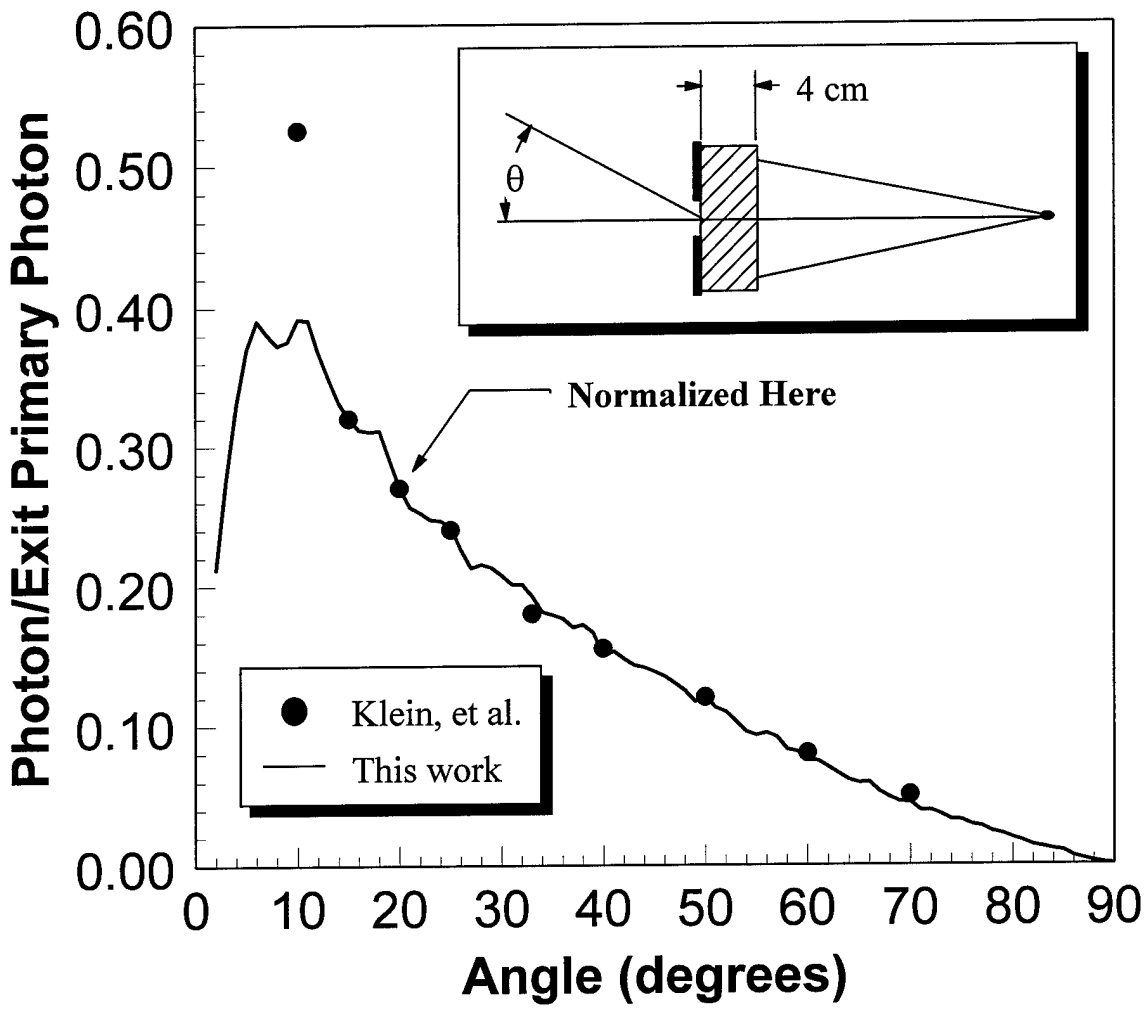
Figure 18
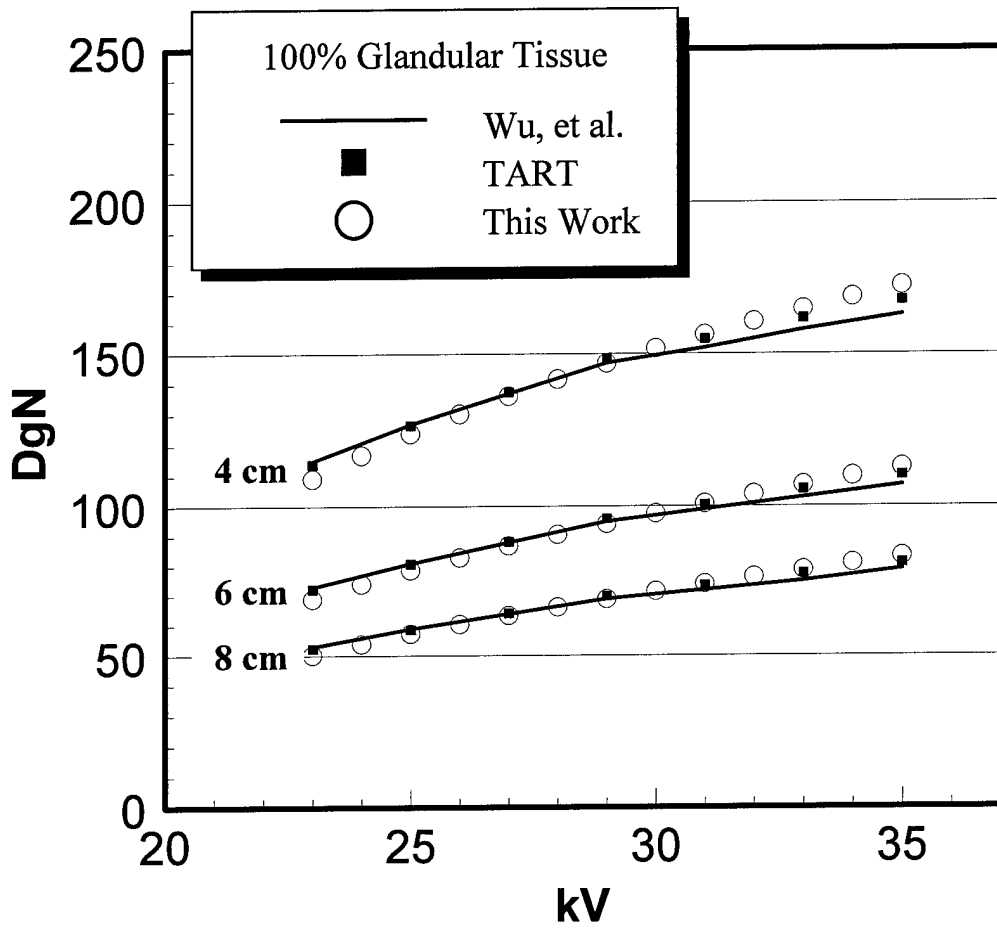
Figure 19
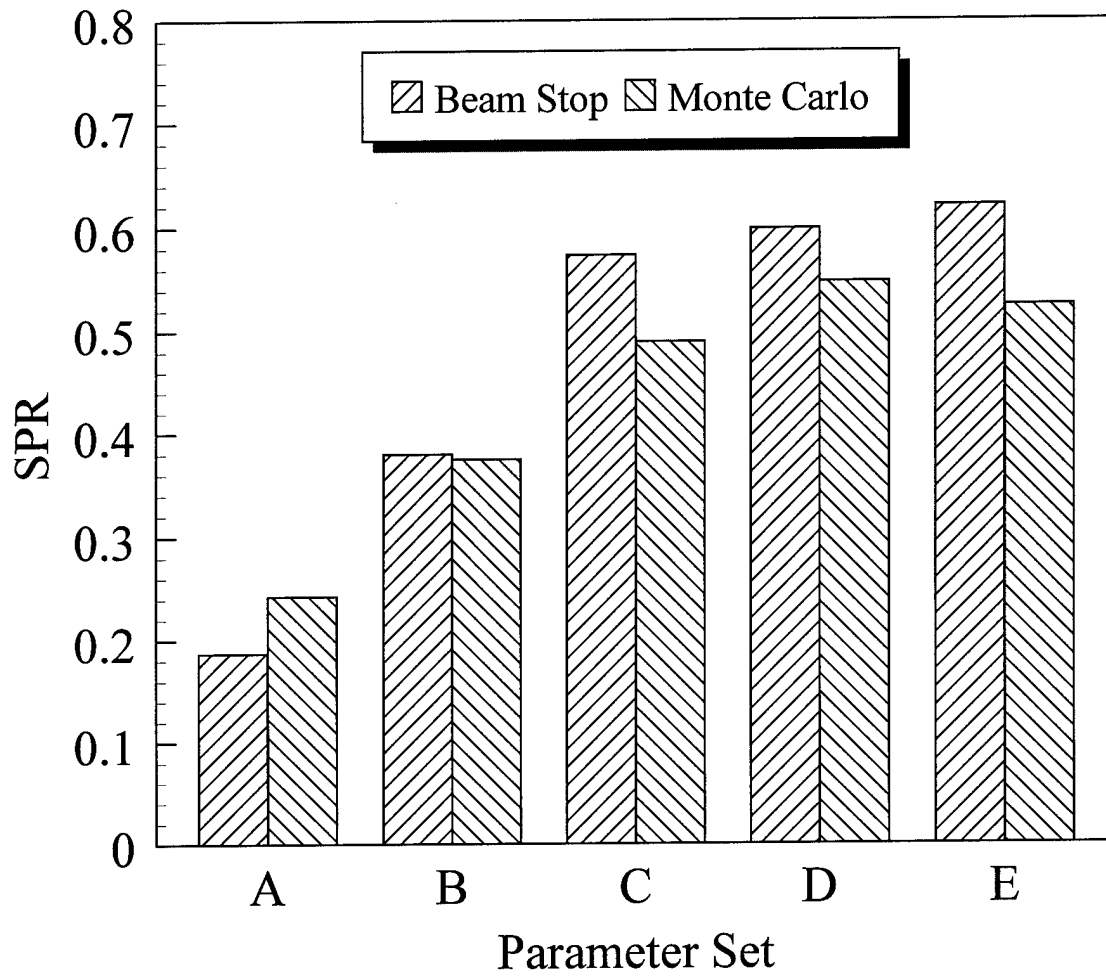
A = 2 cm 100% glandular 24 kV
B = 4 cm 50% glandular 28 kV
C = 6 cm 50% glandular 32 kV
D = 6 cm 100% glandular 32 kV
E = 6 cm   0% glandular 36 kV

Figure 20

50% Glandular, 5:1 Air Core Grid
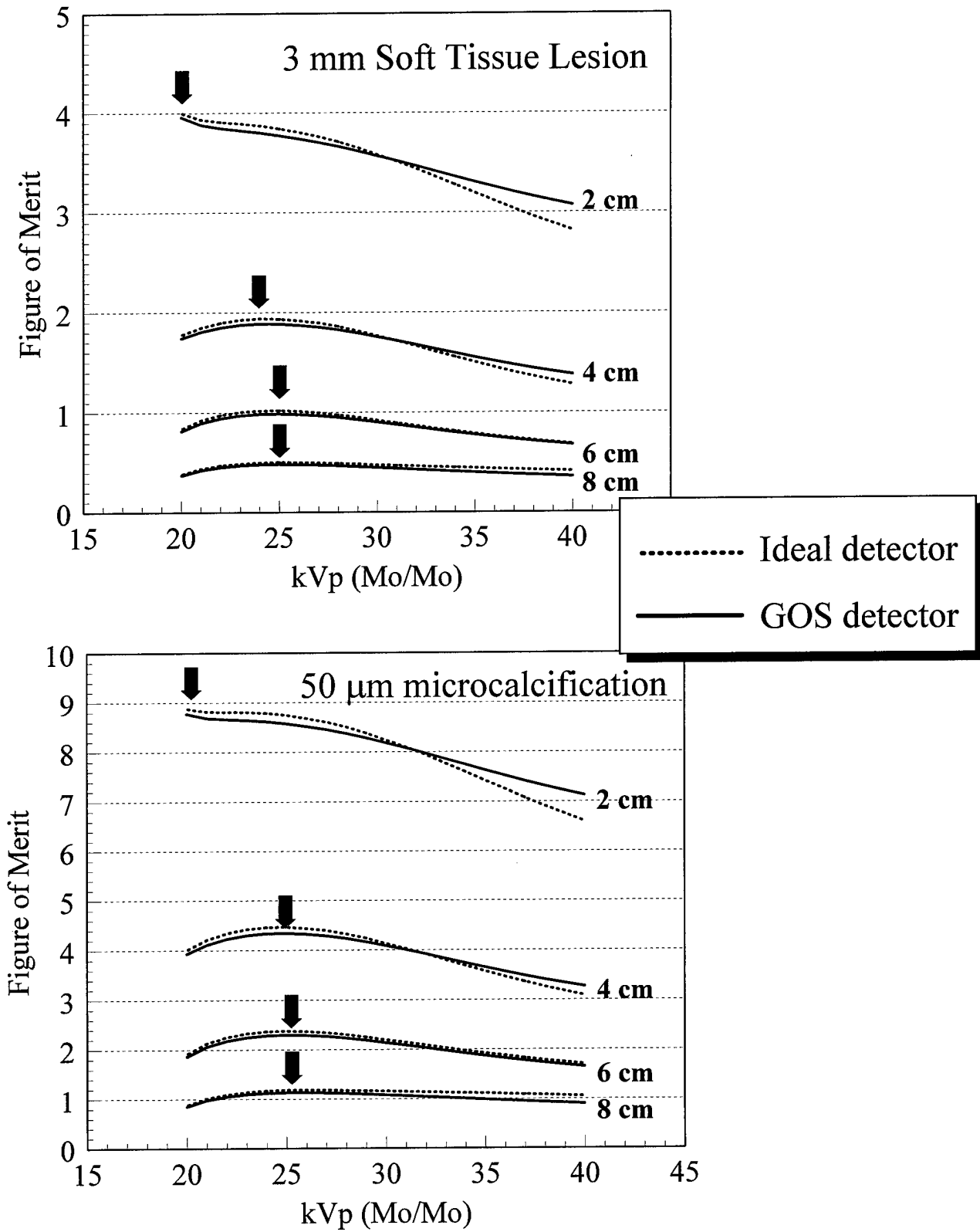
Figure 21

Comparison of Different Anode/Filter combinations

50 μm microcalcification, 5:1 carbon fiber grid,
60 mg/cm**2 GOS detector
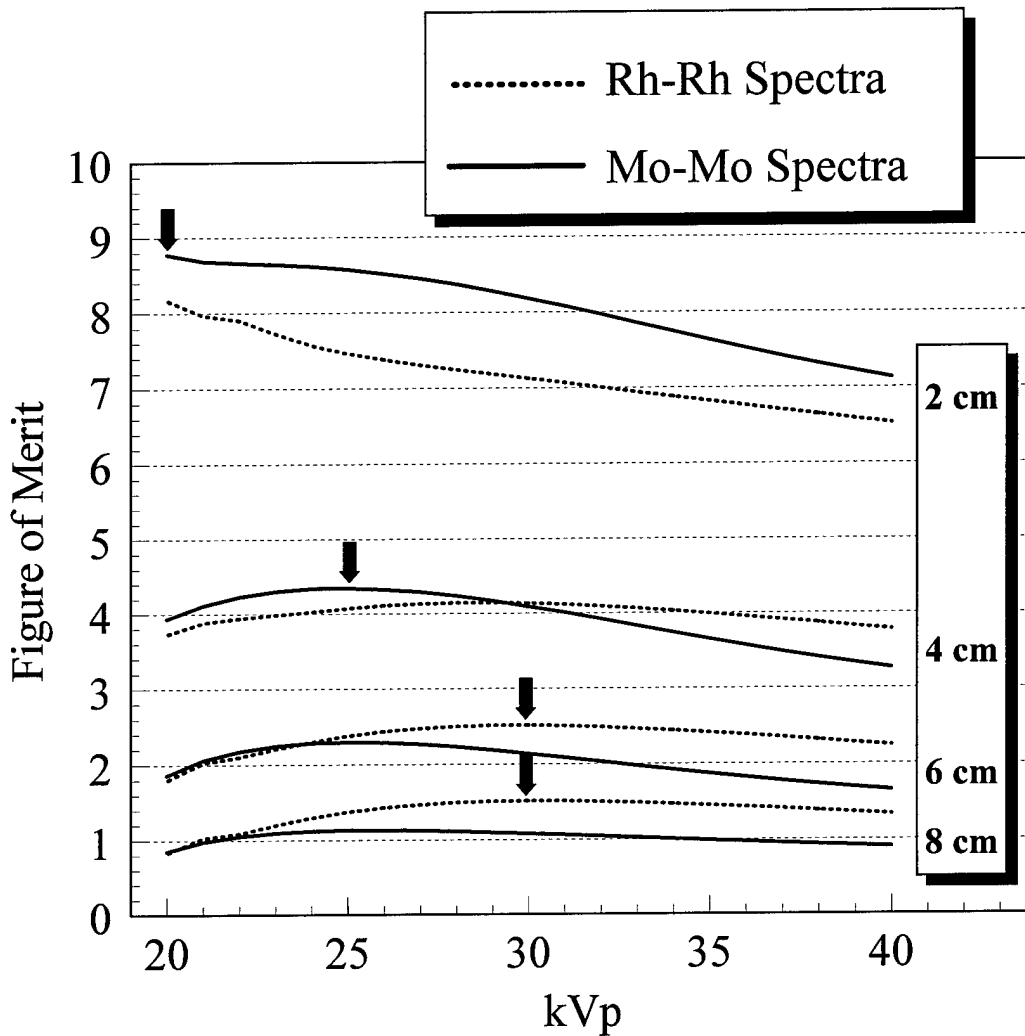
Figure 22

HIGH ENERGY BEAM

50% Glandular, 5:1 Carbon Fiber Grid
50 μm microcalcification
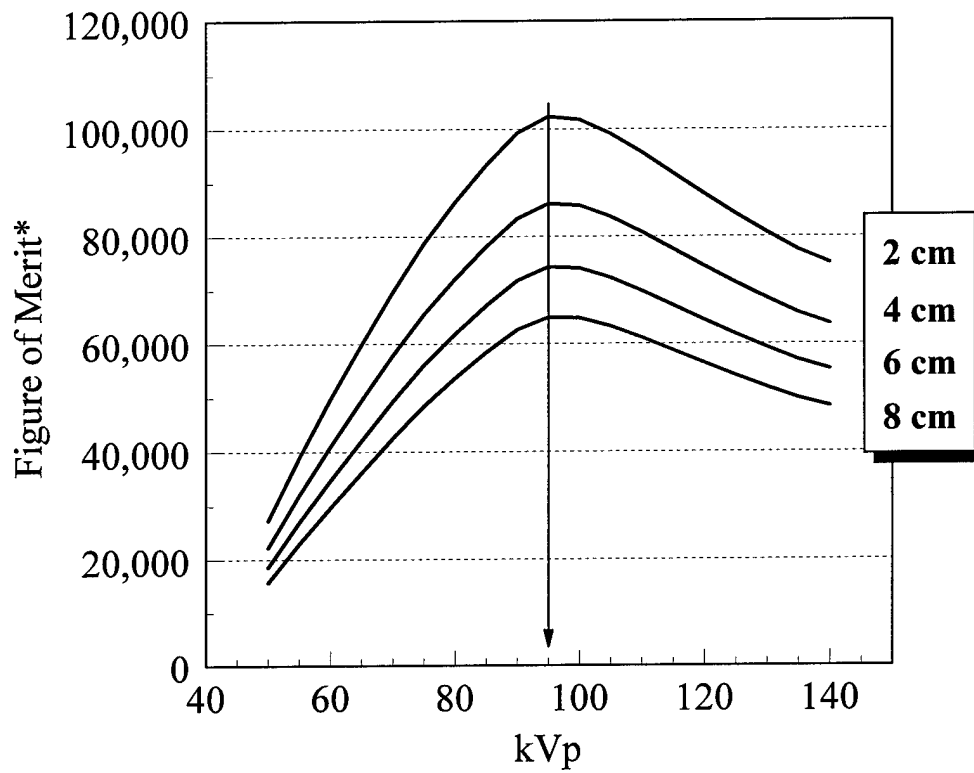
* designed to minimize contrast

Figure 23
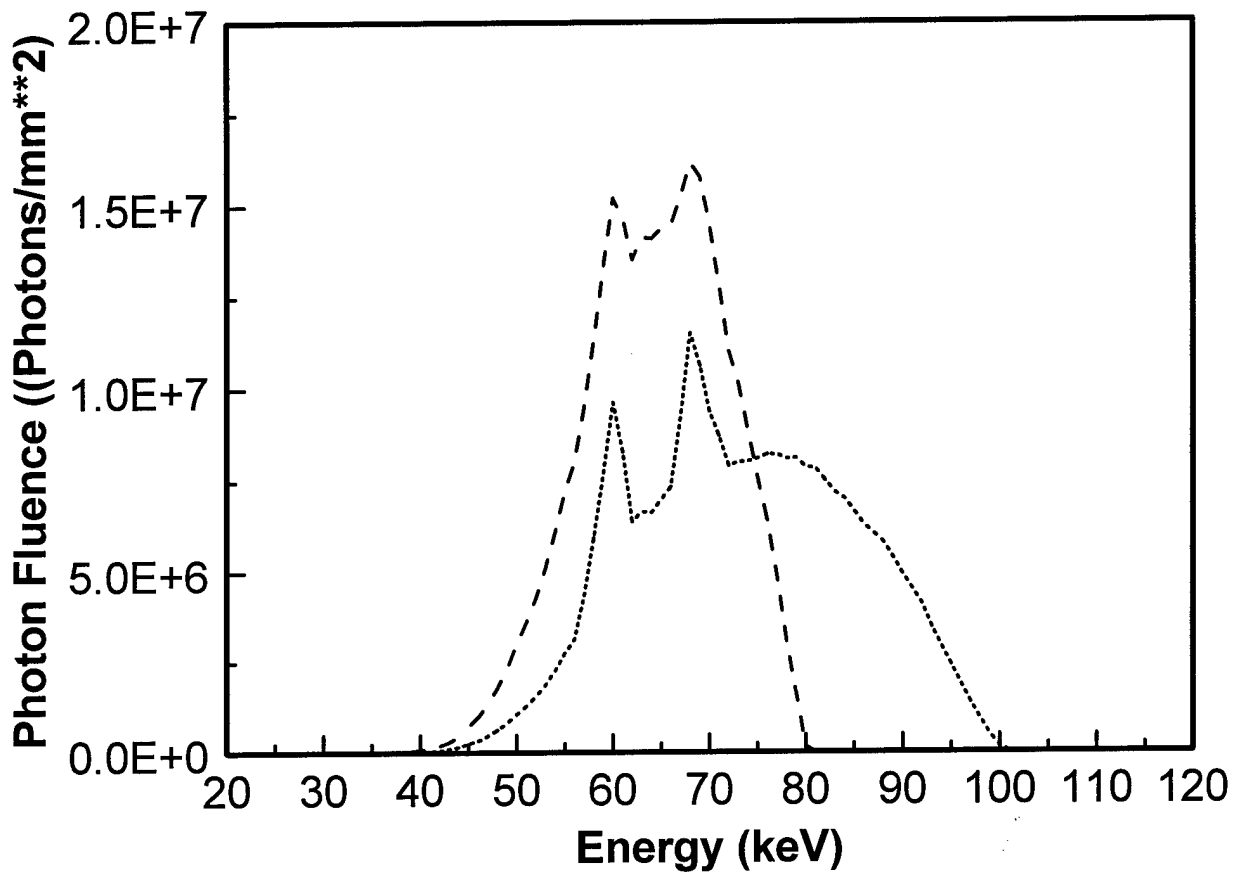
Tungsten Anode High Energy Spectra
1.5 mm Al, 2 mm Cu

Figure 24
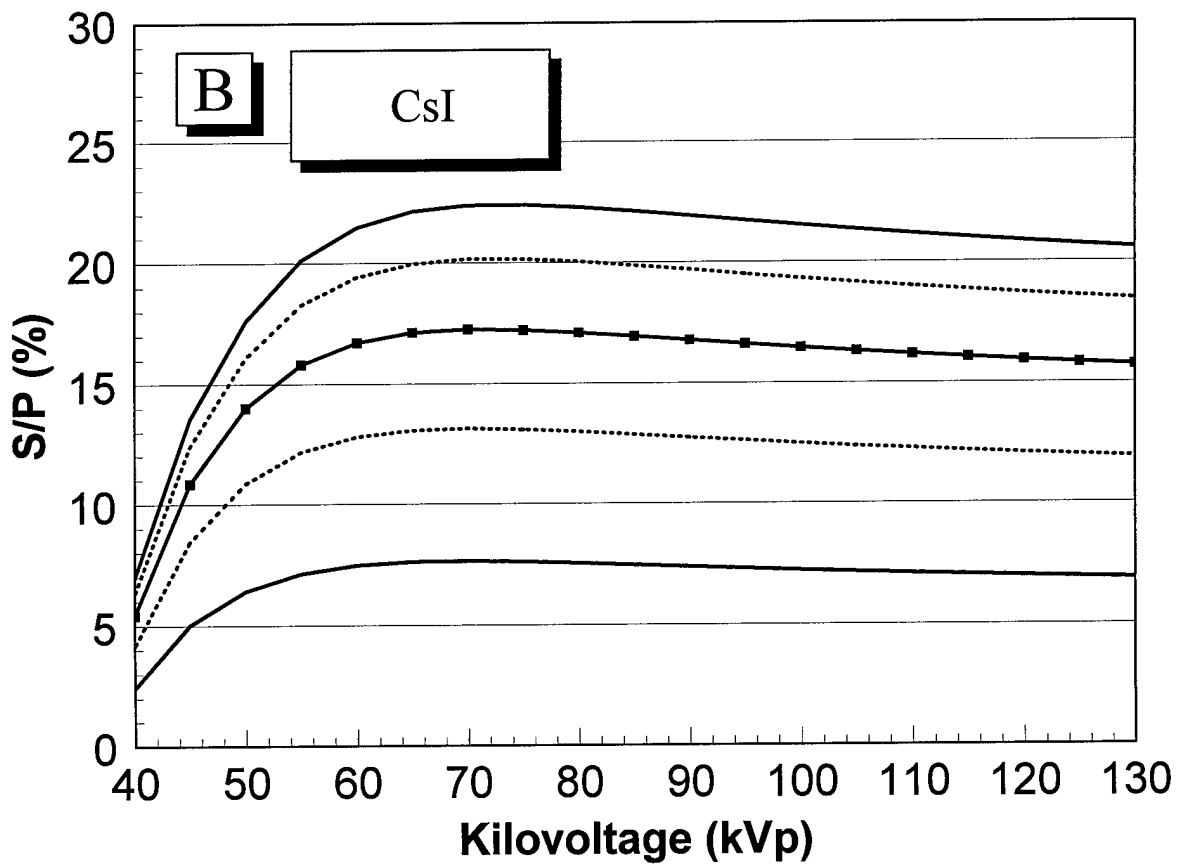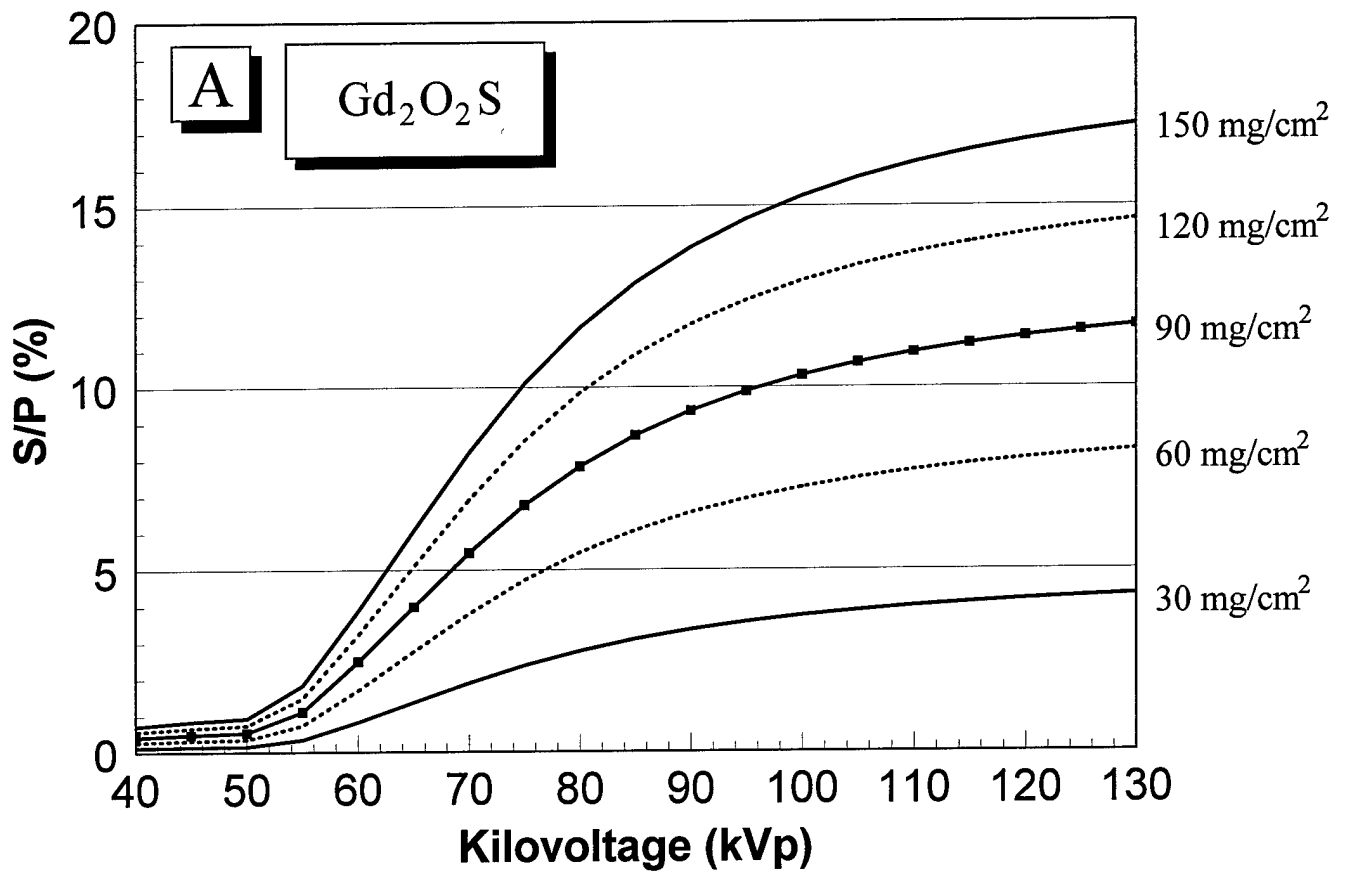
Figure 25
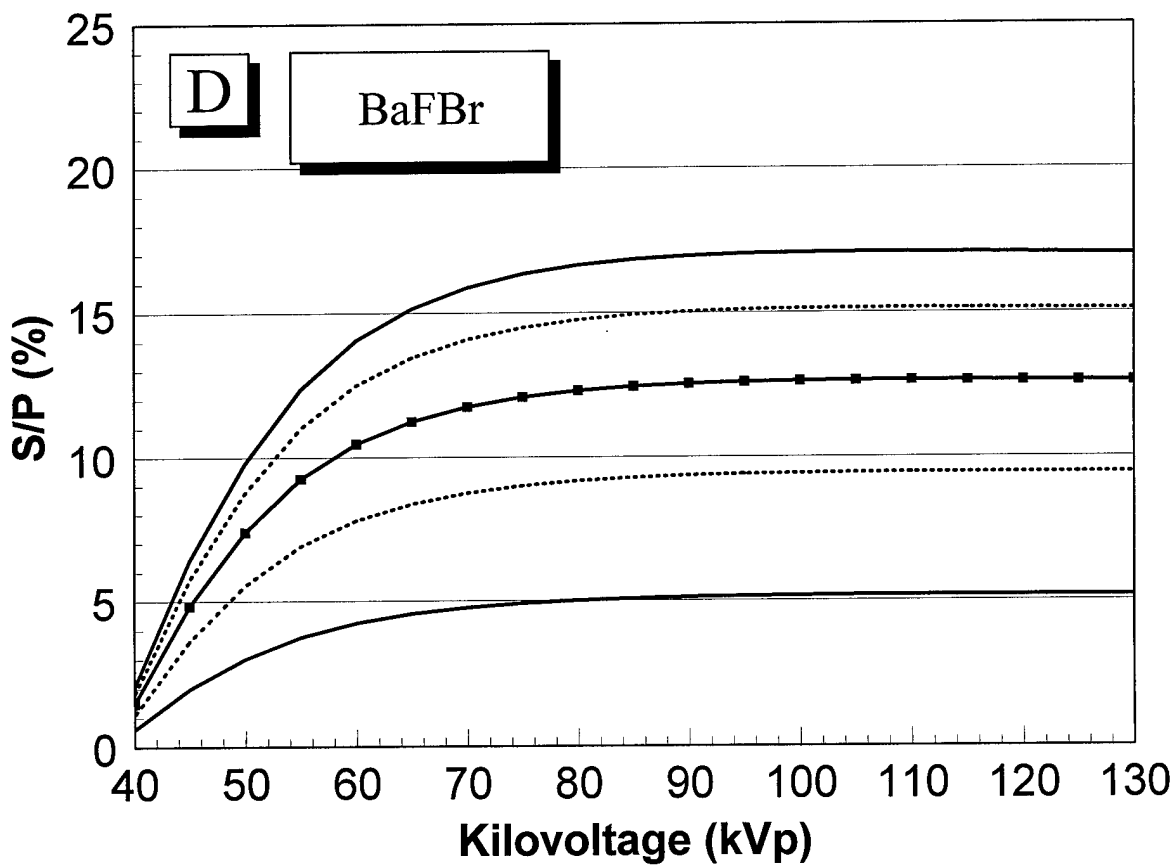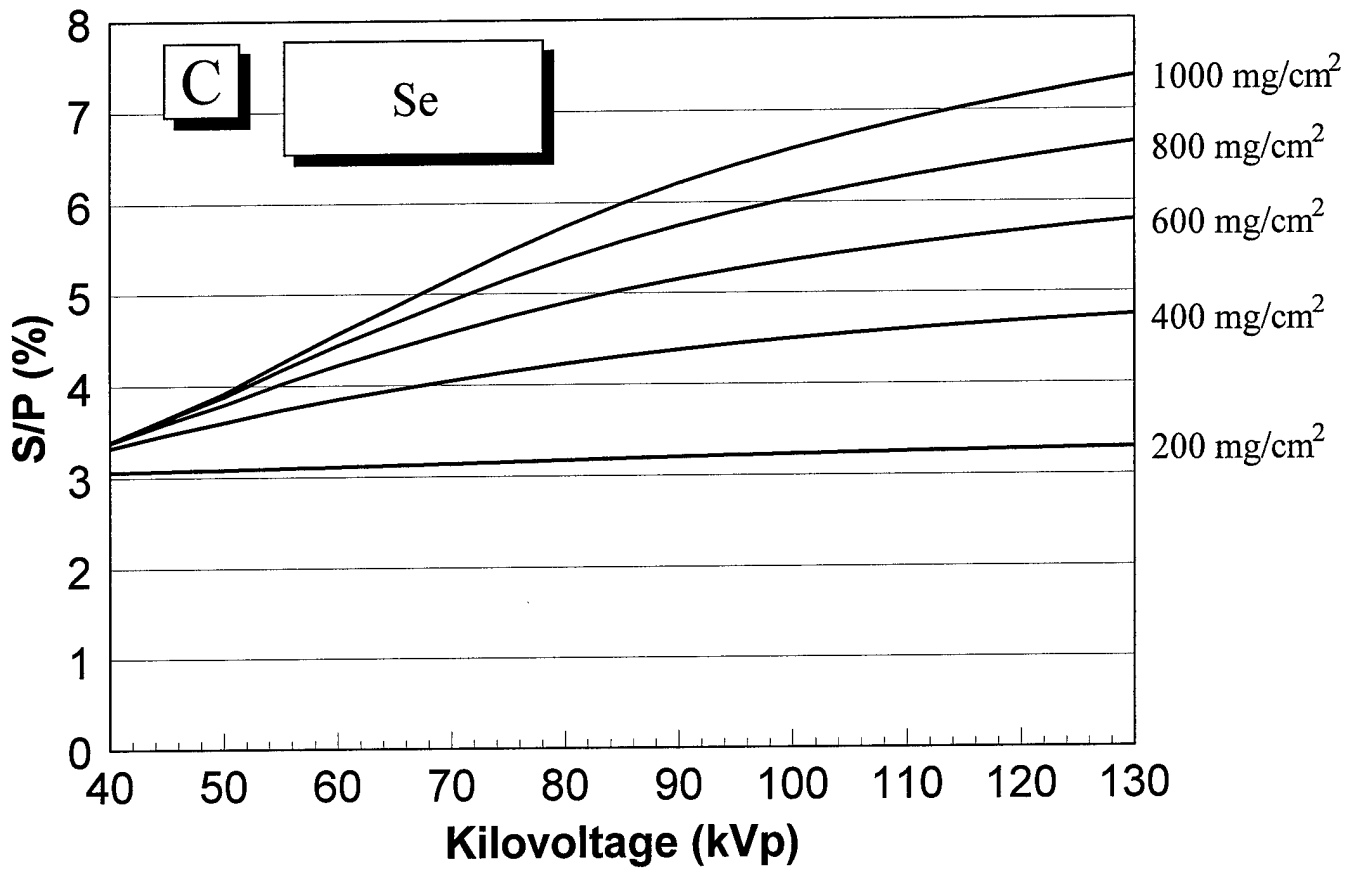
Figure 26
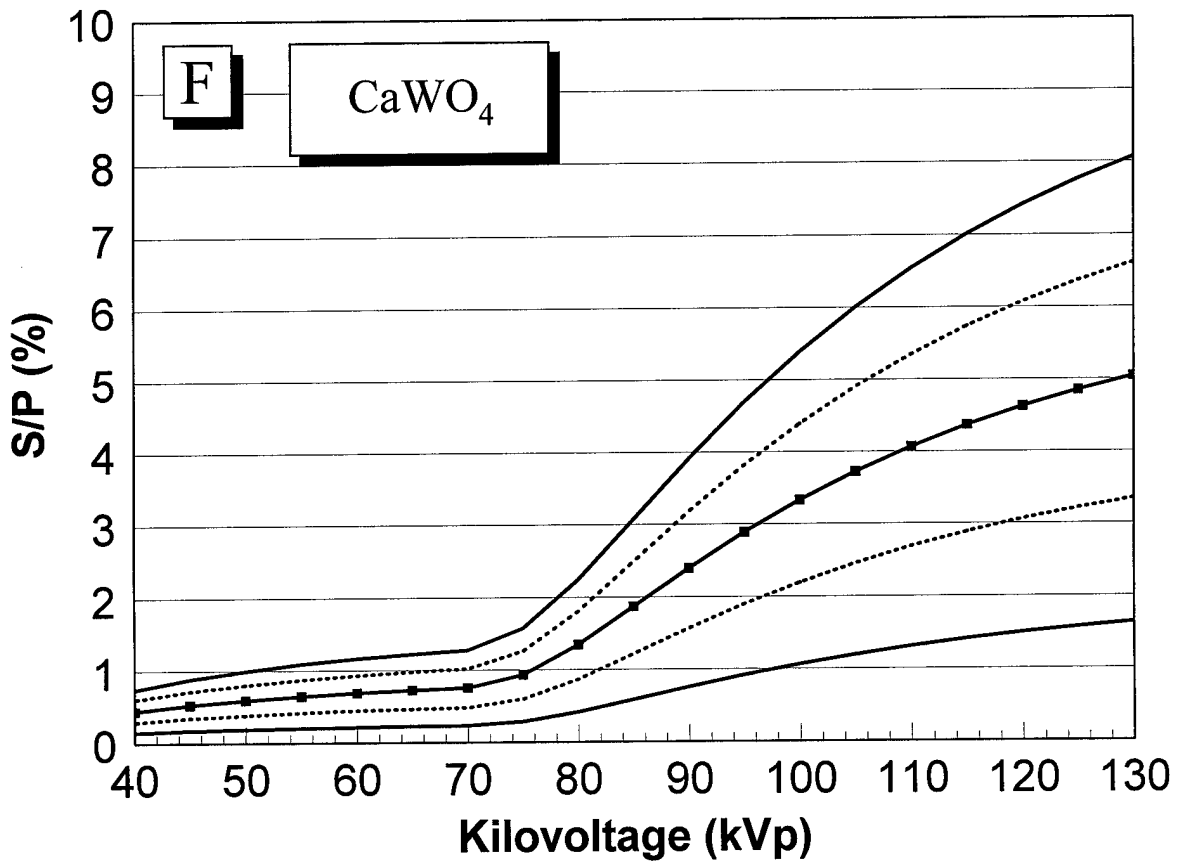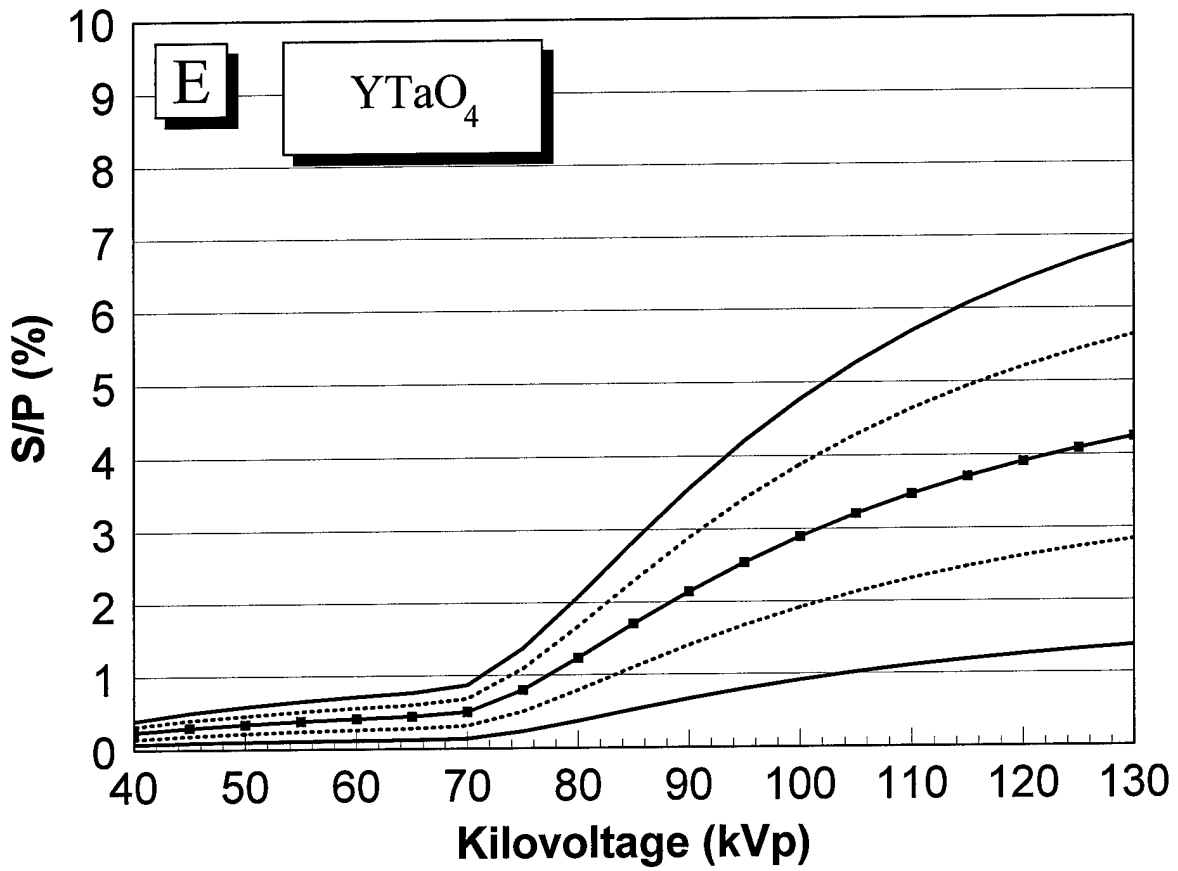
Figure 27
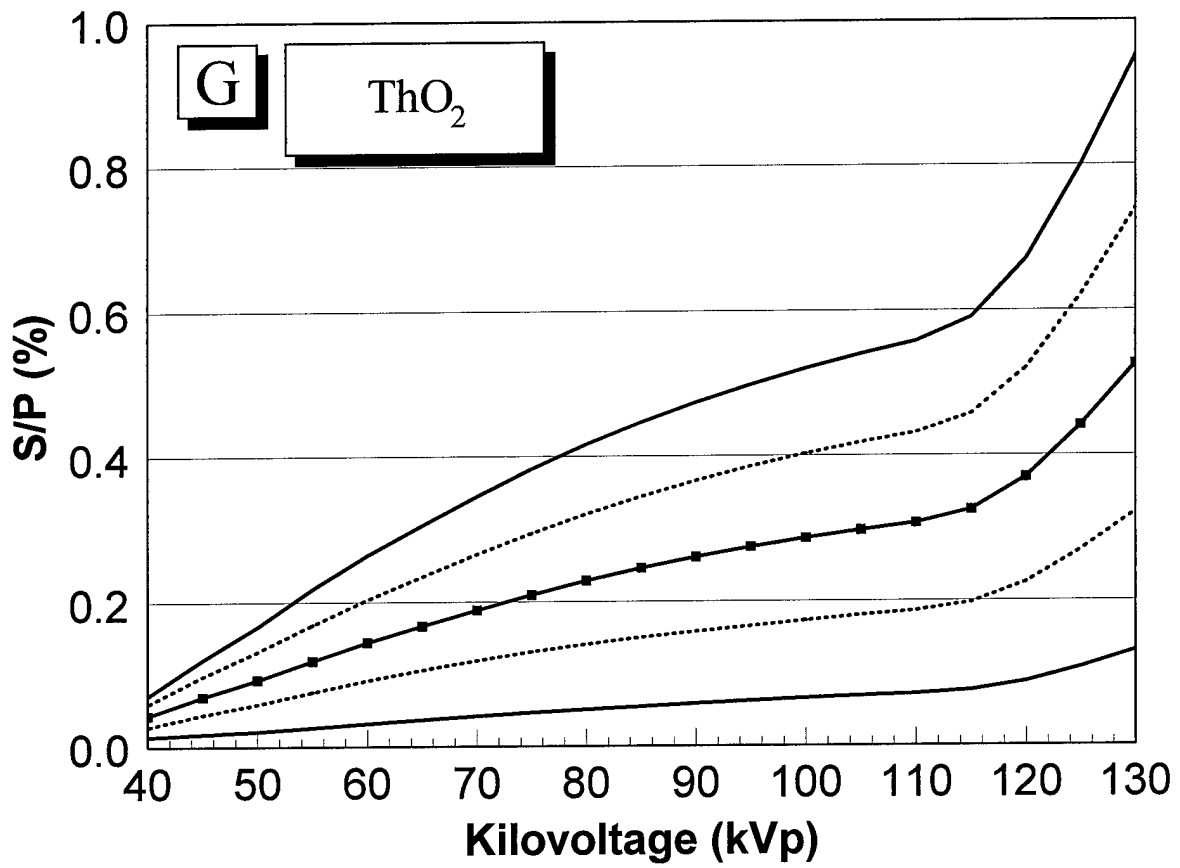
Figure 28
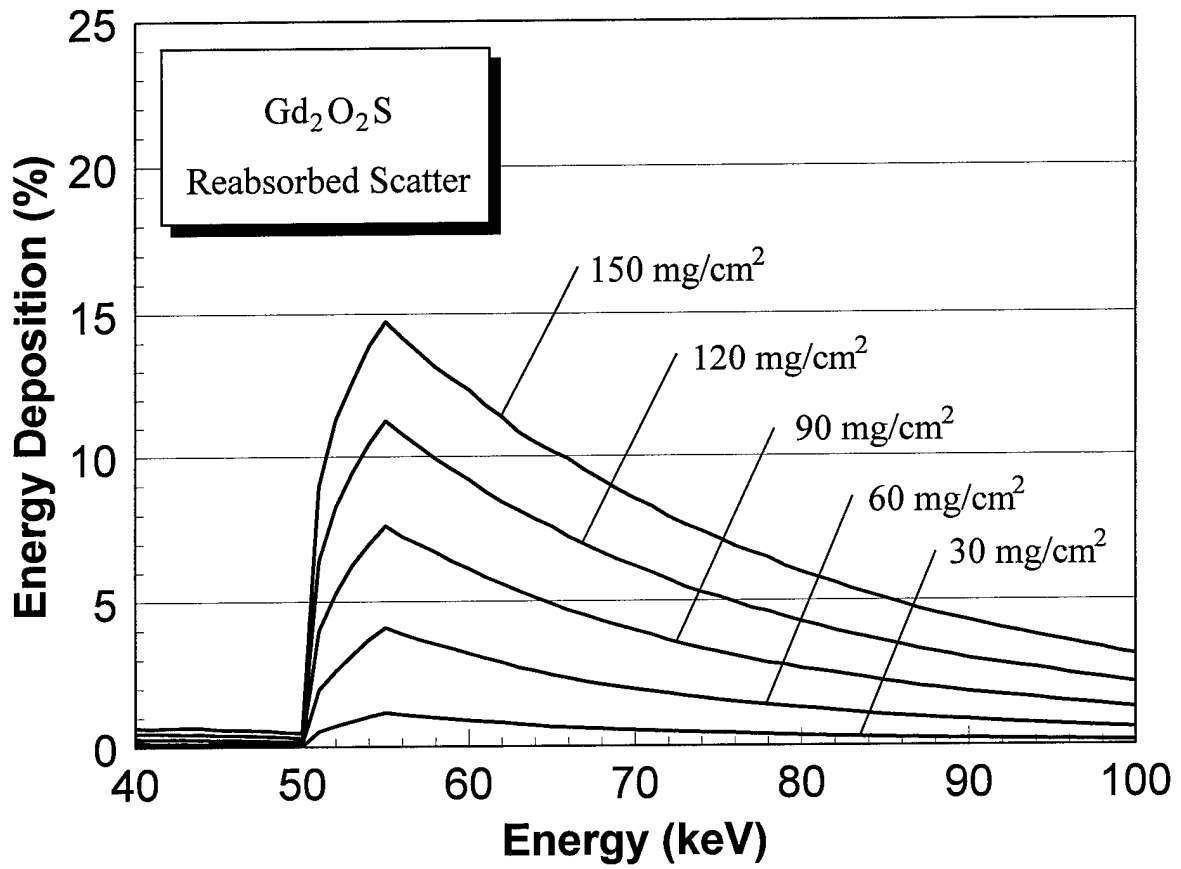
Figure 29
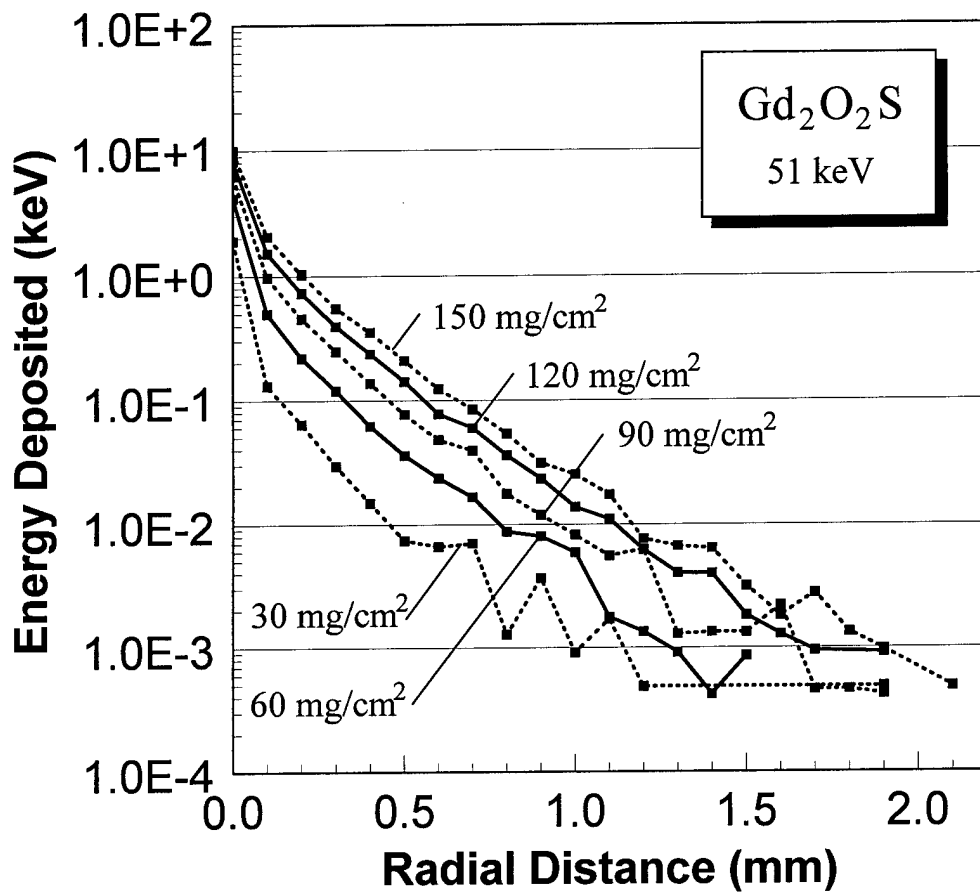
Figure 30
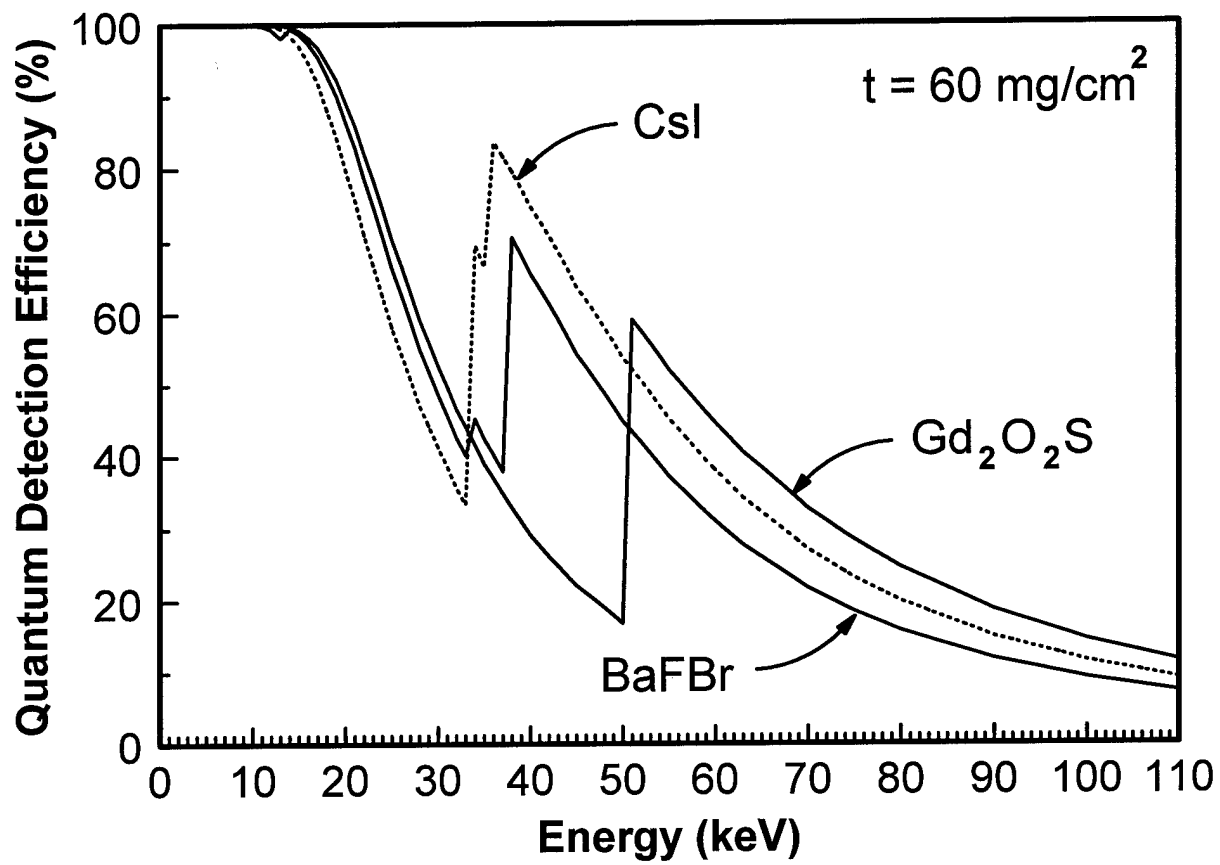
Figure 31
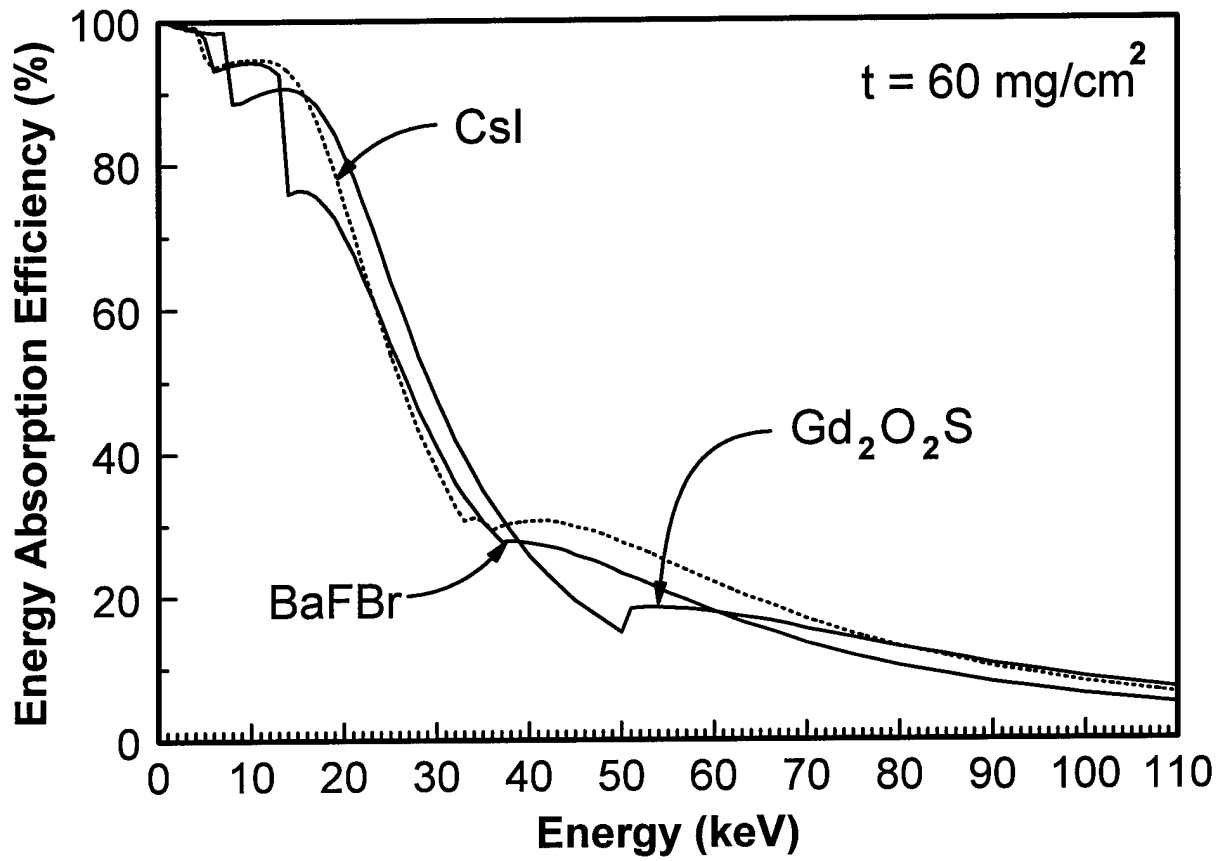
Figure 32
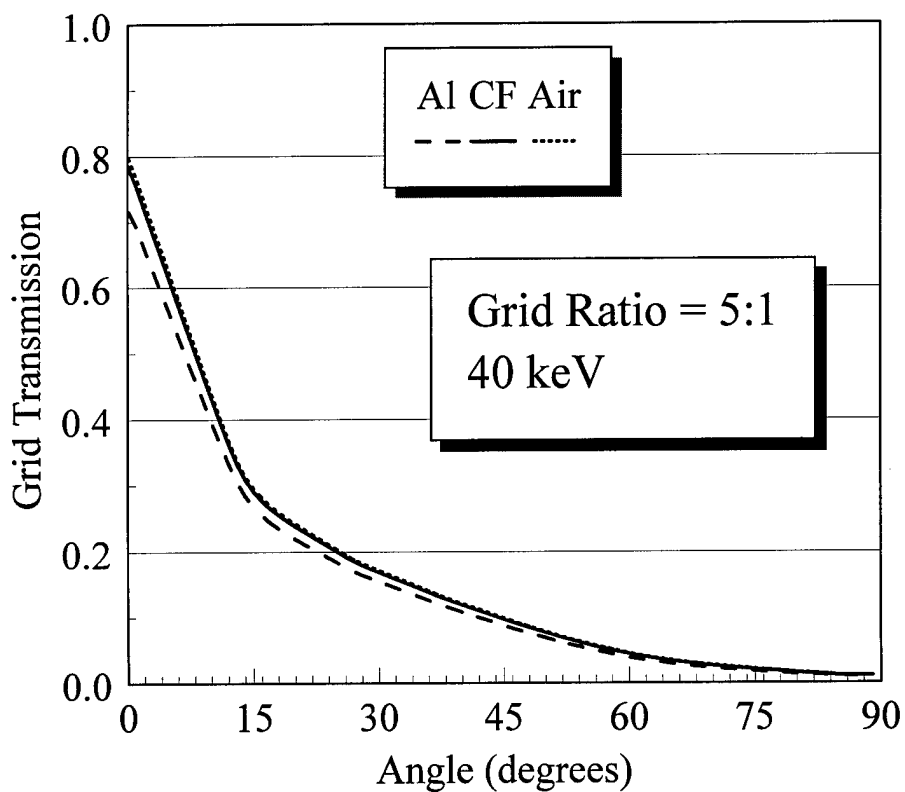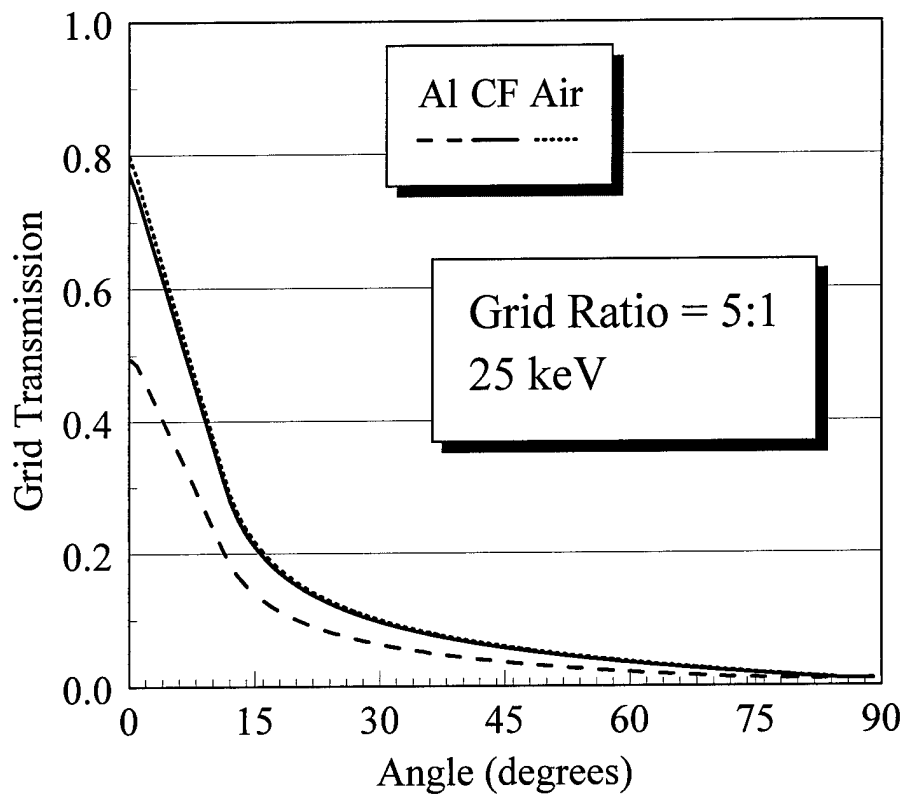
Figure 33
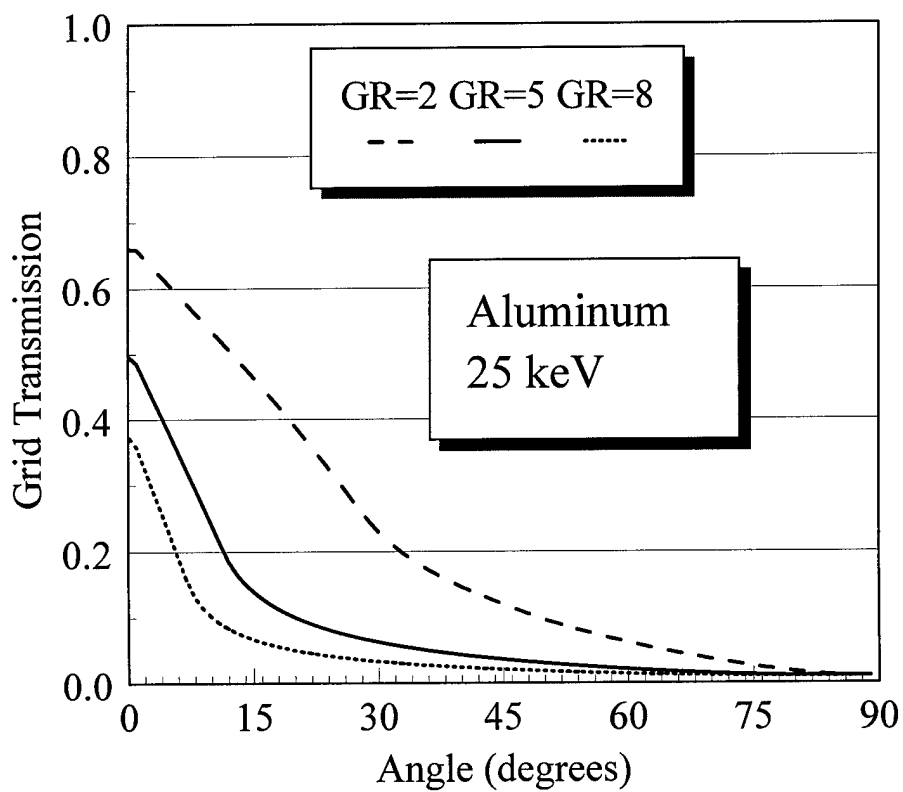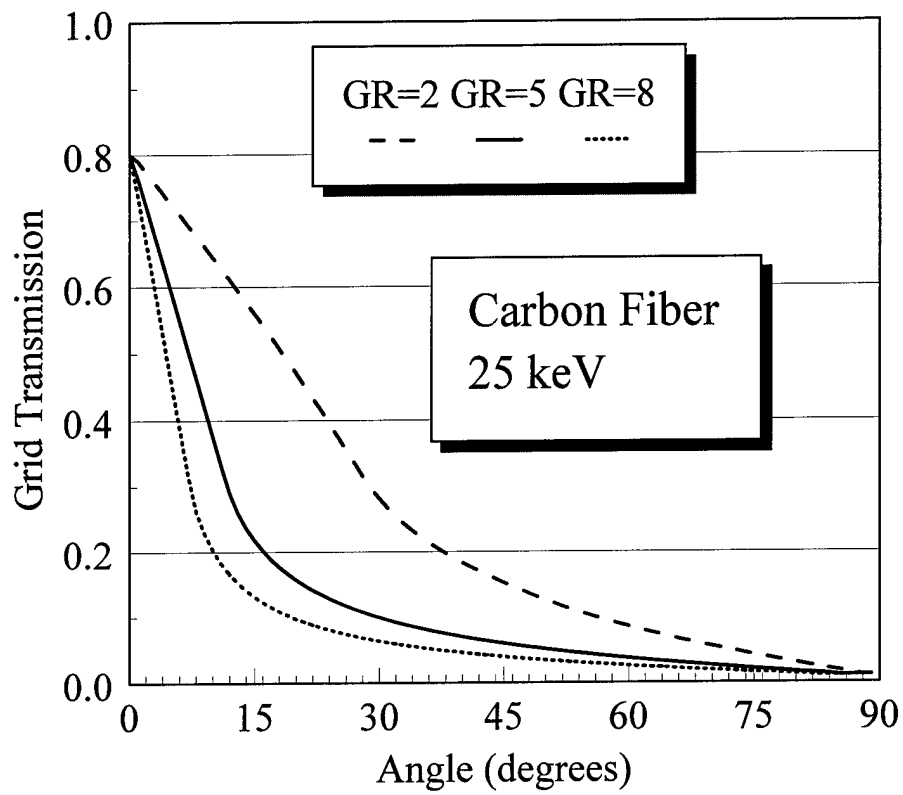
Figure 34
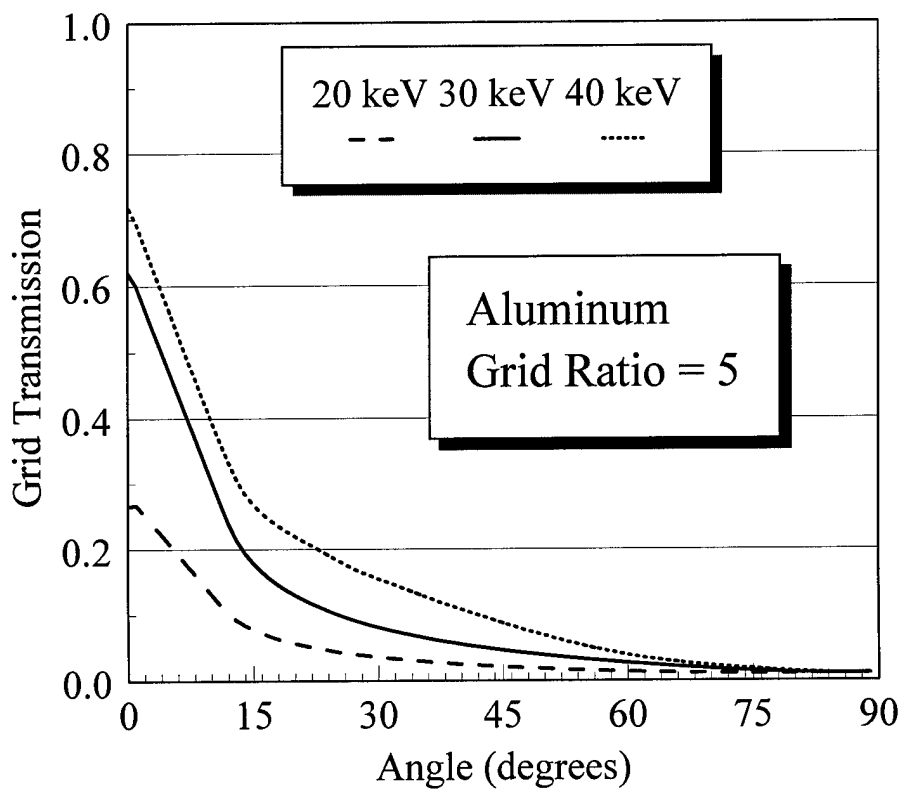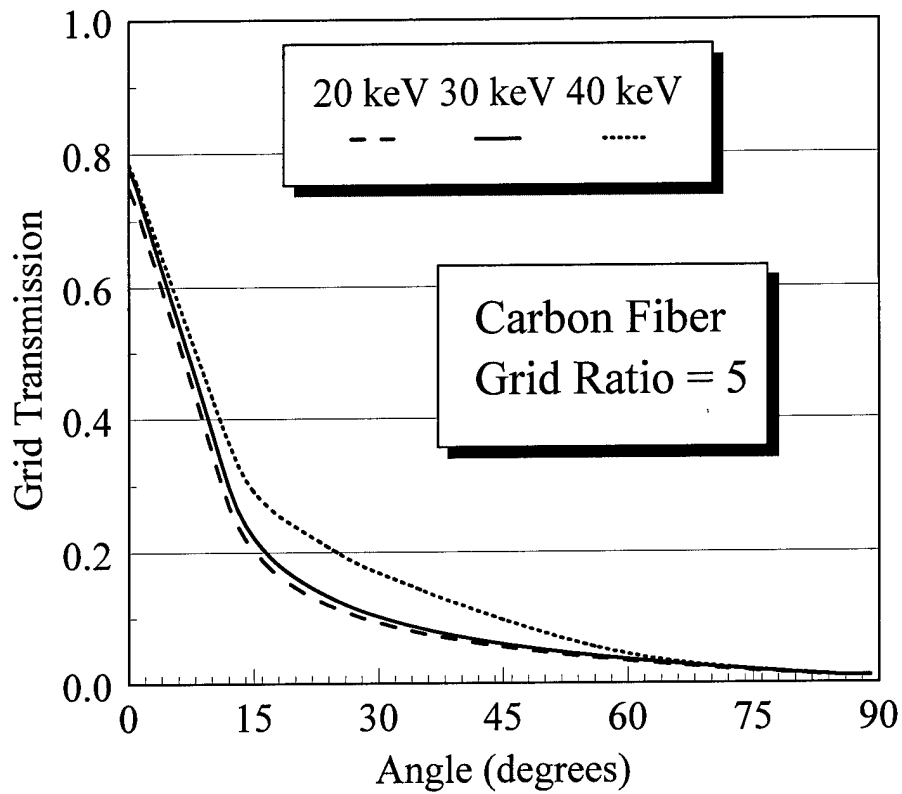
Figure 35

Influence of Grid

50 μm microcalcification

6 cm Breast Thickness

GOS detector

Figure 36

3.0 mm

12.0 mm   25.4 mm

25.4 mm
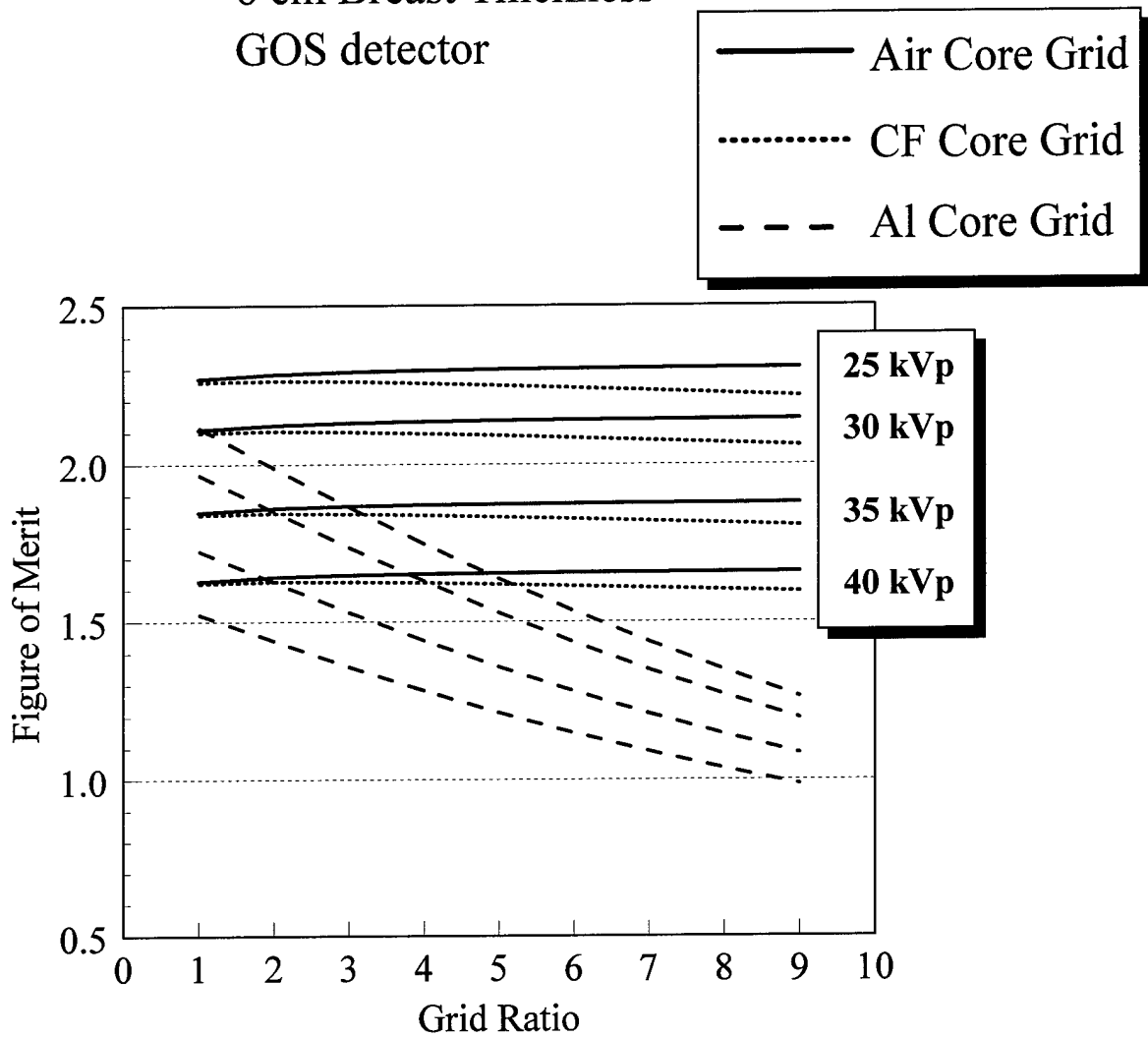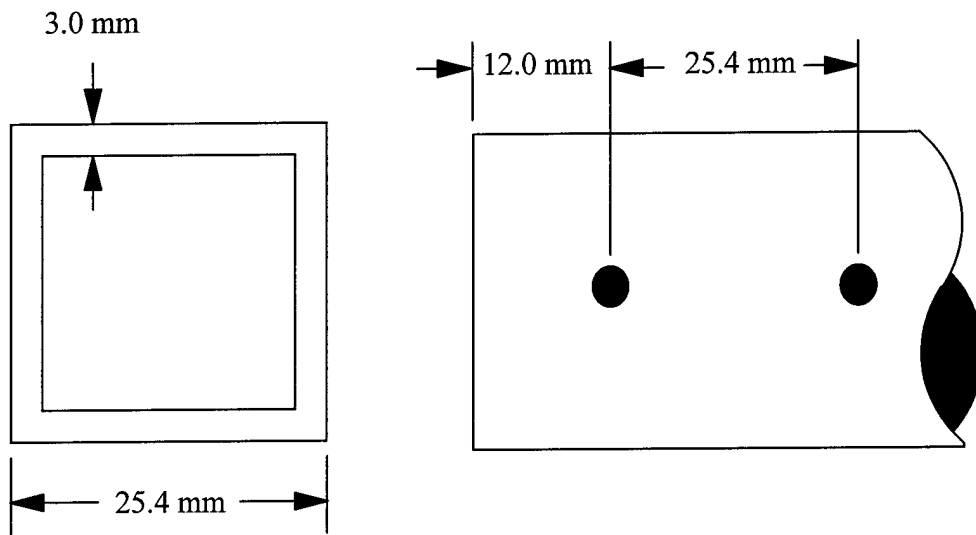
End View   **Side View**
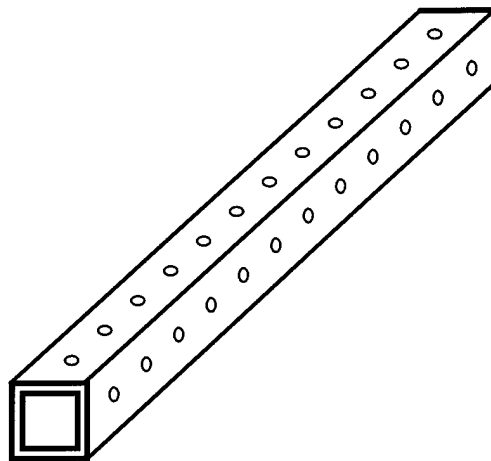
Struts designed for adapting to an optical table with 1" hole pattern

Figure 37

screen-copper-screen
detector sandwich

support

mylar mirror

mirror

breast

CCD - 1

CCD - 2
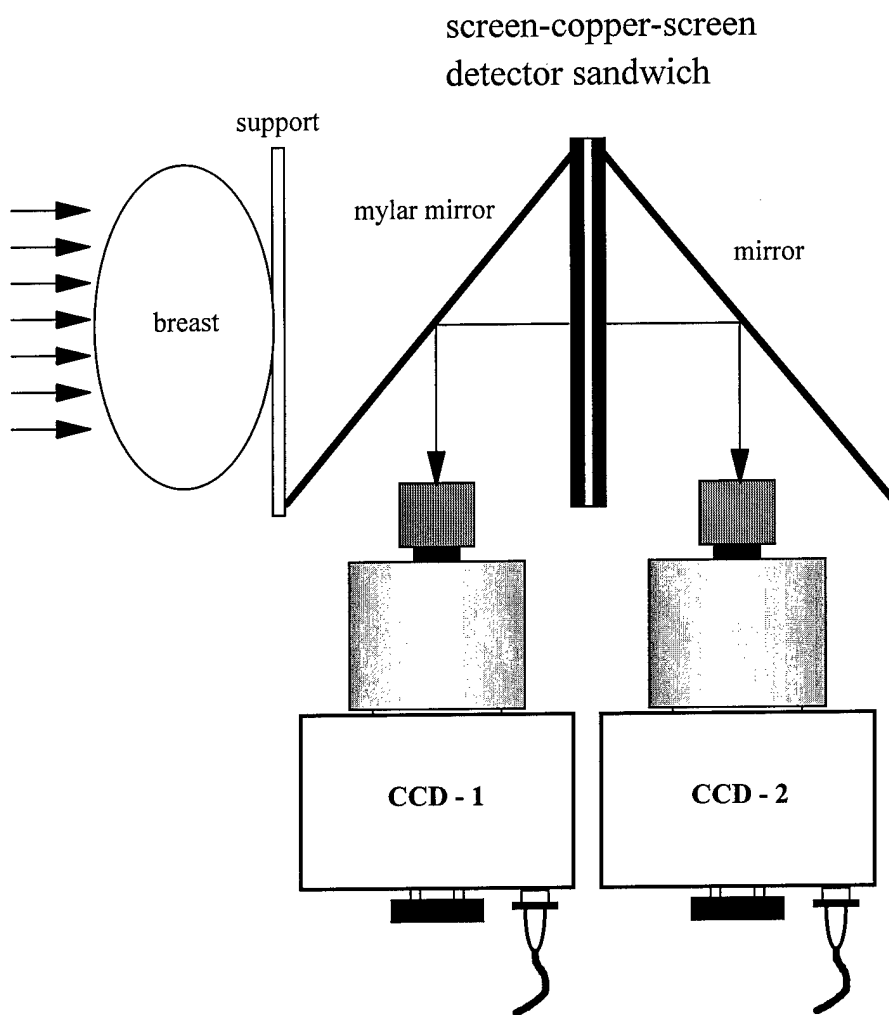
System design for single-pulse, dual-energy acquisition
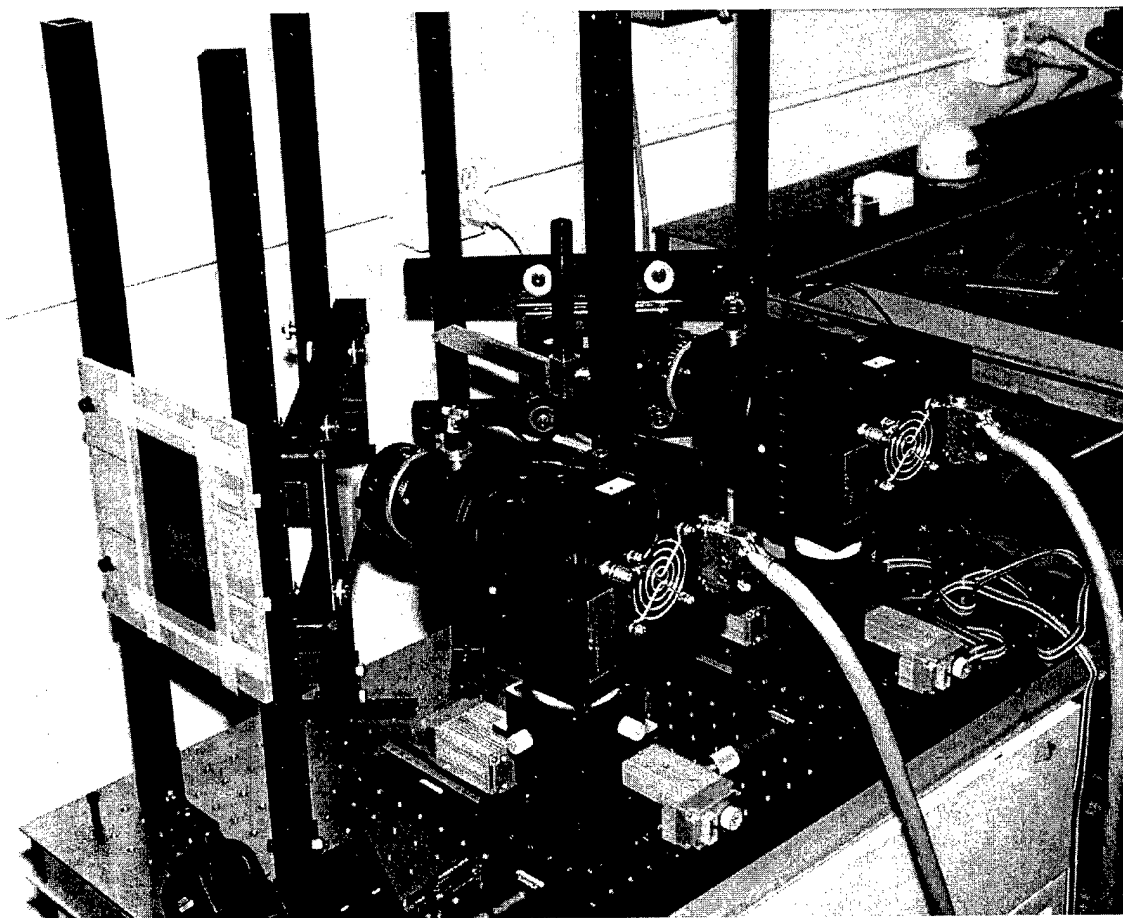
Figure 38

Picture of system built for single-pulse, dual-energy acquisition

Figure 39
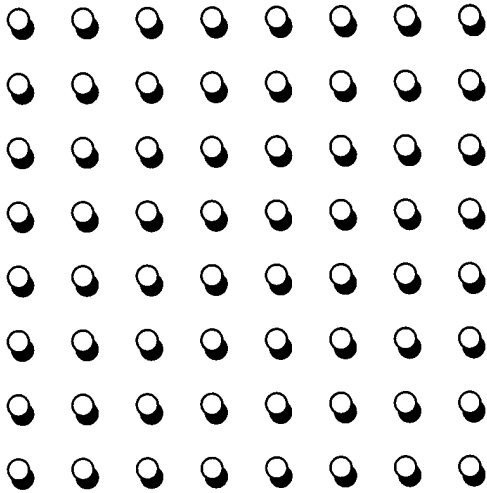
Before Alignment Algorithm   After Alignment Algorithm
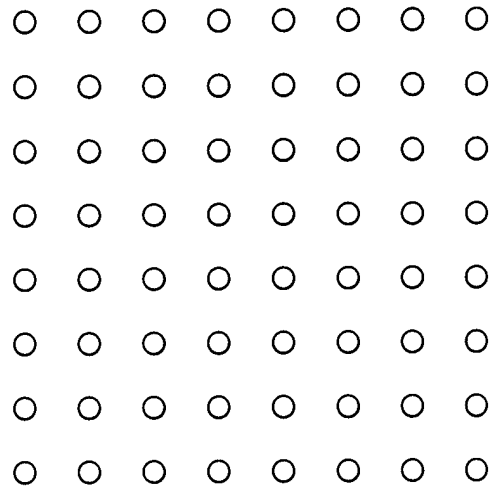
Figure 40

Figure 41

100 kV, 100 mA, 320 ms
MinR, Transmission mode

100 kV, 100 mA, 200 ms
Lanex, Transmission mode

50 kV, 100 mA, 1000 ms
MinR, Reflection mode

50 kV, 100 mA, 1000 ms
Lanex, Reflection mode

reflection mode   transmission mode
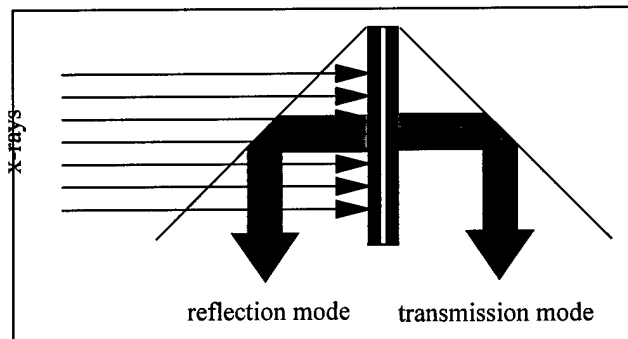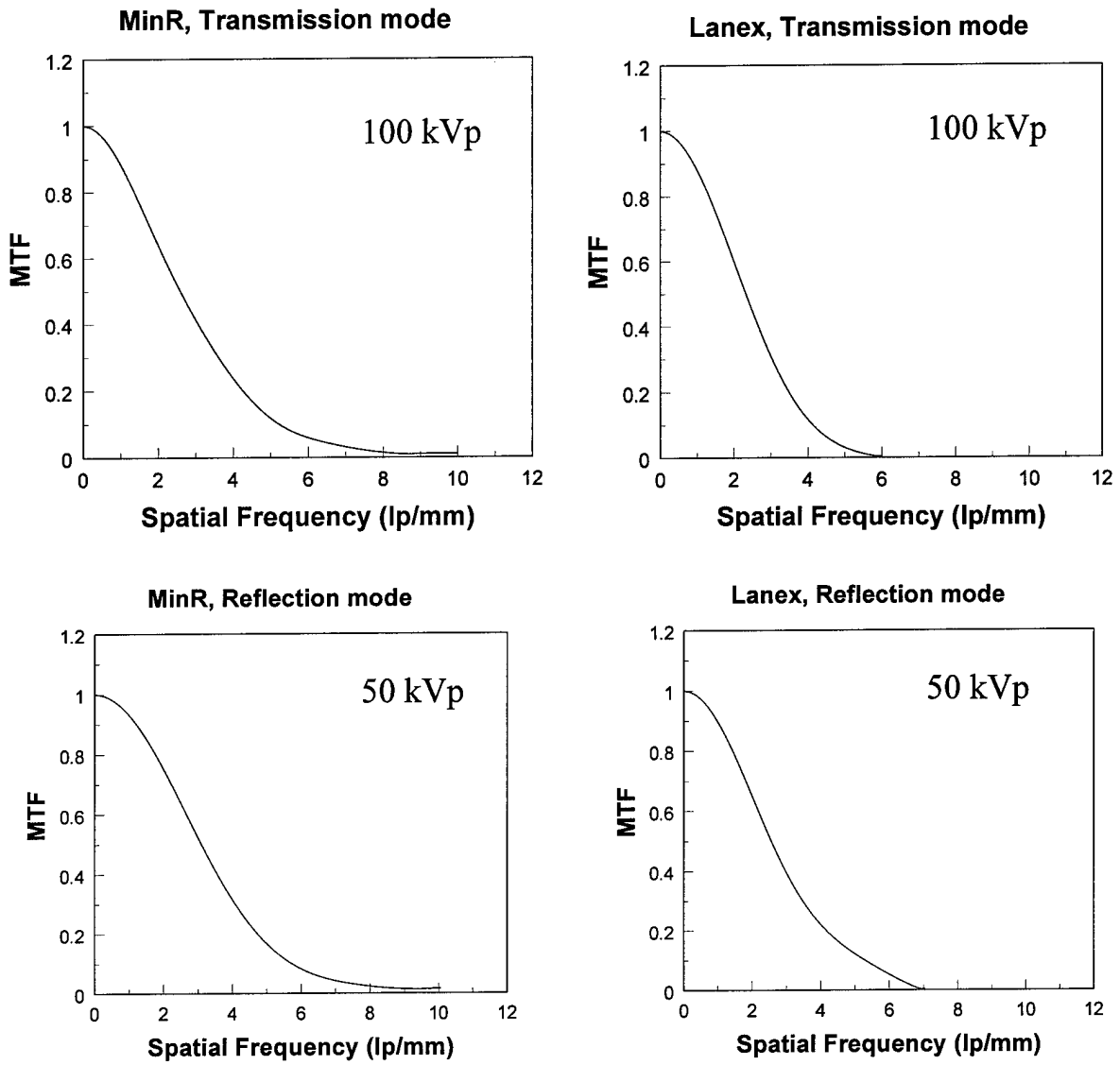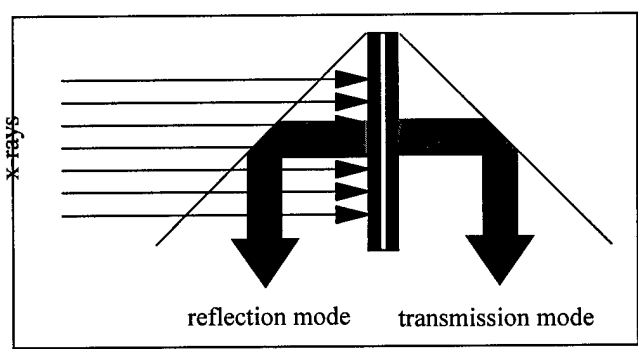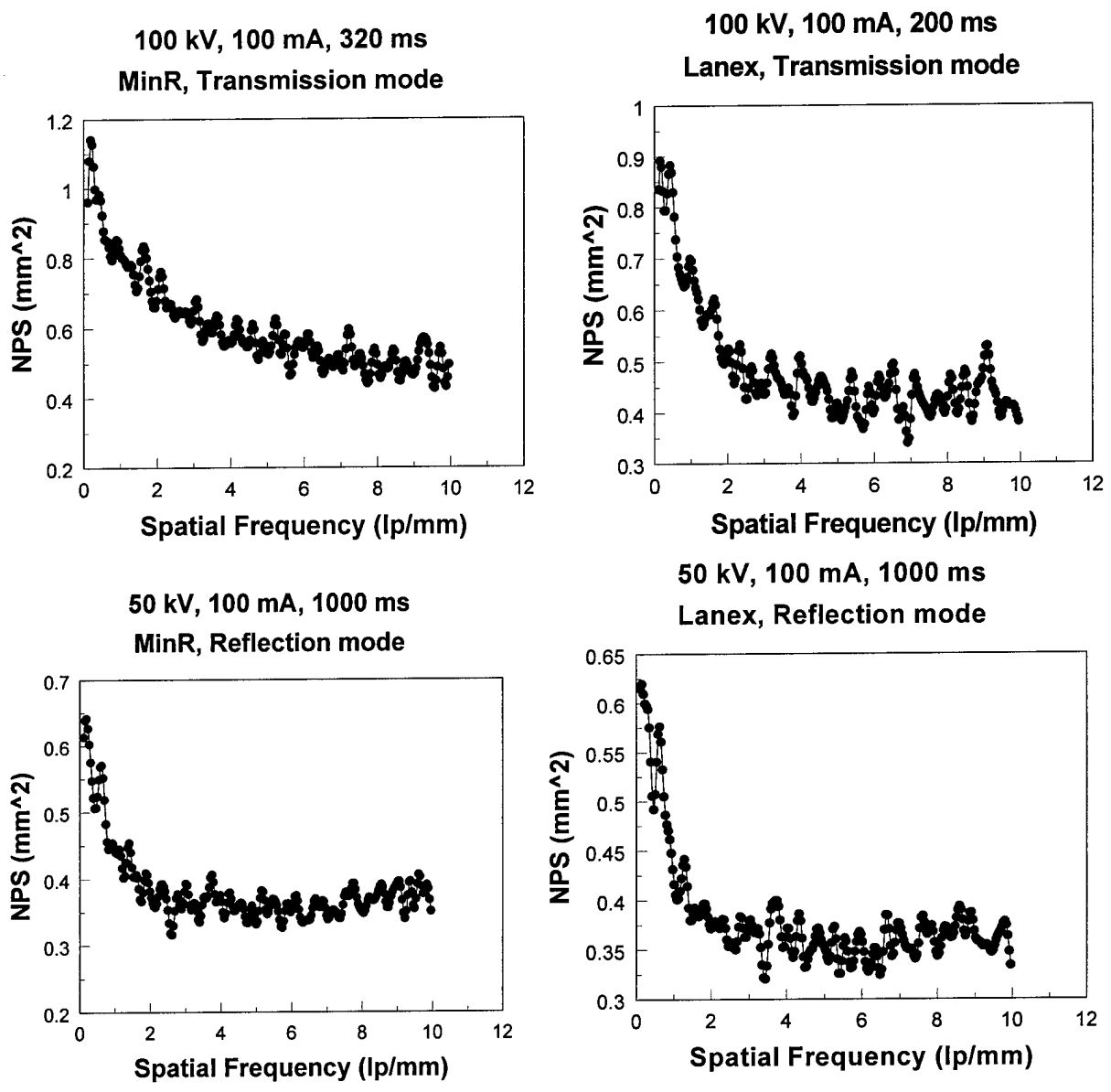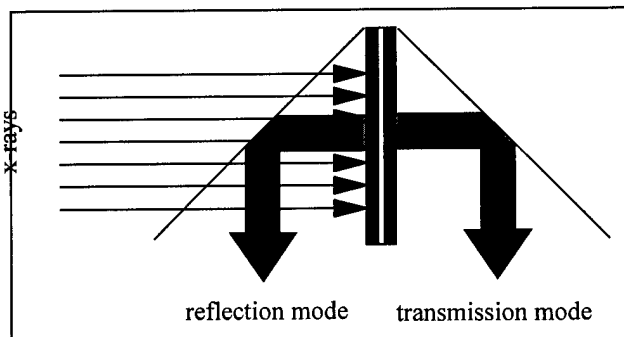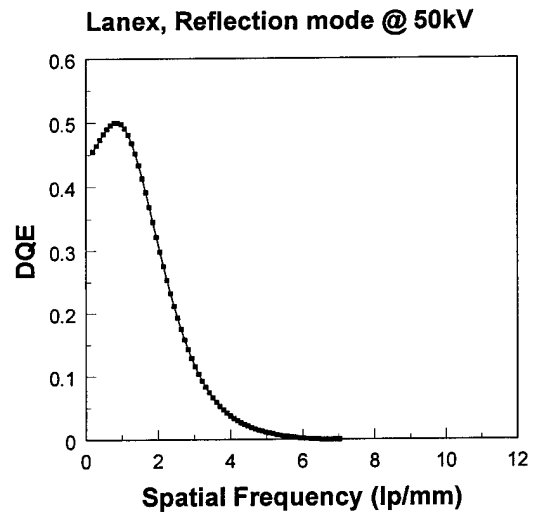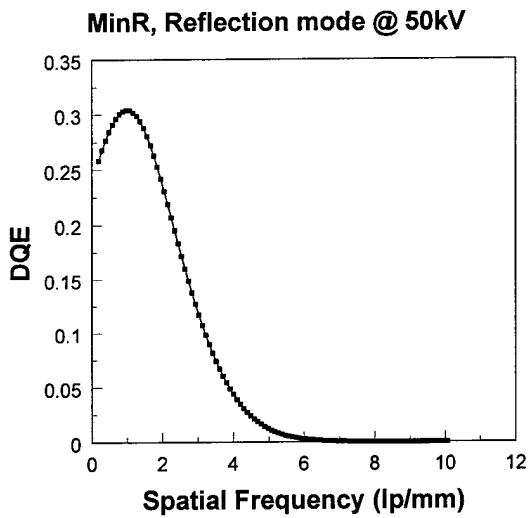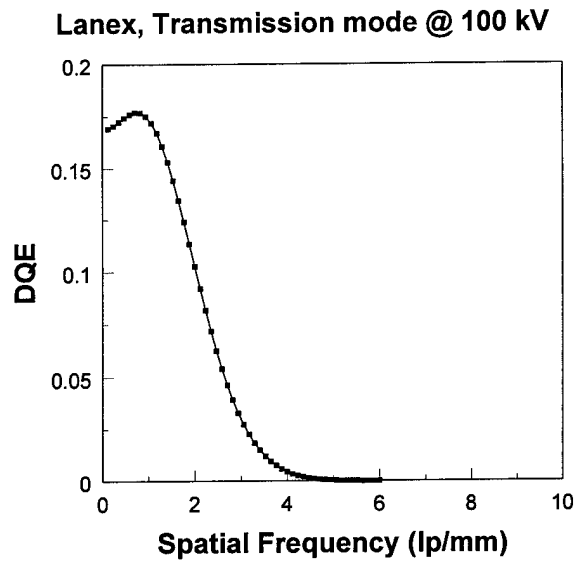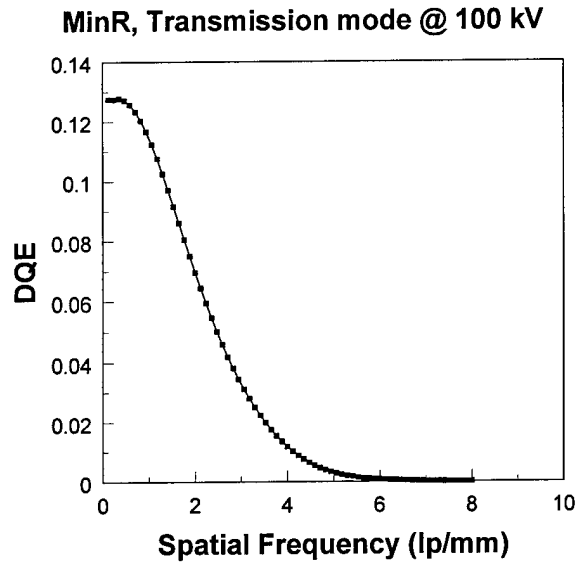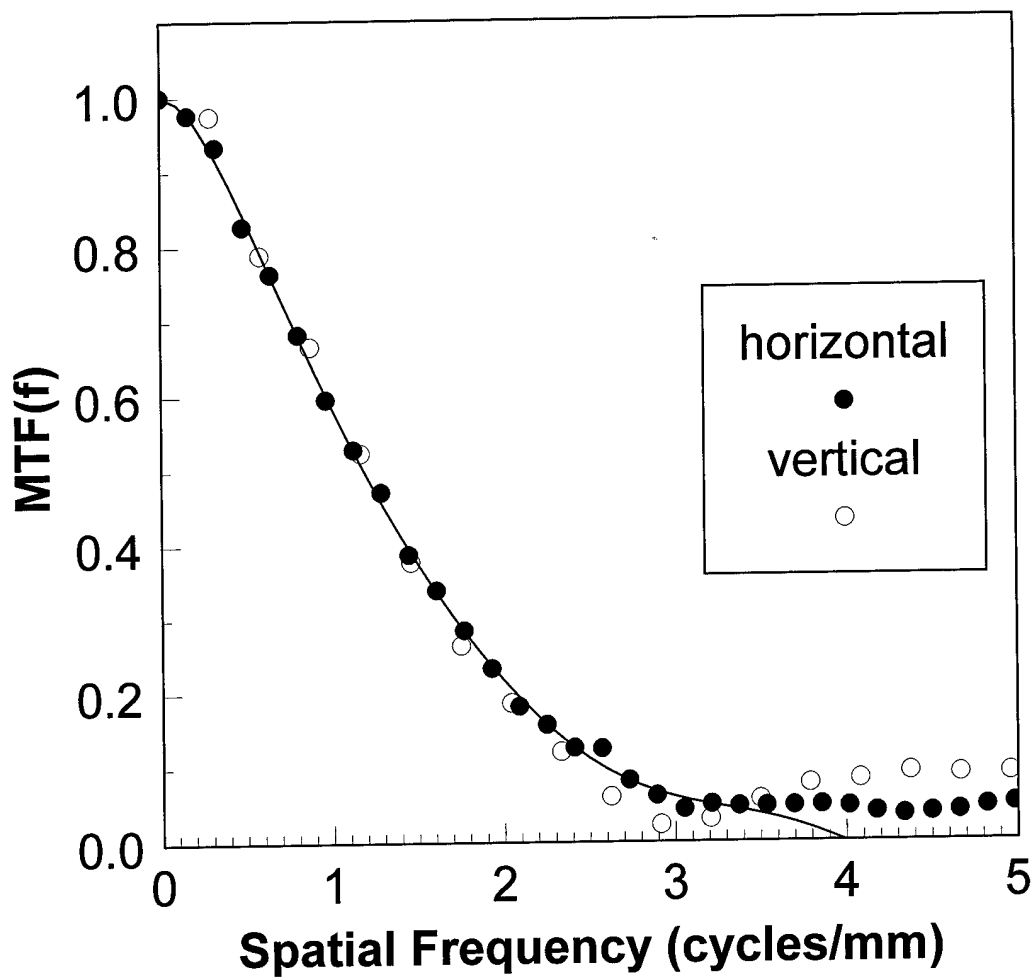
Figure 42

Figure 43

MTF(f) for the flat panel imaging system

Figure 44
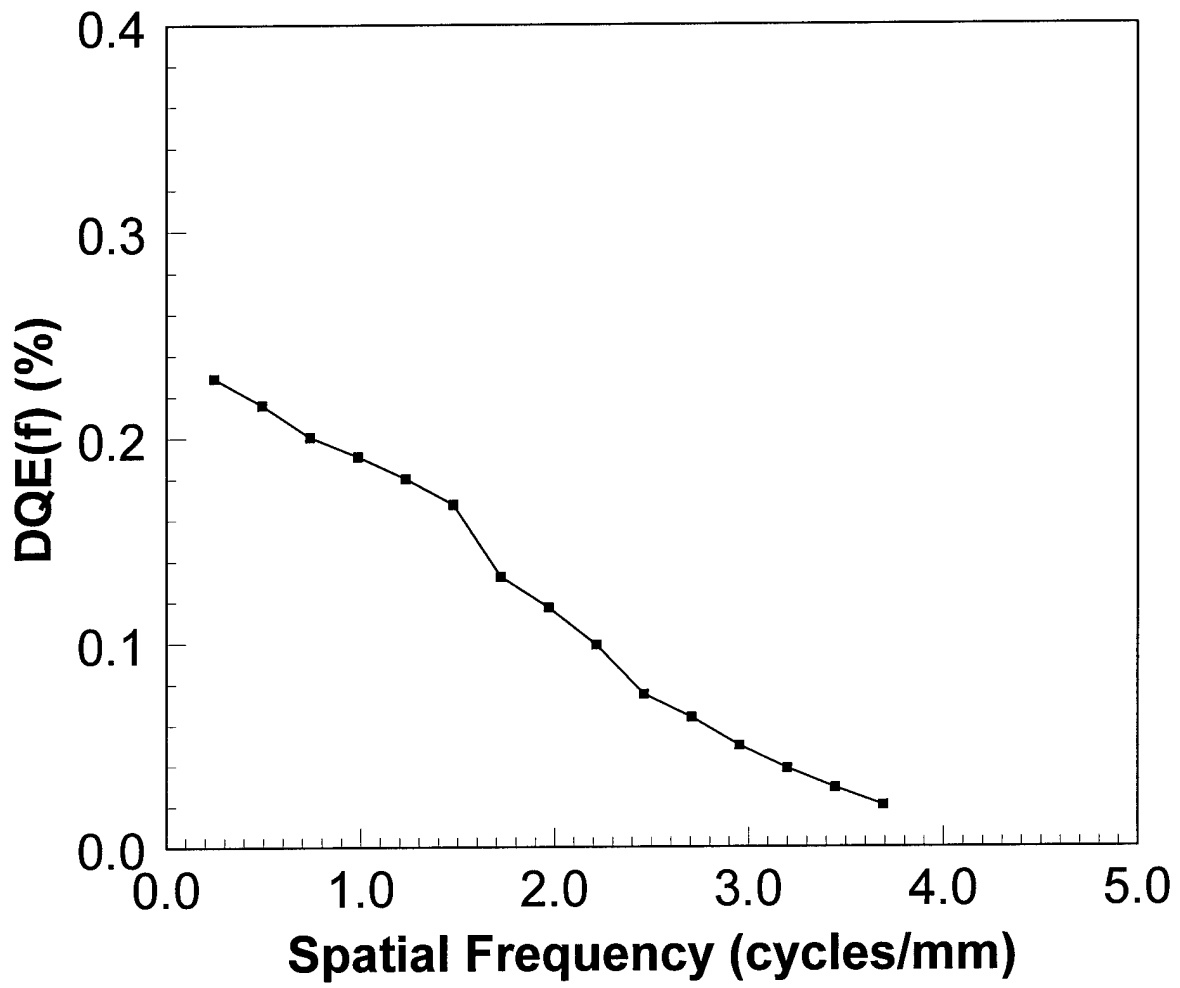
Figure 45
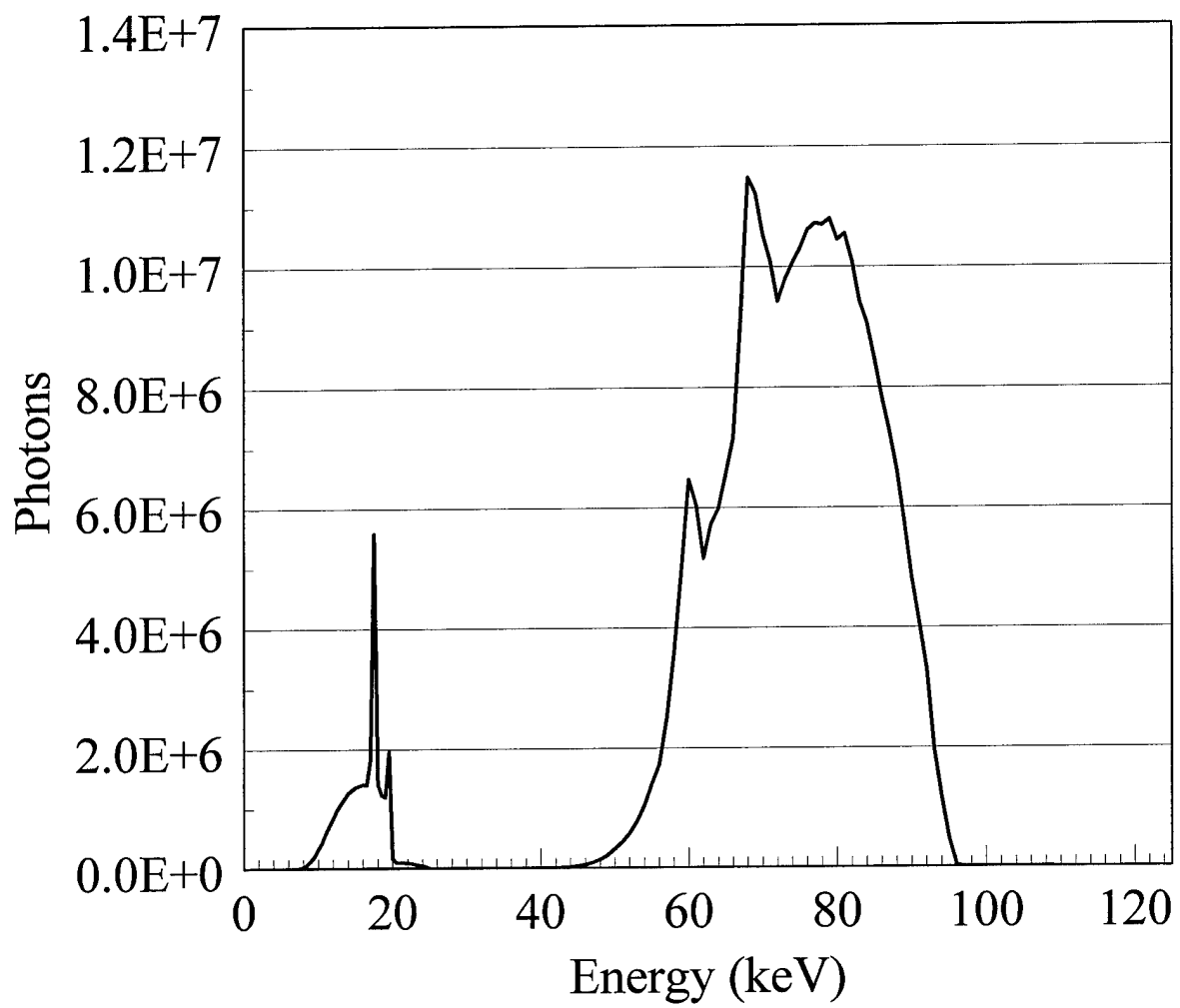
Figure 46
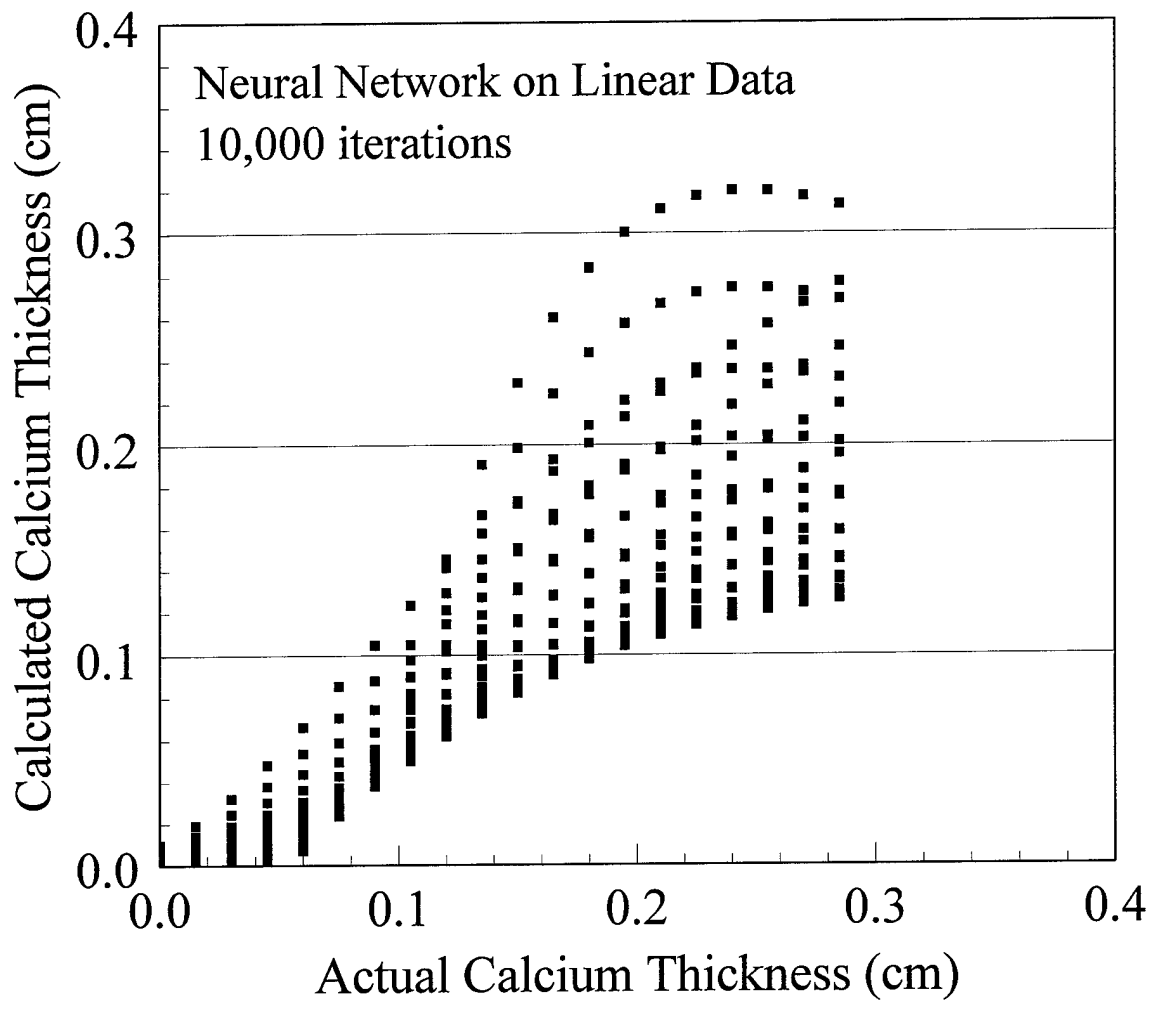
Figure 47

Figure 48

Figure 49

High Energy	Low Energy
calcium strip →	
DE - Linear	DE - Neural Net

Figure 50

Figure 51

High Energy

Low Energy

calcium strip

DE - Linear

DE - Neural Net
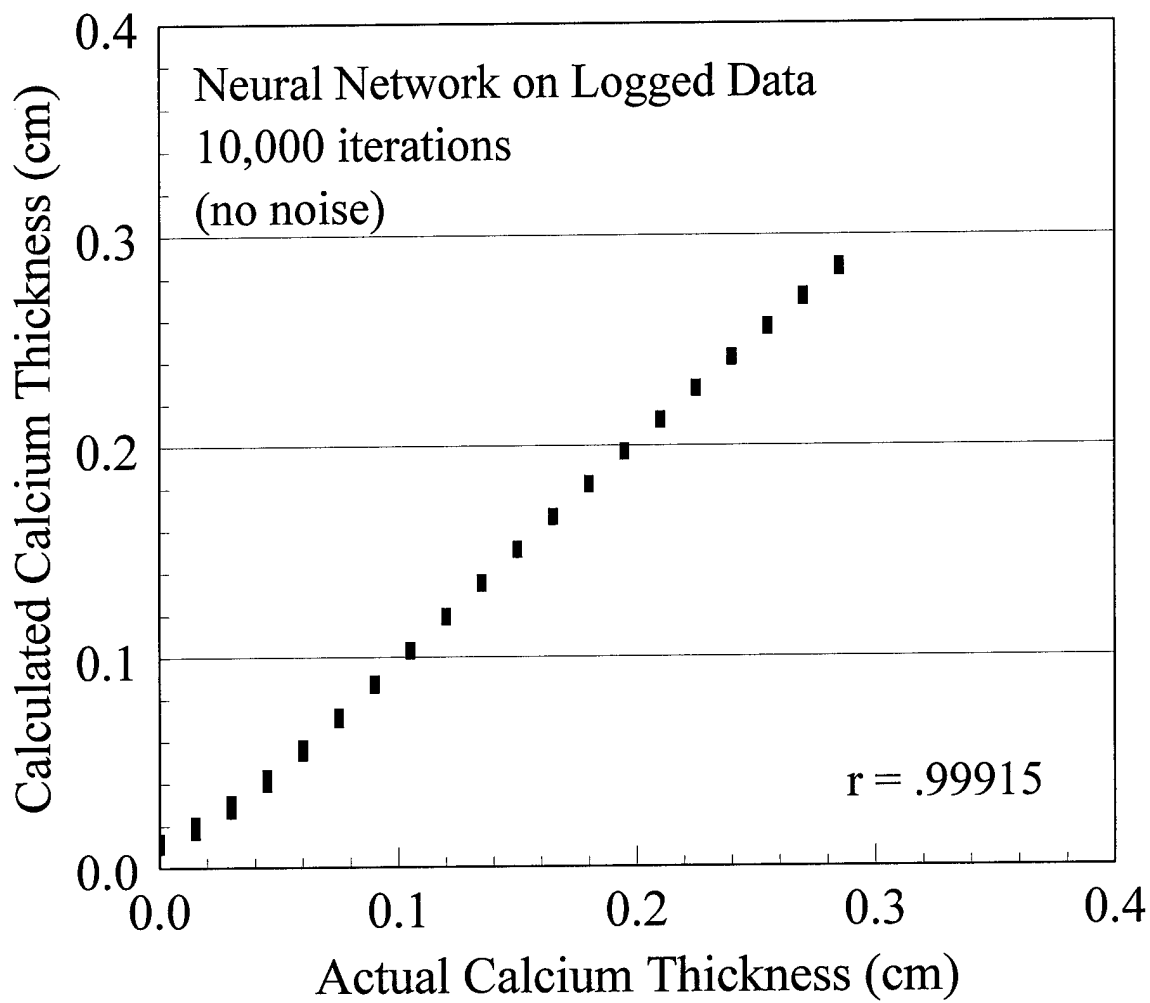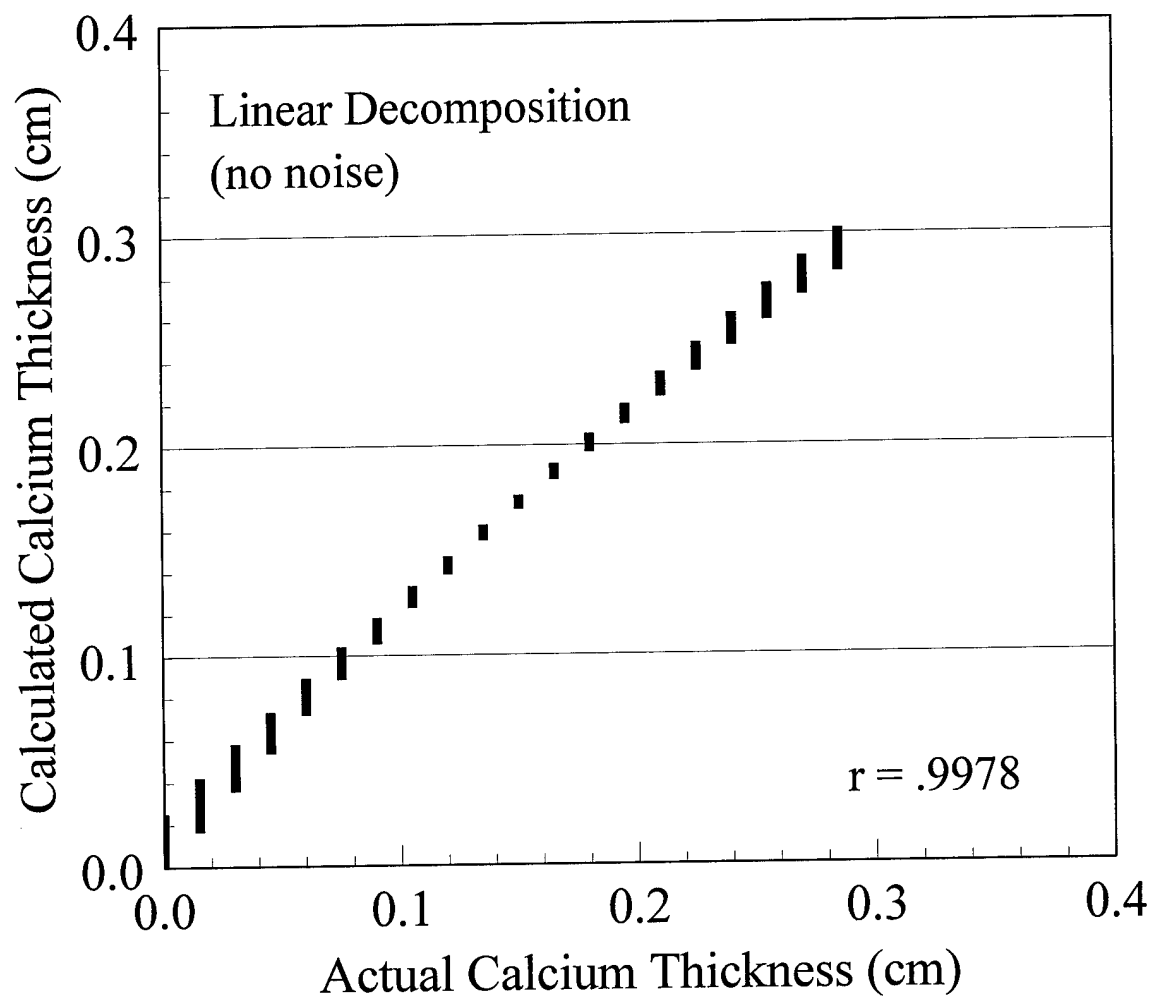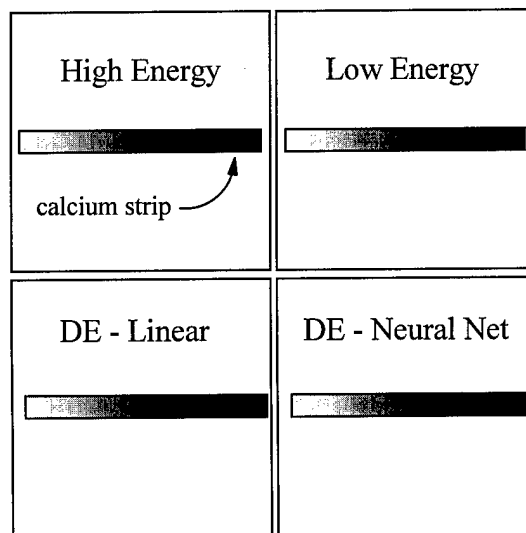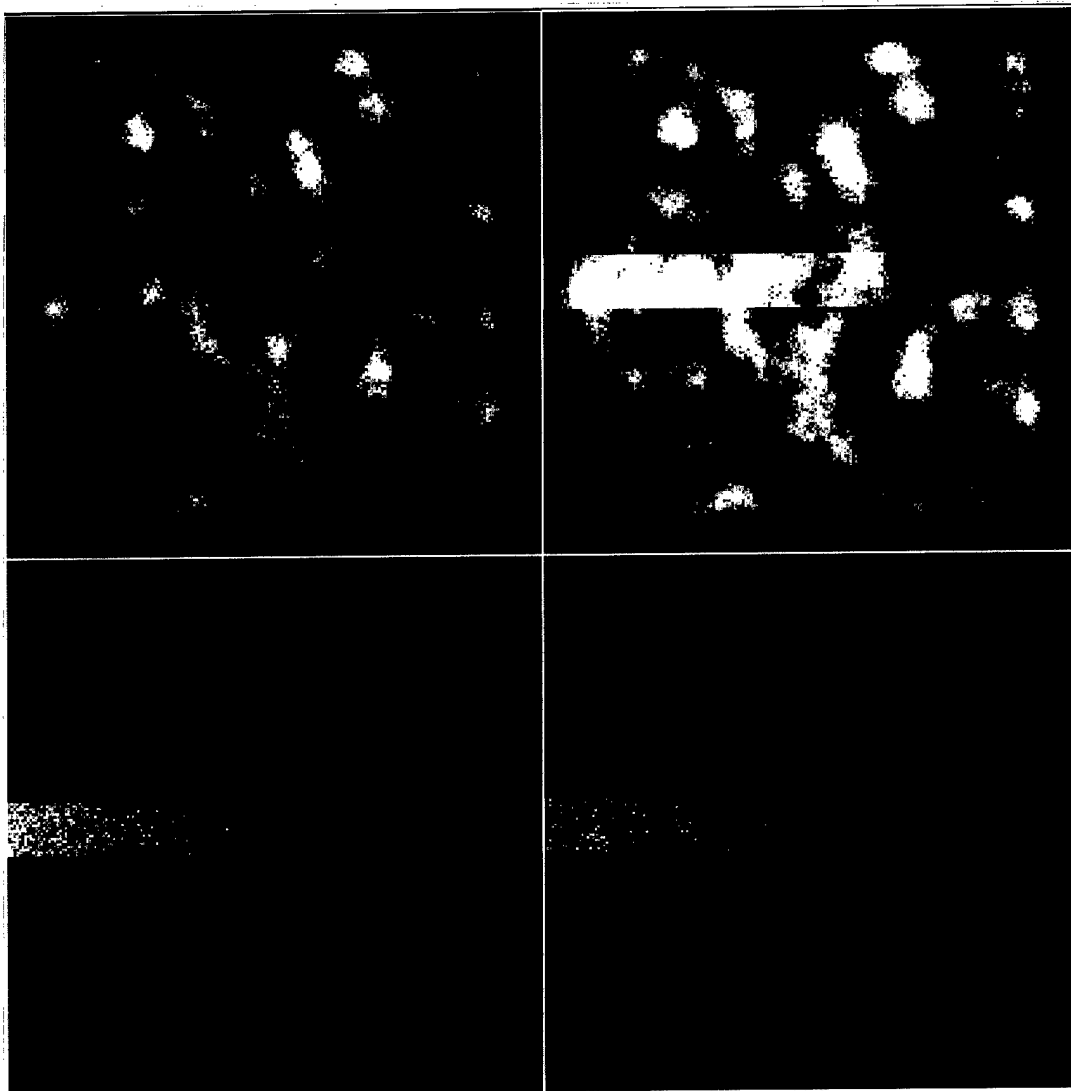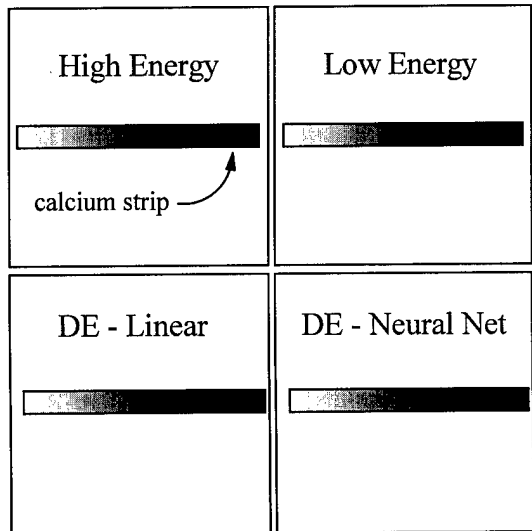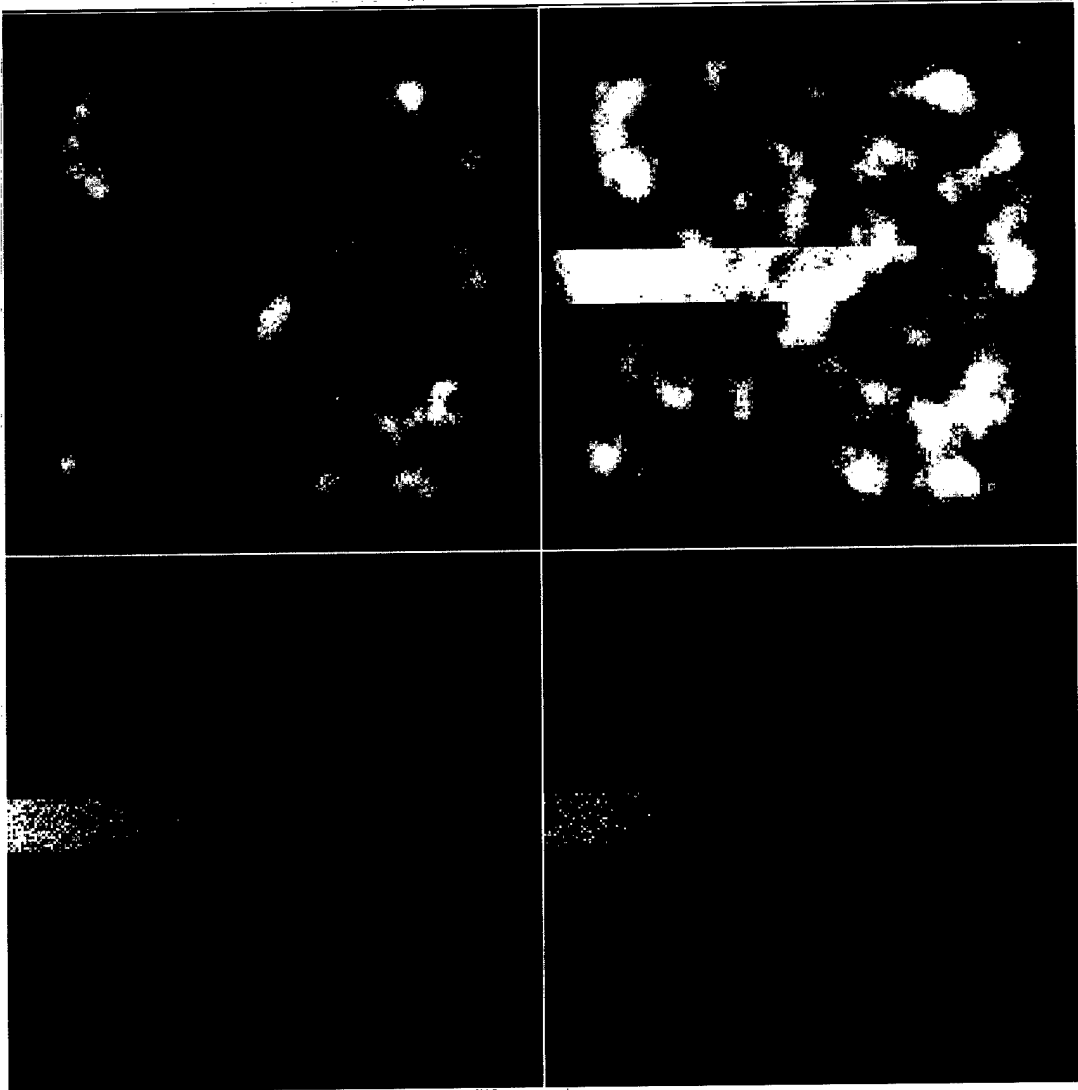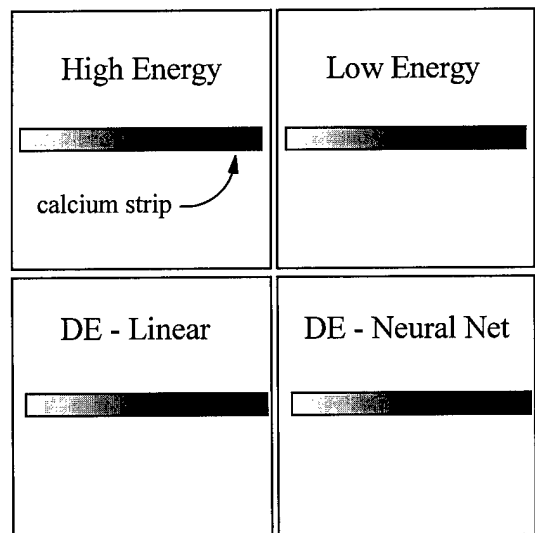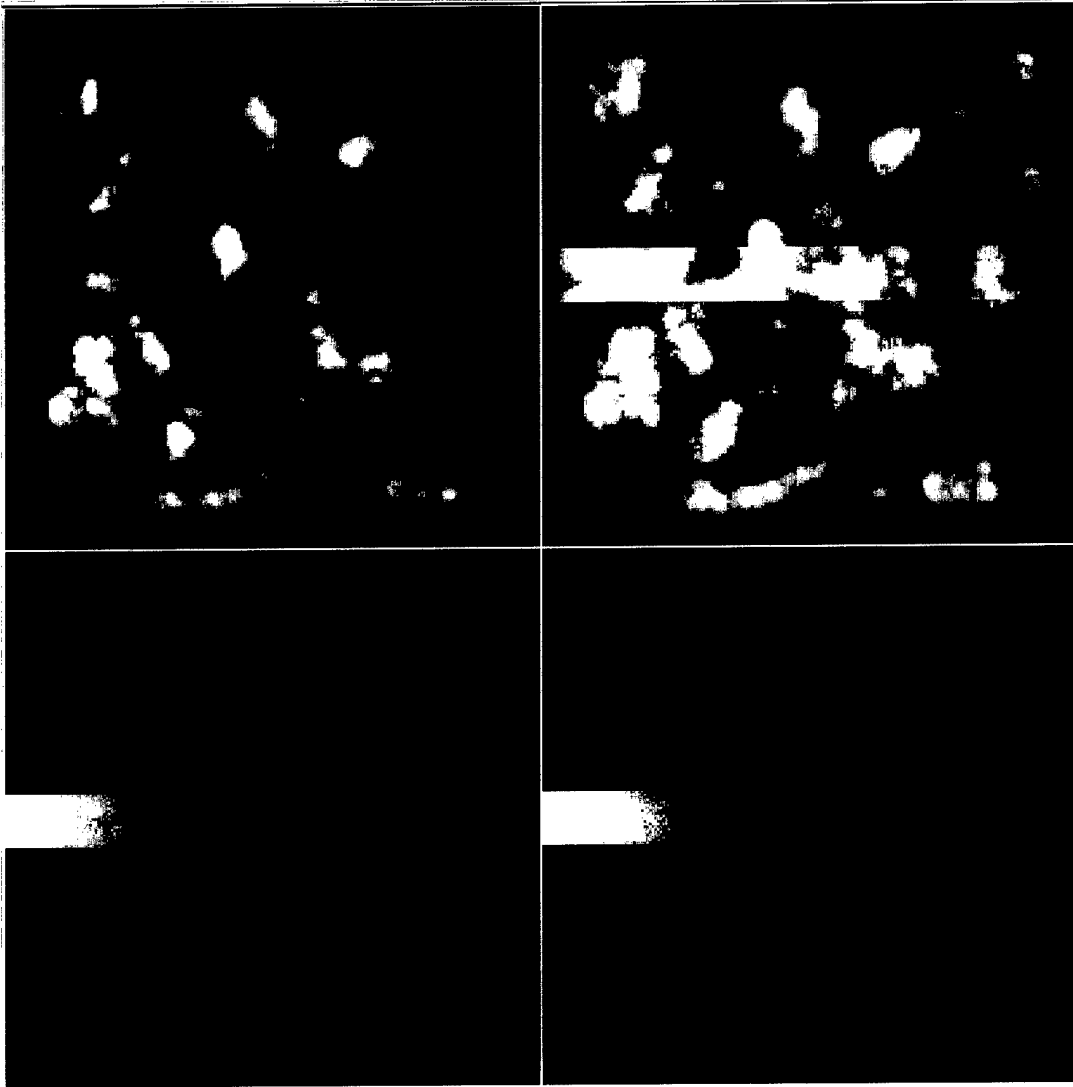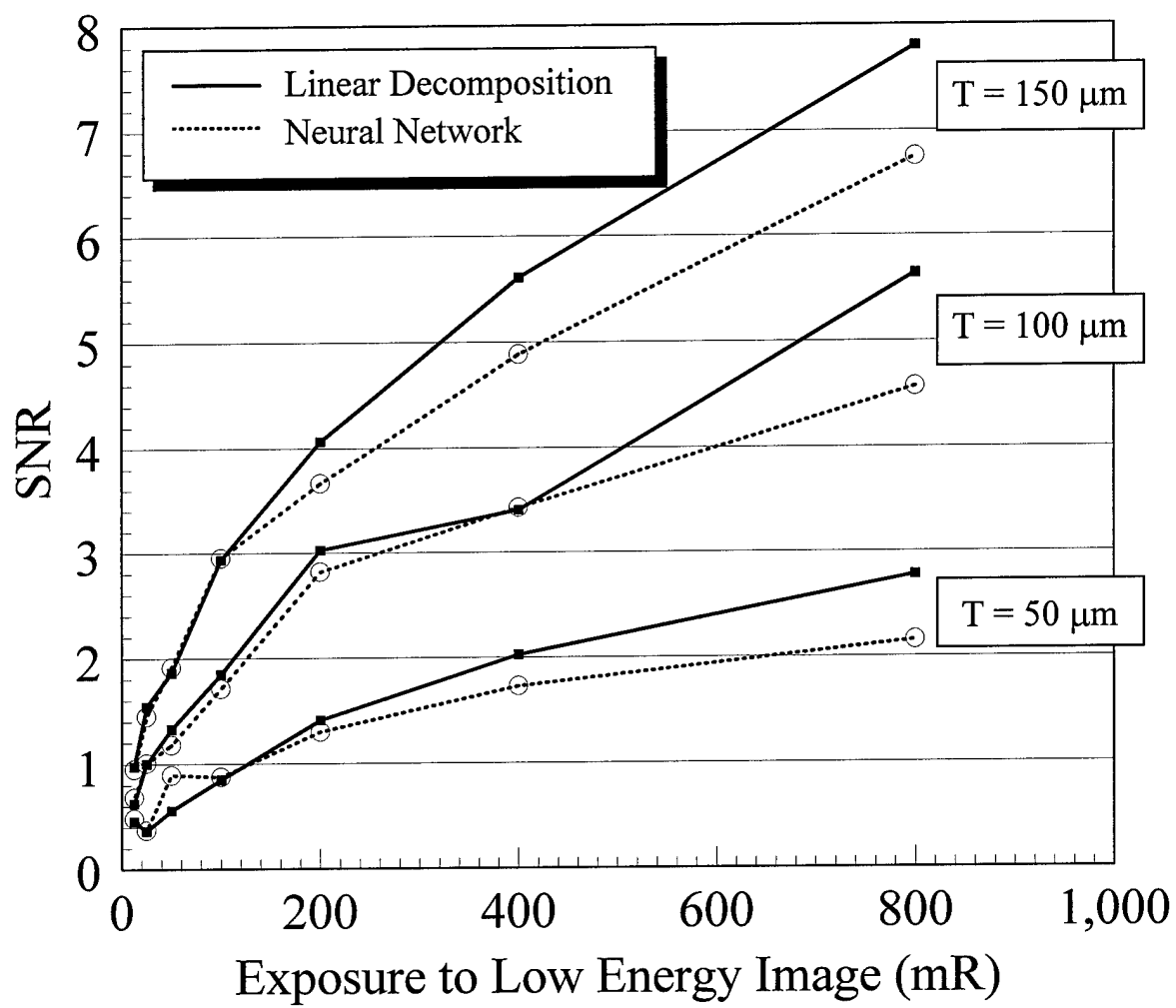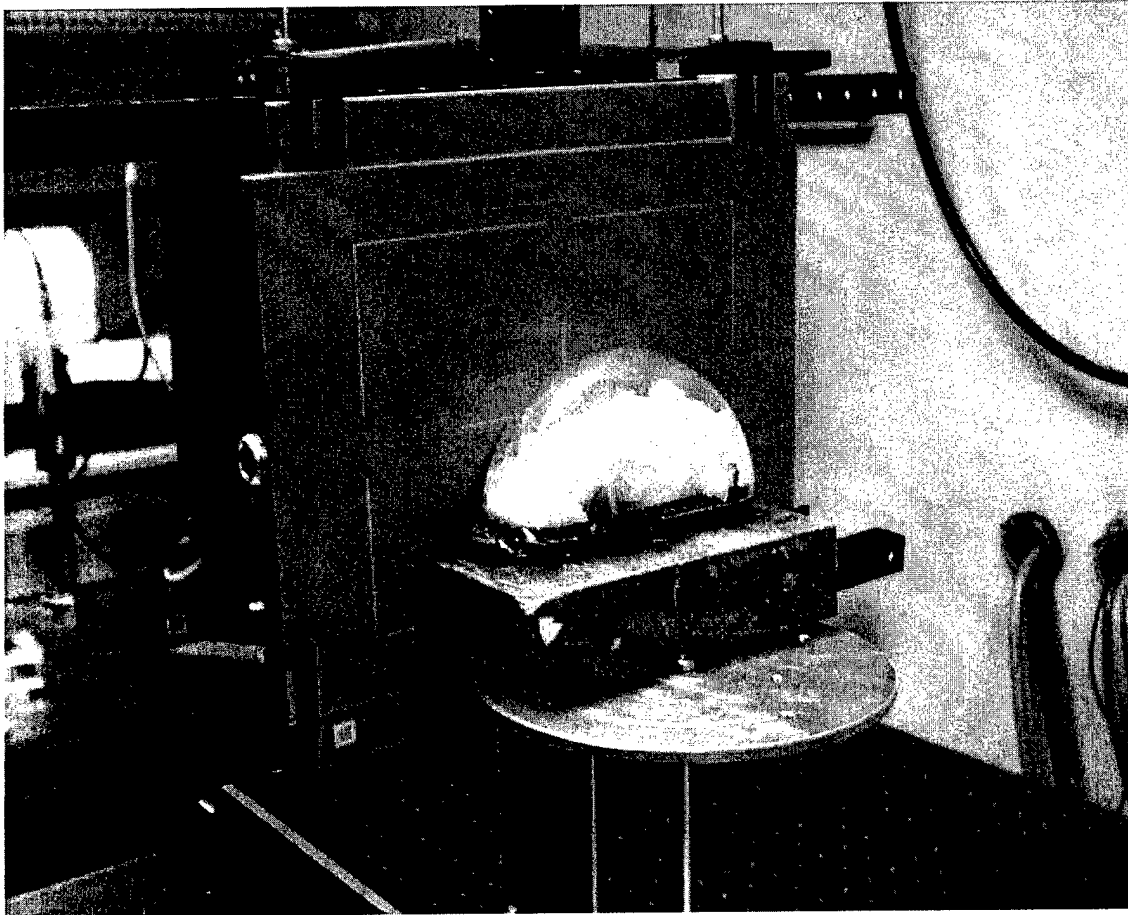
Figure 52

Figure 53

Picture of the flat panel imaging system with breast phantom

Figure 54

Low Energy
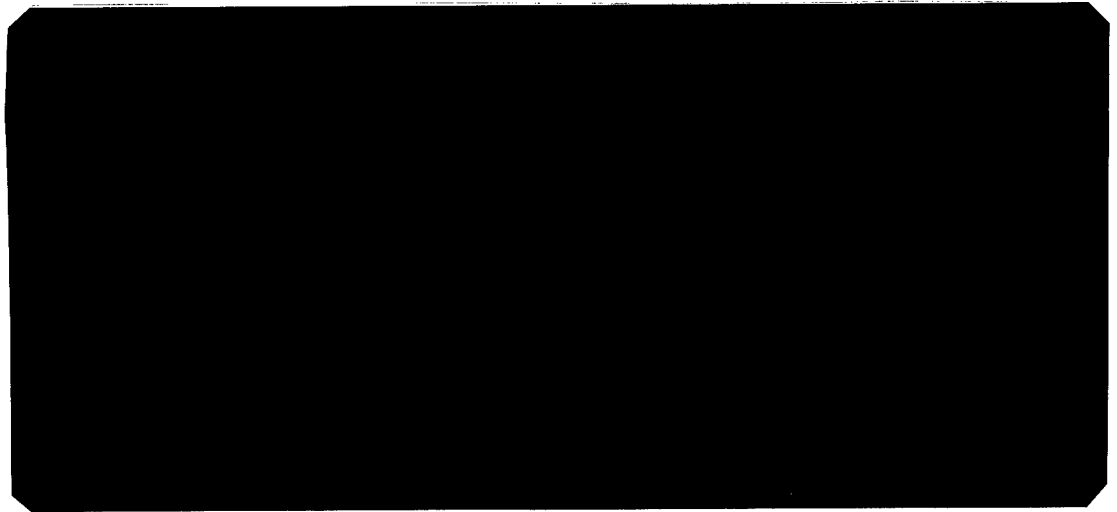
High Energy

Dual Energy

Figure 55

position of microcalcifications

High Energy Image (120 kVp)

Low Energy Image (50 kVp)

Dual Energy Subtraction

Position along Image
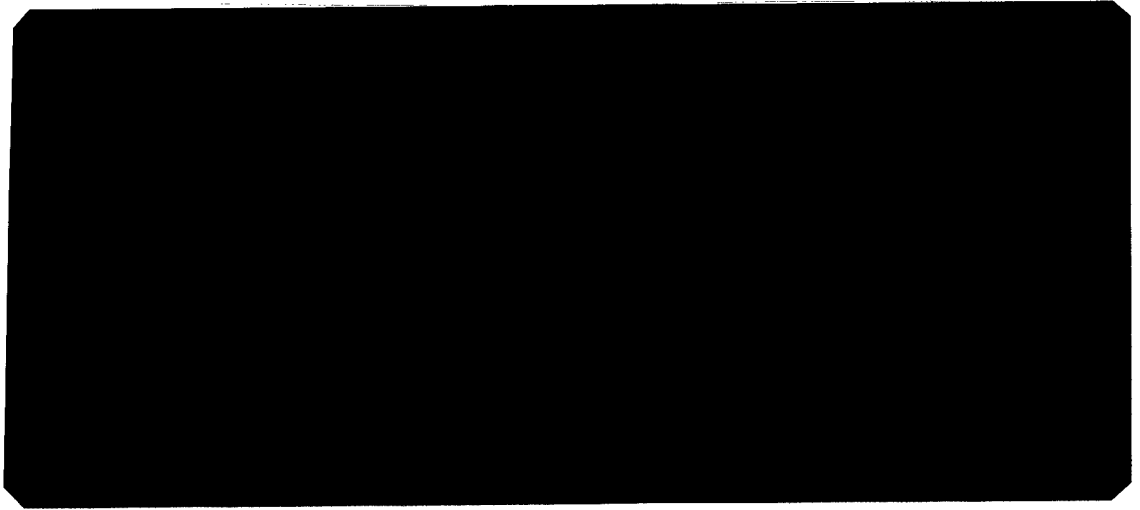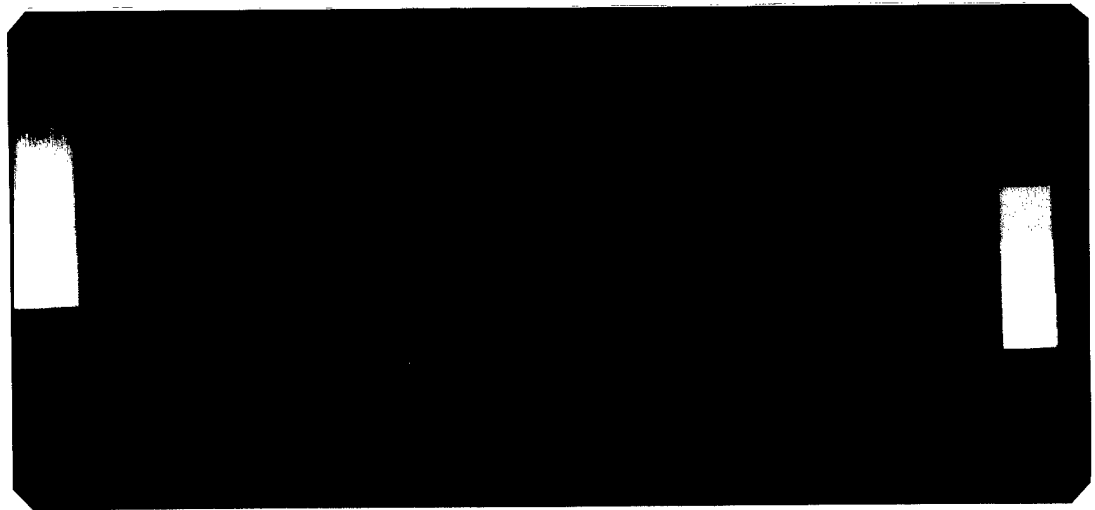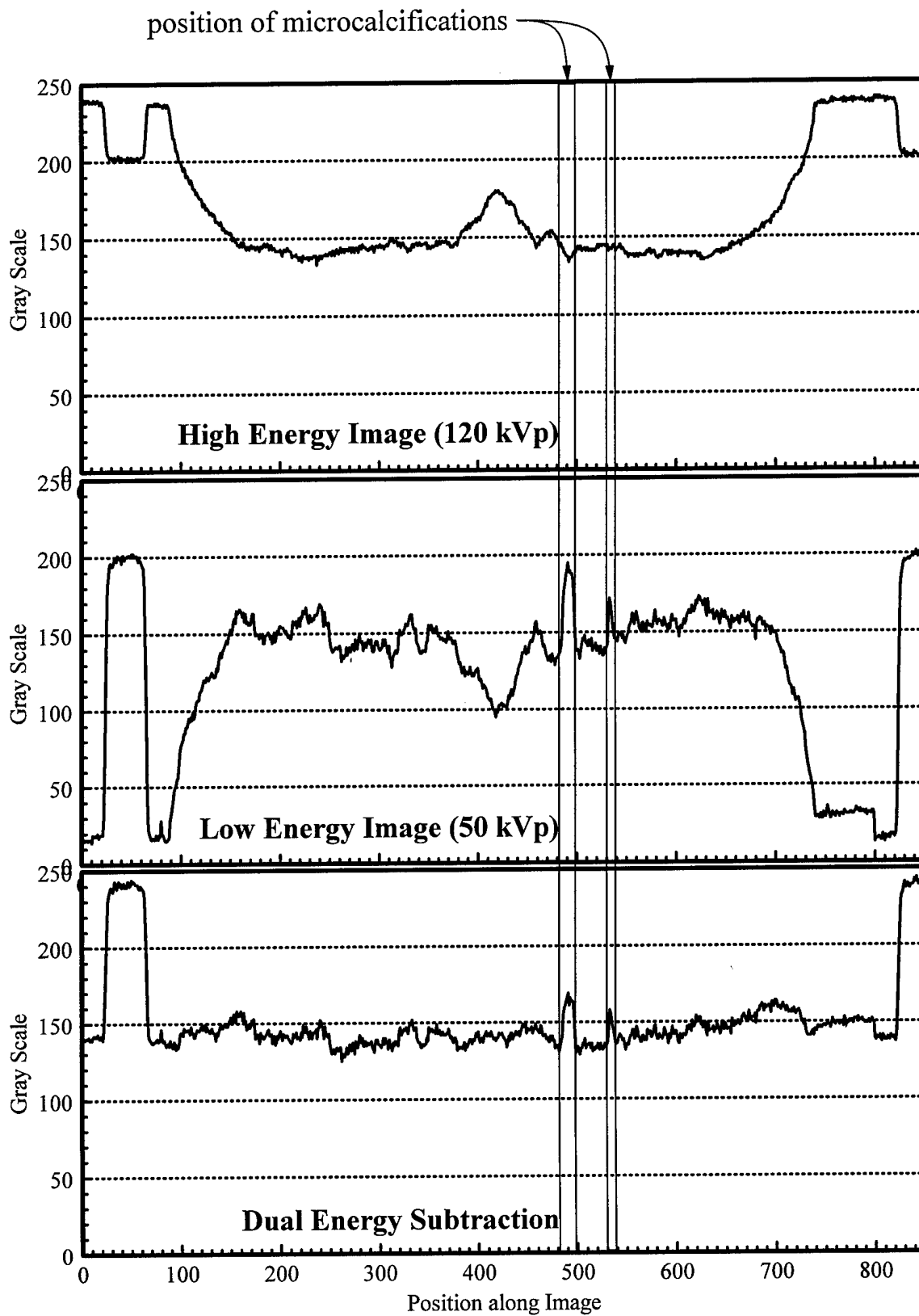
Figure 56

APPENDIX 3:

PUBLISHED PAPERS REFERENCING THIS GRANT AWARD

Sinusoidal modulation analysis for optical system MTF measurements

John M. Boone, Tong Yu, and J. Anthony Seibert
*Department of Radiology, University of California Davis, UC Davis Medical Center, Sacramento,
California 95817*

The modulation transfer function (MTF) is a commonly used metric for defining the spatial reso-
lution characteristics of imaging systems. While the MTF is defined in terms of how an imaging
system demodulates the amplitude of a sinusoidal input, this approach has not been in general use
to measure MTFs in the medical imaging community because producing sinusoidal x-ray patterns is
technically difficult. However, for optical systems such as charge coupled devices (CCD), which
are rapidly becoming a part of many medical digital imaging systems, the direct measurement of
modulation at discrete spatial frequencies using a sinusoidal test pattern is practical. A commer-
cially available optical test pattern containing spatial frequencies ranging from 0.375 cycles/mm to
80 cycles/mm was used to determine the MTF of a CCD-based optical system. These results were
compared with the angulated slit method of Fujita [H. Fujita, D. Tsia, T. Itoh, K Doi, J. Morishita,
K. Ueda, and A Ohtsuka, "A simple method for determining the modulation transfer function in
digital radiography," IEEE Trans. Medical Imaging **11**, 34–39 (1992)]. The use of a semi-
automated profile iterated reconstruction technique (PIRT) is introduced, where the shift factor
between successive pixel rows (due to angulation) is optimized iteratively by least-squares error
analysis rather than by hand measurement of the slit angle. PIRT was used to find the slit angle for
the Fujita technique and to find the sine-pattern angle for the sine-pattern technique. Computer
simulation of PIRT for the case of the slit image (a line spread function) demonstrated that it
produced a more accurate angle determination than "hand" measurement, and there is a significant
difference between the errors in the two techniques (Wilcoxon Signed Rank Test, $p < 0.001$). The
sine-pattern method and the Fujita slit method produced comparable MTF curves for the CCD
camera evaluated. © *1996 American Association of Physicists in Medicine.*

Key words: modulation transfer function, charge coupled device, line spread function, sinusoid

I. INTRODUCTION

Charge coupled devices (CCDs) and other types of light sen-
sitive detectors are increasingly becoming commonplace in
digital radiographic imaging applications. They are the de-
tectors in several digital mammography biopsy units, and are
used with increasing frequency in digital fluoroscopy and
digital photospot systems. In some laboratory settings where
CCD cameras are used for medical imaging, it is often nec-
essary to accurately assess the spatial resolution of the cam-
era and its associated optics. The motivation for this commu-
nication is to demonstrate the use of a sine wave test pattern
for the measurement of the modulation transfer function
(MTF) of optical cameras, and to compare this technique
against the more familiar line spread function (LSF) and
Fourier transform approach.[1,2]

The use of sine wave test patterns in x-ray imaging is
impractical because machining a sinusoidal pattern out of a
suitable attenuator would be costly, and the accuracy of a
sine wave output would be highly dependent on the x-ray
beam quality used. This fact has led to the use of square
wave patterns (line pair phantoms), common to all medical
physicists involved in imaging. However, for a rigorous
MTF measurement of an imaging system, the standard of

practice has been to measure the line spread function, and
calculate the MTF by computing the modulus of the Fourier
transform of the LSF. For digital systems, this calculation is
made more complex due to the influence of the digital sam-
pling, as was discussed in detail by Dobbins[2] and others.[1,3–9]
For the majority of digital imaging systems which make use
of a rectilinear array of pixels, Fujita[1] introduced an MTF
measurement technique whereby the slit is oriented at a
small angle in relation to the pixel matrix. If the slit is ori-
ented at a small angle with respect to the Y axis, then con-
secutive pixel-row samples taken down the Y axis will yield
a data set where the digital sampling comb is slightly shifted
in phase with each successive row. This allows the recon-
struction of the line spread function with much better digital
sampling than is possible by sampling just a single row. Be-
cause this technique overcomes the sampling limitation of
the digital matrix, it is effective at overcoming the Nyquist
criterion and therefore is useful in calculating the so-called
presampled MTF.[1,2] The presampled MTF in this investiga-
tion includes the resolution degrading influence of all com-
ponents in front of the CCD chip, as well as the degrading
influence of the sampling aperture. To illustrate the differ-
ence between a technique which determines the postsampled
MTF and the presampled MTF, the Dobbins expectation
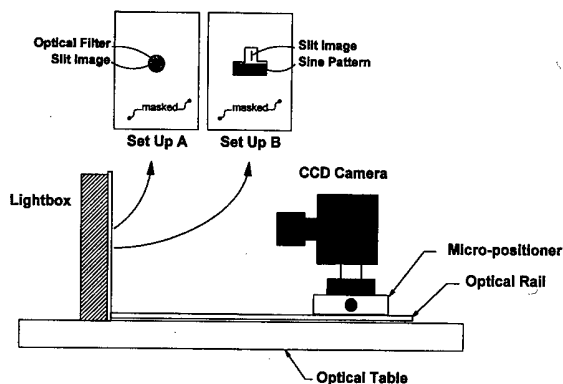
FIG. 1. The experimental setup that was used for the acquisition of line spread functions and sinusoid image data is illustrated. The micropositioner was controlled using stepping motor and computer software.

FIG. 2. A diagram of the Dobbins and Fujita methods is shown. For the Dobbins method, the slit was perfectly aligned with the pixel columns and the shift increment Ω was indexed using a computer controlled micropositioning device. For the Fujita method, the slit input was aligned at a slight angle with respect to the pixel matrix, given by angle θ. For imaging systems with square pixels and pixel width (and height) Δ, the horizontal phase shift per row is Ω, and this is given by the relation $\Omega = \Delta \tan(\theta)$.

MTF method is compared to the Fujita method in calculating the MTF of a CCD camera.

The use of a sinusoidal optical image does not intrinsically overcome the limitations of sampling, and therefore the sinusoidal test pattern also needs to be aligned at a small angle with respect to the pixel matrix. The sinusoidal signal is reconstructed from the slightly phase shifted rows in a manner identical to the LSF synthesis described by Fujita.[1] In this study, a semi-automated procedure dubbed *profile iterated reconstruction technique* (PIRT) was used to optimize, in a least-squares minimization sense, the reconstruction of an oversampled profile (either a line spread function or a sine wave). The expectation MTF technique proposed by Dobbins' was also compared against the Fujita slit method.

II. METHODS

A. Physical experimental setup

A 1024×1024, 12 bit Peltier cooled CCD camera (SpectraSource, Goleta, CA) using a Texas Instruments chip was mounted on an optical bench (Fig. 1). The CCD camera was evaluated and was found to be very linear in terms of its gray scale response to light. There were two different experimental setups used: (A) one in comparing the Fujita method with the Dobbins expectation method; (B) the other in comparing the Fujita method with the sinusoidal test pattern technique.

The relative distances between the lightbox (the focal plane) and the CCD camera shown in Fig. 1, and thus the magnification factor (the size of the pixels measured in the focal plane) were different in setup A versus setup B. The Dobbins expectation method required precise movement of the CCD camera with subpixel ($\frac{1}{25}$ pixel) accuracy to achieve differences in pixel-phase sampling. To do this, given the positioning accuracy limitations of the high quality optical stage used, larger pixels were required.

In x-ray radiography imaging evaluations, the test phantom (e.g., slit) is typically positioned in contact with the detector, because the detector is the imaging plane. With

optical systems such as a CCD-lens system, of course the slit needs to be positioned in the focal plane (the optical equivalent of the imaging plane).

1. Setup A: Comparison of the Dobbins and Fujita methods

The evaluation of the expectation MTF proposed by Dobbins required moving the camera in very small increments in order to shift the digital sampling comb laterally by subpixel increments. This was accomplished using a stepping motor which controlled the movement of a micropositioning optical stage. The stepping motor was controlled by computer software written in our laboratory, using a digital to analog (D/A) converter (Data Translation DT2801A, Marlboro, MA) with transistor–transistor logic (TTL) control logic interfaced to the stepping motor controller. To simulate the pseudomonochromatic emission of an x-ray intensifying screen, an optical filter (Oriel, Stanford, MA) with a narrow bandpass of 520 nm light was positioned over a standard light box, and all peripheral areas of the light box were masked out using superimposed dark films (total OD≈6–7). The lightbox was positioned approximately 400 mm from the CCD camera, and a Nikon $f/1.2$ lens was used (Fig. 1). The stepping motor controlled translational motion of the CCD camera along the horizontal or x dimension in the imaging matrix, or into the plane of the illustration in Fig. 1.

A very thin wire was used with direct exposure x-ray film (Kodak X-Omat TL film, Rochester, NY) to produce a slit image (white slit on dark background). The inner wire of a low current fuse was measured with a micrometer and found to be approximately 20 μm in diameter. The image of the wire was acquired in contact geometry using 23 kV and 600 mAs on a standard mammography unit, with a source-to-image distance (SID) of 65 cm. The slit image was placed in contact with the optical filter and imaged using the CCD camera, using two different geometries (Fig. 2). For all images acquired, a dark current image was acquired with the

same exposure time, and the dark current image was sub-tracted to remove the offset that it introduces. A noiseless digital offset was added to the image to prevent truncation of negative subtraction results.

In a recent article, Dobbins[2] discusses various relation-ships between the presampled MTF (MTF_{pre}), the MTF_{min}, the MTF_{max}, and the expectation MTF (EMTF). The MTF_{max} is the MTF calculated when one of the δ functions (center of the pixel) in the sampling comb is in perfect align-ment with the peak of the LSF. The MTF_{min} is measured with the digital sampling comb phase shifted from the peak by π radians of phase ($\frac{1}{2}$ pixel width). The expectation MTF is effectively the average of a series of phase-shifted MTFs (averaged over 2π of phase angle), individually computed by sampling a single row of pixel data in the image of a slit. For the Dobbins method, the image of the slit was very carefully aligned with the pixel columns (Fig. 2A). Once aligned, a series of 24 images was acquired with very small translation of the CCD camera between each acquisition. With the pixel width measured at 102 μm, the camera was moved approxi-mately 4.25 μm between each acquisition, using a computer/stepping motor/micropositioner system. With this method, oversampling was achieved mechanically and the MTFs were computed from the undersampled LSFs, and then the MTFs were averaged (in the frequency domain) to calculate the expectation MTF.

For the Fujita method,[1] the slit was placed so that a small angle between it and the CCD pixel matrix resulted, as illus-trated in Fig. 2B. The Fujita method requires only one image acquisition, with no shifting of the camera or object, but also results in oversampling of the LSF with much finer sampling increments than the pixel spacing. For this study, the pixel size (linear dimension of square pixel, Δ) in the imaging plane measured 102 μm (Nyquist limit=4.9 cycles/mm). The ~4.6° slit angle used allowed the sampling interval to be reduced to about 8.2 μm (Nyquist limit=61 cycles/mm).

2. Setup B: Comparison between Fujita slit method and sine-pattern method

An alternative but similar experimental setup was used in comparing the Fujita method with the sine-pattern method. In this study, the wavelength filter was removed because of its small field of view, and the sine-pattern template and the optical slit were positioned on the lightbox, together with the rest of the field of view masked out. Five images were ac-quired of the slit and sine pattern ($I_{\text{sin\&slit}}$), and five dark current images taken at the same exposure time were ac-quired (I_{dark}). The optical slit and the sine pattern were po-sitioned on the same image. The phantoms were removed from the lightbox, and five images were acquired of the light field (I'_{flat}). Because of the higher light levels without the optical templates present, the light field images were ac-quired with shorter exposure times. Five dark current images were then acquired at this exposure time (I'_{dark}). The five images in each group were averaged pixel-by-pixel, and then a final image was computed as:

$$I_{\text{final}} = (I_{\text{sin\&slit}} - I_{\text{dark}}) \times \frac{\text{AVE}}{(I'_{\text{flat}} - I'_{\text{dark}})}, \qquad (1)$$

where AVE is the average of the gray scale values in the denominator image ($I'_{\text{flat}} - I'_{\text{dark}}$). The LSF and sinusoid modulation measurements were made on I_{final}. The dark cur-rent and "flat fielding" corrections made here [Eq. (1)] are similar to what is performed with CCD cameras currently in clinical operation. In this setup, the pixel size measured 105.5 μm.

B. Profile iterative reconstruction technique (PIRT)

In the Fujita slit method,[1] the slit is oriented at a slight angle with respect to the pixel matrix and the LSF is reconstructed from the shifted samples from each successive row of data. To calculate the shift increment per pixel row (Ω in Fig. 2B), the angle θ was measured. This angle was measured by dis-playing the slit image on a computer display board (RX20, DOME Imaging Systems, Inc., Waltham, MA with a NEC MultiSync 6FG 21" Monitor), and using a computer pro-gram with hand-eye-mouse-cursor placement software, two locations along the slit were identified resulting in two coor-dinates, (x_1, y_1) and (x_2, y_2). The angle (as defined in Fig. 2B) is calculated as $\tan^{-1}(\Delta x/\Delta y)$, where $\Delta x = |x_1 - x_2|$ and $\Delta y = |y_1 - y_2|$.

With a small slit of finite extent, the precise identification of the center of the slit is subjective and constrained by the discrete nature of the pixelized image. As an illustration of these constraints, take for example the approximately 100 μm pixels in our experiments and a 5° slit angle. Referring to geometry similar to Fig. 2B, if the two points identified using the cursor are 100 vertical pixels (Δy) from each other, the horizontal separation (Δx) would be 8.74 pixels [$100 \times \tan(5°) = 8.74$]. Since cursor identified coordinates are necessarily integer, the cursor placement will be either at 8 or 9 pixels for Δx. These values would result in an angle determination of 4.57° or 5.14°, corresponding to errors of -8.5% or 2.8%. This is really a best case scenario, since the 100 pixel Δy represents a distance of 10 mm, and at this point the straightness of a tiny slit comes into question. Be-cause of these concerns, an automatic profile reconstruction routine was developed as explained below.

The slit angle was evaluated by hand as described above, and the angle θ_{direct} was found. This value is referred to as the "direct measurement" angle value. This angle was then used in a simple profile iterated reconstruction procedure. One hundred angles between ($\theta_{\text{direct}} - 2.5°$) and ($\theta_{\text{direct}} + 2.5°$) were iterated over. For a predefined region of the slit (de-fined by a rectangle placed on the image using hand-eye-mouse-cursor software), the LSF was reconstructed at each angle used in the search procedure. Although adjacent pixel midpoints are separated by integer pixel values, the shift value Ω between each successive pixel row is a real number, and thus the profile is reconstructed on a different (smaller) scale than the original image. The LSFs were reconstructed using a fivefold increase in spatial sampling, so for the 105.5 μm pixels in the original image, the LSF was reconstructed
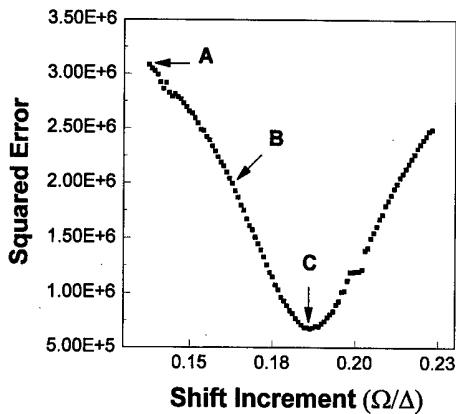
FIG. 3. The squared error versus the phase shift increment, Ω/Δ. The shift increment, Ω/Δ, is gradually changed, the LSF is reconstructed, and the squared error between the mean LSF and all the LSF points is calculated. The shift increment having the smallest squared error is chosen as the optimum shift value, indicated in this figure as "C." The letters refer to the reconstructed LSFs shown in Fig. 4. The abscissa is equivalent to the tangent of the slit angle θ, i.e., $\Omega/\Delta = \tan(\theta)$.

FIG. 4. The reconstructed LSFs, showing different shift values for A, B, and C. The letters correspond to the square error values illustrated in Fig. 3. LSF #C in Fig. 4 is the "best fit," based on the minimum squared error seen in Fig. 3. The error is calculated between all the points shown in these curves and the mean LSF values, illustrated here as a solid line. The mean LSF value is calculated using all the LSF points that are aligned vertically, and then binned into discrete intervals five times smaller than the measured pixel size.

using 21.1 μm pixel sampling. By reconstructing a large number of rows, many data points were rebinned into each 21.1 μm sampled LSF position. At each profile position, the mean gray scale value was computed, and then the sum of the squared differences between the mean and the individual points was computed. By summing this "squared error" over the entire horizontal extent of the reconstructed profile, a global "squared error" value was calculated. To illustrate this, Fig. 3 shows the squared error as a function of the shift value resulting from iterating $\pm 2.5°$ around the θ_{direct} value for a LSF reconstruction. This error-versus-angle curve shows a distinct minima (marked as point C in Fig. 3), which is selected as the best angle, θ_{best}, resulting from the iterated search. Figure 4 shows three reconstructed LSFs, each reconstructed with different angles, marked A, B, and C, corresponding to the same letters indicated on Fig. 3. Reconstructed LSF A is very "unfocused," as seen in Fig. 4, and the reconstruction improves somewhat for LSF B, where the angle is closer to the optimal value. The reconstructed LSF C on Fig. 4 corresponds to a minimum in the squared error, and this point defines θ_{best} and this is the average LSF (solid line) that is used in calculating the MTF using Fourier techniques as described above.

C. Computer simulation of PIRT

Computer simulation was used to compare PIRT against direct measurement of the slit angle. With computer simulation, the actual angle θ is know exactly, since it is generated in the computer, and therefore simulation is useful in comparing the accuracy of direct measurement against the PIRT method. The signal component of the computer generated LSFs were sampled from a Gaussian distribution,

$$G(x) = \exp\{-\tfrac{1}{2}((x-\mu)/\sigma)^2\}. \tag{2}$$

The noise (deviation from the calculated signal value) in the computer-generated LSF images was generated by using a

random generator to randomly issue a noise value for each pixel, according to a Gaussian distribution with the variance set equal to the mean (Poisson approximation). For each pixel row below the top one, where the center of the LSF was aligned with the center of the pixel, the value of μ was shifted by $\tan(\theta_{\text{actual}})$, where θ_{actual} is an angle selected between 2° and 12° using a random number generator, with a linear probability of generating angles over that range. The actual angle was not know to the human observer. To simulate the finite sampling typical of real experiments, σ was chosen as 2 times the pixel width. The width of the LSF as projected onto a row of pixels increased appropriately by $\cos(\theta_{\text{actual}})$.

One hundred computer generated slit images, 50 at high signal to noise ratio (SNR) and 50 at low SNR were generated and evaluated. The SNRs were relative values, and the intention was to test the angle reconstruction capabilities of PIRT under a range of realistic circumstances. The low SNR was estimated to have a SNR of about 2. The higher SNR was approximately 20. The reconstructed LSFs were computed to a pixel sampling five times that of the original computer simulated images. The actual pixel sizes in this simulation were arbitrary, but to give real numbers to the example, if the original pixels were 100 μm, then the reconstructed pixels were 20 μm, and 98% ($\pm 3\sigma$) of the LSF counts fell within 1.2 mm ($6 \times 2 \times 100$ μm).

Software was written to allow for hand-eye-mouse-cursor placement of a cursor, obtaining the two pixel locations (two pairs of coordinates) used to calculate θ_{direct}. This angle is the direct measurement value, but is also the seed value used in the PIRT calculation. The PIRT algorithm was then run as described above.
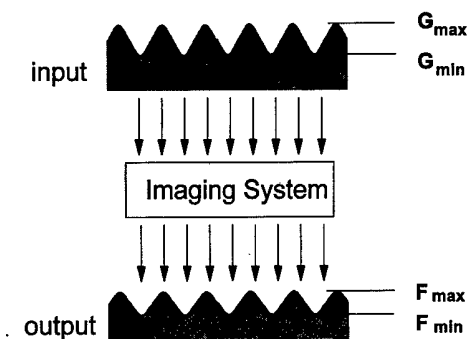
FIG. 5. A graphical reminder of the definition of modulation due to an imaging system is shown. For a sinusoidal input of a single frequency, the input modulation is given by $(G_{max}-G_{min})/(G_{max}+G_{min})$. After the input signal has been received and processed by the imaging system, it outputs a corresponding signal. The output modulation is given by $(F_{max}-F_{min})/(F_{max}+F_{min})$. The modulation attributed to the imaging system at this frequency is the ratio of the output modulation to the input modulation.

D. Optical sine-pattern determination of MTF

A sine wave optical test pattern was purchased (Sine Patterns, Penfield, NJ). The sine pattern was a single sheet of transparent film measuring approximately 48 mm×215 mm, having spatial frequencies of 0.375, 0.50, 0.75, 1.0, 1.5, 2.0, 2.5, 3, 4, 5, 6, 8, 10, 12, 16, 20, 24, 32, 40, 48, 64, and 80 cycles per mm. For the magnification factors used here (105.5 μm pixels in the imaging plane, 24 μm pixels on the CCD chip itself), only the sine patterns $\leq$10 cycles/mm were used. All determinations of spatial frequency and of pixel size are referenced to the image plane, that is, the plane of focus of the CCD camera. By changing distances and focal lengths (using lens extension tubes), a great variation in magnification can be achieved. Depending on the magnification, various components of the imaging system will differ in terms of their overall contribution to MTF degradation. Using the sine wave method, the input modulation at the known spatial frequency is given by:

$$M_{in}=\frac{G_{max}-G_{min}}{G_{max}+G_{min}}, \quad (3)$$

where G_{max} and G_{min} are transmission values (not optical density) and M_{in} was provided by the manufacturer of the sine pattern. The M_{in} values were measured by the manufacturer using a scanning microdensitometer with a 1 μm scanning slit. The values of G_{min}, G_{max}, F_{min}, and F_{max} are defined in Fig. 5. The output modulation was calculated as

$$M_{out}=\frac{F_{max}-F_{min}}{F_{max}+F_{min}}. \quad (4)$$

The system MTF value at a given frequency was calculated as

$$MTF(f)=\frac{M(f)_{out}}{M(f)_{in}}. \quad (5)$$

The MTF values determined using Eq. (5) are normalized at all spatial frequencies by the fact that the $M(f)_{in}$ values [the denominator of Eq. (5)] are provided by the manufac-
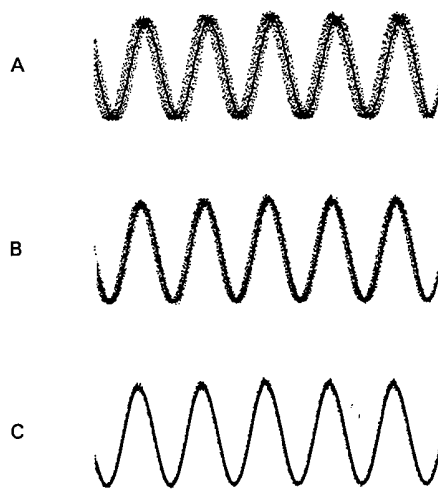
FIG. 6. The reconstructed sine waves from the sinusoidal test pattern, showning three different reconstructions varying by the shift value, Ω. The technique used to optimize the fit was identical to that used for the LSF reconstruction. The sine wave shown in C is the best fit curve, with A being the worst fit and B being intermediate.

turer from microdensitometer scans of the optical sine pattern, in the form of a computer printout for each frequency on the pattern. Because a zero frequency pattern does not exist, the MTFs are not explicitly normalized at the zero frequency, which is a bit different than in most LSF/Fourier techniques. Instead, known modulation values at the different spatial frequencies [$M(f)_{in}$, provided by the manufacturer] are used for absolute calibration of each point along the curve. The $M(f)_{in}$ values for the pattern used in this study ranged from 0.7798 to 0.8422, and since a scanning microdensitometer was used to evaluate these it was felt that errors in these values would be minor in comparison to the other sources of imprecision.

The sine wave patterns were aligned at a small angle with respect to the pixel matrix, as in the Fujita method for slit data. An initial angle (θ_{direct}) was selected (marking a ridge or a trough in the imaged sine pattern using a hand-eye-mouse-cursor routine), and the PIRT algorithm searched for the best shift value, here reconstructing a sine wave instead of a LSF as described previously. Examples of sine patterns being reconstructed are shown in Fig. 6, where Fig. 6C illustrates the best reconstruction based on least squared error. The reconstructed sine wave is the mean of the reconstructed values, as was the case for the LSF. From this segment of a sine wave at each spatial frequency, the minimum and maximum values were found and these were the values F_{min} and F_{max} respectively. The background correction procedure described above [Eq. (1)] compensated for dark current image, but for nothing else. Because the film that the sine pattern was printed onto had some finite density (about 0.14 OD), the mean gray scale value of the background region near the sine pattern was measured and subtracted from the F_{min} and F_{max} measurements, prior to inputting these values into Eq. (4).
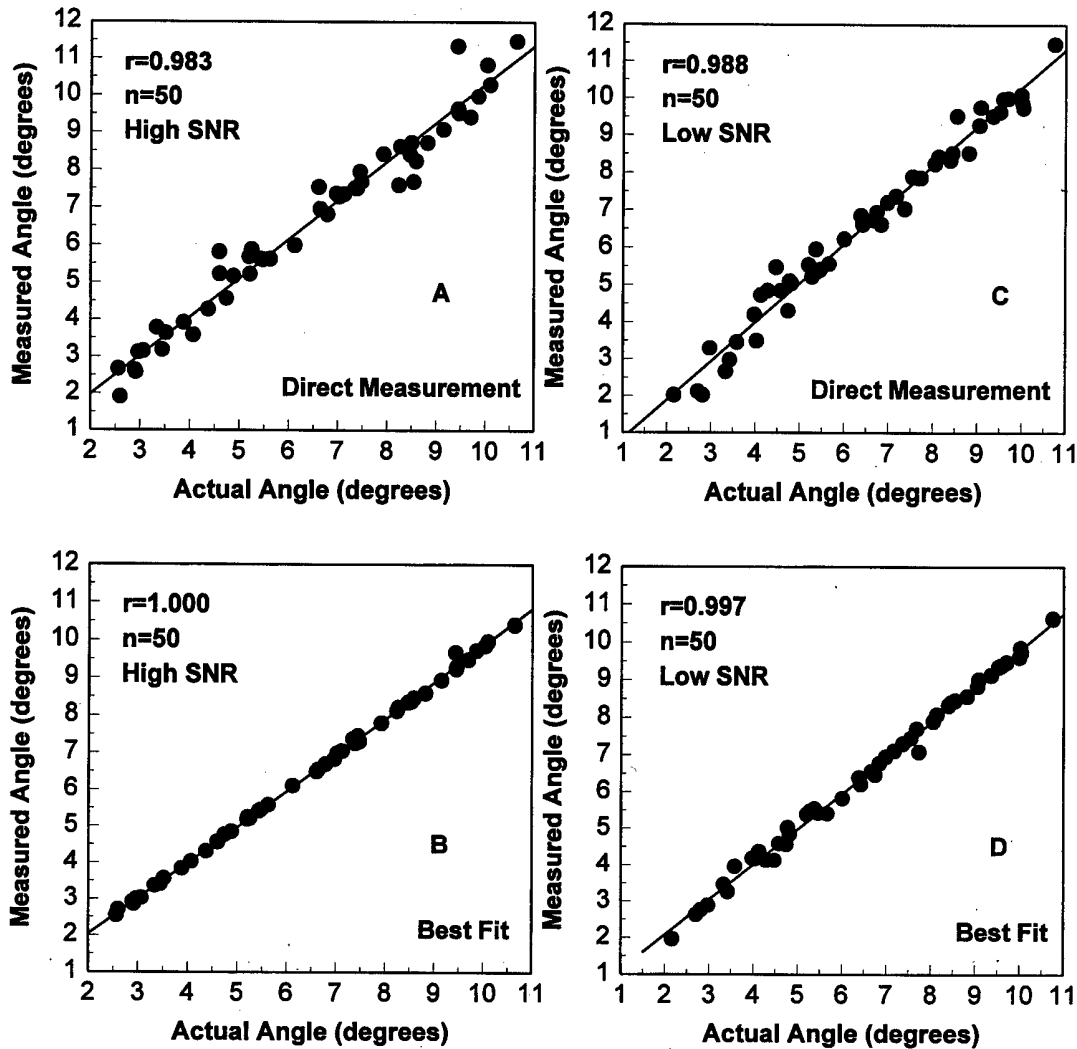
FIG. 7. The relationship between the measured angle and the actual angle, for a computer simulated slit where the actual angle was known. The upper figures (A and C) show the results for measured angles using hand-eye-cursor measurements, where the angle was calculated based on the placement of two cursor points along the image of the slit. The lower figures show the results for the best fit angles, determined using the procedure illustrated in Figs. 3 and 4. The best fit angle is the arctangent of the shift increment resulting in the least squared error, as indicated by arrow "C" in Fig. 3. In the computer simulations, two different signal to noise ratios (SNR) were tested to examine the robustness of the fitting procedure at low SNRs. The low SNR was estimated to be about 2, while the high SNR was approximately 20.

III. RESULTS

A. Profile iterative reconstruction technique (PIRT)

The results of the computer simulation study are shown in Fig. 7. The top two figures (7A and 7C) show the results of the direct measurement determination of angle, and the errors in the angle determination appear as deviations from the line of identity. For the PIRT-determined angles in the bottom two figures (7B and 7D), which use the direct measurement angle values as a seed point, a much better fit between the measured angle and the actual angle is seen. The PIRT algorithm improved the accuracy of angle measurement at both high and low SNR, compared to the direct measurement approach. For the hand measurement errors, the mean error in angular measurement was $+0.1591°$ ($\sigma=0.4740°$), whereas the mean angular error for the PIRT algorithm was $-0.067°$ ($\sigma=0.0903°$). Fifty percent of the angular measure-

ments using PIRT fell within a range of $0.11°$ around the median angular error of $-0.0493°$, whereas 50% of the hand measurement values fell within a range of $0.45°$ around the median error of $0.1221°$. These differences in the errors between hand measurement and the PIRT values are highly significant ($p<0.001$, Wilcoxon Signed Rank Test). To convert degrees to milliradians, multiply by 17.45.

B. Comparison between Dobbins' expectation MTF and Fujita's slit method

Twelve of the 24 measured MTFs using the Dobbins' expectation MTF approach are shown in Fig. 8A. The MTF values near the Nyquist frequency ($f_N=4.9$ cycles/mm) show significant variation depending on the phase sampling of the LSF, as discussed by Dobbins.[2]

The MTF values at 4.8 cycles/mm were plotted for all

FIG. 9. A comparison of the presampled MTF determined by the Fujita slit method (solid line with error bars), and the postsampling expectation MTF (solid line surrounded by dotted line above and below) discussed by Dobbins (Ref. 2). The expectation MTF is the average of the MTF curves shown in Fig. 8A. The error bars represent $\pm 2\sigma$ from the mean. The significant difference between the MTF curves can be attributed to the influence of sampling on the MTF calculation.

FIG. 8. A: A series of MTFs were generated from phase shifted LSFs, using the Dobbins method. The MTF at higher spatial frequencies changes markedly depending on the phase shift, with the highest curve (MTF_{max}) corresponding to the center of a pixel aligned perfectly with the peak of the LSF, and the worse case (MTF_{min}) occurs when the LSF is shifted one-half pixel width in phase. B: The MTF values at $f=4.8$ cycles per mm (just below Nyquist at 4.9 cycles/mm), plotted for different shift increments (Ω/Δ). The ordinate is the MTF amplitude, and the abscissa corresponds to the phase value, where 2π units of phase corresponds to one pixel width (102 μm in this case). The solid circles correspond to the measured values (the points at 4.8 cy/mm on A), and the solid line is a theoretical calculation of these values assuming a Gaussian shaped LSF.

phase shifts in Fig. 8B (solid circles), and this figure illustrates how the MTF amplitude at this frequency depends on phase sampling. The solid line in Fig. 8B corresponds to a computer simulation where the LSF was fit to a noiseless Gaussian function, digitally sampled, Fourier transformed, and where the MTF at 4.8 cycles/mm was computed. The maximum MTF occurs when the center of the center pixel is aligned with the peak of the LSF, and the minimum MTF occurs at a half pixel shift from the maximum, as discussed by Dobbins.[2]

Whereas the Fujita slit method combines the spatial domain information by reconstructing an oversampled LSF in the spatial domain, and then calculates a single Fourier transform, the EMTF method of Dobbins uses many undersampled LSFs, determined over many phase angles, Fourier transforms them, and synthesizes (by averaging) the EMTF in the frequency domain. Both techniques use essentially the same raw data set, but in different ways. The Fujita slit

method and Dobbins' expectation MTF are compared in Fig. 9. The Fujita slit method curve represents the average of three measurements. The expectation MTF is the average of 24 MTF values, and five expectation MTFs were computed and the standard deviation was calculated. The error bars in the figures show the 95% probability estimates for each MTF curve. Whereas at the lower spatial frequencies there is reasonable agreement between the two curves, as the expectation MTF approaches the Nyquist frequency it takes a noticeable turn upward, compared to the Fujita method MTF. These results appear consistent with the characteristics of the two techniques.

C. Sine-pattern technique compared to Fujita slit method

Reconstructed sine wave functions are illustrated in Fig. 10 for several spatial frequencies. Each graph shows the reconstructed sine waves using the PIRT methodology (the mean sine waves are not shown here for clarity). In each curve, there are several hundred to several thousand points in the reconstructed sine wave. All of the sinusoidal traces are plotted in the same relative scale. The demodulation that results from the imaging system is apparent by the reduced amplitude of the sine waves at higher spatial frequency.

The Fujita method determined MTFs and the sine wave determined MTFs are compared in Fig. 11. In this plot, the Fujita method MTF is shown as a solid line surrounded by two dotted lines representing the 95% limits ($\pm 2\sigma$). The sine method MTF is shown as the discrete points, with error bars plotted for each point but only visible in a few cases. While it is seen that the sine wave MTF skirts the top 95% limit of the Fujita method MTF, in general good agreement is observed.

0.50 cycles/mm

0.75 cycles/mm

2.00 cycles/mm

4.00 cycles/mm

8.00 cycles/mm
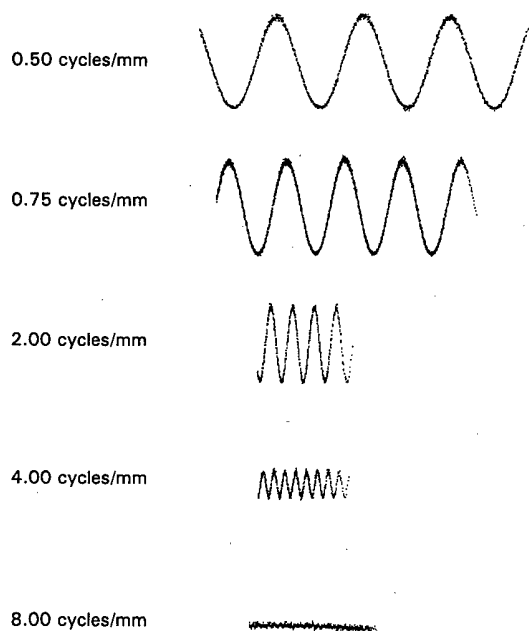
FIG. 10. Several of the reconstructed sine waves, differing by spatial frequency. The mean values are not shown. These five curves are drawn to scale with respect to each other, and the modulation that occurs at higher frequencies is quite apparent.

IV. DISCUSSION

The expectation MTF as introduced by Dobbins has the practical advantage that it describes the range of possible modulation values for a given image, since the MTF of a given structure will depend on the pixel phase at which it is imaged. The downside of the expectation MTF is that its measurement is more tedious than other methods, since very small, mechanical subpixel shifts are required and precise alignment of the slit with the imaging matrix is required.

The Fujita method of angulating the slit is quite easy to perform, and is general in its application. We expect that it
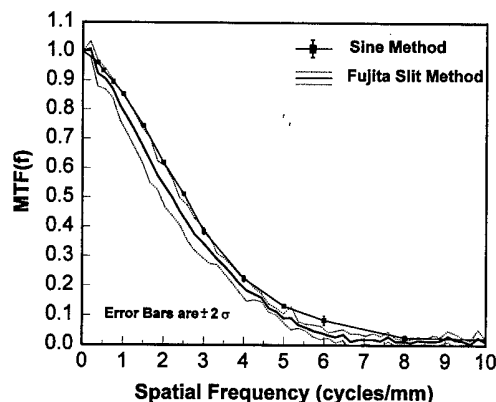
FIG. 11. A comparison between the Fujita slit method and the MTF determined using the sine pattern. The Fujita method shows the mean (solid line) surrounded by the 95% limits (dotted lines). The standard deviation was measured from five different LSF measurements. For the sine method, error bars were computed from three measurements.

will continue to be the defacto standard for measuring the presampled MTF in digital systems. The PIRT method described here for reconstructing the LSF profiles is easy to implement and adds to the accuracy of the angle measurement in the Fujita slit method. The practical advantage of a more accurate angle is not so much that the computed MTFs resulting from the reconstructed LSF are more accurate, but rather that a longer segment of the LSF can be used with confidence. By averaging a longer segment of the LSF, the resulting MTF should, in general, contain less noise and therefore be more reproducible. Using PIRT, reconstructing LSFs from longer segments of the slit is a real possibility, but one has to be certain that the slit is straight over its length. In addition, when combining LSF data from a larger region, nonstationary effects may contribute more to the measurement. For example, even with a perfectly straight slit, a spatial artifact such as the pincushion distortion common in image intensifiers could influence the MTF measurements.

Fourier transform methods are also not without problems, especially in terms of normalization. For example, knowing where the LSF ends and where the background noise begins is not always straightforward. Once a LSF profile is measured on a digital imaging system, there is often a constant "dc" offset that biases the LSF. If this bias is not subtracted away from the LSF prior to the Fourier transform, a low frequency drop will result on the MTF. To accommodate for this, it is common practice to identify a region of the LSF profile where only background exists, average that, and then subtract it away (i.e., "dc" correction). In imaging systems where appreciable amounts of glare exists, long range LSF tails contribute to the so-called low frequency drop on the MTF. Often the long range portion of the LSF is subtracted away in the dc correction, and this will mask an actual low frequency drop in the MTF.

In optical systems, there are some advantages of directly measuring the MTF using the sine wave pattern. The most obvious advantage of the sine wave approach is that it is a direct measurement of system modulation, and the resulting sinusoidal curves give a concrete visual representation of modulation in the spatial domain. Whereas image analysis using Fourier methods presumes a linear stationary system, the direct measurement of modulation does not. For this reason, the sine wave methodology may be preferable when some image processing techniques are considered part of the imaging system and need to be included in the MTF measurement. For example, windowing-and-leveling imposes a decidedly nonlinear thresholding (saturation) at the edges of the window, and therefore a windowed-and-leveled digital image technically cannot be characterized using Fourier techniques. However, the measurement of modulation is still valid.

It is necessary to impose a small angle between the sine pattern and the imaging matrix to achieve oversampling of the sine pattern, for the same reasons that the slit image is angled in the Fujita method. Using the profile iterated reconstruction technique (PIRT) described, the mean sine wave can be determined, and finding F_{max} and F_{min} from the av-

eraged profile is trivial. One concern when using the sine wave method is that noise tends to increase the observed modulation. The reconstruction of the sine wave patterns using PIRT allowed averaging over a large number of rows of pixels. Nevertheless, in Fig. 11 it is clear that the sine method MTF rides at the top edge of the 95% range of the Fujita slit method MTF. We presume that this observation is generalizable, since positive amplitude noise in the sine wave peaks and negative amplitude noise in the valleys will slightly increase the measured modulation.

Which of the three techniques is best for measuring the MTF? Clearly, the Dobbins expectation MTF technique is useful for measuring the MTF which includes sampling effects. Figure 8 illustrates the phase dependence in the postsampled MTFs, and there are many instances where the postsampled MTF is important—the digital image is, after all, what is used for diagnosis in computed radiography (CR) and other digital modalities. It is the postsampling (system) MTF that impacts the radiologist. The presampled MTF is often the focus in the design and optimization of digital imaging systems. The sine wave method is only practical in lens or fiber-optic based imaging systems (with a caveat on this mentioned below), and so the slit method remains the method of choice for determining the presampled MTF in systems such as CR or the selenium based direct radiography (DR) systems currently being investigated.[10] However, for digital optical systems such as microscopes with attached CCD cameras, fluoroscopic image intensifier-TV-digitizer systems, and digital radiographic systems based on CCD and other digital camera technology, the sine wave method or the slit method can be used with equivalent results under most applications. Since the slit method requires the acquisition of only one image, it is perhaps simpler. However, the sine wave method may be preferred in digital optical systems where the low frequency drop needs to be evaluated as part of the MTF.

It is impractical to manufacture a phantom which is capable of producing a sinusoidal distribution of x-ray intensities for a number of different spatial frequencies. Nevertheless, it *is* possible to measure the MTF of an x-ray intensifying screen using sinusoidal modulation techniques using an *optical* sinusoidal test pattern. The x-ray beam is collimated to a vertical slit in front of the screen and the slit is scanned horizontally (for example) across the intensifying screen being evaluated. The sine wave template is placed behind the screen, modulating the light emitted from it such

that the sinusoidal modulation is aligned perfectly with the horizontal direction. In other words, the ridges and valleys of the sine pattern run parallel to the vertical slit. At each infinitesimal point along the horizontal scan of the x-ray slit, the total optical signal reaching the CCD camera is acquired and integrated. In practical terms, this means that the digital numbers over the entire field of view of the camera are summed, with appropriate flat-field correction. A plot of the measured (integrated CCD) values versus horizontal position will indicate the sine pattern demodulated by the spread properties of the screen. A very similar version of this technique was described elsewhere,[11] except that a photomultiplier detector was used in that description instead of a CCD camera.

ACKNOWLEDGMENTS

[1]H. Fujita, D. Tsia, T. Itoh, K Doi, J Morishita, K Ueda, and A Ohtsuka, "A simple method for determining the modulation transfer function in digital radiography," IEEE Trans. Med. Imag. **11**, 34–39 (1992).

[2]J. T. Dobbins, "Effects of undersampling on the proper interpretation of modulation transfer function, noise power spectra, and noise equivalent quanta of digital imaging systems," Med. Phys. **22**, 171–181 (1995).

[3]J. C. Dainty and R. Shaw, *Image Science* (Academic, New York, 1974).

[4]F-F. Yin, M. L. Giger, and K. Doi, "Measurement of the presampling modulation transfer function of film digitizers using a curve fitting technique," Med. Phys. **17**, 962–966 (1990).

[5]J. M. Boone and J. A. Seibert, "An analytical edge spread function model for computer fitting and subsequent calculation of the LSF and MTF," Med. Phys. **21**, 1541–1545 (1994).

[6]I. A. Cunningham and B. K. Reid, "Signal and noise in modulation transfer function determinations using the slit, wire, and edge techniques," Med. Phys. **19**, 1037–1044 (1992).

[7]H. Fujita, M. L. Giger, and K. Doi, "Investigation of basic imaging properties in digital radiography. 12. Effect of matrix configuration on spatial resolution," Med. Phys. **15**, 384–390 (1988).

[8]H. Fujita, K. Doi, and M. L. Giger, "Investigation of basic imaging properties in digital radiography. 6. MTFs," Med. Phys. **12**, 713–720 (1985).

[9]M. L. Giger and K. Doi, "Investigation of basic imaging properties in digital radiography. I. Modulation transfer function," Med. Phys. **11**, 287–295 (1984).

[10]D. L. Lee, L. S. Jeromin, and L. K. Cheung, "New digital detector for projection radiography," Proc. Soc. Photo-Opt. Eng. (SPIE) **2432**, 237–249 (1995).

[11]ICRU Report 41, "Modulation transfer function of screen-film systems," pp. 19–20 (International Commission on Radiation Units and Measurement, Bethesda, MD, 1986)

Comparison of x-ray cross sections for diagnostic and therapeutic medical physics

John M. Boone and Andres E. Chavez
Department of Radiology, UC Davis Medical Center, FOLB II E, 2421 45th Street, Sacramento, California 95817

The purpose of this technical report is to make available an up-to-date source of attenuation coefficient data to the medical physics community, and to compare these data with other more familiar sources. Data files from Lawrence Livermore National Laboratory (in Livermore, CA) were truncated to match the needs of the medical physics community, and an interpolation routine was written to calculate a continuous set of cross sections spanning energies from 1 keV to 50 MeV. Coefficient data are available for elements $Z=1$ through $Z=100$. Values for mass attenuation coefficients, mass-energy-transfer coefficients, and mass-energy absorption coefficients are produced by a single computer subroutine. In addition to total interaction cross sections, the cross sections for the photoelectric, Rayleigh, Compton, pair, and some triplet interactions are also produced by this single program. The coefficients were compared to the 1970 data of Storm and Israel over the energy interval from 1 to 1000 keV; for elements 10, 20, 30, 40, 50, 60, 70, and 80, the average positive difference between the Storm and Israel coefficients and the coefficients reported here are 1.4%, 2.7%, and 2.6%, for the mass attenuation, mass energy-transfer, and mass-energy absorption coefficients, respectively. The 1969 data compilation of mass attenuation coefficients from McMaster *et al.* were also compared with the newer LLNL data. Over the energy region from 10 keV to 1000 keV, and from elements $Z=1$ to $Z=82$ (inclusive), the overall average difference was 1.53% ($\sigma=0.85\%$). While the overall average difference was small, there was larger variation ($>5\%$) between cross sections for some elements. In addition to coefficient data, other useful data such as the density, atomic weight, K, L_1, L_2, L_3, M, and N edges, and numerous characteristic emission energies are output by the program, depending on a single input variable. The computer source code, written in C, can be accessed and downloaded from the World Wide Web at: http://www.aip.org/epaps/epaps.html [E-MPHSA-23-1997] © *1996 American Association of Physicists in Medicine.*

I. INTRODUCTION

Attenuation coefficients for x-ray interactions are commonly employed in Monte Carlo calculations and in many other areas of medical physics, both for diagnostic and therapeutic applications. Whereas medical physicists commonly use these coefficients, the job of accurately measuring, calculating, and cataloging x-ray coefficients for the elements usually falls on physicists in other disciplines. The two sources of attenuation coefficients used previously in our laboratory are from McMasters[1] and Storm and Israel,[2] both groups being from national laboratories which are administered by the University of California. The McMaster report is a 1969 compilation of data from Lawrence Livermore National Laboratory, and the 1970 Storm and Israel report is from Los Alamos National Laboratory. More recently (1996), updated sources of attenuation coefficients were compiled by scientists at Lawrence Livermore National Laboratory (LLNL), and these data were made available to our group. These data include coefficients for elements from $Z=1$ to $Z=100$, and for photon energies from 10 eV to 100 GeV. All subsequent references to LLNL refer to this new (1996) source of cross

section data; this distinction is important because the Mc-Master data also originated from the same laboratory.

The purpose of this report is to provide a brief comparison of the LLNL coefficients to older, commonly used attenuation coefficients in the field of Medical Physics. In addition, the large volume of data published by LLNL scientists has been truncated and repackaged in a form more immediately useful to the medical physicist. Specifically, we have eliminated the very low and very high energy values, resulting in coefficients valid in the energy range from 1 keV to 50 MeV, for elements 1 through 100. Furthermore, these data have been embedded in a C language computer program, along with an interpolation algorithm, and this computer code is presently available on the world wide web. A brief description of the computer code available is given in the Appendix.

II. METHODS

A. The LLNL data

A 1989 LLNL compilation of written data, which is published in two volumes as a University of California Radiation Laboratory document (UCRL-50400, Vol. 6, Part A and Part

TABLE I. This table shows which coefficients are available and their source. A=from Ref. 3; B=from Ref. 4; C=Not Available; D=Always zero.

	(μ/ρ)	(μ_{tr}/ρ)	(μ_{en}/ρ)
Total coefficient	B	A	B
Photoelectric effect	B	A	B
Rayleigh scattering	B	D	D
Compton scattering	B	A	B
Pair production	B	A	B
Triplet production	B	C	C

B, Rev. 4), is available to the public via Ref. 3. We gained access to the data presented in this note by direct transfer of computer files, through the Nuclear Data Group at LLNL. The data used to calculate the mass energy-transfer coefficients were electronically sent to us over the Internet by Dr. Roger M. White, leader of the Nuclear Data Group at LLNL. The electronic data came as one 14 Megabyte ASCII file. Programs were written which parsed this file into more manageable pieces, and then continued to massage the data base into separate files based on the interaction type. Log–log and in some cases linear–linear interpolation routines were used, where appropriate. These data also included the mass attenuation coefficients, and these coefficients were used for much of the code development. However, the following source of data was received more recently and is reported here because it is more recent.

The data used to calculate the mass attenuation coefficients and the mass-energy absorption coefficients reported here were received on diskettes from Dr. Dermott Cullen. The diskettes contained a program called EPICSHOW,[4] which was used to generate tables of data for each element. These data stem from the 1989 data,[3] however they do include some more recent updates of that data. Linear interpolation was used to calculate coefficients between tabulated values, per the methods described in Ref. 4. We point out that the data compiled in EPICSHOW (and hence Ref. 3) relied significantly on the work of others.[4–22] These references are not meant to be comprehensive, but representative.

Both individuals providing data (which actually originated from the same source) gave verbal permission for its publication here. A single subroutine MUCOEFF (flag, Z, keV) was written which calculates the cross section coefficients in units of cm^2/gm. Different interaction types can be selected using the input variable **flag**. Other element-specific values such as density, atomic mass, absorption edges, and emission energies are also produced by MUCOEFF with appropriate selection of the input flag (see the Appendix). The physical interactions which are included are indicated in Table I.

Rayleigh scattering does not result in energy deposition, and therefore the mass energy-transfer and mass-energy absorption coefficients for Rayleigh scattering are zero. The mass energy-transfer coefficient (μ_{tr}/ρ) includes all the energy initially converted from the incoming photon to charged particles. Here, (μ_{tr}/ρ) is a cross section and therefore describes the amount of energy initially absorbed from the transmitted x-ray photon beam. In photoelectric interactions,

the incident, absorbed photon energy is initially converted totally to energetic electrons and ionized atoms, but immediately thereafter the ionized atom often relaxes by emitting a cascade of characteristic radiations. The mass energy-absorption coefficient, (μ_{en}/ρ), includes the contribution of reabsorption of all characteristic radiations. The emission of characteristic radiation can be thought of as the ionized atom giving photon energy back to the x-ray beam (albeit isotropically), and thus the coefficient (μ_{en}/ρ) is always less than (μ_{tr}/ρ). Reabsorption of characteristic emissions is geometry dependent, and in some reports of x-ray coefficients[23,24] a certain sized sphere of absorption is assumed. Even in an infinite medium (with no shape characteristics), such assumptions require knowledge of the medium's density and absorption properties. Since few absorbers pertinent to medical physics are elemental in form, such assumptions are of limited value here. The (μ_{en}/ρ) coefficients reported in this report, as in their original form, do not include any geometrical assumptions: Reabsorption of characteristic radiation is calculated for the ionized atom only.

For the energy absorption data presented in the LLNL data, the initial ionizing events were followed through all possibilities of subsequent re-emission and reabsorption events. As described in the LLNL reference, "For high-Z elements, a single vacancy in the K shell can result in one of hundreds of possible cascades; each cascade results in the emission of many x rays and electrons. The energy deposition presented here includes the energy averaged over all these possible cascades in returning the atom to neutrality."

In some medical physics applications, it is necessary to make geometrical assumptions about the absorber and follow the characteristic radiations emitted to determine their energy deposition properties. To do this, absorption edge energies, characteristic emission energies, density, atomic mass, and fluorescent yield data are needed. These data were tabulated from a variety of sources, and are included as output from the program MUCOEFF mentioned above, which is available at the American Institute of Physics (AIP) website. A more complete description of the data available is given in the Appendix. The yield data (fluorescent yield per vacancy) reported here were derived graphically from Ref. 3.

B. The McMaster data

We have made frequent use of data published in 1969, from Lawrence Livermore National Laboratory, by McMaster et al.[1] in Monte Carlo simulations for diagnostic radiology.[25,26] This source of attenuation coefficients ranged from 1 keV to 1 MeV, elements 1 through 94, and included photoelectric, Rayleigh, and Compton scattering coefficients. Included in this data were log–log polynomial interpolation coefficients, with piecewise fitting required for the photoelectric effect between absorption edges. Most of these coefficients (from $Z=1$ to $Z=82$, and from $E=10$ keV to $E=1000$ keV) were hand entered into the computer in 1987 by one of us (JMB), and incorporated into a computer program which calculated the mass attenuation coefficient as a function of Z and E. The data presented here for the McMas-
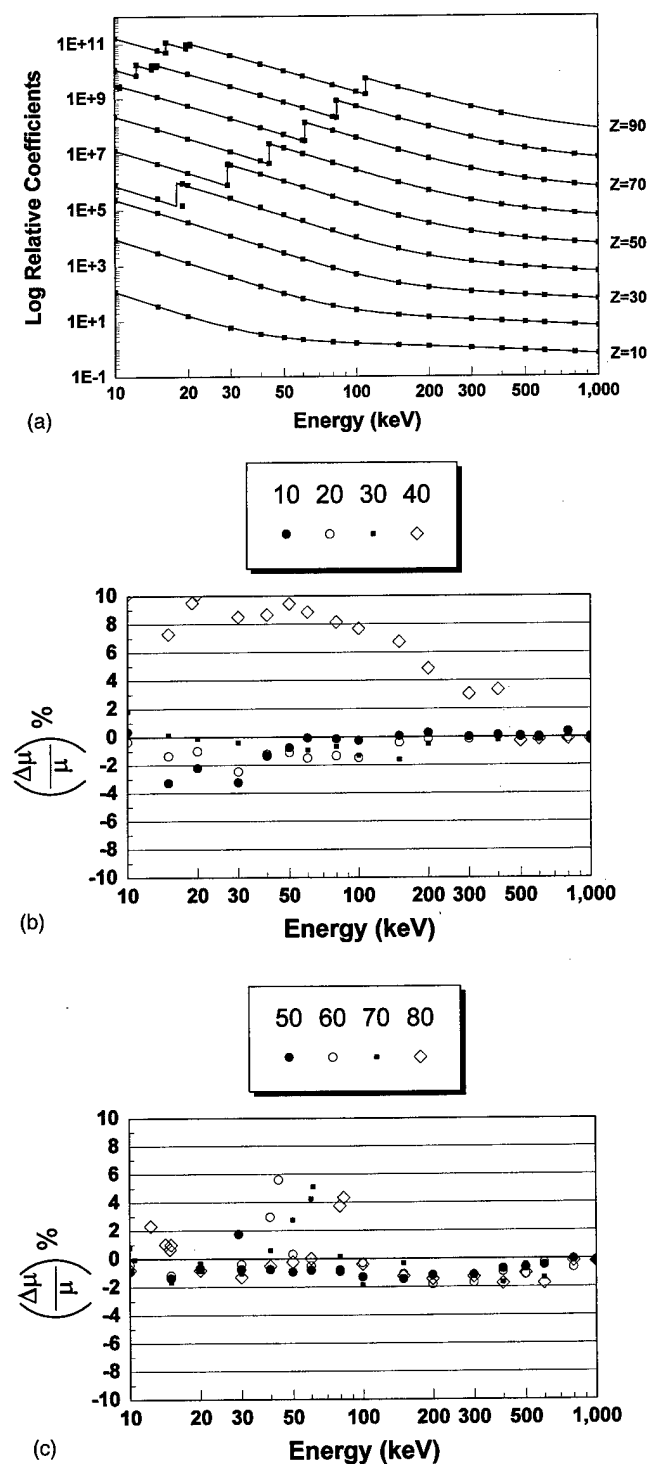
FIG. 1. A comparison between the mass attenuation coefficients (μ/ρ) between various sources and for a variety of elements. (a) The mass attenuation coefficients are shown for elements $Z=10$ through 90, by 10. The values produced by the LLNL data (and the program MUCOEFF described in the Appendix) are shown as solid lines, and the Storm and Israel coefficients are shown as the solid squares. A factor of 10 was added in log space (multiplied in linear space) between each displayed curve, for clarity. This is why the ordinate values are relative. The nonvertical K-edge lines are an artifact of the display sampling. In this display mode, the LLNL and Storm and Israel coefficients appear qualitatively identical. (b) The percent difference between the Storm and Israel data and the LLNL data produced here is illustrated for $Z=10$ (neon), 20 (calcium), 30 (zinc), and 40 (zirconium). (c) The percent difference is shown for the Storm and Israel data and the LLNL data, for $Z=50$ (tin), 60 (neodymium), 70 (ytterbium), and 80 (mercury).

ter coefficients are the output of that computer program. This source of data and the subsequent code that generates it only produces the mass attenuation coefficient; the mass energy-transfer and mass-energy absorption coefficients were not part of the McMaster compilation.

C. Storm and Israel data

The Storm and Israel photon cross section data[2] have been used extensively in medical physics.[27–32] This is a 1970 compilation of data for elements 1 through 100 and energies 1 keV to 100 MeV, and contains mass attenuation coefficients, mass energy-transfer coefficients, and mass-energy absorption coefficients, measured in barns. Some of these values were hand entered into the computer for this project for comparisons. To limit the amount of data that needed to be hand entered, comparisons are made between 1 keV and 1000 keV for elements 10–90 (by 10). Appropriate conversions between barns and cm^2/gm were made for each element, using the formula:

$$(\mu/\rho)(\text{cm}^2/\text{gm}) = (N_0'/A) \times (\mu/\rho)(\text{barns}), \qquad (1)$$

where $N_0' = N_0 \times 10^{-24}$. $N_0 =$ Avagodro's number ($6.022\,045 \times 10^{23}$ mole^{-1}), and A is the atomic mass (gm/ mole). The Storm and Israel data set is important for comparison because, in addition to attenuation coefficients, it contains the mass-energy absorption coefficients, which are important in medical physics for both patient dose calculations and x-ray detector simulations.

III. RESULTS

A comparison of mass attenuation coefficients from Storm and Israel (S&I) and the LLNL coefficients produced by our program MUCOEFF is shown in Fig. 1(a) for elements 10, 20, 30, 40, 50, 60, 70, 80, and 90. A logarithmic offset (a multiplicative factor) was included to allow the curves for all elements to be displayed on one graph. The multiplicative scaling term was computed as: displayed value$=(\mu/\rho) \times 10^x$, where $x = Z/10$, and where Z is the atomic number of the element. The LLNL data (solid lines) and the S&I data (filled squares) are qualitatively similar in this type of display format. The S&I data are shown as discrete points along the curve because only published data points were shown, and these data were hand entered for comparison. In order to better demonstrate differences between the LLNL data and that of S&I, percent differences between the mass attenuation coefficients are shown in Figs. 1(b) and 1(c), where Fig. 1B illustrates elements $Z=10$, 20, 30, and 40, and Fig. 1(c) illustrates elements $Z=50$, 60, 70, and 80. In this plot, as all others showing percent difference, it was calculated as: (percent difference)$=100 \times (\mu_A - \mu_{\text{LLNL}})/\mu_{\text{LLNL}}$, where μ_A is the coefficient being compared and μ_{LLNL} are the coefficients reported here, which are derived from our program MUCOEFF described in the Appendix. It is seen in Figs. 1(b) and 1(c) that the differences are mainly less than 5% or so. Larger differences can be seen near the K or L edges for some of the elements. As a result of small differences in the values of the K edges (and L edges) between data sets, the large disconti-
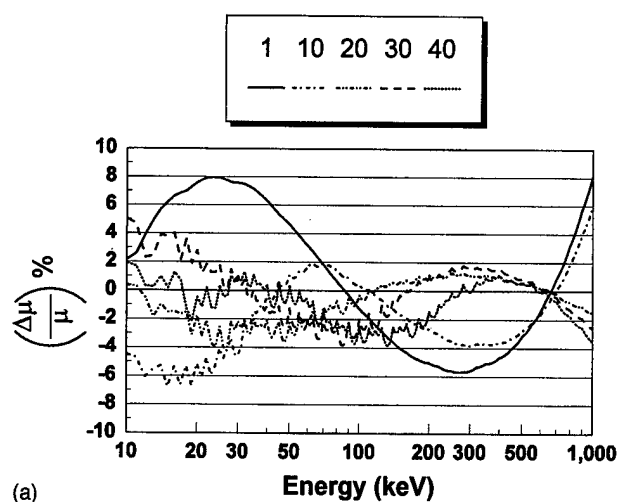
(a)
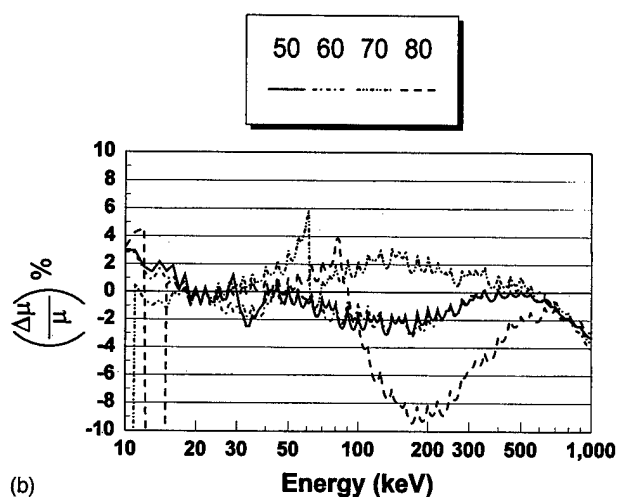
(b)
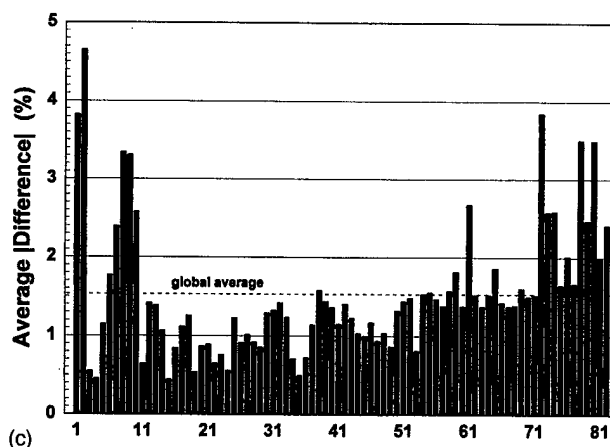
(c)

FIG. 2. (a) This figure shows comparisons (percent different) between the (1969) McMaster data and the (1996) LLNL data, for $Z=1$, 10, 20, 30, and 40. A continuous line is shown in each case because the McMaster data set was parameterized and a computer program capable of energy interpolation was available. Data points were calculated at 1 keV intervals for this plot. (b) As in (a), except showing the percent differences for elements 50, 60, 70, and 80. (c) This bar chart illustrates the average percent of the positive difference between the McMaster data and the LLNL data, for each element from $Z=1$ to $Z=82$. These values were calculated in the energy region between 10 keV and 1000 keV, at 1 keV intervals. The global average over all Z's (1–82) is 1.53%, shown as the dashed line on the figure.

nuity in the coefficient value at the absorption edge can result in a very large difference in the coefficient right near the absorption edges. These errors are actually caused by very small differences in the K-edge and L-edge energies, not in the coefficient values per se, and therefore are not as significant as their magnitude might suggest.

Figures 2(a) and 2(b) show the percent difference in the mass attenuation coefficients between the McMasters data and the LLNL data. The McMaster data were produced from a computer program developed in 1987 by one of the authors as described in the Sec. II; because the coefficients were produced from a program capable of energy interpolation, they were available at any arbitrary energy. Thus, the comparisons made in Figs. 2(a) and 2(b) are continuous, and were calculated between 10 and 1000 keV at 1 keV intervals. Figure 2(a) includes the results for elements 1, 10, 20, 30, and 40, and Fig. 2(b) includes comparisons for elements 50, 60, 70, and 80. The "ringing" that is visible in the difference plots as high frequency quasiperiodic noise is thought to be due to the discrete nature of the source data used for interpolation and differences in interpolation procedures between the McMaster and LLNL data.

For each element $Z=1-82$, the absolute value of the difference between coefficients was calculated at each energy between 10 and 1000 keV (in 1 keV steps), and the percent difference averaged over this energy region was determined. Figure 2(c) illustrates the average (positive) difference between the McMaster data and the LLNL mass attenuation coefficients for elements 1–82. This figure demonstrates that there is no significant trend in the errors as a function of Z. The dashed line shows the percent difference averaged over atomic numbers 1–82, and this value is 1.53% ($\sigma=0.85\%$, median$=1.38\%$, range$=\{0.45\%-4.65\%\}$).

Figures 3(a) and 3(b) show comparisons between the Storm and Israel data and the LLNL mass energy-transfer coefficient data, divided again into two groups for clarity [Fig. 3(a) shows elements 10–40, Fig. 3(b) shows elements 50–90)]. Good agreement is noted for all elements except $Z=30$, which shows that the S&I values are about 10% less than the LLNL coefficients, and for $Z=40$, which shows the same magnitude of error except that the S&I data are larger than the LLNL coefficients.

Figures 4(a) and 4(b) compare the mass-energy absorption coefficients from the S&I data and from the LLNL data.
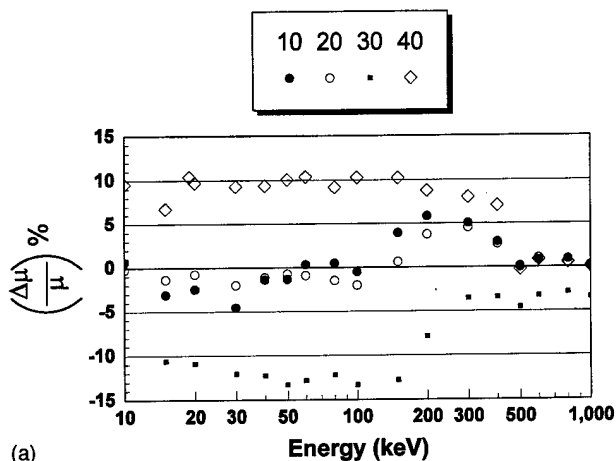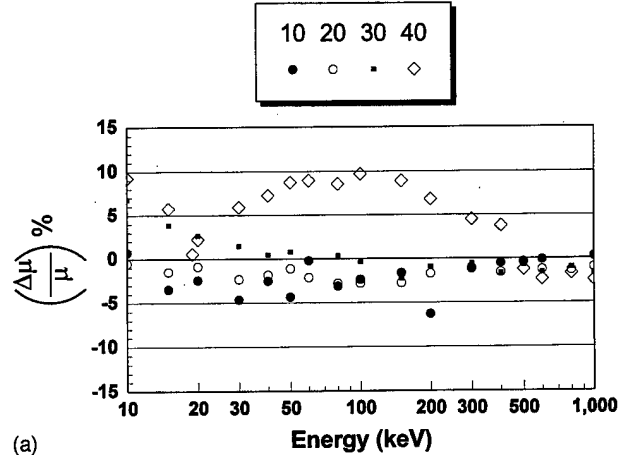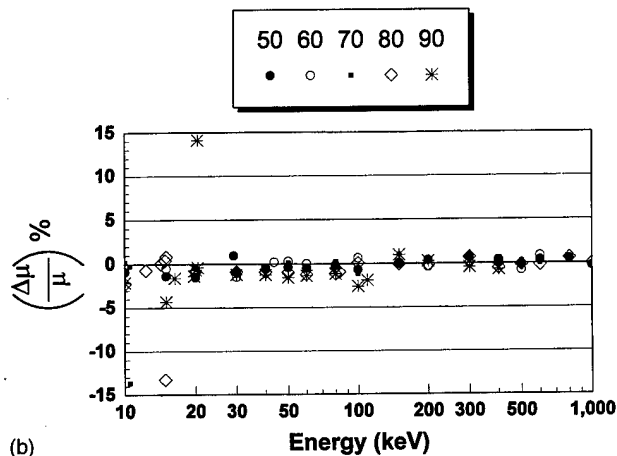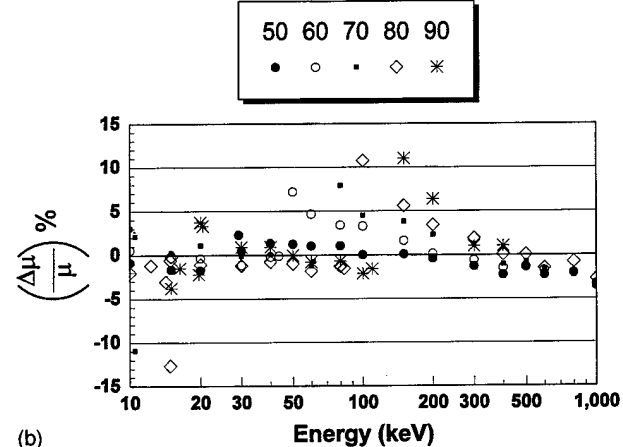
FIG. 3. (a) A comparison between the Storm and Israel and LLNL mass energy-transfer coefficient, (μ_{abs}/ρ), for elements 10, 20, 30, and 40. The global percent difference for each displayed element is given in Table II. (b) A comparison between the Storm and Israel and LLNL mass energy-transfer coefficient, (μ_{abs}/ρ), for elements 50, 60, 70, and 80.

FIG. 4. (a) A comparison between the Storm and Israel and LLNL mass energy-absorption coefficient, $(_{en}/\rho)$, for elements 10, 20, 30, and 40. The global percent difference for each displayed element is given in Table II. (b) A comparison between the Storm and Israel and LLNL mass energy-absorption coefficient, (μ_{en}/ρ), for elements 50, 60, 70, and 80.

With some exceptions, especially for element 40, most of the data points fall within the ±5% region. The average percent difference for Z=10–90 (by 10), and for the three classes of coefficients, were calculated from the points available in the energy region 10 to 1000 keV. These percent differences are summarized in Table II.

The overall purpose of this project is the easy and accurate calculation of three different types of attenuation coefficients for those interactions where data are available, as described in Table I. To illustrate this endpoint, familiar plots of these coefficients are illustrated for carbon, iodine, and lead in Figs. 5(a)–5(c). It is noted that the LLNL coefficient data include the effects of form factors and anomalous scattering factors in the Rayleigh coefficients, with the electron binding energies therefore contributing a noticeable influence on the shape of the Rayleigh coefficients.

The fluorescent yield is sometimes needed in order to calculate what fraction of characteristic interactions actually produce fluorescent radiation(s), since radiative emission competes with nonradiative transitions (Auger and Coster–Kronig). The fluorescent yield per vacancy for the K and L shells, and the K_β/K_α yield ratios are shown in Fig. 6(a). The characteristic photon yield is very low with low Z materials, and for K-shell fluorescence the yield does not reach even 1% yield until Z=10. For tissue, which is composed primarily of carbon (Z=6), hydrogen (Z=1), oxygen (Z=8), and nitrogen (Z=7), clearly fluorescent yield is very low and re-emission is unimportant. The energies of the K and L absorption edges, and the α_1 and β_1 emission photon energies for K and L transitions are illustrated in Fig. 6(b).

Medical physicists are frequently involved in teaching efforts in graduate and residency programs, and a component of the course material often deals with attenuation coefficients and atomic data in general. The coefficients generated by the computer code MUCOEFF can facilitate the generation of data for developing graphs and figures that may be useful in teaching. Figure 7 is an example of such a graph, showing the regions where the three interactions (photoelectric effect, Compton scatter, and pair production) predominate as a function of atomic number and energy.

TABLE II. Global estimates of absolute value of difference (expressed as a percentage of the LLNL coefficient) between Storm and Israel and LLNL coefficients. The table entries were calculated for all tabulated data points in the Storm and Israel compilation between 1 keV and 1000 keV, except those coefficients within 3 keV of L or K edges. The number of data points used in the calculation (N) is also given.

Z	N	(μ/ρ) (%)	(μ_{tr}/ρ) (%)	(μ_{en}/ρ) (%)
10	17	0.76	2.02	3.89
20	17	0.74	1.41	1.57
30	16	0.51	8.69	1.27
40	15	5.33	6.93	6.00
50	18	0.83	0.57	1.32
60	16	0.93	0.47	2.07
70	15	0.98	0.53	2.12
80	16	1.04	0.66	2.24
90	14	11.40	11.41	9.78

IV. DISCUSSION

In this technical report, attenuation, energy-transfer, and energy absorption coefficients are compared with other, quarter-century-old sources that have been used in Monte Carlo and other computer modeling efforts in medical physics. These comparisons indicate that the coefficients reported here, that were derived from the evaluated data from Lawrence Livermore National Laboratory, are in good agreement with the well used, older data bases of coefficients. The global average difference over the energy region 10–1000 keV and for elements 10, 20, 30, 40, 50, 60, 70, and 80 is 1.4% for the mass attenuation coefficients, 2.7% for the mass energy-transfer coefficients, and 2.6% for the mass-energy absorption coefficients. The cross section values produced by the LLNL are thought to be the most up-to-date and accurate coefficients available, and the LLNL database is now a national and international standard for use in the nuclear industry.[33]

A common set of attenuation, absorption, and energy ab-
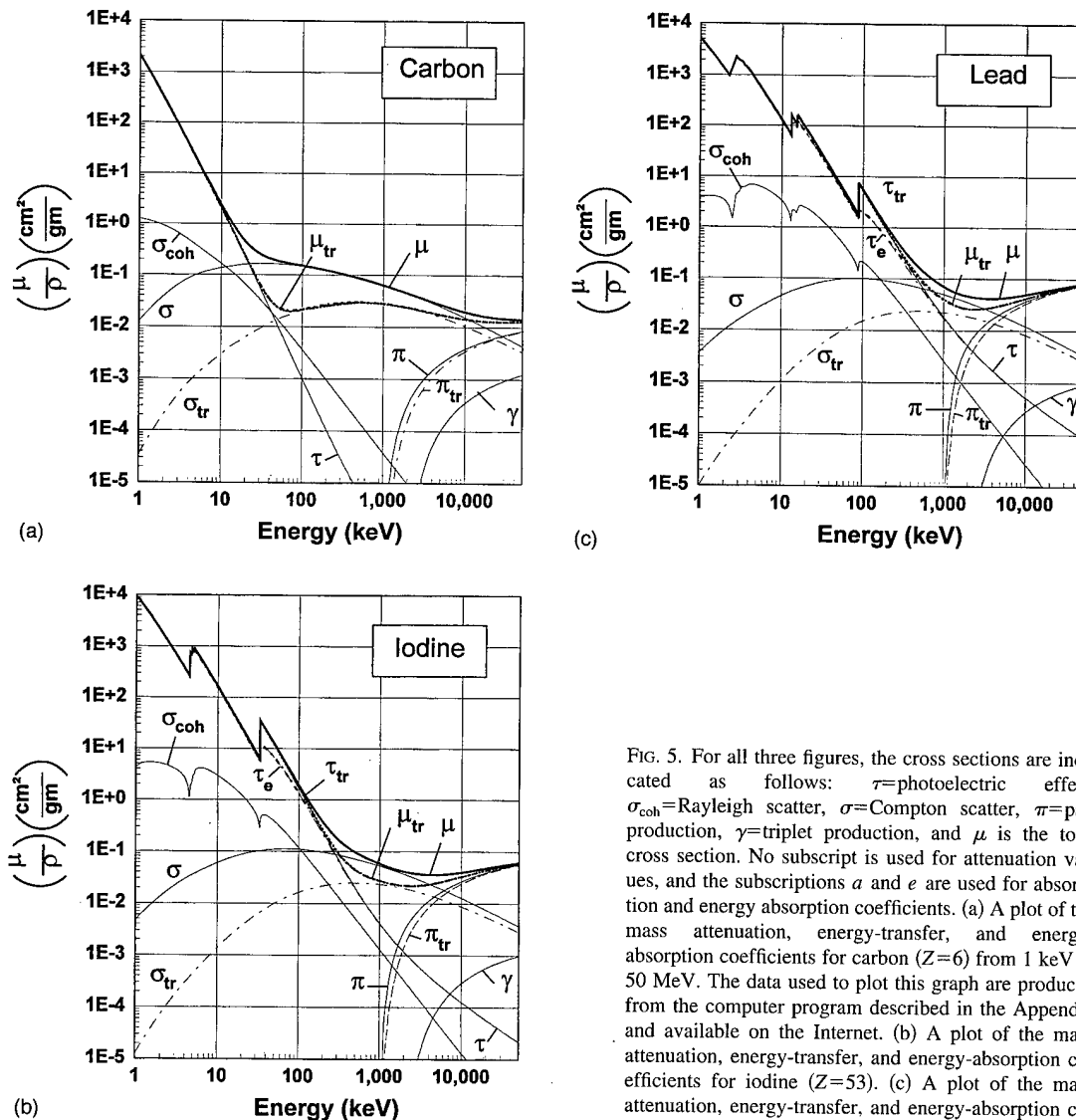
FIG. 5. For all three figures, the cross sections are indicated as follows: τ=photoelectric effect, σ_{coh}=Rayleigh scatter, σ=Compton scatter, π=pair production, γ=triplet production, and μ is the total cross section. No subscript is used for attenuation values, and the subscriptions a and e are used for absorption and energy absorption coefficients. (a) A plot of the mass attenuation, energy-transfer, and energy-absorption coefficients for carbon (Z=6) from 1 keV to 50 MeV. The data used to plot this graph are produced from the computer program described in the Appendix and available on the Internet. (b) A plot of the mass attenuation, energy-transfer, and energy-absorption coefficients for iodine (Z=53). (c) A plot of the mass attenuation, energy-transfer, and energy-absorption coefficients for lead (Z=82).
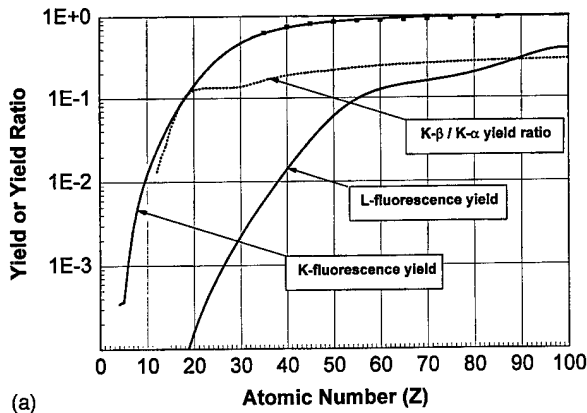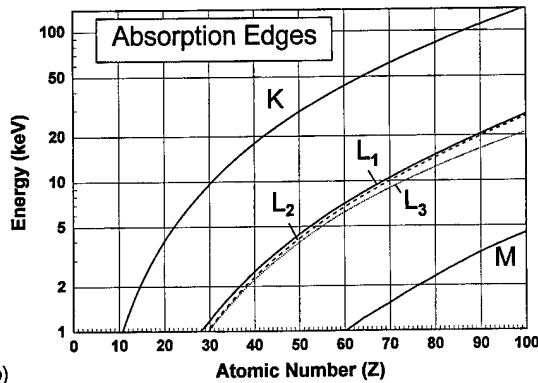
FIG. 6. (a) The yields for K and L fluorescence are shown. The yield ratio between $K\beta$ and $K\alpha$ emission is illustrated as the dashed line. K-fluorescent yield is only about 1% at $Z=10$, and reaches 10% at $Z=18$. L-fluorescent yield is only about 1% at $Z=37$, and reaches 10% at $Z=55$. The solid squares are yield values from Johns and Cunningham.[5] (b) The energies of the K, L edges (L_1,L_2,L_3), and M edges are illustrated as a function of atomic number as dashed lines. The α_1 and β_1 characteristic emissions for both the K and L transitions are shown as solid lines.
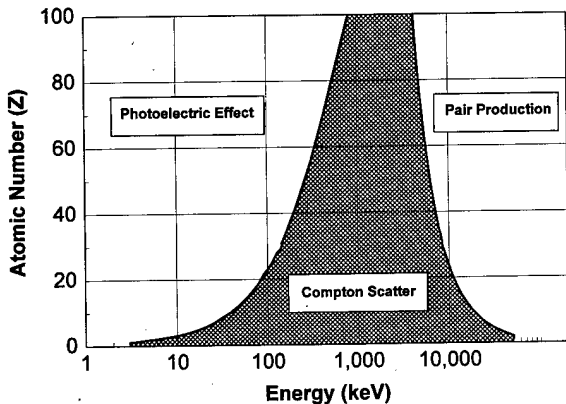
TABLE III. This table shows the value of flag necessary to have MUCOEFF return the following x-ray coefficients. The following values return cross section data in the units of cm^2/gm. If variables for the interaction are set up as TOT=0, PE=1, RAY=2, COM=3, PAIR=4, TRIP=5, and variables for the coefficient type are set up as ATTEN=0, TRANS=8, and ENERGY =16, then the desired coefficient can be achieved by logically orring these variables together. For example, flag=COM|TRANS gives (μ_{tr}/ρ) for Compton scattering (flat=11).

	(μ/ρ)	(μ_{tr}/ρ)	(μ_{en}/ρ)
Total coefficient	0	8	16
Photoelectric effect	1	9	17
Rayleigh scattering	2	10[a]	18[a]
Compton scattering	3	11	19
Pair production	4[b]	12[b]	20[b]
Triplet production	5[c]	not available	not available

[a]Always zero since Rayleigh scattering, by definition, imparts no energy on the absorber.
[b]Returns zero for energies below 1022 keV.
[c]Returns zero for energies below 2044 keV.

sorption coefficients was thought to be of value in a variety of medical physics applications. We have repackaged the data produced by other investigators with the value-added features of units conversion, subroutine development, testing, and comparison with other widely used sources of attenuation coefficients. Since the original data are not readily available to many investigators, an additional purpose of this work was to make the coefficients widely available to investigators in the medical physics community. In the nuclear industry, the national laboratory scientists continually update the coefficient data as new data become available from

FIG. 7. The regions in which each of the three interactions shown, photoelectric effect, Compton scatter, and pair production, are shown as a function of atomic number and x-ray energy. The data used here was generated by the routine MUCOEFF. This type of figure is commonly used in teaching efforts in which medical physicists often participate.

TABLE IV. This table shows the values of flag for data returned from MUCOEFF other than coefficient data. There is no energy dependency in these values (so the value of energy will have no impact, however this parameter must be within the specified range). All of the following values are Z dependent, however.

Interaction value	Description of returned value	Units
6,7,14,15	Unused; always returns (−1.0)	not applicable
13, 21	Values not available; returns 0.0	cm^2/gm
22	Density	gm/cm^3
23	Atomic mass	gm/mole
24	K edge	keV
25	$L1$ edge	keV
26	$L2$ edge	keV
27	$L3$ edge	keV
28	M edge	keV
29	N edge	keV
30	$K_{\alpha1}$	keV
31	$K_{\alpha2}$	keV
32	$K_{\beta1}$	keV
33	$K_{\beta2}$	keV
34	$L_{\alpha1}$	keV
35	$L_{\alpha2}$	keV
36	$L_{\beta1}$	keV
37	K-fluorescent yield	fraction (0–1)
38	L-fluorescent yield	fraction (0–1)
39	Ka/Kb yield ratio	fraction (0–1)

sources around the world. It is specifically not our intention to update the electronic database available at our website, so that it remain a constant throughout its usage and so that the comparisons made here hold true into the future.

The computer code MUCOEFF described here is available on the Internet, at http://www.aip.org/epaps/epaps.html [E-MPHSA-23-1997]. In addition to the cross section coefficients, other elemental data commonly used by medical physicists in teaching and research are produced by the computer program as well, with a complete description given in the Appendix.

ACKNOWLEDGMENTS

APPENDIX: ACCESS TO AND DESCRIPTION OF ELECTRONIC FILES

The LLNL data, derived from two sources, were truncated and repackaged into a form convenient for the medical physics community. We can make no warranties with respect to the accuracy of any of this data, however, the code available was used to compute the coefficients reported here. These data are available over the Internet on the World Wide Web at: http://www.aip.org/epaps/epaps.html [E-MPHSA-23-1997].

A single subroutine, callable from the "C" language, is provided at the above Web site, along with data files in many "include" (*.h) files. Source code is provided. A brief description of its functionality is given below:

float MUCOEFF (flag, Z, energy)
int flag, Z;
float energy;
Description of input variables:
flag: Valid flag values range from 0 to 39. (See Tables III and IV.)
Z: Valid Z values range from 1 to 100, inclusive.

energy: Valid energy values are in the units of keV and range from 1.0 to 50 000.0, inclusive.

Interpolation is performed with floating point precision, so any energy can be input (4.0 keV, 50.030 keV, etc.).

[1]W. H. McMaster, N. Kerr Del Grande, J. H. Mallett, and J. H. Hubbell, "Compilation of x-ray cross sections," National Technical Information Service, US Dept of Commerce. Springfield, VA (1969).

[2]E. Storm and H. I. Israel, "Photon cross sections from 1 keV to 100 MeV, for elements $Z=1$ to $Z=100$." Nuclear Data Tables A **7**, 565–681 (1970).

[3]D. E. Cullen, M. H. Chen, J. H. Hubbell, *et al.*, "Tables and graphs of photon-interaction cross sections from 10 eV to 100 GeV derived from the LLNL evaluated photon data library (EPDL)," National Technical Information Service, US Dept of Commerce. Springfield, VA (1989).

[4]D. E. Cullen, "Program EPICSHOW: A computer code to allow interactive viewing of the EPIC data libraries (Version 94-1)," UCRL-ID-116819 (1994).

[5]J. H. Scofield, Theoretical photoionization cross sections 1 to 1500 keV, Lawrence Livermore National Laboratory, Livermore, CA, URL-51326 (1973).

[6]E. B. Saloman, J. H. Hubbell, and J. H. Scofield, At. Data Nucl. Data Tables **38**, 1 (1988).

[7]J. H. Hubbell and M. J. Berger, "Photon atomic cross sections," Section 4.2 in *The IAEA Engineering Compendium on Radiation Shielding*, Vol. 1, edited by R. G. Jaeger (Springer, New York, 1968).

[8]J. H. Hubbell, "Photon cross sections, attenuation coefficients, and energy absorption coefficients from 10 keV to 100 GeV," National Standard Reference Data Series, NSRDS-NBS 29 (1969).

[9]R. H. Pratt, "Atomic photoelectric effect at high energies," Phys. Rev. **117**, 1017 (1960).

[10]J. H. Hubbell and W. J. Veigele, "Comparison of theoretical and experimental photoeffect data 0.1 keV to 1.5 MeV," National Bureau of Standards, Tech. Note 901 (1976).

[11]J. H. Hubbell, "Photon mass attenuation and mass energy absorption coefficients for H, C, N, O, Ar, and seven mixtures from 0.1 keV to 20 MeV," Radiat. Res. **70**, 58 (1977).

[12]J. H. Hubbell, "Photon mass attenuation and energy absorption coefficients from 1 keV to 20 MeV," Int. J. Appl. Radiat. Isotopes **33**, 1269 (1982).

[13]E. B. Saloman and J. H. Hubbell, "X-ray attenuation coefficients (total cross sections): Comparison of the experimental data base with the recommended values of Henke and the theoretical values of Scofield for energies between 0.1 and 100 keV," National Bureau of Standards, Internal Report NBSIR# 86-3431 (1986).

[14]J. H. Hubbell, H. M. Gerstenberg, and E. B. Saloman, "Bibliography of photon total cross section (attenuation coefficient) measurements 10 eV to 13.5 GeV," National Bureau of Standards, Internal Report NBSIR# 86-3461 (1986).

[15]E. B. Saloman, J. H. Hubbell and J. H. Scofield, "X-ray attenuation cross sections for energies 100 eV to 100 keV and elements Z 1 to Z 92," At. Data Nucl. Data Tables **38**, 1 (1988).

[16]M. J. Berger and J. H. Hubbell, "XCOM: Photon cross sections on a personal computer," National Bureau of Standards, Internal Report NBSIR# 87-3597 (1987).

[17]J. H. Hubbell, W. J. Veigele, E. H. Briggs, R. T. Brown, D. T. Cromer, and R. J. Howerton, "Atomic form factors, incoherent scattering functions, and photon scattering cross sections," J. Phys. Chem. Ref. Data **4**, 471 (1975).

[18]J. H. Hubbell, W. J. Veigele, E. H. Briggs, R. T. Brown, D. T. Cromer, and R. J. Howerton, "Atomic form factors, incoherent scattering functions, and photon scattering cross sections," J. Phys. Chem. Ref. Data **6**, 615 (1977).

[19]J. H. Hubbell and I. Overbo, "Relativistic atom form factors and photon coherent scattering cross sections," J. Phys. Ref. Data **8**, 69 (1969)

[20]D. Schaupp, M. Schumacher, F. Smend, P. Rullhausen, and J. H. Hubbell, "Small angle scattering of photons at high energies," J. Phys. Chem. Ref. Data **12**, 467 (1983).

[21]H. A. Gimm and J. H. Hubbell, "Total photon absorption cross section

measurements, theoretical analysis, and evaluations for energies above 10 MeV,'' National Bureau of Standards, Technical Note 968 (1978).

[22]J. H. Hubbell, H. A. Gimm, and I. Overbo, ''Pair, triplet, and total atomic cross sections (and mass attenuation coefficients) for 1 MeV–100 GeV photons for elements Z 1 to 100,'' J. Phys. Chem. Ref. Data **9**, 1023 (1980).

[23]H. E. Johns and J. R. Cunningham, *The Physics of Radiology*, 3rd ed. (Charles C. Thomas, Springfield, IL, 1974).

[24]D. L. Ergun, R. J. Eastgate, R. J. Jennings, and M. P. Siedband, ''DXSPEC: A computer program for diagnostic x-ray spectral filtration studies,'' Progress Report to NIH grant CB-53914, (1976), M. P. Siedband, Principal Investigator, and Department of Radiology at University of Wisconsin Madison internal report.

[25]J. M. Boone and J. A. Seibert, ''Monte Carlo simulation of the scattered radiation distribution in diagnostic radiology,'' Med. Phys. **15**, 713–720 (1988).

[26]J. M. Boone, ''Parametrized x-ray absorption in diagnostic radiology from Monte Carlo calculations: Implications for x-ray detector design,'' Med. Phys. **19**, 1467–1473 (1992).

[27]H-P. Chan, C. T. Chen, K. Doi, T. R. Fewell, and R. E. Shuping, ''In-vestigation of energy responses of germanium detectors and correction of measured spectra by means of Monte Carlo simulation,'' Radiat. Res. **99**, 443–464 (1984).

[28]H-P. Chan and K. Doi, ''Radiation dose in diagnostic radiology: Monte Carlo simulation studies,'' Med. Phys. **11**, 480–490 (1984).

[29]H-P. Chan and K. Doi, ''Studies of x-ray energy absorption and quantum noise properties of x-ray screens by use of Monte Carlo simulation,'' Med. Phys. **11**, 37–46 (1984).

[30]H-P. Chan and K. Doi, ''The validity of Monte Carlo simulation in studies of scattered radiation in diagnostic radiology,'' Phys. Med. Biol. **28**, 109–129 (1983).

[31]C. S. Chen, K. Doi, C. Vyborny, H. P. Chan, and G. Holje, ''Monte Carlo simulation studies of detectors used in the measurement of diagnostic x-ray spectra,'' Med. Phys. **7**, 627–635 (1980).

[32]H-P. Chan and K. Doi, ''Physical characteristics of scattered radiation in diagnostic radiology: Monte Carlo simulation studies,'' Med. Phys. **12**, 152–165 (1985).

[33]P. Rose, ENDF-201, ENDF/B-VI Summary Documentation, BNL-NCS-17541, Brookhaven National Laboratory (1991).

Scintillating fiber optic screens: A comparison of MTF, light conversion efficiency, and emission angle with Gd$_2$O$_2$S:Tb screens

Tong Yu, John M. Sabol, J. Anthony Seibert, and John M. Boone[a]
Department of Radiology, University of California, Davis, UC Davis Medical Center, Sacramento, California 95817

The widespread effort in developing digital imaging systems has led to large area high pixel density photodetectors such as charge coupled devices (CCDs), amorphous silicon photodiode arrays, and complementary metal oxide semiconductor (CMOS) imagers. These photodetectors have different capabilities, characteristics, and requirements than conventional silver-halide-based film, and this fact has led to a new generation of exotic scintillators, including fiber optic screens made from scintillating glass. The scintillator performance characteristics of five different scintillating fiber optic screens and two conventional Gd$_2$O$_2$S:Tb screens (one 34 mg/cm^2 and the other 60 mg/cm^2) were measured and compared. The measurements that were made included the angular dependence of light emission relative to the normal, the modulation transfer function (MTF), and the absolute effective conversion efficiency (light photons per absorbed x-ray photon). It was found that the light emission of scintillating fiber optic screens is markedly forward peaked (depending on the sample) compared to conventional screens or Lambertian emitters. The MTFs of the five scintillating fiber optic screens measured were comparable and fell approximately midway between the two conventional screen MTFs. One of the scintillating fiber optic screens demonstrated light efficiency similar to the thick (60 mg/cm^2) conventional screen, another had light output capabilities similar to the thin (34 mg/cm^2) conventional screen, and the three others were less efficient than the thin screen. The non-Lambertian characteristics of the fiber optic scintillators will cause errors of up to 75% in lens efficiency calculations if a Lambertian source is assumed. The conventional screens were found to conform within about 5% of an ideal Lambertian emitter. © *1997 American Association of Physicists in Medicine.* [S0094-2405(97)00602-0]

I. INTRODUCTION

Thomas Edison was the first to discover that calcium tungstate (CaWO$_4$) was a good x-ray scintillator,[1] and this led to its widespread use in x-ray intensifying screens for over 70 years. Thirty years ago, Buchanan, Tecotzky, and Wickersheim discovered[2] that rare earth phosphors, principally Y$_2$O$_2$S:Tb and Gd$_2$O$_2$S:Tb, were even better scintillators for intensifying screens. Calcium tungstate and more recently, rare earth screens, have been used in radiography successfully for close to a century and remain a durable and practical receptor capable of good image quality. Popularity notwithstanding, the design of conventional intensifying screens requires a compromise between x-ray absorption characteristics and spatial resolution

Modern fabrication technology has given rise to a different approach to constructing an intensifying screen, in the form of a scintillating fiber optical plate (or "screen") With scintillating fiber optic screens, the light emitted within the screen is channeled along the fibers, and does not experience the isotropic spreading as in conventional screens. In principle, by integrating the light channeling properties of a fiber optical bundle within a scintillating medium, the traditional compromise between resolution and x-ray absorption can be overcome as illustrated in Fig. 1. It should be noted the growth of CsI crystals into monolithic needles similar to individual light-conducting fibers has been used for some time in the manufacture of input phosphors for image intensifiers.

Scintillating fiber optics have also been in use for some time in high energy physics applications.

Large amorphous silicon arrays,[3,4] CCD arrays,[5-7] and large field of view CMOS arrays[8-14] are all technologies currently under development which are targeted for medical imaging applications. Selenium[15-17] and other direct electronic detectors are also being developed but are not relevant to the discussion here because they do not use a scintillator. Electronic detectors are orders of magnitude more expensive than screen-film or computed radiography (CR) cassettes, and therefore are only practical in dedicated imaging systems where they are not routinely handled, for example in a dedicated chest room. If discrete photodetector systems eventually do become practical clinically, the choice of intensifying screen technology still remains. This is perhaps where scintillating fiber optic technology may have a part to play, since fiber optic scintillators are also very expensive and too fragile to be practical for incorporation into screen-film cassettes.

Digital photodetector systems are sensitive to the light emitted from a scintillator, but they are also sensitive to the occasional direct x-ray absorption event ("hit"). Direct hits by x-rays in photodetector systems tuned for optical photons can result in the appearance of "snow" in the image, and the image consequently suffers an additional noise source. This can be minimized by bonding the intensifying screen to a glass fiber optic faceplate (which lets light pass through but absorbs the x rays), which is in turn bonded to the photode-
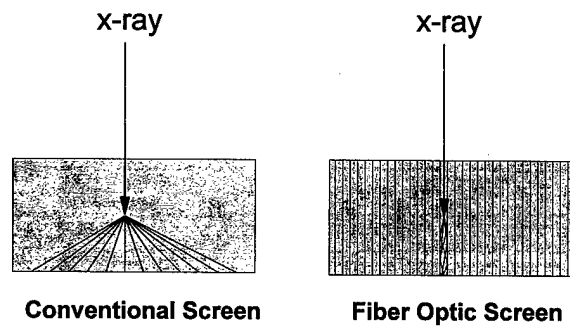
FIG. 1. The difference between conventional screens (left) and fiber optic scintillators (right) is demonstrated with respect to energy conversion distributions. Light emitted in a conventional screen scatters through the screen matrix in all directions, resulting in greater spreading with thicker screens. (In this figure, only straight optical paths were drawn for demonstration, although optical scattering is common in conventional screens.) In fiber optic screens, however, light that is emitted propagates down the fiber optic filaments without significant spreading. One way to increase spatial resolution in conventional screens is to reduce the thickness, reducing the absorption efficiency.

FIG. 2. Geometry used in measuring the angular distribution of light being emitted from the sample is illustrated. The detector was a calibrated radiometer/photometer (IL1700, International Light Inc., Newburyport, MA). Aperture A_{ap} was a thick lead collimator, which absorbed virtually all incident x rays outside the open field area.

tector. With this design, however, the rejection of direct x-ray interactions comes at the expense of a loss of light photons due to inefficiency in coupling the components. For these systems, an alternative to conventional intensifying screen that also addresses the need to protect the photodetector from direct x-ray hits is to use a scintillating fiber optic screen.

In this investigation, the x-ray absorption properties, the spatial resolution characteristics, and the relative sensitivities of several prototype fiber optical screens were measured and compared with traditional intensifying screens. The Gd_2O_2S:Tb screens of thicknesses for mammography (34 mg/cm^2) and general radiography (60 mg/cm^2) were used for comparison. In some systems currently under development,[5,18–21] lens coupling is being explored as an alternative to fiber optical or direct coupling. While lenses allow one to image a field of view larger than the actual photosensor, they are also inefficient at collecting the light emitted from the screen and become more so with increasing magnification factors. Numerous reports in the medical imaging literature in recent years[5,18–21] have described the mathematics of lens coupling efficiency to scintillators, however these formulas are typically based on the assumption of Lambertian emission. However, if the angular distribution of light emitted from a scintillator is markedly different from Lambertian, then the calculated efficiency of the system will be in error. The angular distribution of light emitted from the scintillating fiber optic screens and from conventional screens was measured and compared, since the difference between scintillating fiber optical screens and conventional screens may have a significant influence on the design of lens coupled systems.

II. METHODS

Extending previously reported[22] results on one older prototype scintillator fiber optic screen, measurements were car-

ried out on a series of five different, very new scintillating fiber faceplates and on two phosphor screens. The fiber faceplates. (Collimated Holes Inc., Campbell, CA) were lent to us by the manufacturer to evaluate, albeit for a short period of time. We were not given the details of manufacture concerning each faceplate. The fiber faceplates were given the designations FFP1, FFP2, FFP3, FFP4, and FFP5. Each faceplate was approximately 3.0 mm thick, and three of them (FFP1, FFP2, and FFP3) had a thin plastic cover on the exit surface. The two conventional screens used in the comparisons were Gd_2O_2S:Tb, one was 34 mg/cm^2 and the other was 60 mg/cm^2 thick. A laboratory-based commercial mammography system (Senographe 500t) was used as the x-ray source. X-rays were produced at 27 kV, using a molybdenum anode with a 30 μm Mo filter, a technique typical in mammography. The half-value layer (HVL) was determined to be 0.31 mm Al, and the effective energy was estimated based on aluminum attenuation properties to be 15.7 keV.
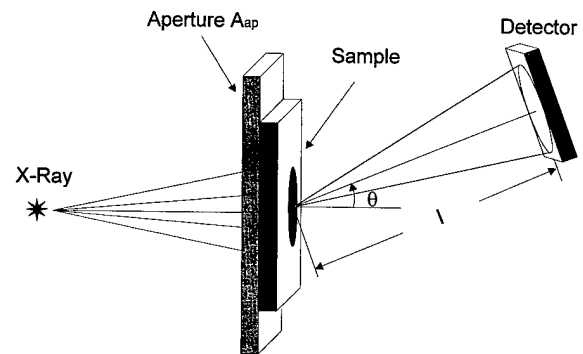
A. Angular measurements

The experimental setup used to measure the angular dependent radiance is shown in Fig. 2. An optical baffle constructed in our laboratory was used to suppress the scattered light. Both the phosphors and fiber faceplates were placed against the x-ray aperture of area A_{ap}, and the distance between scintillator and the detector is denoted as l. The detector used was a calibrated silicon photodetector (detector: SED033 #4291, diffuser: W #7334, and filter: F #15593 IL1700, International Light Inc., Newburyport, MA) with area A_{det}. It was calibrated at the wavelength of 600 nm. From the calibration certificate provided by the manufacturer, the spectral response factor was 78.6% at 600 nm. The radiance of the light output $L(\theta)$ for this configuration is given by Eq. (1):[23]

$$L(\theta) = \frac{\Phi(\theta)l^2}{A_{ap}A_{det}\cos(\theta)} = \frac{E_{det}(\theta)l^2}{A_{ap}\cos(\theta)}, \tag{1}$$
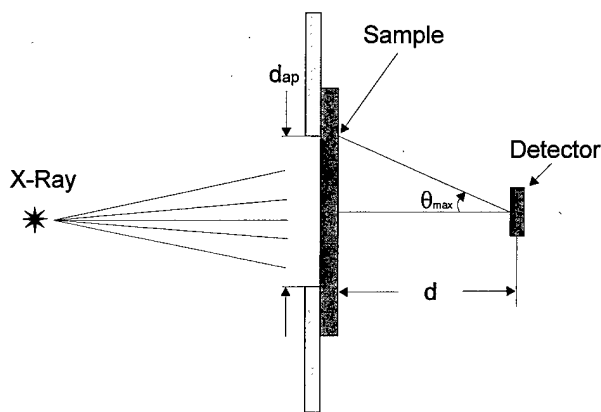
FIG. 3. Geometry used in measuring the effective conversion efficiency of the conventional and fiber optical screens is illustrated.

FIG. 4. The setup for measuring the MTF of the conventional and fiber optic screens is shown. The lead slit was used for measuring the combined MTF of the screen and the camera optics. An optical edge was used to measure the MTF of the camera optics.

where $\Phi(\theta)$ is the photon flux at the detector, and $E_{det}(\theta)$ is the measured irradiance. The aperture area A_{ap} was 78.5 mm^2, detector area A_{det} was 33.0 mm^2, and the distance l was 150.0 mm. This configuration results in an angular resolution of about 6°. Irradiance measurements were performed at 10° increments.

B. Light output and sensitivity measurements

The experimental setup for the sensitivity measurement is illustrated in Fig. 3. The light emitted from the scintillator samples (either fiber faceplates or phosphor screens) passed through an optical diffuser (part of the photodetector system) and was measured by the detector of area A_{det}. The distance between the samples and optical diffuser is d. The diameter of the optical aperture is d_{ap}. By definition, the irradiance can be expressed as[23]

$$E_{det} = \frac{\partial \phi}{\partial A} = \int_0 L(\theta)\cos(\theta)\ d\omega, \qquad (2)$$

where ϕ is the photon flux, ω is the solid angle, and $L(\theta)$ is defined in Eq. (1). Assuming that the optics are axially symmetric, Eq. (2) becomes

$$E_{det} = \int_0^{2\pi} \int_0^{\theta_{max}} L(\theta)\cos(\theta)\sin(\theta)\ d\theta\ d\varphi$$

$$= L(0) \int_0^{2\pi} \int_0^{\theta_{max}} f(\theta)\cos(\theta)\sin(\theta)\ d\theta\ d\varphi. \qquad (3)$$

The differential solid angle is given by $\sin(\theta)\ d\theta\ d\varphi$, where θ is the meridian angle, φ is the azimuthal angle, and θ_{max} is the meridian angle that the marginal ray makes with the optical axis. Here $f(\theta)$ is the normalized radiance angular distribution, where $f(\theta) = L(\theta)/L(0)$. The radiance, $L(0)$, is equal to

$$L(0) = \frac{E_{det}}{\int_0^{2\pi}\int_0^{\theta_{max}} f(\theta)\cos(\theta)\sin(\theta)\ d\theta\ d\varphi}, \qquad (4)$$

where E_{det} is the measured irradiance at 0°, the distance between the exit surface of samples and the detector d is 8 mm,

d_{ap} is 24 mm (d and d_{ap} are defined in Fig. 3), and $\theta_{max} = \tan^{-1}(d_{ap}/2d) = 56.3°$. Some screens did not absorb all of the incident x-ray fluence, and the transmitted x rays could interact with the photometer. The influence of direct x-ray interactions on the photometer reading was subtracted out, based on measurements where a black light absorber was placed alternately in front of the screen (to measure influence of x rays and light) and then between the screen and the photometer (to measure influence of x rays alone). The x-ray photon fluence per milliRoentgen Φ_x/X was obtained by integrating a computer modeled x-ray spectrum[24] of the same kV and filtration. It was estimated that $\Phi_x/X = 3.326 \times 10^4$ x-ray photons mm^{-2} mR^{-1} for this x-ray spectrum. The x-ray exposure (X) was determined using an exposure meter calibrated for mammography (Model 35080 electrometer and 15 cc ionization chamber, Keithley Instruments, Inc., Cleveland, OH) placed at the sample position. The x-ray photon fluence Φ_x was calculated as the product of Φ_x/X and X. The output light photon fluence was calculated as

$$\Phi_p = \frac{\lambda}{hc} L(0) \int_0^{2\pi} \int_0^{\pi/2} f(\theta)\cos(\theta)\sin(\theta)\ d\theta\ d\varphi,$$

$$= \frac{\lambda}{hc} E_{det} \frac{\int_0^{2\pi}\int_0^{\pi/2} f(\theta)\cos(\theta)\sin(\theta)\ d\theta\ d\varphi}{\int_0^{2\pi}\int_0^{\theta_{max}} f(\theta)\cos(\theta)\sin(\theta)\ d\theta\ d\varphi}, \qquad (5)$$

where h is Planck's constant, c is the speed of light, and λ is the average optical emission wavelength, which was measured by using a linear variable interference filter. The emission wavelength of the fiber faceplates was around 560 nm. The spectral response factor (SRF) was 81.8% at that wavelength, so the correction factor was 1.04 (SRF$_{560 \ nm}$/SRF$_{600 \ nm}$=0.818/0.786).

C. MTF measurements

The modulation transfer function (MTF) was determined from the one-dimensional Fourier transform of the line spread function (LSF), using the method described by Fujita *et al.*[25] The experimental setup is illustrated in Fig. 4. A 10 μm wide slit was placed against the phosphor screens or fiber faceplates and uniformly exposed to x rays The light output was detected using a cooled 1024×1024 12 bit CCD camera (SpectraSource, Goleta, CA). The distance between exit surface of samples and CCD was fixed. The slit was aligned carefully with respect to the digital matrix of the

CCD system such that there is a slight angle with respect to the pixel rows or columns. This method permits sampling the system response in steps much smaller than the Nyquist sampling distance which is limited fundamentally by the pixel pitch of the imaging system. A zero-padded 512 point fast Fourier transform (FFT) was used to transform the LSF(x) to the optical transform function [OTF(f)], from which the MTF(f) was computed as the modulus of the OTF(f). The measured MTF included degradation due to both the sample and the CCD camera and its associated optics. The MTF of the samples alone was calculated by deconvolving the influence of MTF$_{optic}$, the MTF of the CCD camera and optics. Since the effective pixel size of the CCD camera was 20 μm, and an optical slit with width $\ll$20 μm was not available, MTF$_{optic}$ was measured by producing an image of an optical knife edge. The distance between the optical knife edge and CCD was the same as above. The edge response was numeri-

cally differentiated, yielding the LSF, from which the MTF was calculated as described above. The MTF of the sample alone, MTF$_{samples}$, was computed by dividing out the influence of the CCD camera and optics from the samples measured MTFs using

$$\text{MTF}(f)_{samples} = \frac{\text{MTF}(f)_{both}}{\text{MTF}(f)_{optic}}. \tag{6}$$

D. Relative error from Lambertian assumption

In some optical experiments, the light output of a screen emitter is measured at some distance away from the screen normal to its surface. Often, the total light output is calculated based on the assumption of Lambertian emission. The relative error caused by such an assumption which affects calculations of parameters such as total light output and optical coupling efficiency can be expressed as

$$\text{RE} = \frac{\int_0^{2\pi}\int_0^{\pi/2} f_L(\theta)\cos(\theta)\sin(\theta) \, d\theta \, d\varphi - \int_0^{2\pi}\int_0^{\pi/2} f(\theta)\cos(\theta)\sin(\theta) \, d\theta \, d\varphi}{\int_0^{2\pi}\int_0^{\pi/2} f_L(\theta)\cos(\theta)\sin(\theta) \, d\theta \, d\varphi}, \tag{7}$$

where $f_L(\theta)$ is the normalized radiance angular distribution for the Lambertian source. By definition, $f_L(\theta)=1$, for angles $\theta=0$ through $\theta=\pi/2$. By substitution, Eq. (7) becomes

$$\text{RE} = 1 - 2\int_0^{\pi/2} f(\theta)\cos(\theta)\sin(\theta) d\theta. \tag{8}$$

In order to evaluate Eqs. (5) and (8), the normalized radiance angle distribution $f(\theta)$ was fit to an analytical equation and was extrapolated to 90° using commercial software (Table-Curve 2D, Jandel Scientific, San Rafael, CA), and a subroutine was created which was capable of accurate interpolation of the measured $f(\theta)$ data. The integral was then evaluated numerically. The analytical equation used to fit all experimentally measured $f(\theta)$ curves (versus θ) was

$$y = a + b \times (a \, \tan((x-c)/d) + \pi/2)/\pi, \tag{9}$$

where a, b, c, and d are fit coefficients, and the r^2 values for all fits averaged 0.970.

III. RESULTS

Phosphor screens have been modeled as Lambertian sources, however, several studies have shown that the radiance of phosphor screens is slightly forward peaked.[18,21] Figure 5 is a plot of the normalized radiance as a function of the angle θ. These results reaffirm that the two phosphor screens measured are not strictly Lambertian sources, since $L(\theta)$ decreases slightly with the angle. This implies that the emission of screens is more forward peaked than a purely Lambertian emitter, confirming the results of Giakoumakis and Miliotis[21] and Maidment and Yaffe.[18] Fiber faceplates FFP1, FFP2, and FFP3 had thin plastic covers on their exit surface (as supplied by the manufacturer). This layer can scatter the

emitted light, redistributing it more broadly in terms of final emission angle. The angular emission of FFP1 is in fact indistinguishable from that of the two conventional screens. The angular emissions of FFP2 and FFP3 are also broader than the two fiber faceplates without the plastic cover, while
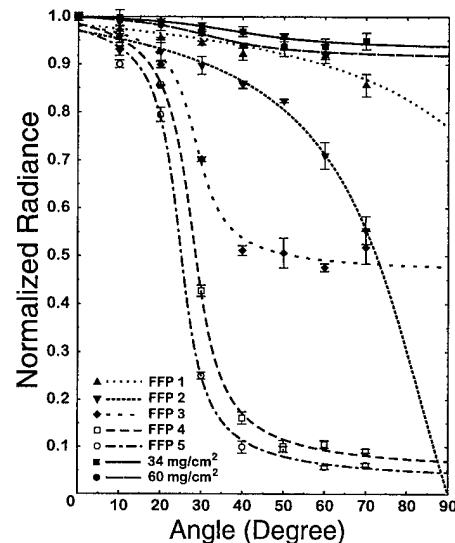
FIG. 5. The measured and best fit normalized radiance as a function of angle is shown for seven different samples extrapolated to 90°. Error bars show the standard error ($\pm 2\sigma$) for the measurements. The conventional screens and fiber faceplate 1 (FFP1) are very close to a Lambertian emitter, with slight forward peaked emission. A pure Lambertian emitter would have radiance=1.0 at all angles shown. FFP4 and FFP5 have markedly forward peaked emissions, while FFP3 has forward peaked emission intermediate between FFP4 and the conventional screens.
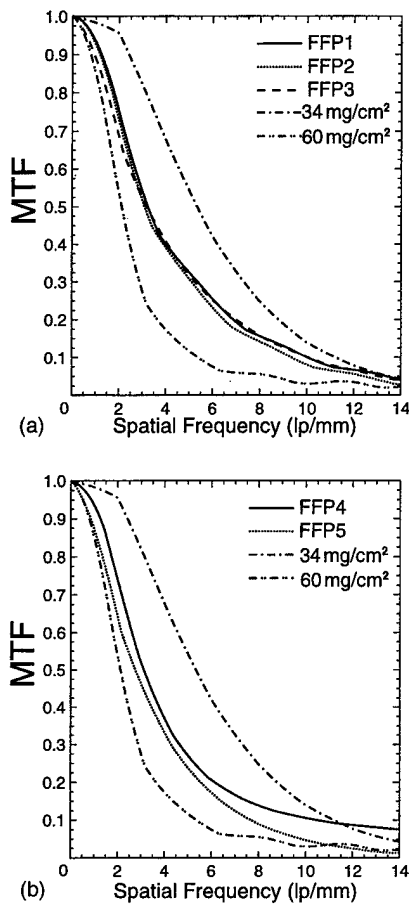
FIG. 6. The measured MTFs for the screens and fiber optic scintillators. (a) The 34 and 60 mg/cm^2 Gd$_2$O$_2$S:Tb screen MTFs are shown as the upper and lower curves, respectively. Fiber faceplates FFP1, FFP2, and FFP3 have virtually overlapping MTFs, which are intermediate between the thick and the thin Gd$_2$O$_2$S:Tb conventional screens. (b) As with the 34 and 60 mg/cm^2 Gd$_2$O$_2$S:Tb screen MTFs are shown as the upper and lower curves, respectively. FFP4 and FFP5 have MTFs intermediate between the two screens.

the angular output of fiber faceplates FFP4 and FFP5, without the plastic cover, generate very strongly forward peaked emission.

The MTF of the two screens and the fiber faceplates are shown in Fig. 6. Error bars were not included in the figure for clarity. The average standard deviation at high special frequency was estimated to be 12%. The MTFs of the fiber faceplates are all quite similar, and fall between the MTFs of the 34 mg/cm^2 Gd$_2$O$_2$S (upper bound) and the 60 mg/cm^2 Gd$_2$O$_2$S screens (lower bound). X-ray absorption for all the fiber faceplates was 100%, and for the 60 mg/cm^2 Gd$_2$O$_2$S and 34 mg/cm^2 Gd$_2$O$_2$S screens it was 97% and 87%, respectively. Figure 7 shows the efficiency of light production for the fiber faceplates and screens measured. FFP1 has the light production efficiency of a 60 mg/cm^2 Gd$_2$O$_2$S screen, but with significantly better spatial resolution.

As pointed out by Maidment,[18] assuming Lambertian emission for conventional screens can lead to underestimates of coupling efficiency on the order of 10%. In Fig. 8, the errors between a calculated Lambertian emitter and the mea-
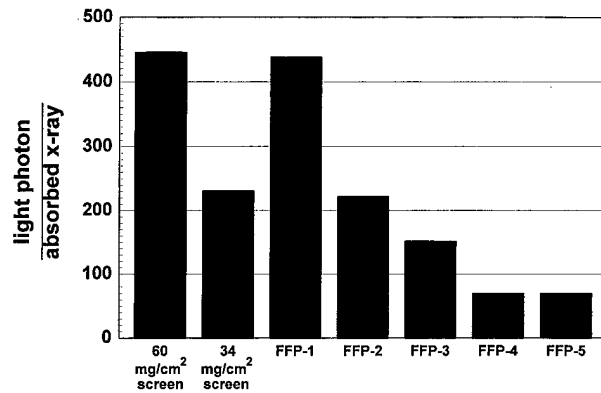
FIG. 7. The measured effective efficiency of the seven samples that were evaluated. FFP1 is the only fiber faceplate that had an efficiency approaching that of the 60 mg/cm^2 screen. It does have a substantially better MTF than the 60 mg/cm^2 screen (as seen in Fig. 6). The very forward peaked fiber faceplates, FFP4 and FFP5, have low light conversion efficiencies even relative to the 34 mg/cm^2 conventional screen.

sured efficiency of the screens and fiber faceplates are shown. For the two conventional screens, the errors are about 5%, consistent with Maidment's results,[18] given differences in overcoating and other variables in screen manufacture. For the more forward peaked scintillating fiber faceplates, much larger errors are seen. For the most forward peaked fiber faceplate, FFP5, an error of 75% would result from the assumption of Lambertian emission.

IV. DISCUSSION

While the MTFs of the fiber faceplates are disappointing when compared to the 34 mg/cm^2 Gd$_2$O$_2$S screen, it has to be kept in mind that the spatial resolution of 34 mg/cm^2 Gd$_2$O$_2$S screen is superb, with modulation at least up to 22 line pairs per mm.[22] For most digital imaging systems, the MTF will be limited fundamentally by the sampling pitch, with 10 cycles/mm being the Nyquist limit for 50 μm pixels. Further-
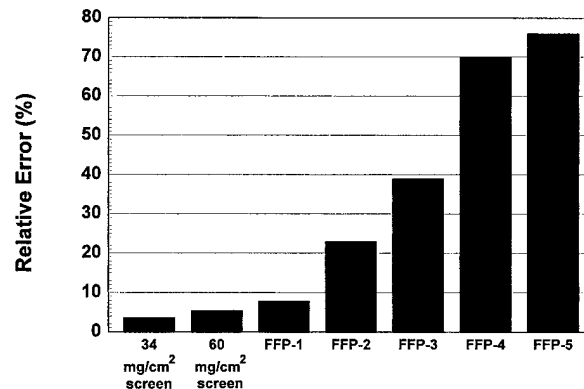
FIG. 8. The relative error in optical efficiency calculations between a theoretical Lambertian emitter and the seven samples evaluated. If a Lambertian assumption is made, the difference shown is essentially the error in the Lambertian assumption.

more, the limitations of digital imaging systems are more often related to optical conversion efficiency than spatial resolution at high spatial frequency.

Fiber optical screens represent a different paradigm of scintillator design, as compared with conventional phosphor-binder screens. While scintillating fiber optics have been in use for some time in high-energy physics applications,[26] the most promising aspects of scintillating fiber screens in the context of other recent developments leading to digital mammography and radiography systems are twofold: (1) the fiber plates absorb almost all of the incident x rays, reducing the direct hits in the silicon imaging system and therefore reducing "snow" artifacts, and (2) the light distribution of fiber optic screens is much more forward peaked than conventional screens, which may result in better coupling efficiency in lens-based imaging systems.

The use of scintillating fiber optic screens would suggest that a compromise between x-ray absorption and spatial resolution does not need to be made. However, scintillating fiber optic screens are not without shortcomings. First and foremost, scintillating glass has a significantly lower intrinsic conversion efficiency as compared to a rare earth phosphor. The intrinsic efficiency of the scintillating glass is approximately 6%, with the effective efficiency closer to 0.5%. The Gd_2O_2S:Tb has an *intrinsic* conversion efficiency of around 15%,[27] and the *effective* efficiency was 6.2% for the 60 mg/cm^2 Gd_2O_2S:Tb screen, and 3.7% for the 34 mg/cm^2 screen. Presumably, the difference in effective efficiency for the two screens is a result of light-absorbing dye in the thinner mammography screen, which will reduce the effective conversion efficiency but improve spatial resolution.

Mickish and Beutel[28] reported the number of light photons per absorbed x-ray photon as a function of x-ray energy for several phosphors. At 17.8 keV, they report a mean of 442 photons emitted by Gd_2O_2S:Tb, which corresponds to 5.7% efficiency. This value is in good agreement with our determination of 6.2% efficiency at an effective energy of 15.7 keV. It is observed that the ratio of the intrinsic efficiency to the effective efficiency for a Gd_2O_2S:Tb screen is about 3 (15%/6%), whereas for the scintillating glass in a fiber optical boule this is about 12 (6%/0.5%). This is reasonable, since the light-channeling properties of a scintillating fiber optic screen are achieved in part by attenuation of light striking the inner glass surfaces at incident angles in which total internal reflection does not occur. Indeed, the inclusion of extramural absorption (EMA) fibers in fiber optic screens is designed to specifically absorb this light which escapes from the glass fibers.

Recent attempts at increasing the efficiency of scintillating glass fiber optical screens have focused on adding thin conventional screens on the side closest to the x-ray source,[29] making a hybrid scintillator. FFP1 is such a scintillator. Incorporating two scintillators with fundamentally different light conversion efficiencies in a hybrid configuration can increase the mean number of emitted light photons per absorbed photon, however, the variance of the photon gain will also be increased. (This observation was mentioned by a participant at the SPIE meeting in Newport Beach on 13 Febru-

ary, 1996 when Ref. 29 was presented orally We give full credit to this unidentified individual for making this observation apparent.) The photon per x-ray distribution will not just be broader, it will be bimodal. The increased width of the histogram describing the number of light photons per absorbed x-ray photon will decrease the Swank factor, and reduce the DQE(f). For a narrow energy range, however, it may be possible to tune the efficiencies of the two components of a hybrid detector to yield a single mode distribution.

V. ACKNOWLEDGMENTS

[a]Address for correspondence: Department of Radiology, UC Davis Medical Center, FOLB II E, 2421 45th Street, Sacramento, CA 95817.

[1]J. A. Seibert, "One hundred years of medical diagnostic imaging technology," Health Phys. **69**, 695–720 (1995).

[2]R. A. Buchanan, M. Tecotzky, and K. A. Wickersheim, "Rare earth phosphors for x-ray conversion screens," U.S. Patent 3,725,704 & 3,829,700.

[3]L. E. Antonuk, J. M. Boudry, Y. El-Mohri, W. Huang, J. H. Siewerdsen, J. Yorkston, and R. A. Street, "Large area, Flat-panel amorphous silicon imagers," Proc. SPIE **2432**, 216–227 (1995).

[4]L. E. Antonuk, J. Boudry, and W. Huang, D. L. McShan, E. J. Morton, J. Yorkston, M. J. Longo, and R. A. Street, "Demonstration of megavoltage and diagnostic x-ray imaging with hydrogenated amorphous silicon arrays," Med. Phys. **19**, 1455–1466 (1992).

[5]A. Karellas, L. J. Harris, H. Liu, M. A. Davis, and C. J. D'Orsi, "Charge-coupled device detector: Performance considerations and potential for small-field mammographic imaging applications," Med. Phys. **19**, 1015–1023 (1992).

[6]M. J. Yaffe, "Direct digital mammography using a scanned-slot CCD imaging system," Med. Prog. Technol. **19**, 13–21 (1993).

[7]A. D. A. Maidment and M. J. Yaffe, "Scanned slot digital mammography," Proc. SPIE **1231**, 316–326 (1990).

[8]E. R. Fossum, "Ultra low power imaging systems using CMOS image sensor technology," Proc. SPIE **2267**, 107–111 (1994).

[9]E. R. Fossum, "Active-pixel sensors challenge CCD's," Laser Focus World, PennWell Publishing, June (1993).

[10]E. R. Fossum, "Active pixel sensors—Are CCD's Dinosaurs?," Proc. SPIE **1900**, 2–14 (1993).

[11]S. Mendis, S. E. Kemeny, R. Gee, B. Pain, and E. R. Fossum, "Progress in CMOS active pixel image sensors," Proc. SPIE **2172**, 19–29 (1994).

[12]S. Mendis and E. R. Fossum, "CMOS active pixel image sensor," IEEE Trans. Electron. Devices **ED-41**, 452–453 (1994).

[13]S. Mendis, B. Pain, R. Nixon, and E. R. Fossum, "Design of a low-light-level image sensor with an on-chip sigma-delta analog-to-digital conversion," Proc. SPIE **1900**, 31–39 (1993).

[14]D. Lake, "Why CMOS Imagers are the rage: a revolution in the making," Advanced Imaging, October, 12–18 (1995).

[15]J. A. Rowlands, D. M. Hunter, and N. Araj, "X-ray imaging using amorphous selenium: a photoinduced discharge readout method for digital mammography," Med. Phys. **18**, 421–431 (1991).

[16]D. L. Lee, L. K. Cheung, and L. S. Jeromin, "New digital detector for projection radiography," Proc. SPIE **2432**, 237–249 (1995).

[17]U. Neitzel, I. Maack, and S. Gunther-Kohfahl, "Image quality of a digital chest radiography system based on a selenium detector," Med. Phys. **21**, 509–516 (1994).

[18]A. D. A. Maidment and M. J. Yaffe, "Analysis of signal propagation in optically coupled detectors for digital mammography: I. Phosphor screens," Phys. Med. Biol. **40**, 877–889 (1995).

[19]A. D. Maidment and M. J. Yaffe, "Analysis of the spatial-frequency-dependent DQE of optically coupled digital mammography detectors," Med. Phys. **21**, 721–729 (1994).

[20]H. Liu, A. Karellas, L. J. Harris, and C. J. D'Orsi, "Methods to calculate the lens efficiency in optically coupled CCD x-ray imaging systems," Med. Phys. **21**, 1193–1195 (1994).

[21]G. E. Giakoumakis and D. M. Miliotis, "Light angular distribution of fluorescent screens excited by x-rays," Phys. Med. Biol. **30**, 21–29 (1985).

[22]J. M. Boone, J. Duryea, and J. A. Seibert, "Imaging performance of a terbium-doped fiber optic screen for diagnostic imaging," Proc. SPIE **2163**, 64–72 (1994).

[23]F. Grum and R. J. Becherer, *Optical Radiation Measurements, Volume 1 Radiometry* (Academic, New York, 1979), Chaps. 2 and 3.

[24]D. M. Tucker, G. T. Barnes, and X. Z. Wu, "Molybdenum target x-ray spectra: a semiempirical model," Med. Phys. **18**, 402–407 (1991).

[25]H. Fujita, D. Y. Tsai, T. Itoh, K. Doi, J. Morishita, K. Ueda, and A. Ohtsuka, "A simple method for determining the modulation transfer function in digital radiography," IEEE Trans. Med. Imag. **MI-11**, 34–39 (1992).

[26]E. J. Fenyves, editor, "Scintillating fiber technology and applications," Proc. SPIE **2007** (1993).

[27]S. Webb, editor, *The Physics of Medical Imaging* (Hilger, Philadelphia, 1988), p. 49.

[28]D. Mickish and J. Beutel, "The determination of x-ray phosphor scintillation spectra," Proc. SPIE **1231**, 327–336 (1990).

[29]C. Bueno, R. L. Rairden, and R. A. Betz, "Hybrid scintillators for x-ray imaging," Proc. SPIE **2708**, 469–481 (1996).

Lens coupling efficiency: Derivation and application under differing geometrical assumptions

Tong Yu and John M. Boone
Department of Radiology, University of California, Davis, UC Davis Medical Center, Sacramento, California 95817

The calculation of lens coupling efficiency is often performed in the design of lens coupled digital radiographic systems, now currently under development. With these systems, an electronic camera is focused onto a planar scintillator such as a conventional intensifying screen. Historically, this calculation has relied on certain assumptions concerning the emission properties of the scintillator, and primarily this assumption is that the scintillator is either a Lambertian emitter (light is emitted over all angles equally) or a point radiator. Because there now exists new classes of scintillators such as scintillating fiber optic screens and pixelated intensifying screens, it is sometimes necessary to perform lens coupling calculations in the absence of the Lambertian and point source assumptions. In this paper we describe the necessary equations to accurately calculate lens coupling efficiency in the most general of cases. Graphical examples demonstrate the lens coupling efficiency for hypothetical Lambertian scintillating sources, for a rare earth intensifying screen, and for a scintillating fiber optical screen. © *1997 American Association of Physicists in Medicine.* [S0094-2405(97)01704-5]

I. INTRODUCTION

There has been intense activity underway in laboratories around the world focused on the development of digital radiographic and digital mammographic detector systems. Many systems have been reported, based on different detector and scintillator technologies.[1-8] A subset of these systems[5-8] makes use of scintillating screens coupled to photosensitive detector systems (most commonly charge coupled devices, CCDs) using lenses. The benefit of lens coupling is that it allows demagnification, so that a relatively small photodetector (e.g., 5 cm×5 cm square) can form an image from a larger region of a scintillator such as an intensifying screen. However, there are compromises made in demagnified systems, most notably the potential for large light losses, which can cause a secondary quantum sink and lead to a reduction in the detective quantum efficiency (DQE). Because lens coupling efficiency is so important to the performance of lens coupled systems, several authors have reported on the equations in which to calculate coupling efficiency, based on either Lambertian emitter or point radiator assumptions.[9-12] In this paper, a general methodology for deriving the equations to calculate lens coupling efficiency is given. Some previous results were reviewed and more detailed derivation was presented. A more broadly applicable equation was obtained, which is useful for computing lens coupling efficiency under the most general of circumstances, free of any assumptions about the emission characteristics of the scintillation screen. The lens coupling efficiency is calculated as a function of f number and magnification factor for Lambertian, a near-Lambertian Gd_2O_2S:Tb intensifying screen, and a very non-Lambertian fiber optical scintillating faceplate.

II. SENSITIVITY OF THE X-RAY IMAGING SYSTEMS

For a linear digital x-ray imaging system, the total number of electrons generated in one pixel can be expressed as a function of the performance characteristics of the various system parameters. Specifically, for a lens coupled CCD x-ray system, we have

$$N_e = \Phi_x A_p \eta_x g_1 g_2 \eta_c, \tag{1}$$

where N_e is the number of electrons, Φ_x is the x-ray photon fluence (x-ray photons/cm^2), A_p is the pixel area (cm^2), η_x is the quantum efficiency of the intensifying screen (absorbed x-ray photons/incident x-ray photon), g_1 is the conversion factor of the screen (number of light photons/absorbed x-ray photon), g_2 is optical coupling efficiency of the lens (optical energy incident upon the detector/optical energy emitted from the scintillator), and η_c is the quantum efficiency of the CCD (number of electrons/light photon).

The sensitivity η_s of the imaging system in terms of the number of the electrons produced per absorbed x-ray photon can be expressed as

$$\eta_s = \frac{N_e}{\Phi_x A_p \eta_x} = g_1 g_2 \eta_c. \tag{2}$$

This quantity is of particular interest because its value should be at least unity, i.e., $\eta_s \geq 1$. Only then will the majority of absorbed x-ray photons contribute toward the final image. However, since g_1 has large fluctuations known as Swank noise, usually $\eta_s \geq 10$ is required.[13] Equation (2) shows that sensitivity η_s is linearly proportional to g_2. It is therefore important to calculate the lens coupling efficiency g_2 correctly in order to evaluate the whole system performance.
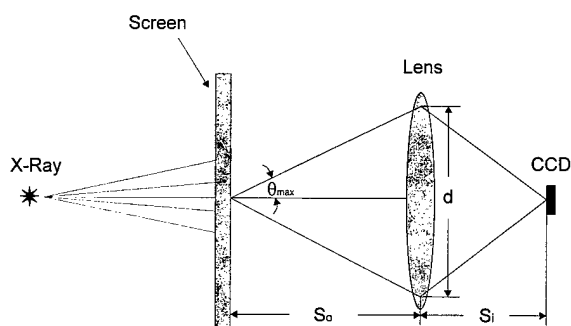
FIG. 1. A schematic diagram of a lens coupled imaging system.

III. LENS COUPLING EFFICIENCY EQUATIONS DERIVATION

As shown in Eq. (2), one has to calculate the screen conversion factor g_1 and lens coupling efficiency g_2, in order to compute the system sensitivity. The correct form of the equation used to calculate g_2 is dependent on the emission characteristics of the intensifying screen used. For instance, if the intensifying screen conversion factor, g_1, refers to the mean number of light photons emitted from one side of the screen per absorbed x-ray photon in the screen, and the screen exhibits true Lambertian properties, a simplified equation is valid; if g_1 is defined as above, but the screen is not strictly a Lambertian source, another form of the equation is needed. If, on the other hand, g_1 refers to the total mean number of light photons generated isotropically over a 4π steradians solid angle within a screen per absorbed x-ray photon, still another form of the equation is required for accurate calculations. In the following, these different equations will be derived under the specific conditions where they are valid.

A. Lambertian source assumption

From the definition, also as shown in Fig. 1, the lens coupling efficiency can be expressed as

$$g_2 = T \frac{\int_{\varphi=0}^{2\pi}\int_{\theta=0}^{\theta_{max}} L(\theta,\varphi)\sin\theta\cos\theta\,d\theta\,d\varphi}{\int_{\varphi=0}^{2\pi}\int_{\theta=0}^{\pi/2} L(\theta,\varphi)\sin\theta\cos\theta\,d\theta\,d\varphi}, \qquad (3)$$

where the T is the bulk transmittance of the lens, the $L(\theta,\varphi)$ is the screen radiance, the θ is the meridian angle, φ is the azimuthal angle, and θ_{max} is the meridian angle that the marginal ray makes with the optical axis.

Under the Lambertian source assumption, $L(\theta,\varphi)$ is a constant independent of θ and φ. Equation (3) becomes

$$g_2 = T \frac{\int_{\varphi=0}^{2\pi}\int_{\theta=0}^{\theta_{max}}\sin\theta\cos\theta\,d\theta\,d\varphi}{\int_{\varphi=0}^{2\pi}\int_{\theta=0}^{\pi/2}\sin\theta\cos\theta\,d\theta\,d\varphi} = T\sin^2(\theta_{max}). \qquad (4)$$

Simply from the geometry, we have

$$\sin^2(\theta_{max}) = \frac{(d/2)^2}{(d/2)^2 + S_o^2}, \qquad (5)$$

where d is the diameter of the lens, and the S_o is the distance between the screen and the lens. From the lens equation,

$$\frac{1}{S_o} + \frac{1}{S_i} = \frac{1}{f}, \qquad (6)$$

where S_i is the distance between the lens and the CCD, and f is the focal length of the lens (Fig. 1). Defining m as the system geometrical magnification factor, $m = S_i/S_o$; and $F_\#$ as the F number of the lens, $F_\# = f/d$, by substituting the m and $F_\#$ expressions into Eqs. (4), (5), and (6), the result is

$$g_2 = \frac{Tm^2}{4(F_\#)^2(1+m)^2 + m^2}. \qquad (7)$$

As expected, this equation is the same as the results obtained by other investigators.[9–11,14] Equation (7) is well known, and is commonly seen in the literature. By showing the derivation of this equation here, a better understanding of what assumptions have been made is conveyed. This expression for g_2 is valid for a planar emission source, which is a Lambertian emitter. The value of g_1 associated with this expression should be defined as the mean number of light photons emitted from one side of the screen per absorbed x-ray photon in the screen.

B. Non-Lambertian source

In the more general case, where the screen does not truly exhibit Lambertian emission characteristics, the lens coupling efficiency is

$$g_2 = T \frac{\int_{\varphi=0}^{2\pi}\int_{\theta=0}^{\theta_{max}} f(\theta)\sin\theta\cos\theta\,d\theta\,d\varphi}{\int_{\varphi=0}^{2\pi}\int_{\theta=0}^{\pi/2} f(\theta)\sin\theta\cos\theta\,d\theta\,d\varphi}$$

$$= T \frac{\int_0^{\theta_{max}} f(\theta)\sin\theta\cos\theta\,d\theta}{\int_0^{\pi/2} f(\theta)\sin\theta\cos\theta\,d\theta}, \qquad (8)$$

where $f(\theta)$ is the normalized angular distribution for the radiance of the screen. Since $f(\theta)$ is typically measured for a given screen, a simple analytic expression for this function is usually not available. Numerical methods are therefore used to evaluate the integrals in Eq. (8), when no further assumptions can be made about the source radiance or the geometry.

The value of g_1 associated with this expression is also defined as the mean number of light photons emitted from one side of the screen per absorbed x-ray photon in the screen. When the source is purely Lambertian, $f(\theta) \equiv 1$, and Eq. (8) reduces to Eq. (4).

C. Point source assumption

For situations where it is appropriate to model the screen as a point source as shown in Fig. 2, the lens coupling efficiency is given by

$$g_2 = T \frac{\int_{\varphi=0}^{2\pi}\int_{\theta=0}^{\alpha_{max}}\sin\theta\,d\theta\,d\varphi}{\int_{\varphi=0}^{2\pi}\int_{\theta=0}^{\pi}\sin\theta\,d\theta\,d\varphi} = \frac{T}{2}(1 - \cos\alpha_{max})$$

$$= T\sin^2\left(\frac{\alpha_{max}}{2}\right), \qquad (9)$$
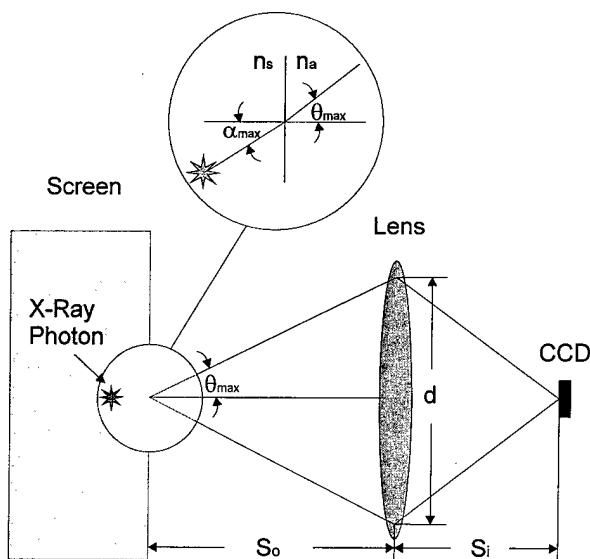
FIG. 2. The point source assumption is illustrated. Light photons propagate across the boundary between the phosphor screen and the air, and Snell's law was applied to get the relationship between the angle α in the screen and the angle θ in the air.

FIG. 3. The normalized radiance as a function of angle is shown for two different scintillating screens. The conventional screen is very close to a Lambertian emitter, with slight forward peaked emission, and the fiber faceplate has markedly peaked emission.

where α_{max} is the meridian angle in the screen that the marginal ray makes with the optical axis. When the angle α_{max} is small, we have

$$g_2 = T \sin^2\left(\frac{\alpha_{max}}{2}\right) = T\left(\frac{1}{2}\sin(\alpha_{max})\right)^2. \tag{10}$$

According to Snell's law, $n_s \sin(\alpha_{max}) = n_a \sin(\theta_{max})$, where n_s is the refractive index of the intensifying screen, n_a is the refractive index of the air, and $n_a \approx 1$. Equation (10) becomes

$$g_2 = T\left(\frac{1}{2n_s}\sin(\theta_{max})\right)^2 \approx T\left(\frac{1}{2n_s}\tan(\theta_{max})\right)^2$$

$$= T\left(\frac{d/2}{2n_s S_o}\right)^2. \tag{11}$$

Here, the tan is substituted for the sin, which for small angles is valid. For example, this substitution results in a 1.5% error for $\theta = 10°$, 0.4% for $\theta = 5°$, and 0.02% for $\theta = 1°$. Typical values for θ_{max} used in the imaging systems are between 5.5° ($m = 0.3$, $F_\# = 1.2$) and 12° ($m = 1$, $F_\# = 1.2$). By substituting the parameters m and $F_\#$ into Eqs. (6) and (11), the final equation becomes

$$g_2 = \frac{Tm^2}{16(F_\#)^2(1+m)^2 n_s^2}. \tag{12}$$

Also, as expected, this equation is the same as previous results,[10,12] in which no derivation was given. We think it is helpful to demonstrate the derivation, so that the equation can be used correctly. The assumptions for this g_2 expression are that the scintillator is a point source, the marginal ray angle is small ($\theta_{max} \leq 10°$ or so), and there is negligible light attenuation within the screen. The value of g_1 associated with this expression should be defined as the mean number

of light photons generated isotropically over a 4π steradians solid angle within a screen per absorbed x-ray photon.

IV. ERROR ESTIMATION FROM LAMBERTIAN ASSUMPTION

The angular-dependent radiance distributions for a scintillating fiber faceplate (Collimated Holes, Inc., Campbell, CA) and a conventional mammography screen (34 mg/cm^2 Gd$_2$O$_2$S:Tb) were measured and reported previously.[15] Figure 3 shows the measured normalized radiance $f(\theta)$ as a function of the angle for these two screens. This figure shows that the light output from the scintillating fiber faceplate is very strongly forward peaked, while the emission of the conventional screen is only slightly forward peaked. Neither screen is a purely Lambertian emitter. Therefore, when using the mathematics that assume Lambertian emission [Eq. (7)] to calculate the lens coupling efficiency, errors will result. The magnitude of the error will depend on the radiant angular distribution of the individual screen. In all of the following calculations, Eq. (8) was used. Of course, this equation will reduce to Eq. (7) when it applies to a Lambertian source. In order to evaluate Eq. (8), the normalized radiance angle distribution $f(\theta)$ was fit to an analytical equation using commercial software (TableCurve 2D, Jandel Scientific, San Rafael, CA), and a subroutine was created that was capable of accurate interpolation of the measured $f(\theta)$ data. The integral was then evaluated numerically. The analytical equation used to fit two experimentally measured $f(\theta)$ curves (versus θ) was

$$y = a + b\{\text{atan}[(x-c)/d] + \pi/2\}/\pi, \tag{13}$$

where a, b, c, and d are fit coefficients, and the r^2 values for two fits averaged 0.98. Figure 4 shows isometric plots of the lens coupling efficiency as a function of the magnification
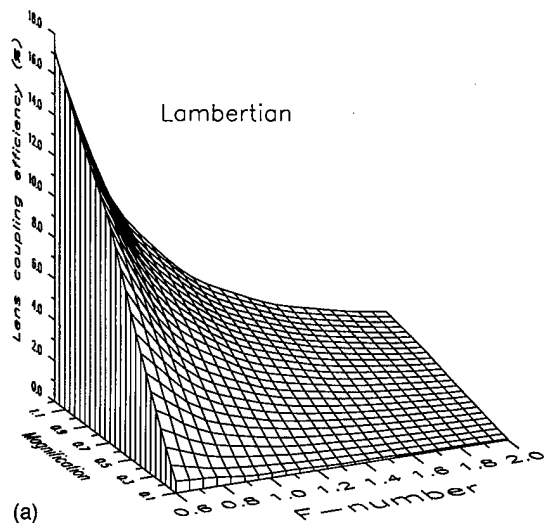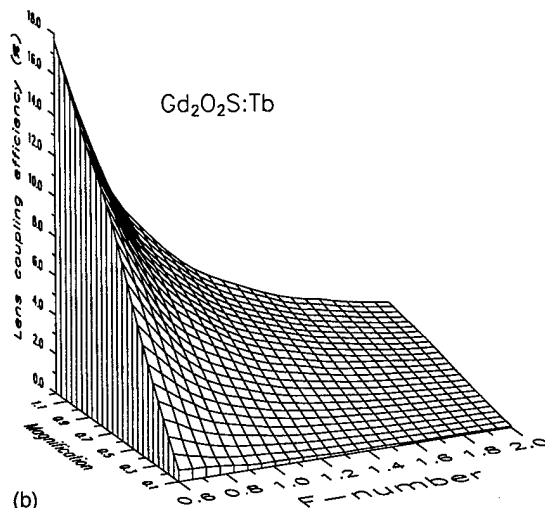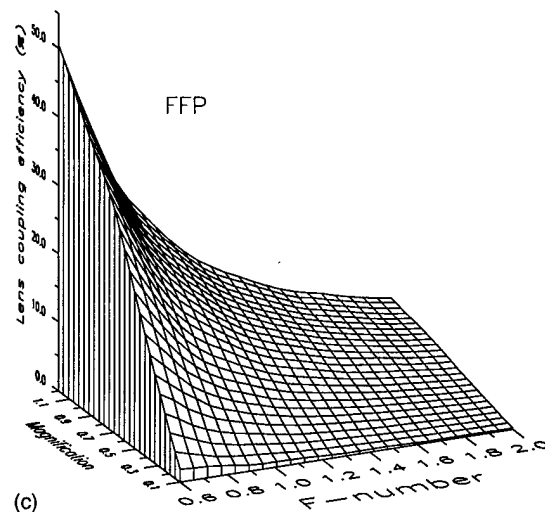
FIG. 4. Lens coupling efficiency as a function of the magnification and the $F_\#$ for a hypothetical Lambertian source (a), a conventional mammography screen (b), and a scintillating fiber faceplate (c). Here the bulk transmittance of lens T is assumed to be unity.
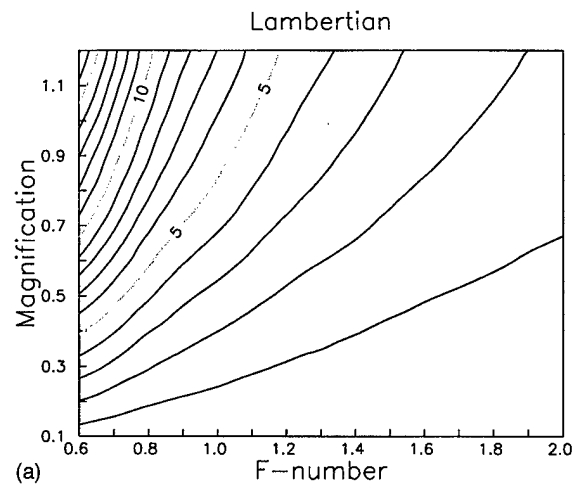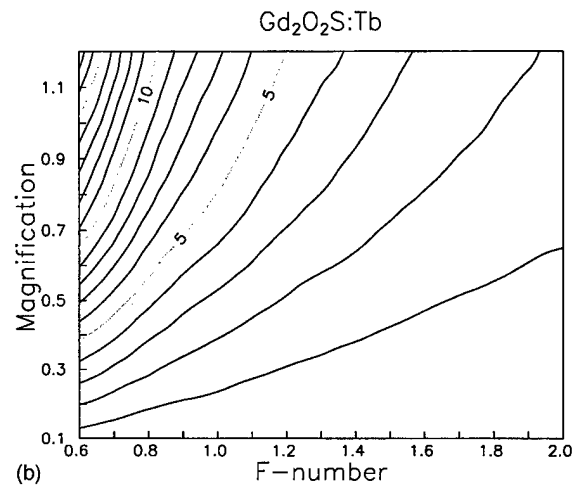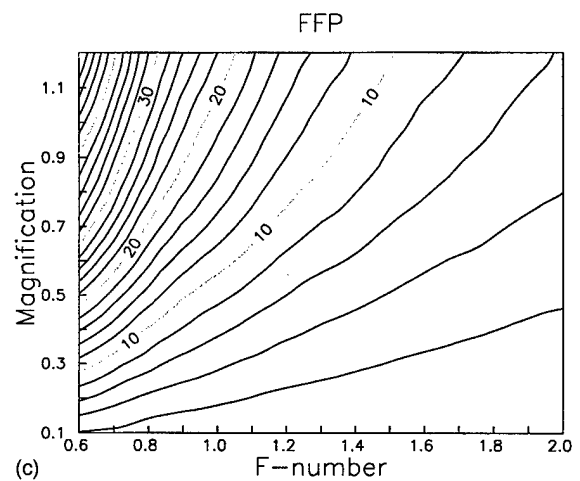
FIG. 5. The lens coupling efficiency's contour plots for a hypothetical Lambertian source (a), where the contour interval is 1%; a conventional mammography screen (b), where the contour interval is 1%; and a scintillating fiber faceplate (c), where the contour interval is 2%.

and the $F_\#$ for a hypothetical Lambertian source [Fig. 4(a)], a conventional mammography screen (34 mg/cm^2 Gd$_2$O$_2$S:Tb [Fig. 4(b)], and a scintillating fiber faceplate [Fig. 4(c)]. Figures 5(a)–5(c) show the contour plots corresponding to the isometric plots in Figs. 4(a)–4(c). The con-
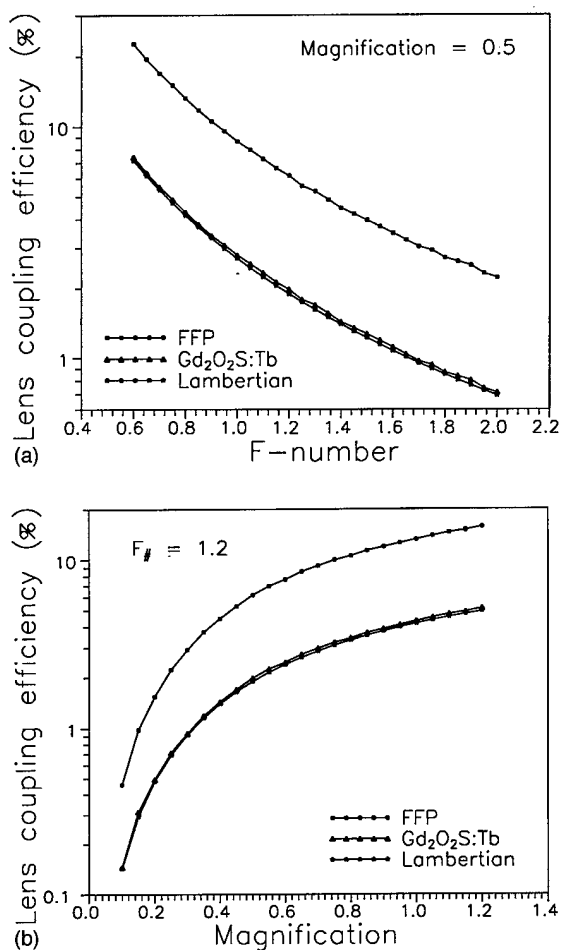
FIG. 6. The lens coupling efficiency as a function of the $F_\#$ for a magnification factor $m = 0.5$ (a), and as a function of the magnification for a F number $F_\# = 1.2$ (b).

which is a reasonable approximation for most of the scintillating screens used in diagnostic radiological imaging. Equation (12) was derived based on the point source assumption. It is more appropriate to use it in the cases where the light attenuation within the screen is negligible. Equation (8) is a more general expression, where the only assumption required is that the light output from the screen is axially symmetric and thus is independent of φ. This assumption applies to Eqs. (7) and (12) as well. In practice, this is an accurate assumption for most scintillating devices.

This work was motivated by the fact that new classes of scintillating devices, including scintillating fiber optic plates[16] exhibit emission properties that are not well described by existing equations. Because Eq. (8) contains an ill-defined function $f(\theta)$, it cannot, in general, be integrated analytically. A suitable approach taken in our laboratory is to fit the experimental data describing $f(\theta)$ to an analytical equation using commercially available curve fitting software, and then perform the integration numerically.

ACKNOWLEDGMENTS

tour plots are useful in quantitatively estimating the lens coupling efficiency. Figure 6(a) shows individual profiles of coupling efficiency with a fixed magnification factor $m = 0.5$, Fig. 6(b) is a plot for a fixed F number $F_\# = 1.2$, which shows that Lambertian approximation will underestimate the lens coupling efficiency, and it can be as high as a factor of 3 for a screen with markedly non-Lambertian emission characteristics, such as a scintillating fiber faceplate. However, the difference between the Lambertian source assumption and the conventional mammography screen (34 mg/cm^2 Gd$_2$O$_2$S:Tb) is quite small. Most scintillating screens used in diagnostic radiological imaging have similar angular dependent radiance distributions.[16] Therefore the Lambertian assumption is reasonable for many of the scintillating screens currently used in diagnostic readilogy.[10]

V. DISCUSSION

Equation (7) is perhaps the most commonly used expression for lens coupling efficiency found in the literature. It was derived based on the Lambertian source assumption,

[1] A. D. A. Maidment, M. J. Yaffe, D. B. Plewes, G. E. Mawdsley, I. C. Soutar, and B. G. Starkoski, "Imaging performance of a prototype scanned-slot digital mammography system," Proc. SPIE 1896, 93–103 (1993).
[2] L. E. Antonuk, J. Boudry, W. Huang, D. L. McShan, E. J. Morton, J. Yorkston, M. J. Longo, and R. A. Street, "Demonstration of megavoltage and diagnostic x-ray imaging with hydrogenated amorphous silicon arrays," Med. Phys. 19, 1455–1966 (1992).
[3] E. R. Fossum, "Ultra low power imaging systems using CMOS image sensor technology," Proc. SPIE 2267, 1–5 (1994).
[4] D. L. Lee, L. S. Jeromin, and L. K. Cheung, "New digital detector for projection radiography," Proc. SPIE 2432, 237–249 (1995).
[5] W. Swindell, E. Morton, P. Evans, and D. Lewis, "The design of megavoltage imaging systems: Some theoretical aspects," Med. Phys. 18, 855–866 (1991).
[6] A. L. Boyer, L. Antonuk, A. Fenster, M. Van Herk, H. Meertens, P. Munro, L. E. Reinstein, and J. Wong, "A review of electronic portal imaging devices (EPIDs)," Med. Phys. 19, 1–16 (1992).
[7] A. Karellas, L. J. Harris, H. Liu, M. A. Davis, and C. J. D'Orsi, "Charge-coupled device detector: Performance considerations and potential for small-field mammographic imaging applications," Med. Phys. 19, 1015–1023 (1992).
[8] E. Krupinski, H. Roehrig, and T. Yu, "Observer performance comparison of digital x-ray systems for stereotactic breast needle biopsy," Acad. Radiol. 2, 116–122 (1995).
[9] A. D. A. Maidment and M. J. Yaffe, "Analysis of signal propagation in optically coupled detectors for digital mammography: II. Lens and fiber optics," Phys. Med. Biol. 41, 475–493 (1996).
[10] H. Liu, A. Karellas, L. J. Harris, and C. J. D'Orsi, "Methods to calculate the lens efficiency in optically coupled CCD x-ray imaging systems," Med. Phys. 21, 1193–1195 (1994).
[11] T. Radcliffe, G. Barnea, B. Wowk, R. Rajapakshe, and S. Shalev, "Monte Carlo optimization of metal/phosphor screens at megavoltage energies," Med. Phys. 20, 1161–1169 (1993).
[12] W. Swindell, "The lens coupling efficiency in megavoltage imaging," Med. Phys. 18, 1152–1153 (1991).

[13]A. D. A. Maidment and M. Yaffe, "Analysis of the spatial-frequency-dependent DQE of optically coupled digital mammography detectors," Med. Phys. **21**, 721–729 (1994).

[14]F. Grum and R. J. Becherer, *Optical Radiation Measurements* (Academic, New York, 1979), Vol. 1, Chap. 3.

[15]T. Yu, J. M. Sabol, J. A. Seibert, and J. M. Boone, "Scintillating fiber optic screens: A comparison of MTF, light conversion efficiency, and emission angle with Gd_2O_2S:Tb screens," Med. Phys. **24**, 279–285 (1997).

[16]A. D. A. Maidment and M. J. Yaffe, "Analysis of signal propagation in optically coupled detectors for digital mammography: I. Phosphor screens," Phys. Med. Biol. **40**, 877–889 (1995).

An accurate method for computer-generating tungsten anode x-ray spectra from 30 to 140 kV

John M. Boone[a)] and J. Anthony Seibert
Department of Radiology, University of California, Davis, 2421 45th Street, Sacramento, California 95817

A tungsten anode spectral model using interpolating polynomials (TASMIP) was used to compute x-ray spectra at 1 keV intervals over the range from 30 kV to 140 kV. The TASMIP is not semi-empirical and uses no physical assumptions regarding x-ray production, but rather interpolates measured constant potential x-ray spectra published by Fewell *et al.* [*Handbook of Computed Tomography X-ray Spectra* (U.S. Government Printing Office, Washington, D.C., 1981)]. X-ray output measurements (mR/mAs measured at 1 m) were made on a calibrated constant potential generator in our laboratory from 50 kV to 124 kV, and with 0–5 mm added aluminum filtration. The Fewell spectra were slightly modified (numerically hardened) and normalized based on the attenuation and output characteristics of a constant potential generator and metal-insert x-ray tube in our laboratory. Then, using the modified Fewell spectra of different kVs, the photon fluence Φ at each 1 keV energy bin (E) over energies from 10 keV to 140 keV was characterized using polynomial functions of the form $\Phi(E) = a_0[E] + a_1[E]\,\text{kV} + a_2[E]\,\text{kV}^2 + \cdots + a_n[E]\,\text{kV}^n$. A total of 131 polynomial functions were used to calculate accurate x-ray spectra, each function requiring between two and four terms. The resulting TASMIP algorithm produced x-ray spectra that match both the quality and quantity characteristics of the x-ray system in our laboratory. For photon fluences above 10% of the peak fluence in the spectrum, the average percent difference (and standard deviation) between the modified Fewell spectra and the TASMIP photon fluence was -1.43% (3.8%) for the 50 kV spectrum, -0.89% (1.37%) for the 70 kV spectrum, and for the 80, 90, 100, 110, 120, 130 and 140 kV spectra, the mean differences between spectra were all less than 0.20% and the standard deviations were less than $\sim 1.1\%$. The model was also extended to include the effects of generator-induced kV ripple. Finally, the x-ray photon fluence in the units of photons/mm^2 per mR was calculated as a function of HVL, kV, and ripple factor, for various (water-equivalent) patient thicknesses (0, 10, 20, and 30 cm). These values may be useful for computing the detective quantum efficiency, DQE(f), of x-ray detector systems. The TASMIP algorithm and ancillary data are made available on line at http://www.aip.org/epaps/epaps.html. © *1997 American Association of Physicists in Medicine.* [S0094-2405(97)00311-8]

Key words: x ray, computer simulation, spectra, computer model, detective quantum efficiency

I. INTRODUCTION

Computer simulation of x-ray detector design[1–6] has become commonplace in the past two decades. Intrinsic to any realistic computer simulation is the use of realistic x-ray spectra. Since the days of Kramer in the 1920s, there have been many different attempts to model x-ray spectra.[7–15] However, the "gold standard" for comparing computer-generated x-ray spectra remains measured x-ray spectra. Because of the experimental complexity of measuring x-ray spectra, however, few research groups have attempted such detailed measurements. The *de facto* standard for measured x-ray spectra remains the seminal measurements performed by Fewell and his colleagues[16–18] at what is now the Center for Devices and Radiological Health. In this report, a technique is presented for computer generating tungsten-anode x-ray spectra at any diagnostic kV. The technique is not model driven or semi-empirical, but rather is completely empirical and is based upon straightforward interpolation techniques using a modified version of Fewell's measured spectra as a data source.

Over the last decade, the evaluation of imaging systems has become more elaborate as the science[19–21] of imaging systems has advanced. The characterization of imaging system performance in the research sector often includes the calculation of the detective quantum efficiency as a function of spatial frequency, DQE(f).[19–24] The DQE(f) is calculated from the experimentally determined modulation transfer function [MTF(f)] and noise power spectrum [NPS(f)]. The relationship[19] between these quantities is

$$\text{DQE}(f) = \frac{k[\text{MTF}(f)]^2}{q\text{NPS}(f)}, \tag{1}$$

where q is the number of x-ray quanta used to measure the NPS(f) and k is a constant which is related to the gain of the detector. For film,[19] $k = (\log_{10} e)^2 \gamma^2$, where e is the base of natural logarithms and γ is the slope of the characteristic curve for film. For linear digital detector systems the value of k is usually expressed in the units of digital number (gray scale value) per incident x-ray quantum.

The TASMIP algorithm was used to develop an accurate estimate of the quantum fluence for a variety of x-ray beams used in measuring the quantum detective efficiency, DQE(f). Figures are given which should allow investiga-
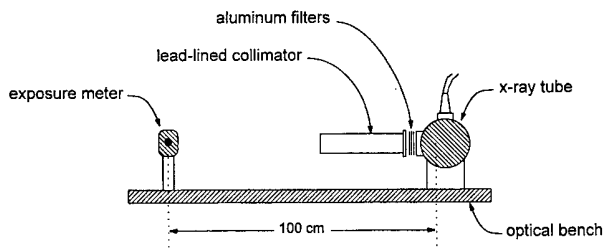
FIG. 1. A diagram of the experimental setup used in the measurements is shown.

tors to quickly estimate the value of q using the half value layer (HVL) measured on their x-ray tube at a given kV. Analytical expressions (from the computer fit) of quantum fluence versus HVL are also provided for several different patient thicknesses (0, 10, 20, and 30 cm).

II. METHODS

A. Measurement of x-ray tube output

The x-ray output of a laboratory x-ray system was measured in the units of mR/mAs measured at a distance of 1000 mm from the focal spot using an ionization exposure meter (MDH Model 2025, 6 cc chamber, RadCal Corporation, Monrovia, CA). The x-ray generator used for these measurements was a constant potential generator (Toshiba 2000 mA, Model 2050 generator), with a dual (1.0/0.3 mm) focal spot x-ray tube (Toshiba "Rotanode" x-ray tube, housing model DRX-5735 HD-S and insert model DR-5735H, manufactured 1992). The 200 mA, 50 ms (10 mAs) small focal spot settings were used at kVs of 50, 56, 60, 66, 70, 76, 80, 86, 90, 96, 100, 106, 110, 116, 120, and 124. On the same day just prior to performing the x-ray measurements reported here, Toshiba service engineers measured the kV accuracy using a voltage divider. The relationship between the kV selected on the control panel ("set kV") and the kV measured by the voltage divider ("actual kV") was a straight line with a linear correlation coefficient of 0.9989 (actual kV$=-0.97822+1.00325\times$set kV). The linear fit was used to calibrate the kV values, and all mention to kV hereafter refers to the actual kV value as measured by the voltage dividers. The waveform of the tetrode-stabilized con-

stant potential generator was observed on an oscilloscope and was found to be essentially dc, with no appreciable ripple ($<2\%$).

The x-ray tube was mounted on an optical table with the x-ray beam facing horizontally (Fig. 1). The standard collimator assembly was removed, and the measurement geometry included only the bare x-ray tube housing with no added filtration. The x-ray tube port was constructed of aluminum. A 10 cm$\times$10 cm$\times$25 cm lead-lined square tube, mounted on the optical table, was used to collimate the x-ray beam and maintain narrow beam geometry. Output measurements over the entire kV series were acquired with aluminum thicknesses of 0, 1.0, 2.0, 3.0, 4.0, and 5.0 mm of type 1100 aluminum added to the x-ray beam.

The exposure readings in units of milliRoentgen were divided by 10 mAs to get the output values in the units of mR/mAs measured at 1 m. At each of the six aluminum thicknesses (including 0 mm), the mR/mAs values were fit as a function of kV to a four-term (third order) polynomial expression using commercially available curve fitting software (TableCurve 2D, Jandel Scientific, San Rafael, CA). While the mR/mAs versus kV is often thought of as a kV^2 dependent curve, no straightforward power relation of this nature was found in the measured data. The polynomial fit results expressing output as a function of kV, for each aluminum thickness, are reported in Table I. These output values will be referred to as OUTPUT(kV,Al).

B. Preprocessing the tabulated spectra

Unfiltered tungsten spectra from Fewell et al.[17] were tabulated in the computer for 70, 80, 90, 100, 110, 120, 130, and 140 kVs. These tabulated spectra correspond to the spectra labeled EI 1 through EI 8 on pages 43–45 of Ref. 17. The spectra were tabulated by Fewell at intervals of 2 keV starting at 10 keV, and the intermediate (odd) spectral values were linearly interpolated to 1 keV intervals. The unfiltered tungsten spectra from Fewell et al.[18] for kVs 30, 40, and 50 were taken from Table MW5 (p. 23), Table MW10 (p. 26), and Table PW15 (p. 31), respectively. These spectra were tabulated at 1 keV intervals, and therefore no interpolation was needed. The details of the methods used by Fewell are deferred to the references; however, a constant potential generator was used for the 70–140 kV spectra. The measured spectra from Fewell were published in 1978[18] and 1981,[17]

TABLE I. The polynomial fit coefficients of the x-ray tube output (mR/mAs @ 1 m) as a function of kV, according to the equation, Output (mR/mAs @ 1 m)$=a_0+a_1$ kV$+a_2$ kV$^2+a_3$ kV^3. This output corresponds to that of a naked (no collimator or added filtration) high-output metal insert x-ray tube operating at a constant potential kV. The stated "inherent" filtration on the x-ray tube was 1.1 mm Al at 62.5 kV.

mm AL	a_0	a_1	a_2	a_3
0	$-1.052\,483\,267\,387\,149$	$0.02\,930\,447\,656\,001\,461$	$0.001\,466\,617\,734\,266\,627$	$3.099\,735\,988\,223\,852E-06$
1	$-0.2\,580\,346\,048\,699\,273$	$-0.01\,734\,121\,710\,087\,892$	$0.001\,507\,526\,660\,207\,658$	$-3.034\,537\,822\,154\,553E-06$
2	$0.2\,931\,022\,580\,370\,263$	$-0.04\,276\,402\,338\,089\,291$	$0.001\,50\,454\,911\,727\,105$	$-3.002\,359\,979\,264\,986E-06$
3	$0.7\,180\,677\,978\,945\,321$	$-0.05\,734\,004\,610\,210\,578$	$0.001\,435\,537\,950\,614\,352$	$-2.671\,430\,120\,748\,248E-06$
4	$1.135\,656\,241\,897\,038$	$-0.07\,125\,412\,642\,842\,751$	$0.001\,43\,250\,965\,607\,749$	$-2.710\,355\,822\,354\,008E-06$
5	$0.7\,383\,175\,101\,583\,323$	$-0.05\,517\,932\,620\,874\,207$	$0.001\,127\,337\,568\,389\,607$	$-1.666\,757\,684\,781\,258E-06$

TABLE II. Aluminum-equivalent thicknesses needed to match the Fewell spectra to the attenuation levels of the x-ray system used in our laboratory.

Constant potential kilovoltage	Added inherent aluminum filtration (micrometers)
30	900[a]
40	870[a]
50	843
70	629
80	626
90	620
100	594
110	584
120	561
130	561
140	561

[a]For the 30 and 40 kV spectra, no comparison attenuation measurements were available because the generator in our lab could only go down to 50 kV. These values were therefore extrapolated based on the other values.

and it is reasonable to assume that x-ray tube insert thickness and composition differences exist between the tubes used by Fewell and the x-ray tube in our laboratory. This is especially true considering that the x-ray tube in our laboratory is a high-output (800 000 heat units) metal insert x-ray tube designed for cardiac catheterization systems.

The parametrized x-ray tube output function discussed above, OUTPUT(kV,Al), was used to calculate attenuation curves from the output of the x-ray system in our laboratory. At any kV value between 50 and 124, attenuation values from thicknesses ranging from 0–5 mm of added aluminum could be accurately calculated. These "measured" attenuation values were compared to attenuation curves calculated from the Fewell spectra with recently compiled attenuation coefficients for aluminum.[25] To compensate for probable differences in the x-ray tube housing attenuation values at each kV, additional thicknesses of aluminum were used to add *inherent* filtration to the Fewell spectra. Aluminum ($Z = 13$) was used because it approximates the beam hardening characteristics of the silicon ($Z = 14$) dioxide used in most glass tube inserts, and furthermore the x-ray tube port in our laboratory was made of aluminum. A least squares approach was used to minimize the difference in (percent) attenuation values between the measured OUTPUT(kV, Al) values and the Fewell spectra. Using this approach, it was found that an additional 500–1000 μm of aluminum were needed (depending on kV) so that the attenuation profiles best matched. The kV-dependent added aluminum thicknesses are given in Table II.

Once the Fewell spectral shapes were slightly hardened to best fit measured attenuation profiles, the number of x-ray photons for each spectra was normalized to the corresponding output (mR/mAs at 1 m) of our laboratory system with no added filtration (0 mm Al). The output values at 30 and 40 kV were extrapolated, since the minimum kV of our generator was 50 kV. Once normalized, these 11 x-ray spectra were, in principle, representative of both the quality and

quantity of the output of our laboratory x-ray system, set at 1 mAs and measured at 1 m. These 11 spectra ranging from 30–140 kV will be referred to as the "modified Fewell" spectra. There was no 60 kV spectrum, as this kV was too high for the mammography application[18] and too low for the CT application.[17]

C. Tungsten anode spectral model interpolating polynomials (TASMIP)

The 11 spectra with kVs ranging from 30–140 (excluding 60 kV) have a low energy cutoff of about 10 keV, and thus the lowest energy resolved in the TASMIP technique was 10 keV. For the sake of discussion, let us start with an energy of 20 keV, since all 11 modified Fewell spectra included a finite photon fluence at 20 keV. If an x-ray system is set to a constant mAs (e.g., 1 mAs), the number of x-ray photons produced at a given energy interval (e.g., 20 keV) will increase as the applied kV across the tube is increased. The precise functional form which describes this increase is a component of most analytic and semi-analytic spectral models. Here, however, the 11 spectral entries at the 20 keV bin were fit to a general polynomial equation of nth order:

$$\text{if } E \leq \text{kV}, \Phi[E] = a_0[E] + a_1[E]\text{kV} + a_2[E]\text{kV}^2$$
$$+ a_3[E]\text{kV}^3 + \cdots + a_n[E]\text{kV}^n, \tag{2}$$
$$\text{else } \Phi(E) = 0.$$

The least squares polynomial fitting routine ("POLFIT") from Bevington[26] was converted from FORTRAN to C and used for determining the coefficients a_0–a_n indicated in Eq. (2). At 20 keV, there were 11 pairs of values ($\{\Phi_i, \text{kV}_i\}$, $i = 1,...,11$) that could be used in the fit (to solve for coefficients a_n). As the energy of the bin to be fit increased, fewer data were available for the fit procedure. For example, at 55 keV, only eight of the modified Fewell spectra produced x-ray photons in the 55 keV energy bin, since, of course, the 30, 40, and 50 kV spectra did not produce any 55 keV photons. Consequently, as the energy of the bin increased, the number of fluence values contributing to the polynomial fit was gradually reduced. Consequently, the order of the polynomial also was gradually reduced as energy increased, with orders starting at 4 for low energies going to order 2 at higher energies. Negative fluence values could be produced by the polynomial at energies higher than the kV of the spectrum; in this case the fluence was set to zero since negative fluence values have no physical meaning.

The polynomial fitting technique was performed at all energies from 10 to 140 keV, in 1 keV steps. The highest-order polynomial that was practical (depending on the number of data points available in the fit) was initially selected by the computer and fit to the data. The raw data points and the polynomial fit results were then visually inspected at each keV. Software was written to allow the interactive selection of the order of the polynomial used for the fit. We found that the visual observation of the fit was a necessary quality assurance step in producing well-behaved interpolating poly-

TABLE III. The value of Φ/X in the units of photons per mm^2 per mR are listed for selected monoenergetic x-ray beam energies.

Energy (keV)	Φ/X	Energy (keV)	Φ/X
1	153	60	303 591
5	2 894	65	307 196
10	12 141	70	305 707
15	28 667	75	295 162
16	33 169	80	283 525
17	37 252	85	271 075
18	42 843	90	258 864
19	47 298	95	246 611
20	53 832	100	235 671
21	58 892	105	222 517
22	66 034	110	210 627
23	71 395	115	200 019
24	78 444	120	190 296
25	86 495	125	181 353
30	123 632	130	173 019
35	168 450	135	165 227
40	210 747	140	157 904
45	248 464	145	151 174
50	277 068	150	144 913
55	295 723		

FIG. 2. This figure shows the output of the constant potential generator in our laboratory. The solid squares show the measured data points, and the corresponding lines represent the polynomial fit to the data. The polynomial coefficients are given in Table I.

$$\text{Total exposure (mR)} = \int_0^{E_{\max}} \frac{X}{\Phi}(E)\Phi(E)\ dE. \qquad (4)$$

The TASMIP spectra from 30 to 140 kV were generated with different amounts of aluminum filtration (0–4 mm) and different thicknesses of (water-equivalent) tissue filtration (0, 10, 20, and 30 cm), and the fluence per unit exposure was calculated for each. In addition, the half value layer (HVL) in aluminum was also computed and the fluence results were presented as a function of HVL.

III. RESULTS

A. Output results

The x-ray output in units of mR/mAs measured at 1 m as a function of actual constant potential kV is shown in Fig. 2. The six curves represent different thicknesses of added aluminum, from 0 to 5 mm as indicated. The solid data points show the actual measured values. The lines corresponding to each set of measured points were calculated by the polynomial fit to the measured data. The polynomial fit coefficients are given in Table I, for those who may have use for kV and filtration-dependent x-ray output values. These are *not* the TASMIP values used for interpolating the spectra.

B. Spectral model results

The attenuation curves calculated from the (parameterized) measured data are shown as the solid squares in Fig. 3. Attenuation profiles for several kV, as indicated, are shown. The solid lines in Fig. 3 demonstrate the attenuation profiles calculated from the modified Fewell spectra. A small amount of added aluminum filtration was added to each Fewell spectra (hence the term *modified*) to match in a least-squares sense the measured attenuation values. The excellent agreement between the measured data (squares) and the calculated data (lines) suggests that the spectral model is sound in terms of quality, but not necessarily in terms of quantity since the attenuation curves are relative values.

nomials. Once the computer code was written, it was a very easy step to rapidly go through and check the polynomial fits at each energy.

As the polynomial coefficients were calculated at each energy from 10 to 140 keV, they were stored to a file for later use. Once the polynomial terms $(a_i[E], i=0,...,n)$ were calculated over the entire energy range and stored, an algorithm was written which used the stored polynomial coefficients to calculate the x-ray spectra at any arbitrary kV value using Eq. (2).

D. X-ray quanta per x-ray fluence

For a monoenergetic x-ray beam at a known exposure level, the number of x-ray quanta per unit of exposure [i.e., the value of "q" in Eq. (1)] can be calculated as derived by Johns:[27]

$$\frac{\Phi}{X} = \frac{5.43\times10^5}{(\mu[E]/\rho)_{en}E} \frac{\text{photons}}{mm^2mR}, \qquad (3)$$

where $(\mu[E]/\rho)_{en}$ is the energy-dependent mass energy absorption coefficient for air, Φ is the photon fluence (photons/mm^2), and X is the exposure in mR. The units of mR are used here to be consistent with John's classic derivation (which was in R). The mass energy absorption coefficients were calculated as described previously,[25] with the weight fractions of air being 0.20946 oxygen, 0.78084 nitrogen, and 0.00934 argon. Selected values of Φ/X are given in Table III for reference.

It is convenient when manipulating spectra in a computer to generate the inverse of Eq. (3), which is an energy-dependent description of the mR per photon. This value is used as a multiplier when integrating the exposure due to a spectrum, $\Phi(E)$, using the expression

FIG. 3. Least-squares analysis was performed to determine the best thickness of aluminum filtration to filter the Fewell spectra, in order to reproduce the attenuation properties of the high-output metal insert x-ray tube in our laboratory. The solid lines demonstrate the attenuation curves for the modified Fewell spectra. The agreement in attenuation curves demonstrates a good match between the modified Fewell spectra and the experimental x-ray system in terms of spectral *quality*.

Figure 4 illustrates the 11 modified Fewell spectra, each normalized in amplitude to the output of the constant potential generator in our laboratory. Each spectrum is normalized to 1 mAs at the corresponding kV. The vertical lines labeled A, B,..., F are meant to show the points used for the polynomial interpolation process. Each of these lettered vertical lines corresponds to an energy bin (e.g., A=20 keV, B=40 keV, and so on). The intersection between the vertical lines and each spectra represents the photon fluence at that
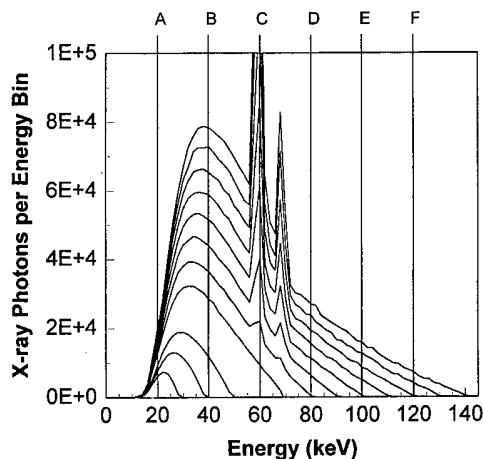
FIG. 4. The modified Fewell spectra were normalized to the output of the experimental x-ray system, and are shown in this figure. At any given "monoenergetic" energy (for example, 40 keV, vertical line B), the photon output increases with kV. The TASMIP spectra are interpolated based on the polynomial fit of the data illustrated in this figure. Values that can be used to solve for polynomial coefficients occur where the vertical lines (A,B,...,F) intersect each of the spectra. These polynomial values, along with the corresponding polynomial fit results, are shown in Fig. 5.
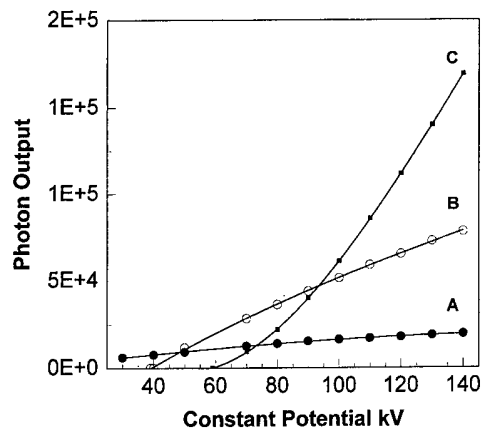
(a)
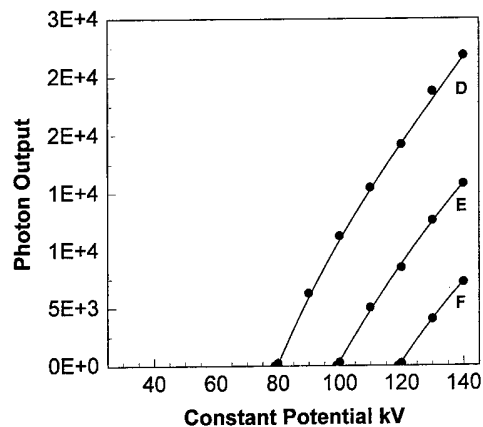
(b)

FIG. 5. This figure demonstrates the photon output (ordinate) as a function of the applied kilovoltage across the x-ray tube. The data corresponding to the vertical lines marked A, B, and C in Fig. 4 are shown in (a), and the data for vertical lines marked D, E, and F are shown in (b). The solid points correspond to the intersection points described in Fig. 4. The solid line represents the polynomial fit to the data points. These are interpolating polynomials referred to in the TASMIP acronym. It is seen in the figure that interpolating output values (for any kV) is straightforward.

energy bin for the kV corresponding to each spectra. The individual data points represented by these intersections in Fig. 4 are shown as the symbols in Figs. 5(a) and 5(b). The data corresponding to the vertical lines A–F shown in Fig. 4 are labeled accordingly in Fig. 5. The solid lines in Fig. 5 show the fit to the data from the polynomial fitting routine. These lines are the result of the interpolating polynomials corresponding to the TASMIP acronym. Notice that the functional dependence of how the photon fluence increases as a function of applied kV varies. The biggest difference is for the 60 keV energy bin (line C), which corresponds to the approximate energy where characteristic radiation (K_α) is produced by the tungsten anode. The shape of this curve is clearly arched upward in contrast to the others shown. The curves labeled A–F in Figs. 5(a) and 5(b) show just 6 of the 131 polynomial curves generated.

The normalization of the modified Fewell spectra, prior to computing the polynomial coefficients, results in photon fluence values that when calculated from the interpolating polynomials are quantitatively accurate. This means that the TASMIP procedure produces not only the appropriate spec-
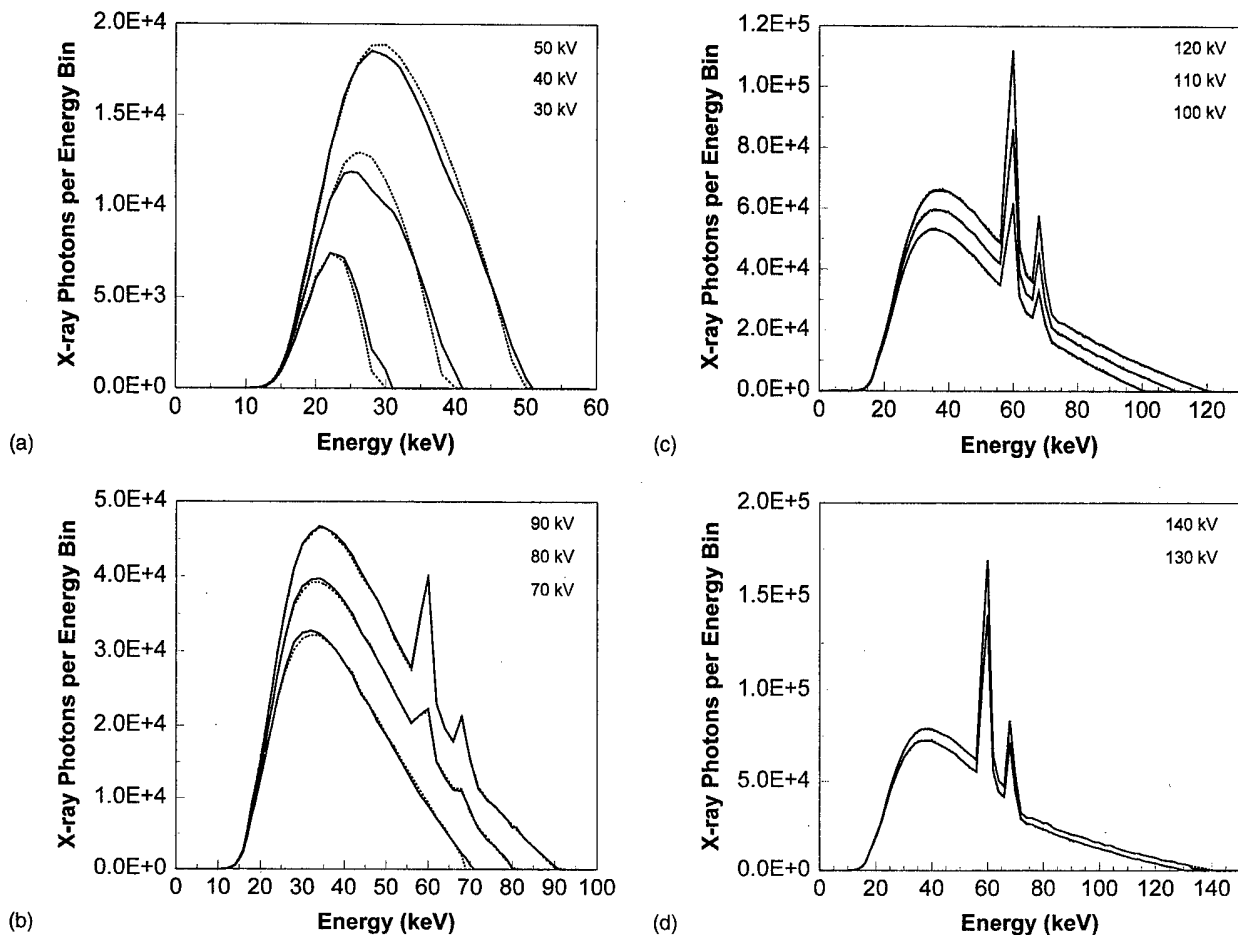
FIG. 6. The modified Fewell spectra are plotted (dashed lines) and compared with the corresponding TASMIP-generated spectra (solid lines). The TASMIP algorithm produces spectra that are accurate in terms of both spectral shape (*quality*) and spectral amplitude (*quantity*). Both properties are compared in this figure.

tral shape, but also the appropriate spectral amplitude (photon fluence per mAs) as well. This fact has important ramifications regarding issues of waveform, which will be discussed later. The spectra from 30 to 140 kV are shown in Figs. 6(a)–6(d), with the modified Fewell spectra shown as dashed lines and the TASMIP-generated spectra as solid lines. The less-than-perfect performance comparisons at 30 and 40 kV are the result of the fact that the normalized output at these two kVs had to be extrapolated from our measurements, since the x-ray system in our laboratory could not operate below 50 kV. At the higher kVs, the modified Fewell spectrum (solid line) is in many cases indistinguishable from the spectrum produced by the TASMIP algorithm. Keep in mind that the TASMIP spectra plotted in Fig. 6 are not normalized after their calculation to the modified Fewell spectra photon fluence; they each represent the raw output of the TASMIP calculation, which produces a photon fluence as if the generator was set to 1 mAs. Consequently, the comparison is made in terms of shape *and* absolute amplitude (photon fluence). The percent difference for photon fluences above 10% of the peak fluence in the spectrum was calculated for each spectral pair shown in Figs. 6(a)–6(d). The 10% cutoff was used to eliminate the influence of low flu-

ence values near the low keV and high keV edges of the spectra, where small absolute differences in photon fluence yield large percent errors. The average percent difference (and standard deviation) between the modified Fewell spectra and the TASMIP spectra were -1.43% (3.8%) for the 50 kV spectrum, -0.89% (1.37%) for the 70 kV spectrum, -0.16% (1.13%) for the 80 kV, 0.14% (0.94%) at 90 kV, -0.06% (1.08%) at 100 kV, -0.09% (0.64%) for the 110 kV spectra, -0.16% (0.55%) at 120 kV spectra, 0.09% (0.69%) at 130 kV spectra, and -0.01% (0.33%) for the 140 kV spectra.

Figure 7 is a graph that is quite similar to Fig. 2, but the distinction between them is very important. The solid squares shown in Fig. 7 represent the measured output data from the x-ray generator in our laboratory, at six different thicknesses of added filtration as shown. The solid line at 0 mm Al is calculated from the TASMIP algorithm directly: the spectra were calculated and their photon fluence was converted to exposure units using Eq. (4). Since the modified Fewell spectra were normalized at these values, it is not that surprising that there is good correspondence between the measured values (squares) and the calculated values (line) at 0 mm. For the other thicknesses of aluminum, the spectra
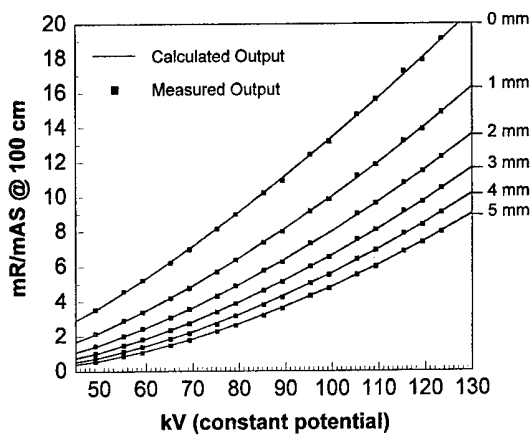
FIG. 7. One of the aims of this investigation was to produce a tungsten anode spectral model which matches the output of the x-ray system in our laboratory, in terms of both spectral shape and amplitude. In this figure, the solid data points are the measured machine output values on the experimental x-ray system (same as in Fig. 2). The solid line at 0 mm Al represents the integrated spectral output from spectra produced by the native TASMIP model. The other solid lines (1–4 mm Al) show the TASMIP output filtered by the appropriate thickness of aluminum, and these data show excellent agreement with the measured output results. Whereas Fig. 3 demonstrates a good match in spectral quality, this figure demonstrates that an excellent match between quality and quantity was achieved.

were calculated by the TASMIP algorithm and then attenuated numerically using the appropriate thickness of aluminum, and then the exposure was calculated using Eq. (4). No normalization was used here; the solid lines at each thickness of aluminum represent absolute output of the TASMIP algorithm. Thus, just as Fig. 3 serves to demonstrate the accuracy of the beam *quality* aspects of the spectral model, Fig. 7 serves to demonstrate both the accuracy of the beam *quantity* and *quality* that is produced by the TASMIP algorithm.

C. The kV ripple

The x-ray generator used by Fewell for spectral measurements (≥ 70 kV) was a constant potential system, as is the x-ray system in our laboratory. Therefore, the TASMIP model generates constant potential spectra. However, most current x-ray generators are of the inverter type, and therefore demonstrate some degree of ripple in the kV waveform. As is common in the field, the "ripple factor" corresponds to the amount of kV fluctuation, represented as a percentage of the maximum kV, present in the waveform. For example, an inverter waveform shape is shown in Fig. 8, and corresponds to a 20% ripple (typical ripple factors are lower than this). The waveform shown in Fig. 8 is given by the equation

$$kV(t) = kV_b + (kV_a - kV_b)|\sin(2\pi f t)| \qquad (5)$$

where kV_a is the "set" kV (formerly called the kV_p) and $kV_b = kV_a(1 - PRF/100)$, where PRF = percent ripple factor. While we state that this equation accurately describes generator voltage waveform without proof, visual comparison between the waveform shown in Fig. 8 and typical inverter
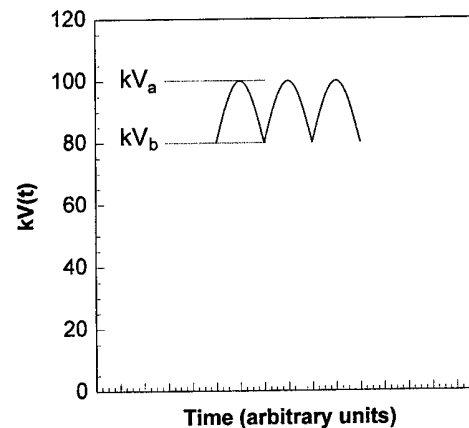
FIG. 8. A typical kilovoltage waveform is illustrated, using Eq. (5) for its calculation. This waveform illustrates 20% ripple, which is probably higher than most inverter generators.

generator waveforms is convincing.[28] Whether or not the waveform is perfectly sinusoidal will probably have little influence in the resulting x-ray spectrum.

To produce an x-ray spectrum from a generator that has a finite ripple component in its waveform, as all inverter, single, and three phase generators do, the TASMIP algorithm is integrated over the time-dependent waveform given in Eq. (5). Because TASMIP accurately produces both the spectral shape and kV-dependent output (fluence), the integrated spectra will be appropriate both in terms of spectral quality and quantity. For high-frequency x-ray systems where the amount of ramp-up and ramp-down time is small compared to the total exposure time, Eq. (5) need only be integrated over one half cycle. Because the integration is performed discretely, the influence of the number of points used to integrate over the half cycle was tested. A 100% ripple spectrum was produced with 1000 points distributed evenly over the half cycle of integration. The number of integration points was reduced until the spectra demonstrated a very slight difference from the one produced with 1000 integration points. It was found that 20 time-points along the half cycle were sufficient to produce a spectrum that is visually identical to the 1000 time-point approach.

The output of the TASMIP model including ripple is shown in Fig. 9 for 100 kV spectra. Most inverter generators produce ripple factors between 5% and 15%. Single-phase generators produce 100% ripple in theory; however, due to line capacitance, the complete drop of kV to zero is usually mitigated to some extent. The influence of ripple on the beam quality as measured by the half value layer was computed and is shown in Fig. 10. The influence of ripple in terms of HVL appears to be more severe at higher kVs, which is not surprising. The larger effect of ripple is on output (mR/mAs), as calculated and shown in Fig. 11. Figures 10 and 11 were computed using 2 mm of added Al filtration.
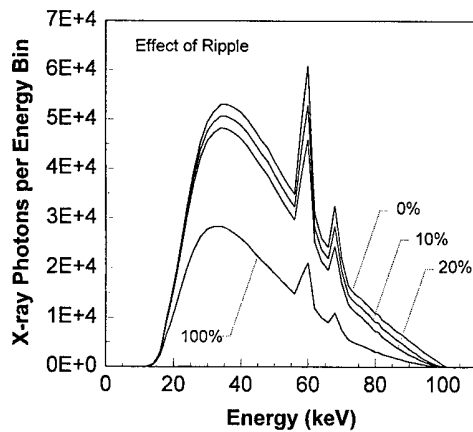
FIG. 9. This figure illustrates the spectra produced at 100 kV by generators of different ripple factors. The spectra were generated using the TASMIP model, integrated over the waveform shown in Fig. 8 using the indicated ripple factors.

FIG. 11. The output in terms of mR/mAs measured at 1 m is reduced as the ripple factor of the waveform increases. This is caused by the reduced efficiency of x-ray production at lower applied potential. These data were calculated using the TASMIP with 2.0 mm of added aluminum filtration.

D. X-ray quanta tabulation

The number of quanta incident upon an x-ray detector is a parameter which is needed to properly calculate the DQE(f) of the detector system, as shown in Eq. (1). The quantum fluence per mR for a monoenergetic x-ray beam is illustrated in Fig. 12, and this curve is derived directly from Eq. (2). Its shape is governed only by the value of the energy-dependent mass energy absorption coefficient of air. Because investigators measuring detector performance in real systems must use polyenergetic spectra, the TASMIP spectral model was used to calculate and tabulate the x-ray quantum fluence for a variety of beam qualities. Beam quality is affected by a number of factors, including kV, ripple, and added aluminum filtration. Furthermore, many investigators seek to measure DQE(f) performance under patient imaging conditions, where the x-ray beam is filtered by the patient. To present data as a function of all these parameters would require a

prohibitive number of graphs. Fortunately, by accepting minimal error (~2%) the data can be compressed to a few plots of quantum fluence versus HVL. These curves fold the kV, the added aluminum filtration, and the waveform into a single plot. The parameter ranges included in Figs. 13(a)–13(d) include kVs from 30 to 140, added Al from 0 to 4 mm, and ripples of 0%, 10%, and 20%. All data points are shown in the figure.

Figure 13(a) shows the fluence versus HVL dependency when no patient is present. The solid line shows a least squares fit to the individual data points, where the average error was calculated as 2.34%. The fit parameters required to calculate the solid line are given in Table IV. Figures 13(b)–13(d) show the points and best fit results for water equivalent patient thicknesses of 10, 20, and 30 cm, where the range of patient thicknesses is included for a variety of x-ray imaging applications. The average error when using the fit results instead of the individual points was calculated as 0.74% for the 10 cm case, 0.39% for the 20 cm case, and 0.26% for the 30 cm case. For those who require a more accurate estimate

FIG. 10. The half value layer (HVL) of the x-ray beam is plotted at the indicated kVs as a function of the ripple factor of the waveform. The HVL of higher kV spectra suffer more due to increased ripple. These data were calculated using the TASMIP with 2.0 mm of added filtration.
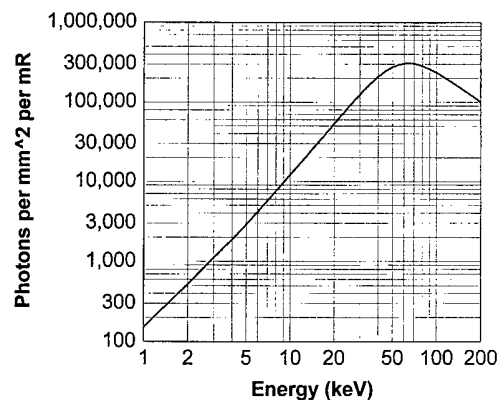
FIG. 12. This figure shows the quantum fluence (photons/mm^2/mR) as a function of energy for a monoenergetic x-ray beam. This data was generated using Eq. (3).
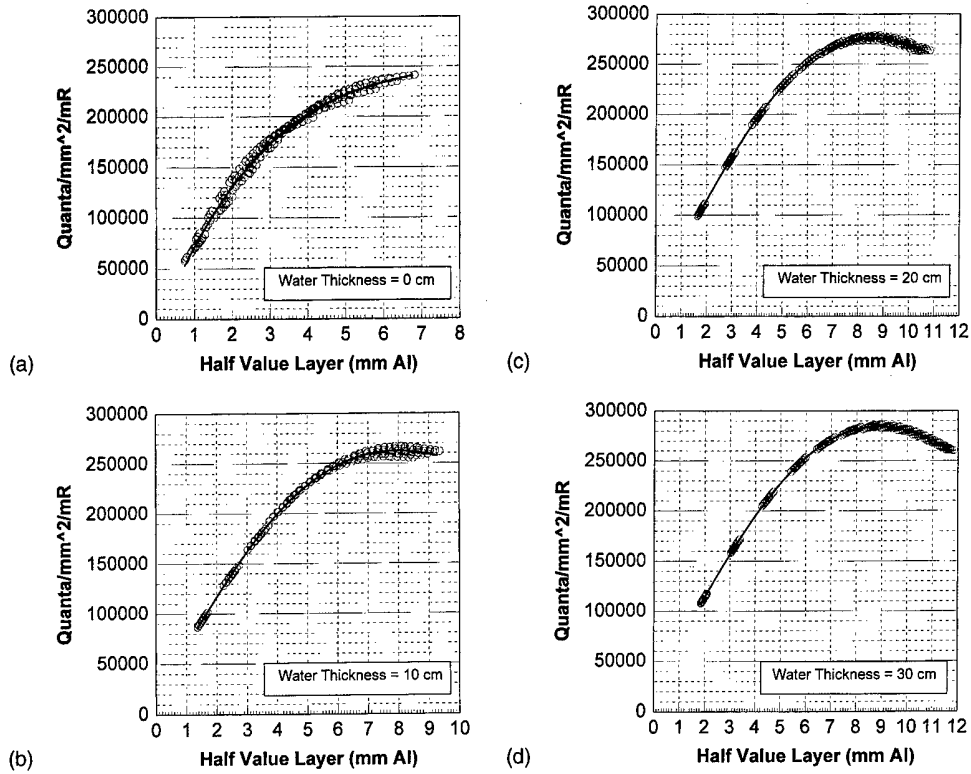
FIG. 13. This figure illustrates the quantum fluence (photons/mm²/mR) for polyenergetic x-ray spectra. For (a, b, c, and d), spectra were generated from 30 to 140 kV, with from 0 to 4 mm of added Al, and with waveforms of 0%, 10%, and 20% ripple. Basically, these spectra should cover the entire range of possible outputs of a modern inverter generator. In some instances it is useful to know the postpatient fluence, and thus (b), (c), and (d) show quantum fluence after the beam has been filtered by 10, 20, and 30 cm (respectively) of water. The open circles illustrate the calculated results, and the solid line in each figure shows the best fit to these data. The fit parameters necessary to generate the best fit equations for all four plots are given in Table IV.

of the x-ray quantum fluence, a large table is available in the EPAPS data set which contains a fairly complete listing of the quantum fluence as a function of kV, HVL, and percent ripple. This data is accessible at the web site address listed in the abstract.

TABLE IV. The analytical fitting functions with fit coefficients for the curves shown in Figs. 13(a)–13(d) are included in this table. The parameter x is the HVL in the units of mm Al, and the parameter y is the photon fluence in units of photons/mm² per mR.

0 cm added water	10 cm added water
$y=a+bx+cx^2+dx^3$	$\ln y=a+bx+cx^{0.5}$
$r^2=0.99324$	$r^2=0.99811$
$a=-8270.266\ 843\ 782\ 573$	$a=+9.223\ 582\ 008\ 093\ 695$
$b=90\ 292.88\ 218\ 322\ 948$	$b=-0.4\ 093\ 659\ 061\ 203\ 211$
$c=-11\ 567.16\ 891\ 240\ 857$	$c=+2.308\ 573\ 244\ 885\ 594$
$d=541.6\ 101\ 860\ 864\ 931$	

20 cm added water	30 cm added water
$\ln y=a+bx\ \ln x+cx^{0.5}$	$y=a+bx+cx^2+dx^3+ex^4$
$r^2=0.99931$	$r^2=0.99968$
$a=9.638\ 685\ 066\ 422\ 506$	$a=24\ 662.65\ 660\ 902\ 052$
$b=-0.08\ 182\ 451\ 868\ 375\ 988$	$b=43\ 476.88\ 985\ 810\ 609$
$c=1.502\ 045\ 158\ 767\ 476$	$c=1557.584\ 762\ 855\ 116$
	$d=-520.1\ 440\ 375\ 910\ 221$
	$e=18.51\ 080\ 477\ 851\ 572$

IV. SUMMARY AND CONCLUSIONS

Spectral models have been used extensively in computer simulations of x-ray interactions and imaging systems. Semi-analytic models such as that of Birch and Marshall[8] and that of Tucker et al.[14,15] have been used particularly in medical imaging simulations and dose calculations in the United States and Europe. The accurate estimation of x-ray spectra is also useful in computed tomography applications, in the correction of beam hardening artifacts. Here we present a method in which measured spectral data were characterized using polynomial expressions, and these expressions can be used to calculate x-ray spectra at any kV. This technique is void of any physical assumptions, and does not require quantification of physical constants. The accuracy of the TASMIP algorithm depends only on the ability of the polynomial interpolating functions to describe the output of a given energy interval as a function of applied kV, as illustrated in Figs. 5(a) and 5(b). The polynomial interpolating functions allow spectra to be computed an any kV from 30 to 140 kV.

Whereas we report here a technique for matching the output characteristics of a specific x-ray tube to a computer-generated spectral model (TASMIP), the likely utility of this work to others lays in simply utilizing the TASMIP computer-generated spectra as is, using the polynomial coefficients derived in this work. The TASMIP algorithm should be considered as a relatively accurate computer-generated

source of unfiltered tungsten anode x-ray spectra.

To facilitate the distribution of the *t*ungsten *a*node *s*pectral *m*odel using *i*nterpolating *p*olynomials (TASMIP) algorithm, the polynomial coefficients and computer code to calculate tungsten anode spectra as reported here are available on EPAPS, an electronic distribution facility maintained by the American Institute of Physics, the publisher of this journal.[29] The Internet address for this web site is http://www.aip.org/epaps/epaps.html. The spectra produced by the C subroutine (available at the web site) match the quality and quantity of the metal-insert x-ray tube (with no added filtration) in our laboratory, and these spectra should be representative of tungsten anode spectra in general. The model was extended in a straightforward manner to include the effect of kV ripple introduced by most x-ray generators, and computer code is also included at the web site to allow the generation of spectra with varying ripple. Added filtration of any type can be included easily using the Lambert Beers law and tabulated x-ray attenuation coefficients.[25] Also included at the web site is a large table relating x-ray quantum fluence to kV, ripple, and HVL.

Although Fewell's x-ray spectra which were used to produce the TASMIP algorithm were measured nearly two decades ago, the physics concerning the production of x-rays has not changed. The fact that the constant potential spectra reported by Fewell was easily adapted to the output characteristics of a modern high-output metal insert x-ray tube in our laboratory is evidence of the high quality of the tabulated Fewell data.

[a]Address for correspondence: Department of Radiology, UC Davis Medical Center, FOLB II E, 2421 45th Street, Sacramento, CA 95817. Electronic-mail: jmboone@ucdavis.edu

[1]H. N. Cardinal, D. W. Holdsworth, M. Drangova, B. B. Hobbs, and A. Fenster, "Experimental and theoretical x-ray imaging performance comparison of iodine and lanthanide contrast agents," Med. Phys. **20**, 15–31 (1993).

[2]C. S. Chen, K. Doi, C. Vyborny, H. P. Chan, and G. Holje, "Monte Carlo simulation studies of detectors used in the measurement of diagnostic x-ray spectra," Med. Phys. **7**, 627–635 (1980).

[3]R. Fahrig and J. Yaffe, "A model for optimization of spectral shape in digital mammography," Med. Phys. **21**, 1463–1471 (1994).

[4]R. Fahrig and M. M. J. Yaffe, "Optimization of spectral shape in digital mammography: Dependence on anode material, breast thickness, and lesion type," Med. Phys. **21**, 1473–1481 (1994).

[5]D. McLean, "Computer model to optimise contrast in chest radiography," Australasian Phys. Eng. Sci. Med. **16**, 179–185 (1993).

[6]M. Sandborg, C. A. Carlsson, and G. A. Carlsson, "Shaping X-ray spectra with filters in X-ray diagnostics," Med. Biol. Eng. Comp. **32**, 384–390 (1994).

[7]H. A. Kramers, "On the theory of x-ray absorption and of the continuous x-ray spectrum," Philos. Mag. **46**, 836–840 (1923).

[8]R. Birch and M. Marshall, "Computation of bremsstrahlung X-ray spectra and comparison with spectra measured with a Ge(Li) detector," Phys. Med. Biol. **24**, 505–517 (1979).

[9]J. P. Bissonnette and L. J. Schreiner, "A comparison of semiempirical models for generating tungsten target x-ray spectra," Med. Phys. **19**, 579–582 (1992).

[10]J. M. Boone, "The three parameter equivalent spectra as an index of beam quality," Med. Phys. **15**, 304–310 (1988).

[11]J. M. Boone, "Equivalent spectra as a measure of beam quality," Med. Phys. **13**, 861–868 (1986).

[12]B. R. Archer, T. R. Fewell, and L. K. Wagner, "Laplace reconstruction of experimental diagnostic x-ray spectra," Med. Phys. **15**, 832–837 (1988).

[13]B. R. Archer and L. K. Wagner, "Determination of diagnostic x-ray spectra with characteristic radiation using attenuation analysis," Med. Phys. **15**, 637–641 (1988).

[14]D. M. Tucker, G. T. Barnes, and X. Z. Wu, "Molybdenum target x-ray spectra: a semiempirical model," Med. Phys. **18**, 402–407 (1991).

[15]D. M. Tucker, G. T. Barnes, and D. P. Chakraborty, "Semiempirical model for generating tungsten target x-ray spectra," Med. Phys. **18**, 211–218 (1991).

[16]T. R. Fewell and R. E. Shuping, "Photon energy distribution of some typical diagnostic x-ray beams," Med. Phys. **4**, 187–197 (1977).

[17]T. R. Fewell, R. E. Shuping, and K. E. Healy, *Handbook of Computed Tomography X-ray Spectra*, HHS Publication (FDA) 81-8162 (U.S. Government Printing Office, Washington, D.C., 1981).

[18]T. R. Fewell and R. E. Shuping, *Handbook of Mammographic X-ray Spectra*, HEW Publication (FDA) 79-8071 (U.S. Government Printing Office, Washington, D.C., 1978).

[19]J. C. Dainty and N. Shibata, *Image Science* (Academic, New York, 1974).

[20]R. M. Nishikawa and M. J. Yaffe, "Model of the spatial-frequency-dependent detective quantum efficiency of phosphor screens," Med. Phys. **17**, 894–904 (1990).

[21]I. A. Cunningham, M. S. Westmore, and A. Fenster, "A spatial-frequency dependent quantum accounting diagram and detective quantum efficiency model of signal and noise propagation in cascaded imaging systems," Med. Phys. **21**, 417–427 (1994).

[22]A. D. Maidment and M. J. Yaffe, "Analysis of the spatial-frequency-dependent DQE of optically coupled digital mammography detectors," Med. Phys. **21**, 721–729 (1994).

[23]D. W. Mah, J. A. Rowlands, and J. A. Rawlinson, "Measurement of quantum noise in fluoroscopic systems for portal imaging," Med. Phys. **23**, 231–238 (1996).

[24]R. M. Nishikawa, M. J. Yaffe, and R. B. Holmes, "Effect of finite phosphor thickness on detective quantum efficiency," Med. Phys. **16**, 773–780 (1989).

[25]J. M. Boone and A. E. Chavez, "Comparison of x-ray cross sections for diagnostic and therapeutic medical physics," Med. Phys. **23**, 1997–2005 (1996).

[26]P. R. Bevington, *Data Reduction and Error Analysis for the Physical Sciences* (McGraw–Hill, New York, 1969).

[27]H. E. Johns and J. R. Cunningham, *The Physics of Radiology* (Thomas, Springfield, IL, 1974).

[28]K. J. Strauss, Radiographic Equipment and Componnets: Technology overview and Quality Improvement, in *Syllabus: A categorical course in physics—technology update and quality improvement of diagnostic x-ray imaging equipment,* edited by R. G. Gould and J. M. Boone (RSNA, Oak Brook, IL, 1996).

[29]See AIP Document No. E-PAPS: E-MPHYA-24-1661 for the TASMIP algorithm and ancillary data. E-PAPS document files may be retrieved free of charge from our FTP server (http://www.aip.org/epaps/epaps.html) or from ftp.aip.org in the directory/epaps/. For further information: e-mail: paps@aip.org or fax: 516-576-2223.

Molybdenum, rhodium, and tungsten anode spectral models using interpolating polynomials with application to mammography

John M. Boone[a)]
Department of Radiology, University of California, Davis, UC Davis Medical Center, Sacramento, California 95817

Thomas R. Fewell and Robert J. Jennings
Center for Devices in Radiological Health HFZ-142, Food and Drug Administration, 12720 Twinbrook Parkway, Rockville, Maryland 20857

Computer simulation is a convenient and frequently used tool in the study of x-ray mammography, for the design of novel detector systems, the evaluation of dose deposition, x-ray technique optimization, and other applications. An important component in the simulation process is the accurate computer-generation of x-ray spectra. A computer model for the generation of x-ray spectra in the mammographic energy range from 18 kV to 40 kV has been developed. The proposed model requires no assumptions concerning the physics of x-ray production in an x-ray tube, but rather makes use of x-ray spectra recently measured experimentally in the laboratories of the Center for Devices and Radiological Health. Using x-ray spectra measured for molybdenum, rhodium, and tungsten anode x-ray tubes at 13 different kV's (18, 20, 22,...,42 kV), a spectral model using interpolating polynomials was developed. At each energy in the spectrum, the x-ray photon fluence was fit using 2, 3, or 4 term (depending on the energy) polynomials as a function of the applied tube voltage (kV). Using the polynomial fit coefficients determined at each 0.5 keV interval in the x-ray spectrum, accurate x-ray spectra can be generated for any arbitrary kV between 18 and 40 kV. Each anode material (Mo, Rh, W) uses a different set of polynomial coefficients. The molybdenum anode spectral model using interpolating polynomials is given the acronym MASMIP, and the rhodium and tungsten spectral models are called RASMIP and TASMIP, respectively. It is shown that the mean differences in photon fluence calculated over the energy channels and over the kV range from 20 to 40 kV were -0.073% ($\sigma = 1.58\%$) for MASMIP, -0.145% ($\sigma = 1.263\%$) for RASMIP, and 0.611% ($\sigma = 2.07\%$) for TASMIP. The polynomial coefficients for all three models are given in an Appendix. A short C subroutine which uses the polynomial coefficients and generates x-ray spectra based on the proposed model is available on the World Wide Web at http://www.aip.org/epaps/epaps.html. © *1997 American Association of Physicists in Medicine.* [S0094-2405(97)02512-1]

Key words: x-ray production, x-ray spectrum, mammography, computer simulation, computer modeling

INTRODUCTION

Computer models for generating realistic polyenergetic x-ray spectra are an important aspect of computer simulation in medical imaging. Computer-generated spectra in mammography applications are used to calculate x-ray doses to the breast,[1] for optimizing techniques in mammography,[2–4] and for evaluating detector performance.[5,6] Many techniques have been developed or used for generating tungsten anode x-ray spectra in the diagnostic range[7–16] and in the therapeutic energy realm;[17,18] however, the spectral model of Tucker *et al.*[19] stands alone for computer-generating molybdenum spectra used routinely in mammography.

Fewell *et al.* has been involved in the physical measurement of x-ray spectra for over two decades, and has published many measured spectra[20–22] over the years. Fewell *et al.* have reported measured x-ray spectra for mammography,[21] and while these measured data are excellent resources and serve as the gold standard for comparing

spectral models, they are measured at slightly coarser intervals that one would like for computer modeling and simulation purposes. The experimentally determined spectra used here for computer parametrization were measured recently (1996) by Fewell, and the specific details of the measurement procedure have been reported previously.[20–22] Publication of the more recent spectral data used in this work is expected.[23]

A technique in which measured spectra are parameterized using polynomial interpolation of spectral data is presented. The polynomial interpolation is not to the photon fluence versus spectral energy, as discussed previously by others.[16] The technique does not require or utilize any physical assumptions concerning x-ray production; rather, it is completely based on recently acquired mammography-energy x-ray spectra measured by Fewell and colleagues in the spectroscopic laboratories of the Center for Devices in Radiological Health. The technique presented is capable of pro-

ducing realistic polyenergetic x-ray spectra at any kV be-
tween 18 kV and 40 kV inclusive, for molybdenum,
rhodium, and tungsten anodes. Additional spectral shaping
by elemental filters such as molybdenum or rhodium, which
is routine in mammography systems used clinically, can be
applied to the raw spectra produced by the model using the
energy-dependent Lambert–Beers law with appropriate at-
tenuation coefficients.[24] The software used to produce mam-
mographic spectra, which is contained in a single C subrou-
tine, is available on the World Wide Web at: http://
www.aip.org/epaps/epaps.html.

METHODS

Spectral measurements

   X-ray spectra were measured in the x-ray spectroscopic
laboratories of the Medical Imaging and Computer Applica-
tions Branch at the Center for Devices and Radiological
Health. A high frequency inverter x-ray generator (Tran-
sworld X-ray Corporation) was used to power the three dif-
ferent x-ray tubes used during the spectral measurements.
This generator was modified to provide both negative and
positive ground, to accommodate different tube designs. The
high frequency inverter generator is what is used in virtually
all modern mammography systems, so the generator wave-
form used during the measurement of the x-ray spectra is
comparable to most clinical mammography systems. Each
x-ray tube had approximately 0.5 mm of beryllium as the
x-ray tube window, but no other added filtration was used in
the measurements. The rhodium x-ray spectra were gener-
ated by an x-ray tube supplied by General Electric Corpora-
tion (tube housing model: Statorix M52, x-ray tube model:
GS412-49); this is the same tube used in the Senographe
DMR unit. The molybdenum anode and tungsten anode x-
ray tubes were both manufactured by Eureka X-ray Tube,
Inc., and had identical model numbers (model Mam Rad
100, Insert 71HR).

   The experimentally determined spectra used to develop
the models reported here were measured relatively recently;
however, the techniques for making these measurements are
similar to the measurement methods and stripping protocols
described elsewhere.[20–22] The spectra used here were pro-
duced from 18 kV to 42 kV at even kV settings (e.g., 18, 20,
22,...,42 kV), for three different x-ray tubes employing mo-
lybdenum, rhodium, and tungsten anodes. The spectra were
essentially normalized to constant mAs. A high purity ger-
manium detector coupled to a multichannel analyzer was
used, with calibrated energy channels of 100 eV. For the
molybdenum and the tungsten anodes, the measured x-ray
spectra were rebinned into 500 eV intervals starting at 0.5
kV, with energy bins centered at 0.5, 1.0, 1.5, 2.0, 2.5,...,50.0
keV. For the rhodium anode x-ray tube, spectra were also
rebinned into 500 eV intervals; however, these bins started at
0.2 keV, with energy bins centered at 0.2, 0.7, 1.2,
1.7,...,49.7 keV. This rebinning difference was designed to
best accommodate the energies of the characteristic x-ray
lines, in terms of how they fell into the individual energy
channels or "bins."
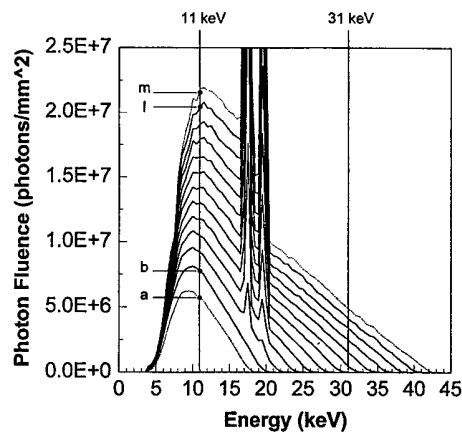
FIG. 1. A graphical description of the MASMIP procedure is presented. The
13 measured molybdenum anode spectra are shown. The 18 kV and 42 kV
spectra are shown with dotted lines, for reference. The spectra were mea-
sured at even kV's from 18 kV through 42 kV, with no added filtration in
the x-ray beam. Each spectrum was normalized in terms of area to corre-
spond to a constant mAs setting on the x-ray machine. The vertical line at 11
keV intersects 13 photon fluence values, one at each kV. The polynomial
interpolation procedure presented performs the x-ray photon fluence inter-
polation essential along vertical lines such as those illustrated at 11 keV and
31 keV. At 31 keV, fewer spectra contribute nonzero fluence values to the
polynomial fit because this energy is above the accelerating voltage (and
resulting x-ray emission energies) for the 18–30 kV spectra. The fluence
values intersecting the two vertical lines are illustrated in Fig. 2 as a func-
tion of kV. The individual points a, b, l, and m marked on this figure
correspond to the fluence data for the 18, 20, 40, and 42 kV spectra, and
these data points are also shown in Fig. 2A.

Spectral interpolation technique

   The technique for interpolating the spectra is identical for
all three anode materials, so it will be described only for the
molybdenum anode spectrum. Let $\Phi(E,V)$ represent the
photon fluence (photons/mm^2) at energy E when a voltage V
is applied to the x-ray tube. At each energy "bin" (0.5 keV
intervals were used), a polynomial function was defined as

$$\Phi(E,V) = a_0[E] + a_1[E]V + a_2[E]V^2 + a_3[E]V^3. \quad (1)$$

The coefficient arrays $a_0[E]$, $a_1[E]$, $a_2[E]$, and $a_3[E]$ de-
fine the polynomial coefficients for each anode material, for
the 85 values of E from 0.0 and 42.5 keV. These arrays are
all that is needed to generate x-ray spectra over the interval
(0–42.5 keV) at any kV value from 18 kV to 42 kV, includ-
ing all noninteger kV values as well. The coefficient values
$a_0[E]-a_3[E]$ were solved for using the experimentally mea-
sured spectra. Thirteen measured x-ray spectra $\Phi(E,V)$ mea-
sured at known, even kV's ranging from 18 to 42 kV were
used to solve for the polynomial coefficients at each energy
bin. The polynomial routine POLFIT from Bevington[25] was
converted to C from FORTRAN and used to determine the
polynomial coefficients.

   The method is demonstrated graphically in Figs. 1 and 2.
The 13 raw molybdenum x-ray spectra are illustrated in Fig.
1. Each measured spectra was normalized to a constant mAs
setting, and the photon fluence increases as expected at each
energy interval with increasing voltage (kV) applied across
the x-ray tube. For a given energy E, for example at 11 keV,
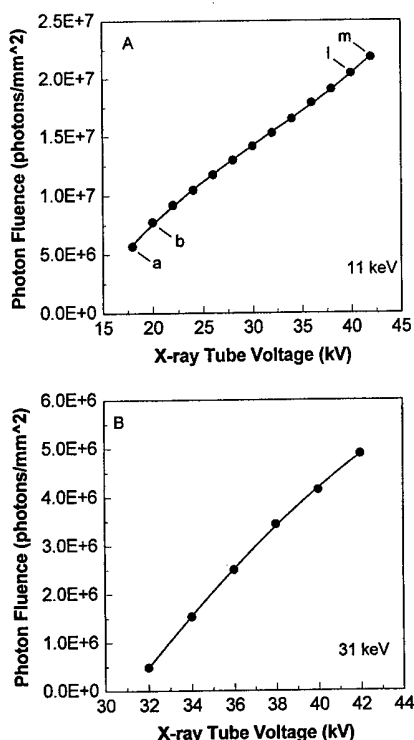
FIG. 2. In Fig. 1, two vertical lines corresponding to 11 keV and 31 keV were shown intersecting the plotted x-ray spectra. In this figure, the x-ray photon fluence values are plotted (solid circles) as a function of the kV of the corresponding spectrum. At 11 keV (Fig. 2A), 13 fluence kV data points are shown, and the indicated points at a, b, l, and m correspond to the fluence values illustrated in Fig. 1. At 31 keV, only six fluence kV points are shown for reasons discussed in the text. The measured data points were fit to polynomials and the fit coefficients were used to generate the interpolated data (solid lines, both A and B plot). For any arbitrary kV between 18 and 40 kV, the polynomial coefficients were used at each energy in the spectrum to calculate the photon fluence at that energy.

the vertical line shown in Fig. 1 intersects all 13 spectra. These intersection points (points a, b, l, and m are labeled) define values of $\Phi(E,V)$. These 13 values of $\Phi(E,V)$, coupled with the 13 known kV values (V), are the data required to solve for the polynomial coefficients $a_0[11]$, $a_1[11]$, $a_2[11]$ and $a_3[11]$. In Fig. 2A, the 13 measured $\Phi(E,V)$ values are plotted as solid circles as a function of tube voltage V, with the corresponding points a, b, l, and m, labeled in Fig. 1, shown here as well. The polynomial coefficients a_0-a_3 given in Eq. (1) were solved for, and these coefficients were used to generate the solid line also shown in Fig. 2A. This solid line defines the interpolated values of $\Phi(E,V)$ for kV's ranging from 18 to 42 kV.

As the energy of the bin increases, the number of photon fluence values defined at that bin decreases. For example, at 31 kV, only the spectra generated at 32, 34, 36, 38, 40, and 42 kV generate x-ray photons with 31 keV of energy. The lower kV values (30 kV and below) produce exactly zero x-ray photons at 31 keV. Thus the vertical line shown in Fig. 1 at 31 kV intersects only six spectra. The photon fluence versus kV data at 31 keV is shown in Fig. 2B, along with the polynomial-interpolated data. As the number of data points available for the polynomial fit gradually dwindle at higher

kV's, the order of the polynomial was gradually reduced to accommodate the degree-of-freedom constraints of the polynomial fit routine. A simple algorithm for reducing the number of polynomial fitting terms N_{terms} was arrived at empirically. This algorithm determined the highest order polynomial (ranging from just 2 to 4 terms) for the polynomial fit at each energy; however, the polynomial orders from 2 to 4 were fit and the χ^2 value was used to select the number of polynomial terms that resulted in a best fit at each energy. The polynomial interpolation is combined with a constraint that the result cannot be less than zero, and if it is, the fluence value for that energy is set to zero. In addition to these automated measures, the polynomial fit was monitored using interactive custom graphical software which allowed real time "quality assurance" of the computer fit (the polynomial order could be changed interactively). This was found to be a necessary component of developing the model, since higher order polynomials can sometimes yield good fits (lower χ^2 values), but suffer from oscillations between measured data points.

The polynomial interpolation technique described here generates not only the shape of the spectra; the kV-dependent photon fluence results from the polynomial fit and is a feature of the model as well. In other words, the model produces spectra accurate both in terms of *quality* and *quantity*. The model described here is really three different models; one for each anode material. For ease of reference, the molybdenum anode spectral model using interpolating polynomials was given the acronym MASMIP; RASMIP and TASMIP corresponding to the rhodium and tungsten anode models, respectively.

RESULTS AND DISCUSSION

Figure 3A illustrates the polynomial fit results (solid lines) in bins centered about 0.5 keV intervals, from 4.5 keV to 38.5 keV, along with the measured data (solid circles), for molybdenum. This composite plot of 35 different curves shows the normalized photon fluence as the ordinate, and the x-ray tube kilovoltage as the abscissa spanning from 15 keV to 45 keV in each panel. While most of the curves have a convex shape, the curves at 17.5 and 19.5 keV show distinctly concave profiles. These profiles correspond to the characteristic K-shell emissions for molybdenum at 17.4 and 19.6 keV. Those channels having characteristic emission include both bremsstrahlung and characteristic emissions, and the concavity would seem to be a consequence of increased characteristic yield with higher applied kilovoltage.

A composite plot for rhodium is shown in Fig. 3B, illustrating the energy channels from 4.2 to 38.2 keV. In this figure, the convex-upward curves are seen at 20.2 and 23.2 keV, corresponding to the characteristic x-ray emission energies of rhodium at 20.2 and 22.7 keV. The composite plots for tungsten are shown in Fig. 3C. For the tungsten anode, the K-characteristic lines are never realized at these kV's, however multiple L characteristic radiations are present in these spectra. There are about 30 possible emission lines for tungsten between 7.6 and 12.06 keV. These L characteristic
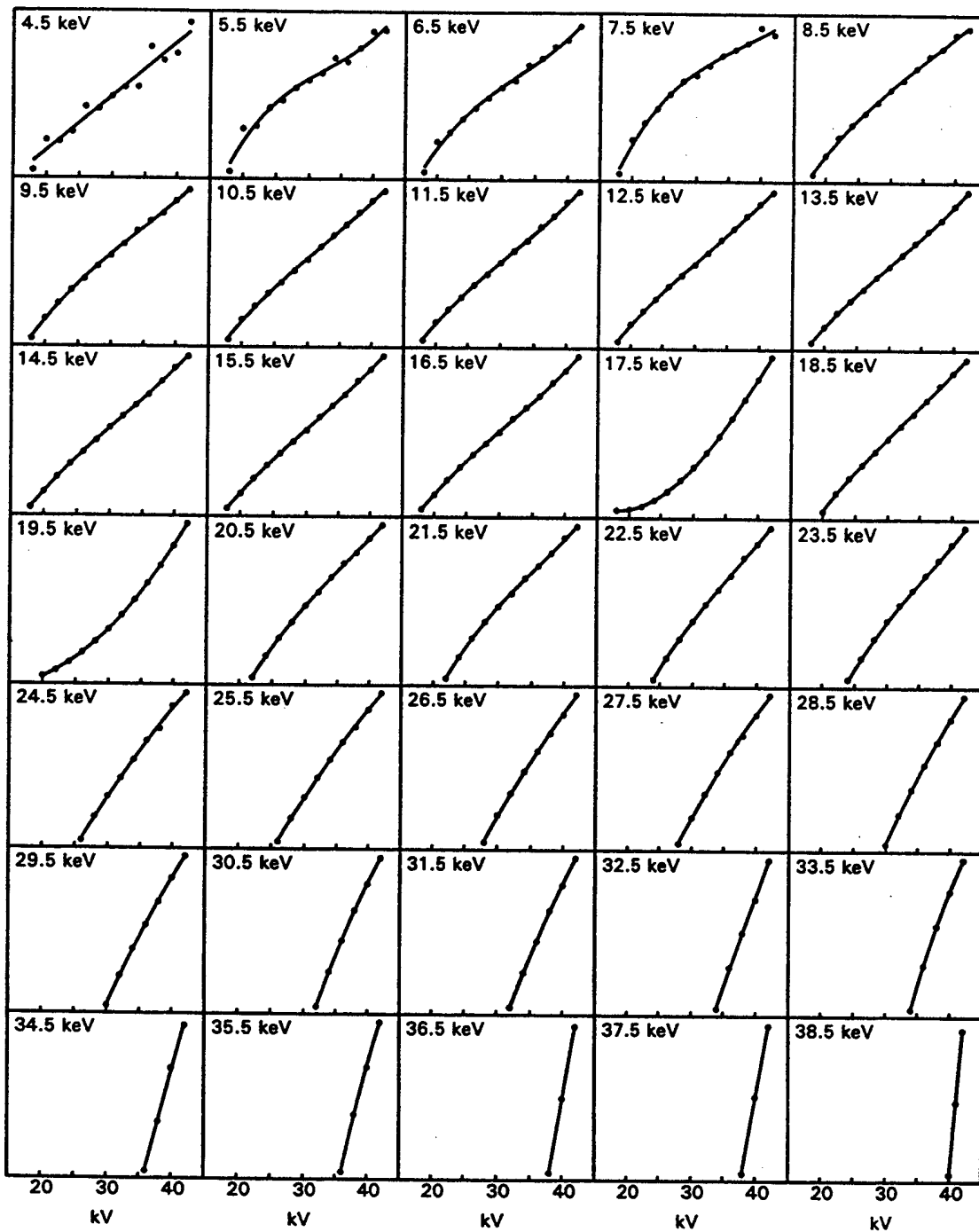
(a)

FIG. 3. The measured spectral data points are illustrated as solid circles, and the interpolated results are shown as the solid lines, for molybdenum spectra (A), rhodium spectra (B), and tungsten spectra (C). In each figure, 35 different curves at different energies spanning the mammography energy spectrum are shown to illustrate *en masse* the quality of the polynomial fit to the measured data. The curves at each energy indicated illustrate the increase in x-ray photon fluence (at that energy) as a function of the applied voltage of the x-ray tube, at constant milliAmpere seconds. For the individual curves near the K-emission lines of molybdenum (the 17.5 keV and 19.5 keV curves in A) and rhodium (20.2 keV in B) show a different shape as a result of the characteristic x-ray emission at those energies.

lines do not result in convex-upward curves as with the *K* emission lines of molybdenum or rhodium.

Figure 4A illustrates the measured molybdenum x-ray spectra (dashed lines) compared graphically with the MAS-MIP generated spectra (solid lines). Excellent agreement be-

tween the measured and computer generated spectra is observed. Similar agreement is seen with the rhodium spectra compared in Fig. 4B. The tungsten spectra seen in Fig. 4C compare very well with each other, however not as well as the molybdenum or rhodium spectra. Perhaps a more mean-
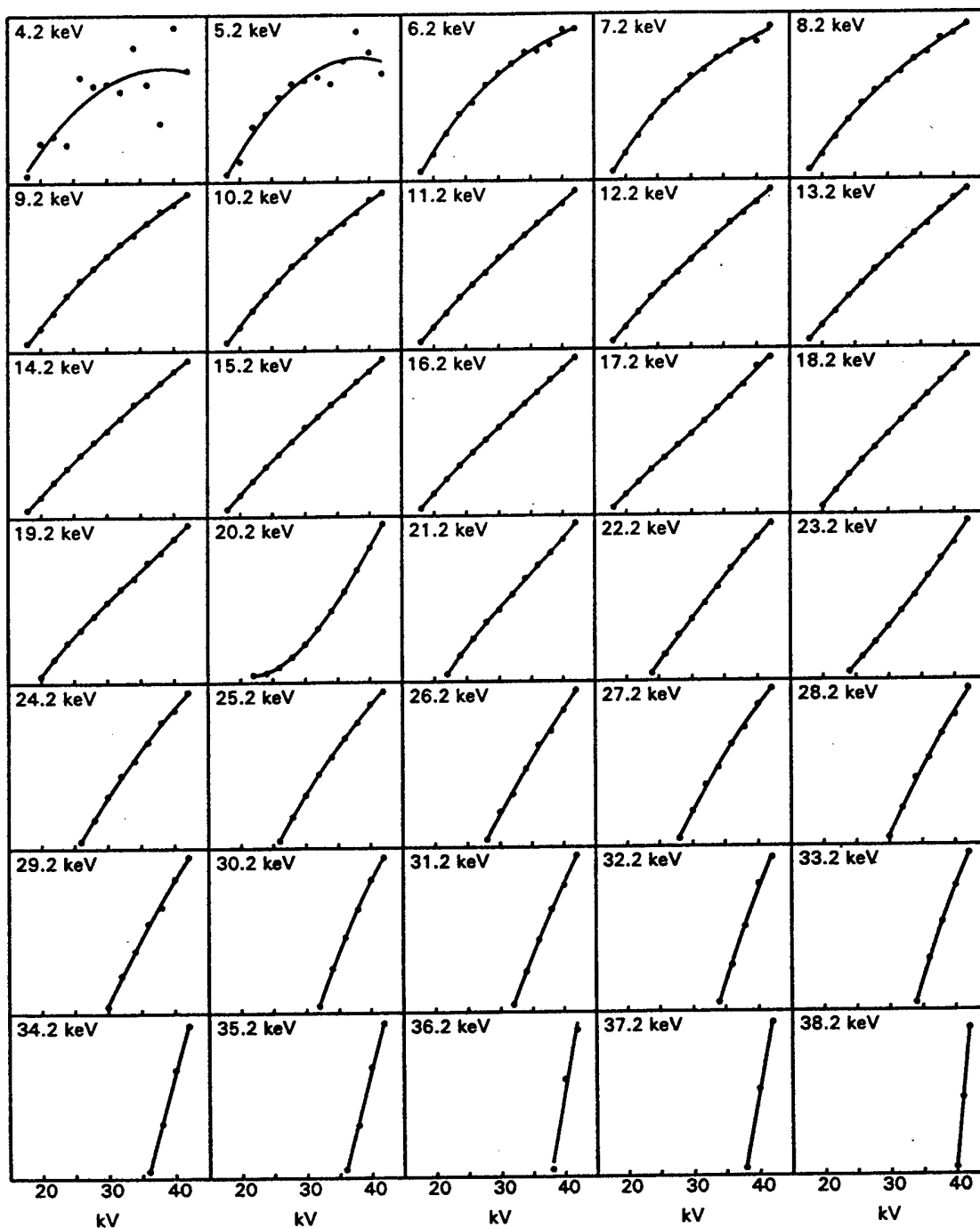
(b)

FIG. 3 (*Continued.*)

ingful measure of the correspondence between the measured and the modeled spectra is a histogram of the percent errors as shown in Fig. 5. The percent difference (or "error") between the measured x-ray spectrum and the modeled spectrum was calculated for each data point (at each 0.5 keV interval). Photon fluence values below 5% of the maximum amplitude were omitted from this analysis, because they contribute little to the total photon fluence and with these smaller fluence values, small absolute differences can result in large percent errors. Figure 5A shows a histogram of these error values for all the points (>5% of peak) in the molybdenum spectra ranging from 18 to 40 kV combined. It is seen that the differences between the measured and the modeled spectra are quite small, with 50% of all comparison points falling within about 0.5% error, and 90% of all the points having an error less than 2.5%. For rhodium the combined spectra (18–40 kV) errors are also quite small (Fig. 5B), with 50% of the comparison data points at or below a 0.6%
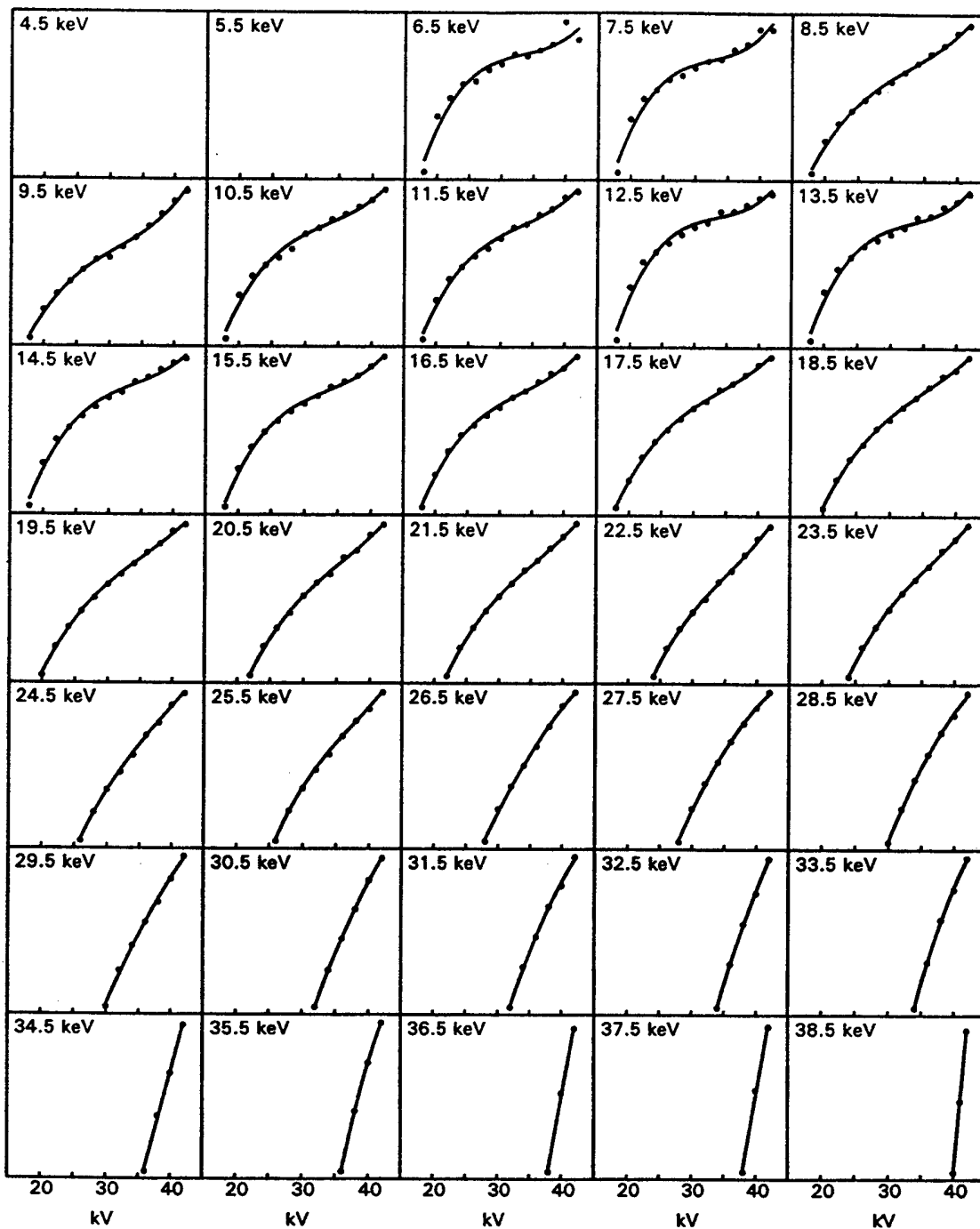
(c)

FIG. 3 (Continued.)

difference, and 90% of the data points fall below an error of 2%. The error histogram for the tungsten spectra (Fig. 5C) shows a much broader histogram, with 50% of the data points falling less than 1.3% error and 90% of the data points falling below 6% error. The poorer performance of the TAS-MIP model compared to the MASMIP and RASMIP models is probably related to the complex distribution (>30 different L-emission lines) of x-ray emission in the 7 keV–12 keV energy range, and the resulting complexity of fitting these

kV-dependent photon fluences with simple polynomials. If the lower (18, 20, 22, and 24 kV) tungsten spectra are eliminated from the histogram analysis, then 50% of the points fall below 2%, and 90% of points fall below 3.5% error levels. Since tungsten spectra for mammography would only be used clinically at higher kV's and with added filtration, the small errors at the lower kV's have little practical affect on computer modeling. In terms of parametric statistics, the mean differences in photon fluence calculated over all energy

TABLE I. Polynomial coefficients for the molybdenum anode x-ray tube (MASMIP). At each energy bin E, the photon fluence (photons/mm^2) at a given kV is given by: $\Phi(\text{photons/mm}^2) = a_0 + a_1 \times kV + a_2 \times kV^2 + a_3 \times kV^3$.

Energy (keV)	a_0	a_1	a_2	a_3
3.5	+0.000000e+000	+0.000000e+000	+0.000000e+000	+0.000000e+000
4.0	-1.444468e+004	+1.505384e+004	+0.000000e+000	+0.000000e+000
4.5	-2.157610e+004	+1.756251e+004	+0.000000e+000	+0.000000e+000
5.0	-1.069419e+006	+1.569301e+005	-4.043083e+003	+3.914996e+001
5.5	-3.062868e+006	+4.184705e+005	-1.177408e+004	+1.196206e+002
6.0	-4.916993e+006	+6.789471e+005	-1.904982e+004	+1.963841e+002
6.5	-6.925022e+006	+9.227469e+005	-2.431684e+004	+2.485349e+002
7.0	-9.240879e+006	+1.197607e+006	-3.016570e+004	+2.894177e+002
7.5	-1.196409e+007	+1.506369e+006	-3.734140e+004	+3.358694e+002
8.0	-1.433777e+007	+1.725903e+006	-4.149616e+004	+4.076118e+002
8.5	-1.346037e+007	+1.602853e+006	-3.417208e+004	+3.197254e+002
9.0	-1.703271e+007	+1.992354e+006	-4.714275e+004	+4.732125e+002
9.5	-1.735496e+007	+1.964368e+006	-4.346886e+004	+4.179785e+002
10.0	-1.806311e+007	+2.014349e+006	-4.465826e+004	+4.502301e+002
10.5	-1.680020e+007	+1.840469e+006	-3.830591e+004	+3.793459e+002
11.0	-2.131791e+007	+2.320385e+006	-5.571021e+004	+5.947650e+002
11.5	-1.837808e+007	+1.941591e+006	-4.164300e+004	+4.369608e+002
12.0	-1.984031e+007	+2.051260e+006	-4.550193e+004	+4.825815e+002
12.5	-1.868657e+007	+1.856300e+006	-3.785170e+004	+3.944230e+002
13.0	-2.294681e+007	+2.290842e+006	-5.356084e+004	+5.760982e+002
13.5	-2.231694e+007	+2.181380e+006	-5.004156e+004	+5.412009e+002
14.0	-2.281241e+007	+2.182148e+006	-4.982511e+004	+5.395803e+002
14.5	-2.223463e+007	+2.055223e+006	-4.472059e+004	+4.753687e+002
15.0	-2.138391e+007	+1.910704e+006	-3.956225e+004	+4.187863e+002
15.5	-2.183426e+007	+1.905475e+006	-3.938379e+004	+4.207844e+002
16.0	-2.210670e+007	+1.880798e+006	-3.838533e+004	+4.106319e+002
16.5	-2.341731e+007	+1.966213e+006	-4.140524e+004	+4.524618e+002
17.0	+4.410687e+006	-1.228638e+006	+5.956400e+004	-1.509388e+002
17.5	+2.393001e+008	-2.799296e+007	+9.214276e+005	-5.792732e+003
18.0	-1.687220e+007	+1.111509e+006	-1.417979e+004	+2.537656e+002
18.5	-2.685072e+007	+2.144921e+006	-4.691376e+004	+4.874623e+002
19.0	-3.181105e+007	+2.602798e+006	-6.209036e+004	+6.590199e+002
19.5	+3.735285e+006	-1.520292e+006	+6.688979e+004	+0.000000e+000
20.0	-7.801074e+006	-3.623279e+004	+2.136239e+004	+0.000000e+000
20.5	-2.607519e+007	+1.984240e+006	-4.278393e+004	+3.803342e+002
21.0	-3.235224e+007	+2.581614e+006	-6.219627e+004	+5.856532e+002
21.5	-2.883215e+007	+2.182060e+006	-4.876334e+004	+4.424922e+002
22.0	-2.762892e+007	+2.061974e+006	-4.578730e+004	+4.210210e+002
22.5	-3.111678e+007	+2.317619e+006	-5.247238e+004	+4.795377e+002
23.0	-2.692913e+007	+1.845917e+006	-3.656864e+004	+3.073399e+002
23.5	-3.602581e+007	+2.706274e+006	-6.425582e+004	+5.998871e+002
24.0	-2.948700e+007	+2.084902e+006	-4.552940e+004	+4.157864e+002
24.5	-1.634090e+007	+7.942274e+005	-4.991084e+003	+0.000000e+000
25.0	-1.891984e+007	+9.291174e+005	-6.896883e+003	+0.000000e+000
25.5	-1.813234e+007	+8.642746e+005	-5.958818e+003	+0.000000e+000
26.0	-1.772540e+007	+8.280173e+005	-5.458039e+003	+0.000000e+000
26.5	-1.908858e+007	+8.867837e+005	-6.205095e+003	+0.000000e+000
27.0	-5.870978e+007	+4.326653e+006	-1.055765e+005	+9.471267e+002
27.5	-1.951479e+007	+8.763217e+005	-5.994696e+003	+0.000000e+000
28.0	-1.873200e+007	+8.200074e+005	-5.262214e+003	+0.000000e+000
28.5	-1.988762e+007	+8.638795e+005	-5.760048e+003	+0.000000e+000
29.0	-1.989074e+007	+8.507146e+005	-5.634714e+003	+0.000000e+000
29.5	-2.091310e+007	+8.944657e+005	-6.235000e+003	+0.000000e+000
30.0	-1.976925e+007	+8.214290e+005	-5.284905e+003	+0.000000e+000
30.5	-2.486637e+007	+1.079714e+006	-8.691732e+003	+0.000000e+000
31.0	-2.916641e+007	+1.297188e+006	-1.158454e+004	+0.000000e+000
31.5	-2.523419e+007	+1.069977e+006	-8.528449e+003	+0.000000e+000
32.0	-2.576746e+007	+1.095557e+006	-8.985011e+003	+0.000000e+000
32.5	-1.388773e+007	+4.327039e+005	+0.000000e+000	+0.000000e+000
33.0	-2.630931e+007	+1.076203e+006	-8.433643e+003	+0.000000e+000
33.5	-3.190475e+007	+1.368707e+006	-1.241636e+004	+0.000000e+000
34.0	-2.139757e+007	+7.921584e+005	-4.691571e+003	+0.000000e+000
34.5	-1.498973e+007	+4.408404e+005	+0.000000e+000	+0.000000e+000
35.0	-3.664991e+007	+1.552772e+006	-1.441075e+004	+0.000000e+000
35.5	-3.575070e+007	+1.494224e+006	-1.368656e+004	+0.000000e+000
36.0	-2.285521e+007	+8.235004e+005	-5.143063e+003	+0.000000e+000
36.5	-1.491104e+007	+4.134720e+005	+0.000000e+000	+0.000000e+000
37.0	-1.569037e+007	+4.286760e+005	+0.000000e+000	+0.000000e+000
37.5	-1.571175e+007	+4.220360e+005	+0.000000e+000	+0.000000e+000
38.0	-1.559272e+007	+4.143320e+005	+0.000000e+000	+0.000000e+000
38.5	-1.597894e+007	+4.182650e+005	+0.000000e+000	+0.000000e+000
39.0	-1.646647e+007	+4.259945e+005	+0.000000e+000	+0.000000e+000
39.5	-1.809636e+007	+4.597110e+005	+0.000000e+000	+0.000000e+000
40.0	-1.676175e+007	+4.227545e+005	+0.000000e+000	+0.000000e+000
40.5	-1.980247e+007	+4.895522e+005	+0.000000e+000	+0.000000e+000
41.0	-2.153375e+007	+5.258515e+005	+0.000000e+000	+0.000000e+000
41.5	-2.594940e+007	+6.260341e+005	+0.000000e+000	+0.000000e+000
42.0	-1.435279e+008	+3.420986e+006	+0.000000e+000	+0.000000e+000
42.5	-1.435279e+008	+3.420986e+006	+0.000000e+000	+0.000000e+000
43.0	-1.435279e+008	+3.420986e+006	+0.000000e+000	+0.000000e+000
43.5	-1.435279e+008	+3.420986e+006	+0.000000e+000	+0.000000e+000
44.0	-1.435279e+008	+3.420986e+006	+0.000000e+000	+0.000000e+000
44.5	-1.435279e+008	+3.420986e+006	+0.000000e+000	+0.000000e+000
45.0	-1.435279e+008	+3.420986e+006	+0.000000e+000	+0.000000e+000
45.5	-1.435279e+008	+3.420986e+006	+0.000000e+000	+0.000000e+000

TABLE II. Polynomial coefficients for the rhodium anode x-ray tube (RASMIP). At each energy bin E, the photon fluence (photons/mm^2) at a given kV is given by: $\Phi(\text{photons/mm}^2) = a_0 + a_1 \times kV + a_2 \times kV^2 + a_3 \times kV^3$.

Energy (keV)	a_0	a_1	a_2	a_3
3.7	+0.000000e+000	+0.000000e+000	+0.000000e+000	+0.000000e+000
4.2	-1.192045e+005	+1.367483e+004	-1.778029e+002	+0.000000e+000
4.7	-1.530890e+005	+2.993084e+004	-3.532862e+002	+0.000000e+000
5.2	-4.149003e+005	+8.345416e+004	-1.083803e+003	+0.000000e+000
5.7	-2.110957e+006	+3.086459e+005	-6.845642e+003	+5.278299e+001
6.2	-2.895965e+006	+4.286116e+005	-8.011144e+003	+5.426242e+001
6.7	-5.555697e+006	+7.440265e+005	-1.642142e+004	+1.359430e+002
7.2	-6.230149e+006	+8.173703e+005	-1.611456e+004	+1.222256e+002
7.7	-6.721657e+006	+8.681462e+005	-1.532193e+004	+1.103395e+002
8.2	-9.068231e+006	+1.096678e+006	-2.023126e+004	+1.549885e+002
8.7	-8.560903e+006	+1.021060e+006	-1.534351e+004	+9.531149e+001
9.2	-9.932459e+006	+1.131318e+006	-1.756427e+004	+1.235573e+002
9.7	-8.539150e+006	+9.150594e+005	-7.607820e+003	+0.000000e+000
10.2	-1.230498e+007	+1.299176e+006	-2.007492e+004	+1.400943e+002
10.7	-1.258838e+007	+1.281049e+006	-1.888631e+004	+1.459051e+002
11.2	-1.117718e+007	+1.123389e+006	-1.388007e+004	+9.606536e+001
11.7	-1.341985e+007	+1.322989e+006	-2.081445e+004	+1.790645e+002
12.2	-1.165702e+007	+1.092111e+006	-1.302265e+004	+9.547466e+001
12.7	-9.828931e+006	+8.537916e+005	-4.495113e+003	+0.000000e+000
13.2	-1.315013e+007	+1.166460e+006	-1.522815e+004	+1.211643e+002
13.7	-1.055732e+007	+8.516584e+005	-4.450458e+003	+0.000000e+000
14.2	-1.226238e+007	+9.997632e+005	-9.875705e+003	+6.619936e+001
14.7	-1.138493e+007	+8.582543e+005	-4.631944e+003	+0.000000e+000
15.2	-1.421375e+007	+1.145459e+006	-1.533291e+004	+1.259442e+002
15.7	-9.209721e+006	+5.087933e+005	+8.598628e+003	-1.587797e+002
16.2	-1.549092e+007	+1.206348e+006	-1.766176e+004	+1.532736e+002
16.7	-1.932713e+007	+1.607190e+006	-3.258084e+004	+3.306037e+002
17.2	-1.655464e+007	+1.245415e+006	-2.068765e+004	+2.442210e+002
17.7	-1.425125e+007	+9.396121e+005	-9.776435e+003	+1.238981e+002
18.2	-1.815094e+007	+1.364727e+006	-2.403874e+004	+2.285077e+002
18.7	-1.216617e+007	+7.156276e+005	-2.695818e+003	+0.000000e+000
19.2	-2.145288e+007	+1.616216e+006	-3.195334e+004	+3.094406e+002
19.7	-2.414743e+006	-3.452748e+005	+2.379756e+004	+0.000000e+000
20.2	+3.003396e+008	-3.075391e+007	+9.339644e+005	-7.017946e+003
20.7	+5.462775e+006	-1.213200e+006	+5.677435e+004	-4.994289e+002
21.2	-2.351651e+007	+1.690655e+006	-3.414655e+004	+3.187491e+002
21.7	-2.467444e+007	+1.753499e+006	-3.541516e+004	+3.220338e+002
22.2	-1.450545e+007	+7.268329e+005	-3.060708e+003	+0.000000e+000
22.7	+3.578927e+007	-4.382693e+006	+1.475727e+005	-1.066008e+003
23.2	-1.096621e+007	+3.159859e+005	+6.759924e+003	+0.000000e+000
23.7	-1.482286e+007	+7.697687e+005	-5.920930e+003	+0.000000e+000
24.2	-1.353926e+007	+6.892985e+005	-4.922390e+003	+0.000000e+000
24.7	-1.585640e+007	+8.193523e+005	-6.915169e+003	+0.000000e+000
25.2	-2.091730e+007	+1.281929e+006	-2.166006e+004	+1.561249e+002
25.7	-1.682020e+007	+8.387164e+005	-7.058292e+003	+0.000000e+000
26.2	-1.371139e+007	+6.412199e+005	-4.135089e+003	+0.000000e+000
26.7	-1.317428e+007	+5.910486e+005	-3.312845e+003	+0.000000e+000
27.2	-1.527150e+007	+7.058618e+005	-5.108053e+003	+0.000000e+000
27.7	-1.893962e+007	+8.966009e+005	-7.635881e+003	+0.000000e+000
28.2	-1.501063e+007	+6.731629e+005	-4.715857e+003	+0.000000e+000
28.7	-1.677653e+007	+7.439650e+005	-5.437238e+003	+0.000000e+000
29.2	-1.554349e+007	+6.616319e+005	-4.284524e+003	+0.000000e+000
29.7	-2.030067e+007	+9.246585e+005	-8.056714e+003	+0.000000e+000
30.2	-2.059148e+007	+9.300864e+005	-8.139347e+003	+0.000000e+000
30.7	-1.812410e+007	+7.722229e+005	-5.847742e+003	+0.000000e+000
31.2	-1.698671e+007	+7.030718e+005	-4.949130e+003	+0.000000e+000
31.7	-1.091269e+007	+3.485818e+005	+0.000000e+000	+0.000000e+000
32.2	-1.862237e+007	+7.666374e+005	-5.758571e+003	+0.000000e+000
32.7	-1.053842e+007	+3.292848e+005	+0.000000e+000	+0.000000e+000
33.2	-2.136943e+007	+8.979092e+005	-7.560643e+003	+0.000000e+000
33.7	-1.962580e+007	+7.851751e+005	-5.951071e+003	+0.000000e+000
34.2	-1.086196e+007	+3.225121e+005	+0.000000e+000	+0.000000e+000
34.7	-2.630957e+007	+1.132011e+006	-1.068638e+004	+0.000000e+000
35.2	-1.119069e+007	+3.212166e+005	+0.000000e+000	+0.000000e+000
35.7	-1.796286e+007	+6.417951e+005	-3.830313e+003	+0.000000e+000
36.2	-1.129583e+007	+3.160500e+005	+0.000000e+000	+0.000000e+000
36.7	-1.254071e+007	+3.441640e+005	+0.000000e+000	+0.000000e+000
37.2	-1.238993e+007	+3.357620e+005	+0.000000e+000	+0.000000e+000
37.7	-1.180338e+007	+3.155950e+005	+0.000000e+000	+0.000000e+000
38.2	-9.228471e+006	+2.500255e+005	+0.000000e+000	+0.000000e+000
38.7	-1.315735e+007	+3.420035e+005	+0.000000e+000	+0.000000e+000
39.2	-1.271111e+007	+3.264835e+005	+0.000000e+000	+0.000000e+000
39.7	-1.352841e+007	+3.425655e+005	+0.000000e+000	+0.000000e+000
40.2	-1.338335e+007	+3.333319e+005	+0.000000e+000	+0.000000e+000
40.7	-1.414444e+007	+3.479542e+005	+0.000000e+000	+0.000000e+000
41.2	-1.537484e+007	+3.736247e+005	+0.000000e+000	+0.000000e+000
41.7	-1.716400e+007	+4.120892e+005	+0.000000e+000	+0.000000e+000
42.2	-1.716400e+007	+4.120892e+005	+0.000000e+000	+0.000000e+000
42.7	-1.716400e+007	+4.120892e+005	+0.000000e+000	+0.000000e+000
43.2	-1.716400e+007	+4.120892e+005	+0.000000e+000	+0.000000e+000
43.7	-1.716400e+007	+4.120892e+005	+0.000000e+000	+0.000000e+000
44.2	-1.716400e+007	+4.120892e+005	+0.000000e+000	+0.000000e+000
44.7	-1.716400e+007	+4.120892e+005	+0.000000e+000	+0.000000e+000
45.2	-1.716400e+007	+4.120892e+005	+0.000000e+000	+0.000000e+000

channels ($>5\%$ of peak) and over the kV range from 20 to 40 kV were -0.073% ($\sigma = 1.58\%$) for the MASMIP molybdenum model, -0.145% ($\sigma = 1.26\%$) for the RASMIP rhodium anode model, and 0.611% ($\sigma = 2.07\%$) for the TASMIP tungsten anode model.

Perhaps a more meaningful comparison between spectra than percent error is a comparison of attenuation curves that result as an x-ray spectra is propagated through some medium. The net effect of any spectrum is, after all, its attenuation versus thickness performance. Attenuation curves for

TABLE III. Polynomial coefficients for the tungsten anode x-ray tube (TAS-MIP). At each energy bin E, the photon fluence (photons/mm^2) at a given kV is given by: $\Phi(\text{photons/mm}^2) = a_0 + a_1 \times kV + a_2 \times kV^2 + a_3 \times kV^3$.

| Energy (keV)	a$_0$	a$_1$	a$_2$	a$_3$
5.5	+0.000000e+000	+0.000000e+000	+0.000000e+000	+0.000000e+000
6.0	-6.873489e+007	+7.187753e+006	-2.159918e+005	+2.221631e+003
6.5	-6.070034e+007	+6.345849e+006	-1.857021e+005	+1.845997e+003
7.0	-8.743849e+007	+9.280132e+006	-2.839093e+005	+2.922466e+003
7.5	-1.026951e+008	+1.081317e+007	-3.267757e+005	+3.355058e+003
8.0	-2.469562e+008	+2.591247e+007	-8.003514e+005	+8.518917e+003
8.5	-4.706627e+008	+4.614004e+007	-1.283757e+006	+1.301409e+004
9.0	-1.560684e+008	+1.572514e+007	-4.455923e+005	+4.439223e+003
9.5	-3.606819e+008	+3.634391e+007	-1.070835e+006	+1.140357e+004
10.0	-3.068500e+008	+2.869390e+007	-7.291643e+005	+7.155739e+003
10.5	-1.276861e+008	+1.288114e+007	-3.660513e+005	+3.644392e+003
11.0	-1.257411e+008	+1.297512e+007	-3.854823e+005	+3.942138e+003
11.5	-1.363437e+008	+1.364892e+007	-3.889844e+005	+3.882684e+003
12.0	-1.029163e+008	+1.055863e+007	-3.115667e+005	+3.143828e+003
12.5	-8.470663e+007	+8.705748e+006	-2.556132e+005	+2.545929e+003
13.0	-8.670866e+007	+8.952853e+006	-2.672010e+005	+2.712157e+003
13.5	-8.561442e+007	+8.769771e+006	-2.593430e+005	+2.613102e+003
14.0	-8.318715e+007	+8.460735e+006	-2.485027e+005	+2.499402e+003
14.5	-7.335074e+007	+7.279689e+006	-2.054119e+005	+2.011454e+003
15.0	-7.627260e+007	+7.608005e+006	-2.192303e+005	+2.200747e+003
15.5	-7.756584e+007	+7.662825e+006	-2.195321e+005	+2.191898e+003
16.0	-7.462895e+007	+7.294175e+006	-2.069436e+005	+2.060917e+003
16.5	-7.097482e+007	+6.859915e+006	-1.925960e+005	+1.912045e+003
17.0	-7.072362e+007	+6.763036e+006	-1.891083e+005	+1.882858e+003
17.5	-6.219645e+007	+5.788333e+006	-1.555985e+005	+1.516050e+003
18.0	-5.502960e+007	+4.926868e+006	-1.247321e+005	+1.166320e+003
18.5	-6.065437e+007	+5.395190e+006	-1.389085e+005	+1.311125e+003
19.0	-7.070298e+007	+6.342366e+006	-1.699210e+005	+1.646678e+003
19.5	-6.271249e+007	+5.382715e+006	-1.357499e+005	+1.262038e+003
20.0	-5.812485e+007	+4.840952e+006	-1.172847e+005	+1.060619e+003
20.5	-6.740821e+007	+5.686414e+006	-1.441134e+005	+1.340266e+003
21.0	-6.699264e+007	+5.464481e+006	-1.336550e+005	+1.206979e+003
21.5	-7.662571e+007	+6.357553e+006	-1.627368e+005	+1.518921e+003
22.0	-6.756454e+007	+5.414589e+006	-1.327032e+005	+1.210007e+003
22.5	-7.591042e+007	+6.173340e+006	-1.570560e+005	+1.469012e+003
23.0	-8.531624e+007	+6.865103e+006	-1.744268e+005	+1.609156e+003
23.5	-8.404450e+007	+6.628089e+006	-1.650829e+005	+1.498164e+003
24.0	-8.668162e+007	+6.854728e+006	-1.730579e+005	+1.590682e+003
24.5	-6.495929e+007	+4.651735e+006	-1.020722e+005	+8.478419e+002
25.0	-1.070874e+008	+8.469419e+006	-2.174418e+005	+1.997402e+003
25.5	-9.403950e+007	+7.084522e+006	-1.716615e+005	+1.508351e+003
26.0	-8.754474e+007	+6.488524e+006	-1.551625e+005	+1.359698e+003
26.5	-3.529739e+007	+1.744532e+006	-1.503964e+004	+0.000000e+000
27.0	-3.813298e+007	+1.870898e+006	-1.668576e+004	+0.000000e+000
27.5	-4.450025e+007	+2.221201e+006	-2.179242e+004	+0.000000e+000
28.0	-4.272417e+007	+2.092002e+006	-1.996507e+004	+0.000000e+000
28.5	-4.416447e+007	+2.137812e+006	-2.045019e+004	+0.000000e+000
29.0	-3.691062e+007	+1.668331e+006	-1.338276e+004	+0.000000e+000
29.5	-3.907555e+007	+1.774209e+006	-1.498448e+004	+0.000000e+000
30.0	-1.195746e+008	+8.396072e+006	-1.961298e+005	+1.641245e+003
30.5	-4.365839e+007	+1.975074e+006	-1.762596e+004	+0.000000e+000
31.0	-4.651813e+007	+2.091356e+006	-1.891025e+004	+0.000000e+000
31.5	-5.022499e+007	+2.257714e+006	-2.101889e+004	+0.000000e+000
32.0	-4.846810e+007	+2.147030e+006	-1.960649e+004	+0.000000e+000
32.5	-4.732332e+007	+2.059328e+006	-1.836286e+004	+0.000000e+000
33.0	-5.582990e+007	+2.475062e+006	-2.368736e+004	+0.000000e+000
33.5	-6.325837e+007	+2.830780e+006	-2.814664e+004	+0.000000e+000
34.0	-6.455889e+007	+2.905371e+006	-2.948107e+004	+0.000000e+000
34.5	-2.215968e+007	+6.551200e+005	+0.000000e+000	+0.000000e+000
35.0	-5.679439e+007	+2.407766e+006	-2.232638e+004	+0.000000e+000
35.5	-8.115400e+007	+3.604377e+006	-3.716713e+004	+0.000000e+000
36.0	-7.735838e+007	+3.421578e+006	-3.521819e+004	+0.000000e+000
36.5	-2.213949e+007	+6.210240e+005	+0.000000e+000	+0.000000e+000
37.0	-2.489510e+007	+6.823500e+005	+0.000000e+000	+0.000000e+000
37.5	-2.619137e+007	+7.038040e+005	+0.000000e+000	+0.000000e+000
38.0	-2.658188e+007	+7.053680e+005	+0.000000e+000	+0.000000e+000
38.5	-2.316312e+007	+6.122530e+005	+0.000000e+000	+0.000000e+000
39.0	-2.999583e+007	+7.719365e+005	+0.000000e+000	+0.000000e+000
39.5	-2.840658e+007	+7.219850e+005	+0.000000e+000	+0.000000e+000
40.0	-2.741783e+007	+6.895365e+005	+0.000000e+000	+0.000000e+000
40.5	-3.342120e+007	+8.262318e+005	+0.000000e+000	+0.000000e+000
41.0	-3.816755e+007	+9.320471e+005	+0.000000e+000	+0.000000e+000
41.5	-3.830466e+007	+9.241070e+005	+0.000000e+000	+0.000000e+000
42.0	-2.052079e+008	+4.891130e+006	+0.000000e+000	+0.000000e+000
42.5	-2.052079e+008	+4.891130e+006	+0.000000e+000	+0.000000e+000
43.0	-2.052079e+008	+4.891130e+006	+0.000000e+000	+0.000000e+000
43.5	-2.052079e+008	+4.891130e+006	+0.000000e+000	+0.000000e+000
44.0	-2.052079e+008	+4.891130e+006	+0.000000e+000	+0.000000e+000
44.5	-2.052079e+008	+4.891130e+006	+0.000000e+000	+0.000000e+000
45.0	-2.052079e+008	+4.891130e+006	+0.000000e+000	+0.000000e+000
45.5	-2.052079e+008	+4.891130e+006	+0.000000e+000	+0.000000e+000
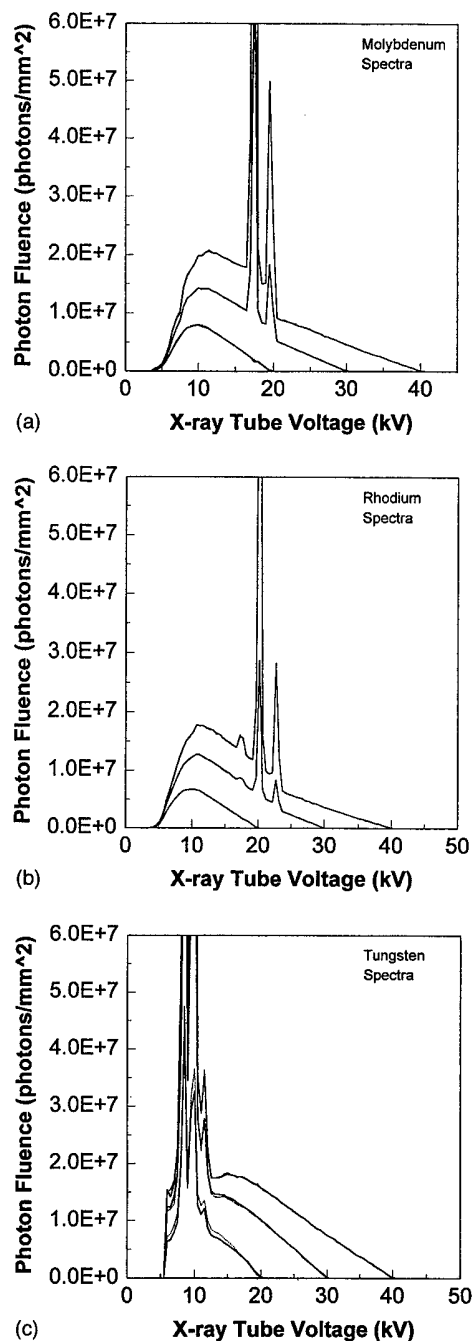
FIG. 4. The measured spectra are shown (dotted lines) and are compared to the computer generated x-ray spectra (solid lines), at 20 kV, 30 kV, and 40 kV. The molybdenum spectra are shown in A, the rhodium spectra in B, and the tungsten spectra are compared in C. These comparisons are representative of the spectra at intermediate kV's, that were not shown. For the molybdenum and rhodium spectra (A and B), the comparison between the measured and the computer-generated spectra is quite good—to the point that most of the plotted measured spectra (dotted lines) were obscured by the overlaying computer generated spectra (solid lines). In the comparison between the measured versus computer-generated tungsten spectra (C), the 20 kV spectra show some slight differences. However, the higher voltage spectra at 30 and 40 kV compare quite well.

molybdenum spectra are illustrated in Fig. 6A. Only the 20, 30, and 40 kV attenuation profiles are illustrated for clarity. These curves (solid lines are for the model, dotted lines are calculated from measured spectra) demonstrate near identical attenuation properties between the measured spectra and the modeled spectra. Figure 6B demonstrates that excellent
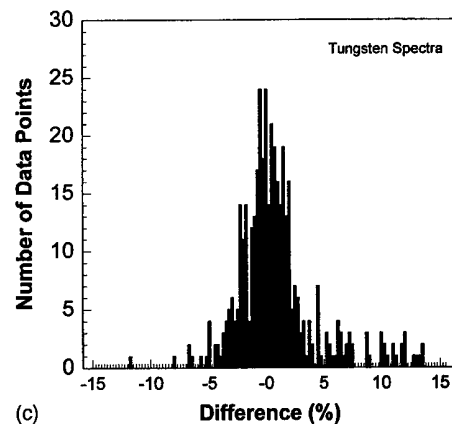
agreement in attenuation profiles was achieved for the rhodium spectra as well. In Fig. 6C for the tungsten anode spectra, some discrepancy in the attenuation profile for the 20 kV spectrum is seen between the measured and modeled
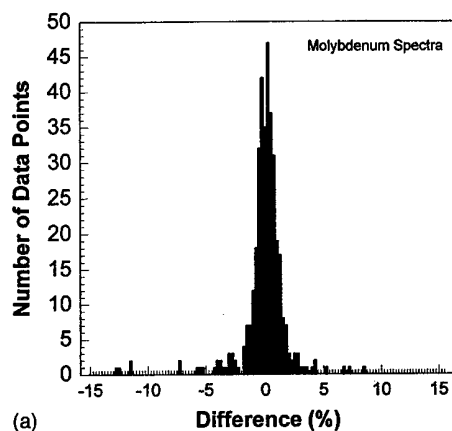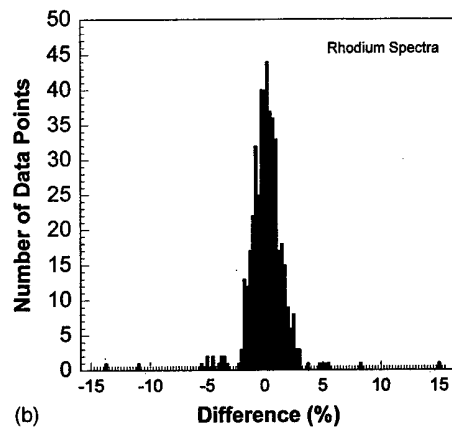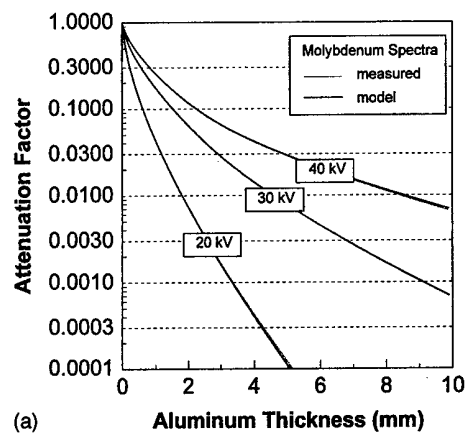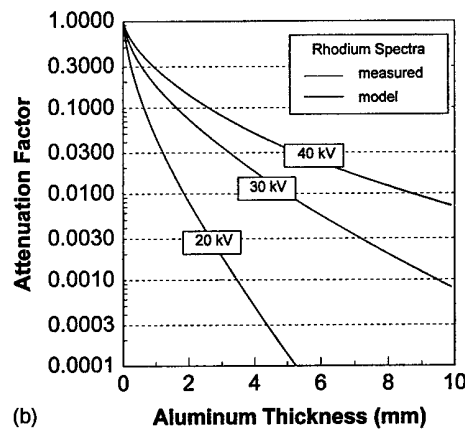
FIG. 5. The percent difference between the measured and the computer-generated x-ray spectra was calculated at each data point (data points were at 0.5 keV intervals), for all spectra between 20 kV and 40 kV (inclusive). Data that was below 5% of peak amplitude in each spectrum was not included in this analysis, because small differences in photon fluences would result in the calculation of large relative (percent) errors. The differences between the molybdenum (A), rhodium (B), and tungsten (C) spectra are illustrated as histograms. The mean difference (and standard deviations) for these three histograms were $-0.073\%(1.58\%)$ for molybdenum, $-0.145\%(1.263\%)$ for rhodium, and $0.611\%(2.07\%)$ for tungsten.

FIG. 6. The importance of generating accurate x-ray spectra is in many instances related to how well the attenuation profiles of the spectra match. The attenuation as a function of aluminum thickness is shown for the molybdenum spectra (A), for the rhodium spectra (B), and for the tungsten spectra (C). The semi-logarithmic axes accentuates even small differences in the attenuation profiles over the four decades shown. While only trivial differences are seen for the molybdenum (A) and rhodium anode spectra (B), there is noticeable difference between the measured and computer generated results for the 20 kV tungsten spectra (C). This difference is a manifestation of the differences in the shape of the 20 kV tungsten spectra shown in Fig. 4C. In Fig. 4C, the 22 kV tungsten spectra is also shown to illustrate that the attenuation profiles compare well at this kV. Similar performance was observed for all tungsten spectra between 22 and 40 kV (not shown).

spectra. The differences in the attenuation profile result from the slightly different shapes of the measured versus modeled spectra at 20 kV as illustrated in Fig. 4C.
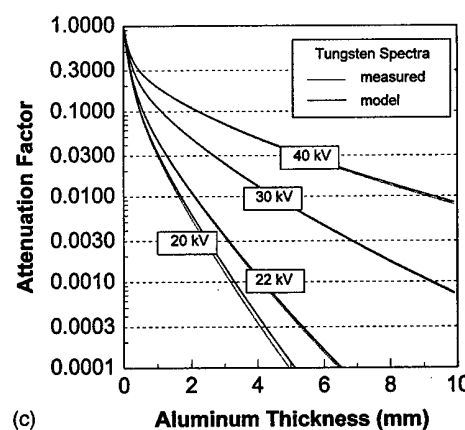
The comparisons shown in Figs. 4, 5, and 6 compare the measured x-ray spectra with the MASMIP, RASMIP, and

TASMIP spectral models, but these comparisons are between the original data and the computer fit to that same data. How well do the three models work when the spectrum to be reconstructed is of a kV not used to produce the poly-

nomial coefficients? In other words, how well do the models interpolate? Unfortunately, there are no measured spectra to compare the interpolated spectra with, indeed that is why interpolation is necessary. Nevertheless, the ability of the model to interpolate accurately can be demonstrated subjectively.

Figure 3 demonstrates the original data as solid circles and the polynomial interpolated data as solid lines, for a total of 35 energies out of the ~85 nonzero energy bins defined by each model. The intention of presenting a large number of the fits as shown in Figs. 3A, 3B, and 3C was to visually demonstrate that the interpolated results in all cases are excellent, except at the lowest energies which are unimportant because photons at these energies are virtually eliminated by added filtration. The accuracy of computer-generated interpolated spectra is equivalent to the accuracy of the interpolation between the discrete points as illustrated in Fig. 3 for the three models. Because the fits in Fig. 3 *are* excellent, and the functional form of each curve is clearly smooth and well behaved, it is arguable that the interpolated lines have a very high probability of accurately describing the true spectral fluence values between the measured points. The 35 curves shown in Figs. 3A, 3B, and 3C represent about half of all the spectral data points. The other half, not shown for the sake of brevity, demonstrates performance comparable to the curves shown.

Figure 7 shows several interpolated spectra with the measured spectra interleaved for comparison. It should be understood that the spectra shown in Fig. 7 shows essentially the same data as that shown in Fig. 3, plotted differently. While no measured ''gold standard'' spectra are available at the kV's for the interpolated spectra shown in Fig. 7, the visual comparison seen in the figures does provide subjective evidence indicating excellent performance of the three computer models discussed for each target material.

The half-value layers (HVL's) for aluminum were measured on a clinical mammography system (Senograph 600T, General Electric Corporation, Milwaukee, WI), with a recently calibrated exposure meter (Keithley Triad 3050A, Cleveland, OH), and are shown as the solid circles in the Fig. 8. The MASMIP model was used to generate spectra between 20 and 40 kV, 30 μm Mo filtration was imposed numerically to each spectrum, and the HVL's were calculated and are shown in Fig. 8 as the solid line. The two dashed lines are the HVL's calculated with a 27 μm Mo filter (-10%) and a 33 μm Mo filter ($+10\%$), showing the influence of slight differences in filtration on the HVL. Given the unknown additional components in the inherent filtration of the clinical mammography system (such as the mirror), which would tend to increase the measured HVL's (i.e., the observed trend), the comparison between measured and theoretical HVL's is considered very good.

The technique presented here is capable of generating x-ray spectrum which match *measured* x-ray spectra well, but this also means that the MASMIP, RASMIP, and TASMIP models include the influences intrinsic to measured spectra. For example, the computer models presented here include the influence of the finite energy response of the spectro-
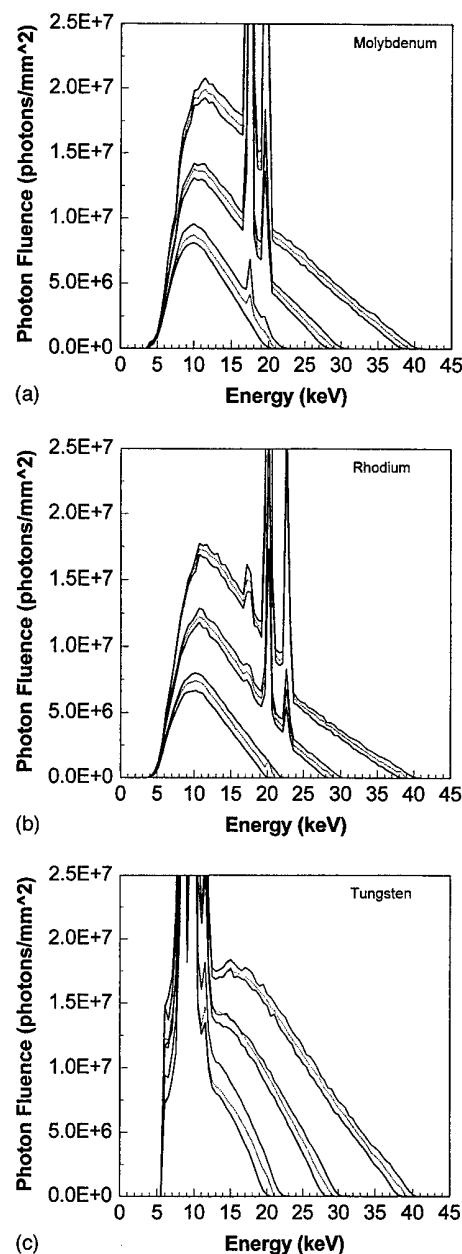

FIG. 7. Interpolated x-ray spectra are illustrated, for molybdenum (A), rhodium (B), and tungsten anodes (C). The computer-generated interpolated spectra are illustrated as dashed lines, and the measured spectra at adjacent kV's are illustrated as solid lines. For each figure, two even kV measured spectra surround one odd kV spectrum, for a total of nine spectra demonstrated per figure. The three sets of kV's shown are 20-21-22, 28-29-30, and 38-39-40. The subjective visual comparison shown in this figure provides convincing evidence as to the high quality of the interpolation results. It is noted that these plots show the same results as those illustrated in Fig. 3, albeit plotted in a more traditional manner.

scopic detector. The ''true'' spectra are convolved with the energy response of the detector system, and the intrinsic germanium detector system used has an approximately 300 eV full width half maximum energy response in the mammographic energy range. The energy resolution of the detector coupled with the discrete binning results in the slight broadening of the characteristic x-ray lines (Fig. 4). This is a phe-
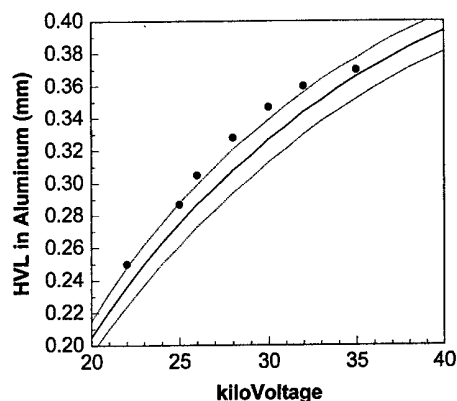
FIG. 8. A comparison between HVL's measured on a clinical mammography system (Senograph 600T) (solid circles) and HVL's calculated from the MASMIP model is shown. The solid line was calculated using 30 μm of added Mo filtration to the x-ray beam, and the two dashed lines were calculated using $+10\%(33 \mu$m Mo) and $-10\%(27 \mu$m Mo) filtration. The difference between the solid and dashed lines indicates the sensitivity of the HVL to small differences in beam filtration. The agreement between the measured and the calculated HVL's is considered very good considering the unknown amount and composition of additional filtration (e.g., the mirror) in the clinical mammography system.

nomenon which theoretical spectra[19] do not experience. Nevertheless, the influence of the detector's energy response is expected to be negligible in most computer simulation applications. Furthermore, this effect could easily be removed using deconvolution methods should this be deemed necessary for a particular simulation application.

SUMMARY

A mathematical model for interpolating x-ray spectra was presented, and was shown to produce realistic x-ray spectra for Mo, Rh, and W anode x-ray systems operating in the 20–40 kV range. While the MASMIP (and RASMIP and TASMIP) models lack the solid theoretical and physical underpinnings in regards to the theory of x-ray production in a thick target that the Tucker model enjoys,[19] the presented spectral models are nevertheless capable of generating accurate x-ray spectra that correspond well to measured, "gold standard" spectra. The polynomial interpolation of measured data, which is the basis of the three computer models discussed, implies that they are completely empirical in contrast to the semi-empirical model proposed by Tucker et al.[19]

It is expected that the MASMIP, RASMIP, and TASMIP spectral models may be helpful in computer simulation studies involving mammographic spectra. Towards that end, the polynomial coefficients for all three spectral models are provided in Tables I, II, and III. For those with Internet access, the polynomial coefficients and a short program which generates the three spectral models is made available through an electronic data repository service of the American Institute of Physics (the publisher of Medical Physics). The source code, written in C, along with the polynomial coefficients can be downloaded at http://www.aip.org/epaps/epaps.html.[26]

[a])Address for correspondence: John M. Boone, Ph.D., Department of Radiology, University of California, Davis, UC Davis Medical Center, FOLB 2E, 2421 45th Street, Sacramento, CA 95817, Electronic-mail: jmboone@ucdavis.edu

[1]X. Wu, G. T. Barnes, and D. M. Tucker, "Spectral dependence of glandular tissue dose in screen-film mammography," Radiology **179**, 143–148 (1991).

[2]R. Fahrig and M. J. Yaffe, "A model for optimization of spectral shape in digital mammography," Med. Phys. **21**, 1463–1471 (1994).

[3]R. Fahrig and M. J. Yaffe, "Optimization of spectral shape in digital mammography: Dependence on anode material, breast thickness, and lesion type," Med. Phys. **21**, 1473–1481 (1994).

[4]M. Sandborg, C. A. Carlsson, and G. A. Carlsson, "Shaping x-ray spectra with filters in x-ray diagnostics," Med. Biol. Eng. Comput. **32**, 384–390 (1994).

[5]C. S. Chen, K. Doi, C. Vyborny, H-P. Chan, and G. Holje, "Monte Carlo simulation studies of detectors used in the measurement of diagnostic x-ray spectra," Med. Phys. **7**, 627–635 (1980).

[6]A. D. A. Maidment, R. Fahrig, and M. J. Yaffe, "Dynamic range requirements in digital mammography," Med. Phys. **20**, 1621–1633 (1993).

[7]D. M. Tucker, G. T. Barnes, and D. P. Chakraborty, "Semiempirical model for generating tungsten target x-ray spectra," Med. Phys. **18**, 211–218 (1991).

[8]R. Birch and M. Marshall, "Computation of bremsstrahlung x-ray spectra and comparison with spectra measured with a Ge(Li) detector," Phys. Med. Biol. **24**, 505–517 (1979).

[9]B. R. Archer, T. R. Fewell, and L. K. Wagner, "Laplace reconstruction of experimental diagnostic x-ray spectra," Med. Phys. **15**, 832–837 (1988).

[10]B. R. Archer and L. K. Wagner, "Determination of diagnostic x-ray spectra with characteristic radiation using attenuation analysis," Med. Phys. **15**, 637–641 (1988).

[11]H. J. Patrocinio, J.-P. Bissonnette, M. R. Bussière, and L. J. Schreiner, "Limiting values of backscatter factors for low-energy x-ray beams," Phys. Med. Biol. **41**, 239–253 (1996).

[12]J. M. Boone and J. A. Seibert, "A comparison of mono- and polyenergetic x-ray beam performance for radiographic and fluoroscopic imaging," Med. Phys. **21**, 1853–1863 (1994).

[13]D. McLean, "Computer model to optimise contrast in chest radiography," Aust. Phys. Eng. Sci. Med. **16**, 179–185 (1993).

[14]H. N. Cardinal, D. W. Holdsworth, M. Drangova, B. B. Hobbs, and A. Fenster, "Experimental and theoretical x-ray imaging performance comparison of iodine and lanthanide contrast agents," Med. Phys. **20**, 15–31 (1993).

[15]J. M. Boone, "Equivalent spectra as a measure of beam quality," Med. Phys. **13**, 861–868 (1986).

[16]H-P. Chan, C. T. Chen, K. Doi, T. R. Fewell, and R. E. Shuping, "Investigation of energy responses of germanium detectors and correction of measured spectra by means of Monte Carlo simulation," Radiat. Res. **99**, 443–464 (1984).

[17]R. M. Harrison, G. D. Lambert, and C-L. Chapple, "Spectral estimation and contrast calculation in the design of contrast-detail test objects for radiotherapy portal imaging," Phys. Med. Biol. **38**, 545–556 (1993).

[18]P. H. Huang, K. R. Kase, and B. E. Bjarngard, "Simulation studies of 4-MV x-ray spectral reconstruction by numerical analysis of transmission data," Med. Phys. **9**, 695–702 (1982).

[19]D. M. Tucker, G. T. Barnes, and X. Wu, "Molybdenum target x-ray spectra: A semiempirical model," Med. Phys. **18**, 402–407 (1991).

[20]T. R. Fewell and R. E. Shuping, "Photon energy distribution of some typical diagnostic x-ray beams," Med. Phys. **4**, 187–197 (1977).

[21]T. R. Fewell and R. E. Shuping, *Handbook of Mammographic X-ray Spectra*, HEW Publication (FDA) 79–8071. Rockville, MD (1978).

[22]T. R. Fewell, R. E. Shuping, and K. E. Healy, *Handbook of Computed Tomography X-ray Spectra*, HHS Publication (FDA) 81-8162. Rockville, MD (1981).

[23]T. R. Fewell (personal communication).

[24]J. M. Boone and A. E. Chavez, "Comparison of x-ray cross sections for diagnostic and therapeutic medical physics," Med. Phys. **23**, 1997–2005 (1996).

[25]P. R. Bevington, *Data Reduction and Error Analysis for the Physical Sciences* (McGraw–Hill, New York, 1969).

[26]See AIP Document No. E-PAPS: E-MPHYA-24-1863 for the polynomials and a short program which generates the three spectral models. E-PAPS document files may be retrieved free of charge from our FTP server (http://www.aip.org/epaps/epaps.html) or from ftp.aip.org in the directory/epaps/. For further information: e-mail: paps@aip.org or fax: 516-576-2223.

Journal of Digital Imaging

A Breast Density Index for Digital Mammograms Based on Radiologists' Ranking

John M. Boone, Karen K. Lindfors, Carol S. Beatty, and J. Anthony Seibert

The purpose of this study was to develop and evaluate a computerized method of calculating a breast density index (*BDI*) from digitized mammograms that was designed specifically to model radiologists' perception of breast density. A set of 153 pairs of digitized mammograms (cranio-caudal, CC, and mediolateral oblique, MLO, views) were acquired and preprocessed to reduce detector biases. The sets of mammograms were ordered on an ordinal scale (a scale based only on relative rank-ordering) by two radiologists, and a cardinal (an absolute numerical score) BDI value was calculated from the ordinal ranks. The images were also assigned cardinal BDI values by the radiologists in a subsequent session. Six mathematical features (including fractal dimension and others) were calculated from the digital mammograms, and were used in conjunction with single value decomposition and multiple linear regression to calculate a computerized BDI. The linear correlation coefficient between different ordinal ranking sessions were as follows: intraradiologist intraprojection (CC/CC): $r = 0.978$; intraradiologist interprojection (CC/MLO): $r = 0.960$; and interradiologist intraprojection (CC/CC): $r = 0.968$. A separate breast density index was derived from three separate ordinal rankings by one radiologist (two with CC views, one with the MLO view). The computer derived *BDI* had a correlation coefficient (*r*) of 0.907 with the radiologists' ordinal *BDI*. A comparison between radiologists using a cardinal scoring system (which is closest to how radiologists actually evaluate breast density) showed $r = 0.914$. A breast density index calculated by a computer but modeled after radiologist perception of breast density may be valuable in objectively measuring breast density. Such a metric may prove valuable in numerous areas, including breast cancer risk assessment and in evaluating screening techniques specifically designed to improve imaging of the dense breast.
Copyright © 1998 by W.B. Saunders Company

KEY WORDS: breast cancer, mammography, breast density, digital mammography, computer aided diagnosis

WOMEN WITH DENSE BREASTS appear to have a four to six fold increase in breast cancer risk,[1-4] yet imaging the dense breast contin-

ues to be problematic. Cancers are detected at later stages in dense breasts and radiologists recognize that their diagnostic accuracy is lower in such women. Consequently, efforts to improve the detectability of breast cancer in the dense breast have received increased attention. Refinements in mammography and new techniques including digital mammography,[5] high definition and Doppler ultrasound,[6,7] magnetic resonance imaging,[8-10] positron emission tomography (PET),[11,12] and single photon emission computed tomography imaging (SPECT)[13,14] are all under development. Many of these techniques are aimed at overcoming the limitations of conventional mammography in the radiographically dense breast, yet there is no truly quantitative method for grading breast density. Such a metric would have many uses, including the assessment of the impact of these new modalities on the detection of early cancer in the dense breast.

Wolfe was the first to describe a discrete classification scheme with four classes of mammographic density patterns.[1,2,15-18] More recently, the Breast Imaging Reporting and Data System (BIRADS) was introduced by the American College of Radiology. It also makes use of four classifications of breast density. Although these classifications are helpful for communication of diagnostic sensitivity, they are both subjective and crude. The study presented here was designed to evaluate sets of

computer-calculated features which could be used to quantify breast density on a continuous scale from digital (or digitized) mammograms. In addition, the breast density index (*BDI*) developed was specifically modeled to adhere to a radiologist's perception of breast density.

The number of useful breast density categories that one can assign a mammogram to is an important consideration; with too many categories, assignment can become less reproducible and arbitrary, while with too few categories, useful density strata would go unappreciated and benefits of breast density classification would be under-realized. Therefore, we have analyzed the many classifications performed in this study in a manner that may shed light on what a reasonable number of categories might be for breast density categorization.

METHODS AND MATERIALS

Case Selection and Film Digitization

A series of normal left mammograms (Cranio-caudal view [CC] and mediolateral oblique [MLO]) of 160 different patients was selected from the breast imaging service at our institution. For each set of films, the patient's name, date of birth, and the examination date was recorded. The patient population at our medical center is representative of the broad ethnic distribution typical of large urban centers in California. Cases were selected serially, and no selection criteria was used to limit incorporation into the study.

The film images were digitized using a Lumisys 200 laser film digitizer (Lumisys, Sunnyvale, CA). The pixel size was 50 μm × 50 μm, and the gray scale was digitized to 12 bits. The large (40 Mbyte) files were cropped using software written for this purpose, eliminating some of the area beyond the silhouette of the breast, and the cropped images were stored at original resolution on a series of optical disks. For realistic manipulation, display, and computation, the images were reduced in size by pixel averaging to 500 μm × 500 μm pixels. At this spatial resolution (for the CC view, the down-sampled images averaged 195.3 ± 4.2 pixels wide and 394.0 ± 4.2 pixels tall), a good overall view of the breast architecture could be appreciated.

Radiologist Ranking Scheme

The radiologist's determination of breast density was used as the gold standard in this study. To rank-order the mammograms in this study, all images needed to be visualized simultaneously by the radiologist. The CC and MLO image sets were therefore replicated in miniature using the following procedure.

The relationship between the digitized gray scale value and the film optical density (OD) was measured by digitizing a sheet of film which contained steps of known optical densities, and the average gray scale value in each region was quantified. The OD as a function of gray scale was fit to a straight line ($r > 0.9999$). The relationship between gray scale value and optical density was also measured for a laser imager, and this relationship was characterized using commercially available software (Table-

Curve 2D; Jandel Scientific, San Rafael, CA). From these data, a transformation curve was calculated which allowed the digitized mammograms to be printed onto laser film at their original optical densities. Using this method, small replicas of the original mammograms were printed which had the "identical" densities as the original analog film mammograms. Each mammogram replica was approximately 3.5 cm × 8.0 cm, but varied slightly with breast size from image to image. Of the 160 original pairs of mammograms, there were technical difficulties with seven, including digitizer errors (corrupted data files), and lost or duplicate miniature films. Consequently, 153 pairs of mammograms were used in the subsequent analyses. Using a 4-over-1 lightbox placed flat on a countertop (area of view box was 142 cm wide by 43 cm tall), all 153 miniature mammograms could be placed in order with simultaneous visualization of all images for comparison purposes. Whereas the effect of using miniature mammograms was not explicitly evaluated, it is anticipated that this had little or no effect on the results because the present task involved the assessment of breast density only, and not diagnosis.

Both radiologists involved in this study are experienced in the interpretation of mammograms. They were instructed to place in order, from most dense to least dense, the 153 images in each set. The rank ordering process required approximately 2-3 hours for each session. Radiologist 1 (RAD_1) rank-ordered the CC set twice (referred to as RAD_1 CC_1 and CC_2), in sessions that were performed more than 4 months apart. The MLO set was rank ordered by RAD_1 once. To evaluate inter-observer variability, a second radiologist (RAD_2) rank-ordered the CC image set (RAD_2 CC_1) as well.

Rank ordering a series of mammograms with the entire image set in full view of the radiologist is a conceptually different task than viewing an individual mammogram and assigning a density value. To measure the difference between these two distinct tasks, both radiologists assigned a "freehand" breast density index to each image, which was viewed alone and months apart from any other ranking session. This assignment used the scale where 100 corresponded to a very dense breast and 0 was a totally fatty replaced breast. The freehand assignment of breast density will be referred to as the CC_3 ordering session for each radiologist (Rad_1 and Rad_2).

The Breast Density Index (BDI)

To generate a quantitative scale of breast density, a breast density index (BDI) was computed from the radiologist's rank ordering of the images. The BDI was designed to range from 0 to 100 on a continuous scale, where 100 corresponds to an extremely dense breast, and 0 coincides with an extremely non-dense (fatty replaced) breast. The BDI was calculated for each of the ordinal rankings described above (RAD_1 CC_1, RAD_1 CC_2, RAD_1 MLO_1, or RAD_2 CC_1). In order to do this, the ordinal ranking scale was used to produce the cardinal BDI scale. There is justification for going from ordinal to cardinal scales when the number of cases is large.[19] To do this, the maximum rank score (S_{max}), corresponding to the least dense mammogram and the minimum rank score (S_{min}) corresponding to the most dense mammogram were computed from the rank ordering data, and then the BDI_j for image j which received a

rank score of S_j was calculated using the equation:

$$BDI_j = 100 \times \left[1 - \frac{S_j - S_{min}}{S_{max} - S_{min}}\right] \quad \text{[Equation 1]}$$

A consensus score from three separate ordinal ranking sessions from a single radiologist (RAD$_1$) was used for the "gold standard" BDI (referred to as the standard BDI, s-BDI). The three ranks assigned by radiologist 1 during the CC$_1$, CC$_2$ and MLO$_1$ ordering sessions were summed for each image, and the *s-BDI* was calculated using Equation 1.

The assignment of BDI values in session CC$_3$ did not employ a rank ordering (ordinal scale) of images, but rather was a direct assignment of (cardinal) BDI values by the radiologists. Therefore, the BDI values from session CC$_3$ (Rad$_1$ and Rad$_2$) did not make use of the ordinal to cardinal conversion shown in Equation 1.

Image Preprocessing

H and D Curve Correction. While film mammograms were used in this study, the technique described is intended to be applicable for the more general class of digital mammography images. Digital mammography systems for full field imaging may be commercially available in the next few years, and these systems will in general exhibit a linear response to the x-rays incident upon them (the characteristic curve will be a straight line). In order to make the technique described here applicable to linear images, the non-linear influence of the film was removed using the following pre-processing steps.

The characteristic curve of the screen-film system (Dupont Microvision, Wilmington, DE) was measured over approximately 20 steps by varying the x-ray exposure; the film was processed normally, and the optical density of each step was measured using a calibrated densitometer (TBX-U; Tobias Associates, Ivyland, PA). The exposure to the screen-film cassette (in milliroentgen, 1 mR = 2.58 × 10^{-7} C/kg) as a function of optical density (in OD units) was computer-fit using commercial software (TableCurve 2D; Jandel Scientific, San Rafael, CA) to an eighth-order polynomial ($r > 0.9999$). The gray scale value-to-exposure transform was combined with the linear relationship between OD and digital number (described previously) to create a function which converted the gray scale values of the digitized images (the raw digital numbers from the film digitizer) to the corresponding x-ray exposure (in mR) to the detector. This transform, shown in Fig 1, was applied to each pixel, effectively reversing the nonlinearity caused by the "H and D" curve of the film.

Image Log-Normalization. The next step in the image pre-processing was performed with the intent to make the digital images more dependent upon the physical characteristics of the breast, while reducing the dependency on absolute exposure levels. In the background regions of the image, outside the breast anatomy (where no breast was in the x-ray beam), the exposure theoretically corresponds to the unattenuated x-ray beam intensity, I_o. Under the breast silhouette, the exposure striking the detector is equal to $I_{\mu x} = I_o e^{-\mu x}$, where μx corresponds to the attenuation properties of the voxel of breast tissue corresponding to each pixel: μ is the linear attenuation coefficient of the tissue in the voxel, and x is the thickness of the
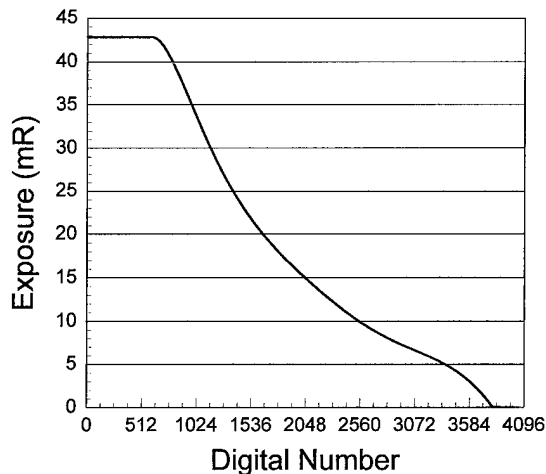

Fig 1. The shape of the functional curve that was used to transform the raw digital number (from digitizing the film) to exposure to the screen-film detector. This curve was generated from the H and D curve of the film, and the (linear) OD-to-digital number response of the laser digitizer used. Using this transform, digital images were corrected for the non-linearities of the screen film detector system.

voxel. In the compressed breast, the voxel thickness is quite uniform towards the center of the breast and the variability in μx is therefore strongly influenced by μ, which is desirable.

All of the mammograms had regions outside the breast silhouette which received unattenuated x-ray exposure, I_o, since of course the compressed breasts were approximately semi-circular and the images were rectangular. Each digital image was displayed on an imaging workstation and a small rectangular region outside the breast silhouette in a background area was hand positioned using mouse/cursor software written for this purpose. In this background region of interest, the mean gray scale value was calculated and then transformed using the gray scale-to-exposure curve (shown in Fig 1) to estimate I_o for that image. The value of $I_{\mu x}$ was then calculated for each pixel in the image using the gray scale-to-exposure transform, and the attenuation factor, $\mu x = LN(I_o/I_o e^{-\mu x})$ was calculated, multiplied by 1000 for scaling, and the resulting value was stored as an integer for each pixel. To further clarify the fact that these images were pre-processed images, and are not simply digitized mammograms, the digital images processed as described above will be referred to as "μx-mammograms."

It is acknowledged that the log-normalization of the image is only an estimate of μx, since beam hardening owing to the polyenergetic x-ray spectrum and spatial non-uniformities due to x-ray scatter and other factors were not accounted for. However, this procedure was performed to reduce the dependency of the analyses on absolute exposure and to reduce the dependency of the results on the non-linear response of film. Breast density is intrinsically related to μx; it is therefore only logical to computer-process the images using the available information such that they reflect this quantity to the extent possible.

Image Cropping. When radiologists look at a mammogram, they ignore the background (the region beyond the border of the

breast anatomy) on which the image is projected. This is not automatic, however, for computer analysis and specific efforts have to be taken to focus the computer algorithms on only the breast parenchyma. In order to do this, a threshold of $\mu x = 500$ was set, and based on visual feedback from the images this value was able to segment the breast parenchyma (where in general $\mu x > 500$) from the background periphery (where in general $\mu x < 500$). In some cases, simple thresholding was not sufficient to segment breast from non-breast areas, and therefore each image was inspected and individual image cropping was performed as needed. The predominant structures that required hand cropping were the lead markers ("LCC" and "LMLO"). Cropping was also used to eliminate regions where skin folds resulted in obviously artifactual high attenuation. A final reason for individually editing the images was that, in some images the laser digitizer presented some overshoot near the leading edge of the film, and these areas were cropped out of the μx-mammograms as well.

Regions outside of the breast parenchyma that were segmented out by thresholding and cropping were set to a uniform pixel value of 0 (zero). Since all areas of the image containing breast parenchyma had gray scale values greater than 500, this difference allowed the application of algorithms to only regions of the image containing breast parenchyma.

Computer Algorithms

When a radiologist looks at a mammogram, the human visual (eye-brain) complex applies an incredible array of subjective computations on the image, which can result in the ranking of breast density. For the computer to do this, specific *features* have to be mathematically quantified from each μx-mammogram. A feature is really anything that can be calculated from the images, and there are infinite possibilities of features. Examples of simple features can be the mean gray scale value on the μx-mammograms, or the standard deviation in gray scale values from those images. Much more complicated features can be calculated as well. For each feature, a single numerical value is calculated for each image, using an algorithm specific for that feature applied to each image. Finding the features which most closely correlate with breast density as determined by the radiologist was a principal focus of this study.

In this study, about two hundred features were evaluated for their ability to predict the radiologist's ranking of the images in terms of breast density. During the feature development phase, one third of the data base (51 images) was used for evaluation of features. As the features which were most effective became identified, the full data base was then used for analysis. No single feature that was evaluated was found to correlate with the BDI-standard with a linear correlation coefficient (r) of better than 0.78, calculated over the 153 images in the data base. Therefore, multiple features were combined to improve the computerized determined BDI (referred to as *c-BDI*) fit to the *s-BDI*. This approach required both the delineation of features which performed well, and the identification of the most effective combination of features.

While the calculation of each feature needs to be described mathematically, the details of these calculations may be of interest to only a subset of readers. Therefore, the mathematical description of how each of the six features was calculated is included in the Appendix. A list of the six image features that were ultimately used in the *c-BDI* is given in Table 1. A list of

Table 1. A Brief Description of the Parameters Used to Calculate the Computer-Derived BDI (c-BDI). A Full Discussion of How These Parameters Were Calculated From the μx-Mammograms Is Given in the Appendix

Para-meter Number	Parameter Abbreviation	Description	Linear Correlation Coefficient (r)*
1	FD_Th_75	Fractal Dimension with threshold = 75%	−0.7457
2	FD_Th_85	Fractal Dimension with threshold = 75%	−0.6640
3	FD_Sigma	Fractal Dimension of Standard Deviation	−0.0083
4	CD_Yint	Y intercept of Continuous Dimension	0.5715
5	CD_Slope	Slope of Continuous Dimension	0.7327
6	HZ_Proj	Standard Deviation in Horizontal Projections	0.5022

*The linear correlation coefficient was calculated for 153 images, comparing the *s-BDI* with only this parameter value.

some of the candidate features that were studied but ultimately not incorporated into the Breast Density Index model is given in Table 2.

Multiple Linear Regression Technique

A multiple linear regression algorithm using single value decomposition was developed using commercially available subroutines.[20] Using the multiple linear regression technique, given 6 features ($F_1(j)$, $F_2(j)$, . . . $F_6(j)$) that were calculated for

Table 2. A Brief Description With the Linear Correlation Coefficients of Some of the More Obvious Features That Were Studied Over the Course of This Investigation

Parameter Number	Parameter Description	Linear Correlation Coefficient (r)*
1	Area of the breast	−0.4003
2	Standard Deviation	0.4586
3	Mean GS value	0.0772
4	Median GS value	−0.0045
5	Mean-Median GS value	0.3514
6	Gray Scale value at 95% of Maximum GS value	0.3909
7	Width of image (nipple to chest wall)	−0.2986
8	Height of image (top to bottom)	−0.0951
9	Fractal dimension calculated on image histogram	0.0204
10	Fractal dimension on moments calculated on histogram	0.0546
11	Coefficient of Variation (standard deviation/mean)	−0.2310
12	Total image counts	−0.0230

*The linear correlation coefficients calculated here were calculated on ⅓ of the image set.

Table 3. The Values of the Coefficients Used to Calculate the Breast Density Index ($BDI = A_0 + A_1P_1 + A_2P_2 + A_3P_3 + A_4P_4 + A_5P_5 + A_6P_6$)

Co-efficient	Parameter (P_n) Associated with	Mean[a]	Standard Deviation[b]	Representative Values[c]
A0	(constant)	245.57845	2.7743060	246.07840
A1	FD_Th_75	−28.78644	0.9250735	−28.95025
A2	FD_Th_85	−23.30803	0.8287140	−23.26487
A3	FD_Sigma	−86.79803	2.0627900	−86.80530
A4	CD_Yint	54.64385	0.7178585	54.55355
A5	CD_Slope	406.09454	4.6207106	406.39166
A6	HZ_Proj	1.52770	0.0267123	1.52822

Notes: (a) Mean of 153 jackknifed trials with 152 in each trial; (b) Standard Deviation (1 s) of 153 jackknifed trials with 152 in each trial; and (c) Specific values for the coefficients for the last of 153 jackknifed trials.

each image j, the BDI for that image was calculated using Equation 2:

$$BDI(j) = A_0 + A_1 \cdot F_1(j) + A_2 \cdot F_2(j) + A_3 \cdot F_3(j)$$

$$+ A_4 \cdot F_4(j) + A_5 \cdot F_5(j) + A_6 \cdot F_6(j) \quad \text{[Equation 2]}$$

For a given image j, the six features $F_1(j) - F_6(j)$ were calculated from the image using specific algorithms described in the Appendix. The values for the 7 coefficients in Equation 2, A_0, A_1, . . . A_6 were solved for using the single value decomposition (SVD) multiple linear regression technique. The data needed to solve Equation 2 for the coefficients (A_N) are the 6 feature values calculated from a set of μx-mammograms *and* the corresponding *s-BDI* values [BDI(j)] for the same set of mammograms (Table 3).

There were a total of 153 cases acquired for this study, so $N_{cases} = 153$. The data set used to solve for the 7 coefficients may include as few as 7 cases (this is a constraint of the single value decomposition technique) or may include up to all the 153 cases that were compiled. However, in order to independently demonstrate the feasibility of this method, the available cases need to be divided up into a *training set* and a *testing set*. A training set is a set of a number of cases (N_{train}) that are used to solve for (hence "train") the coefficients ($A_0, A_1, . . . A_6$) using SVD multiple linear regression. The testing set makes use of a number of cases (N_{test}) that were *not a part* of the training set. The testing set, also called the *validation set*,[21] is used to evaluate the performance of the technique independently of the cases used to find the coefficients.

There are a huge number of permutations in which 153 different cases can be distributed between the two sets, but the validity and applicability of the results are dependent on some of the finer points of the methodology. A typical approach might be to take half of the cases and assign them to the training set, and take the other half for the testing set, however there is no assurance that this is the most efficient split of the data. There are many conflicting views on the "correct" way to allocate the data between training and testing.[21-26] We have therefore attempted to be very thorough in addressing this important issue. There are two general approaches to allocating the available data to the training and testing sets, a *straightforward split approach* and a *jackknife approach*. Both techniques were used, and will be described separately below.

The Straightforward Split Approach. This approach simply splits the available cases (N_{cases}) between the training set and the testing set, such that $N_{train} + N_{test} = N_{cases} = 153$. Let us also stipulate that we keep at least 5% of the cases in either set, meaning that N_{test} or N_{train} cannot be less than 7 cases ($\sim 0.05 \times 153$). There are 140 possible choices for selecting N_{train} and N_{test}. Specifically, these choices are: ($N_{train} = 7$, $N_{test} = 146$), ($N_{train} = 8$, $N_{test} = 145$), ($N_{train} = 9$, $N_{test} = 144$), . . . ($N_{train} = 146$, $N_{test} = 7$). However, there are an enormous number of possible distributions of the 153 cases amongst the training and testing sets, for each (N_{train}, N_{test}) point. In this study, all 140 possible choices for N_{train} and N_{test} were examined 1000 times *each,* where a different random distribution of cases between training and testing sets was used. A random number generator[27] was used to randomize the ordering of the cases, and then the N_{train} cases were assigned to the training set and were used to calculate the multiple linear regression coefficients, A_0-A_6. The remaining N_{test} cases were then used to compare the performance of the *c-BDI* approach with the *s-BDI*. The performance metric used in this study was the linear correlation coefficient, *r*. The different case mixes at each (N_{train}, N_{test}) point were used to quantify the mean and standard deviation in the linear correlation coefficients (*r*) at these points.

The Jackknife Approach. The jackknife approach[23,28,29] to separating N_{cases} into training and testing sets is designed to maximize the number of cases in the training set, but to still get N_{cases} independent cases for testing. With this approach, of the available N_{cases}, the first one was placed in the testing set ($N_{test} = 1$), and the remaining ($N_{cases} - 1$) cases were placed into the training set. The SVD multiple linear regression technique was used to solve for the coefficients using the ($N_{cases} - 1$) cases in the training set, and the *c-BDI* of the single case in the testing set was calculated using Equation 2 and stored. This procedure was executed again, except that the second case was placed in the testing set, and all remaining cases were used for training as before. Performance of case 2 was then calculated as above and stored. This process was repeated until each case had its turn sitting out of the training set, and being used in the testing set. The linear correlation coefficient r was then calculated on all N_{cases} independent test cases that were stored using this jackknife procedure. The average linear regression coefficient from all N_{cases} training sessions was also computed.

To evaluate the performance of the jackknife approach as a function of the number of cases used, the jackknife method was run using a number of cases ($N_{jackknife}$) ranging between 20 to 153. For each value of $N_{jackknife}$, 1000 different random samples of cases taken from the 153 total cases were made and evaluated. As $N_{jackknife}$ approached the total number of cases available (153), however, the amount of diversity in terms of case mix was reduced such that when $N_{jackknife} = 153$, all 1000 random realizations were identical and there was no diversity between the 1000 random samples ($\sigma = 0$).

Shrinkage. For both the straightforward split and the jackknife approaches discussed above, the linear correlation coefficient (*r*) was calculated for both the training set (r_{train}) and the testing set (r_{test}). In general, the value of r_{train} was higher than r_{test} because the SVD multiple linear regression procedure is designed to essentially maximize r_{train}. The test set represents new cases, not used in training, which are necessary to

independently verify the performance of the overall technique. As a result of this, r_{test} will usually fall short of r_{train}, since the coefficients were not specifically optimized for that (testing) data set. *Shrinkage* is a general term[21,22,30,31] that refers to the lower performance of the testing set, relative to the performance of the training set. If shrinkage is very small or zero, this implies that the technique was robust and the coefficients that were derived from the training set also worked well with the testing set. This further implies that the overall approach being studied generalizes well to an independent population of cases. To specifically quantify shrinkage for this study, where the linear correlation coefficient was used as the metric of performance, an equation was needed in which shrinkage is zero when $r_{test} = r_{train}$, and increases as the ratio (r_{test}/r_{train}) decreases. The equation which meets these criteria is given below:

$$\text{shrinkage}(\%) = 100 \times \left(1 - \frac{r_{test}}{r_{train}}\right) \quad \text{[Equation 3]}$$

The calculation of shrinkage was used in this study to indicate the degree to which the overall technique is able to generalize to an independent population of cases.

Other Issues

The computer used in this study was a Pentium class PC equipped with image display (DOME Imaging Systems, Waltham, MA; and an NEC 6FG Monitor), and removable WORM drives for data storage. All code was written by the authors, except for the single value decomposition and multiple regression algorithms which were commercially available as source code and were ported to our compiler. All programs were written using the C language, and a 32 bit C compiler (Intel C Code Builder, no longer available commercially). Over 400 computer programs were written specifically for this study, including programs for displaying, cropping and analyzing the images, and others for calculating, analyzing, and graphing breast features, and so on. The SVD/multiple linear regression software developed by the authors was verified for accuracy against other commercially available software capable of this analysis (SigmaStat 1.0; Jandel Scientific, San Rafael, CA). The SVD/multiple linear regression subroutines were executed well over a million times in this study, and therefore it was not feasible to utilize the commercial software directly because each run would have required user interaction. Statistical analysis was also performed using SigmaStat 1.0.

RESULTS

Radiologist Intraobserver Variability

The intraobserver variability for determining breast density is shown in Fig 2A. The breast density index for the second ranking of the CC images is plotted as a function of the *BDI* calculated from the first ranking, where both rankings were performed by a single radiologist (RAD_1). An excellent fit is illustrated ($r = 0.978$), demonstrating very reproducible performance. A histogram showing the deviation from the linear regression (best fit) line is inset in Fig 2A. In the histogram,

the "*BDI* Residual" is the difference between a plotted data point and the best fit line. Breast density is an attribute that is related to the breast, and should therefore be relatively independent of the x-ray projection through the breast. The *BDI* determined from the MLO projection images is plotted as a function of the *BDI* for the first CC ranking in Fig 2B. RAD_1 performed both rankings. The correlation coefficient calculated between x-ray projections ($r = 0.960$) was only slightly less than that calculated using repeated rankings of the same projection. The very obvious correlations ($P < 0.001$) with both the CC_1/CC_2 and the MLO_1/CC_1 comparisons lends support to the notion that the BDI is relatively projection-independent. However, there is a statistically significant difference in the *precision* (reproducibility) obtained from the intraprojection (CC_1/CC_2) comparisons and the interprojection (MLO_1/CC_1) comparison ($P < .01$, F test on ratio of variances[32]).

Radiologist Interobserver Variability

The *BDIs* resulting from the rank-ordering performed by two different radiologists on the same data set (CC_1) are compared in Fig 2C. The interobserver variability is quite low, as demonstrated by a very high correlation coefficient of $r = 0.968$. This degree of correlation is only slightly lower than the $r = 0.978$ value found for intraobserver variability, suggesting that these two radiologists apparently make use of very much the same criterion in their ranking of breast density. Despite the excellent match between radiologists seen in Fig 2C, there was a statistically significant difference in precision between interradiologist classification performance and intraradiologist performance ($P \approx .01$, F test on the ratio of variances).

Figure 2C shows the comparison between two radiologists *ordinal* ranking of the images ($r = 0.968$), whereas Fig 2D shows the comparison between the two radiologist's *cardinal* scoring of the breast density of the same image set ($r = 0.913$). In the ordinal ranking the radiologists ranked all the mammograms together, while in the cardinal scoring the radiologist simply assigned a density value while looking at only one image at a time. The cardinal scoring is more akin to how mammographers currently assess breast density. There is a significant difference in the precision between ordinal ranking and cardinal scoring ($P < .01$, F test on the ratio of variances) of the breast density.
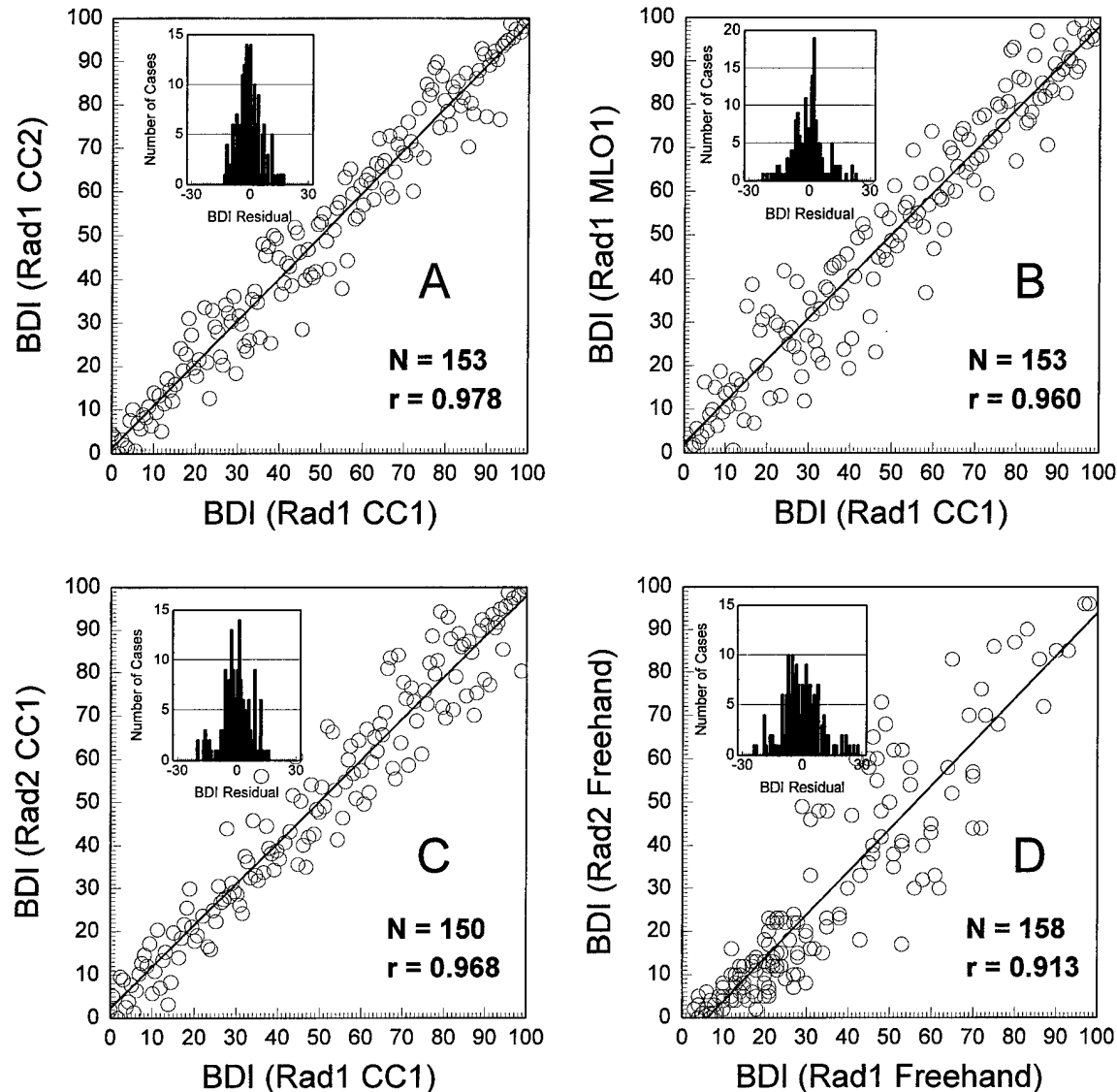
Fig 2. (A) The performance of a single radiologist, on the same set of CC mammograms, ordered in two different sessions (CC1 and CC2) four months apart. (B) The performance of a single radiologist, on CC and MLO mammograms from the same patients. The numbering scheme between the two sets of miniature mammograms was randomized to reduce bias, and the two orderings were performed 3 months apart. (C) A comparison of the *BDI* assigned by rank ordering, between two different radiologists on the same set of miniature CC mammograms is shown. The rank data were converted to a *BDI* scale using Equation 1. (D) Two different radiologists operating on the same CC data set, viewed each image independently (alone) and assigned a (cardinal) density value ranging between 0 and 100. This is similar to how radiologists assign breast density currently using the 4 classification scheme of the BIRADS, except that the scale was expanded.

Computer Determined BDI Performance

Each of the six features used in the computer-determined *BDI* (*c-BDI*) is plotted as a function of the radiologist determined gold standard (*s-BDI*) in Fig 3. It can be seen from the figure that some of the features demonstrated good correlation with the BDI standard, others showed only poor correlation. It is noted that by combining six features in a

multiple regression fit, one is actually striving for some of the features to correlate with the *residuals* between the other features and the *BDI*.

The training and testing correlation values for the straightforward split analysis paradigm are shown in Fig 4A, as a function of the percentage of the 153 case data set that was used in the training set. Towards the left hand side of the plot, for
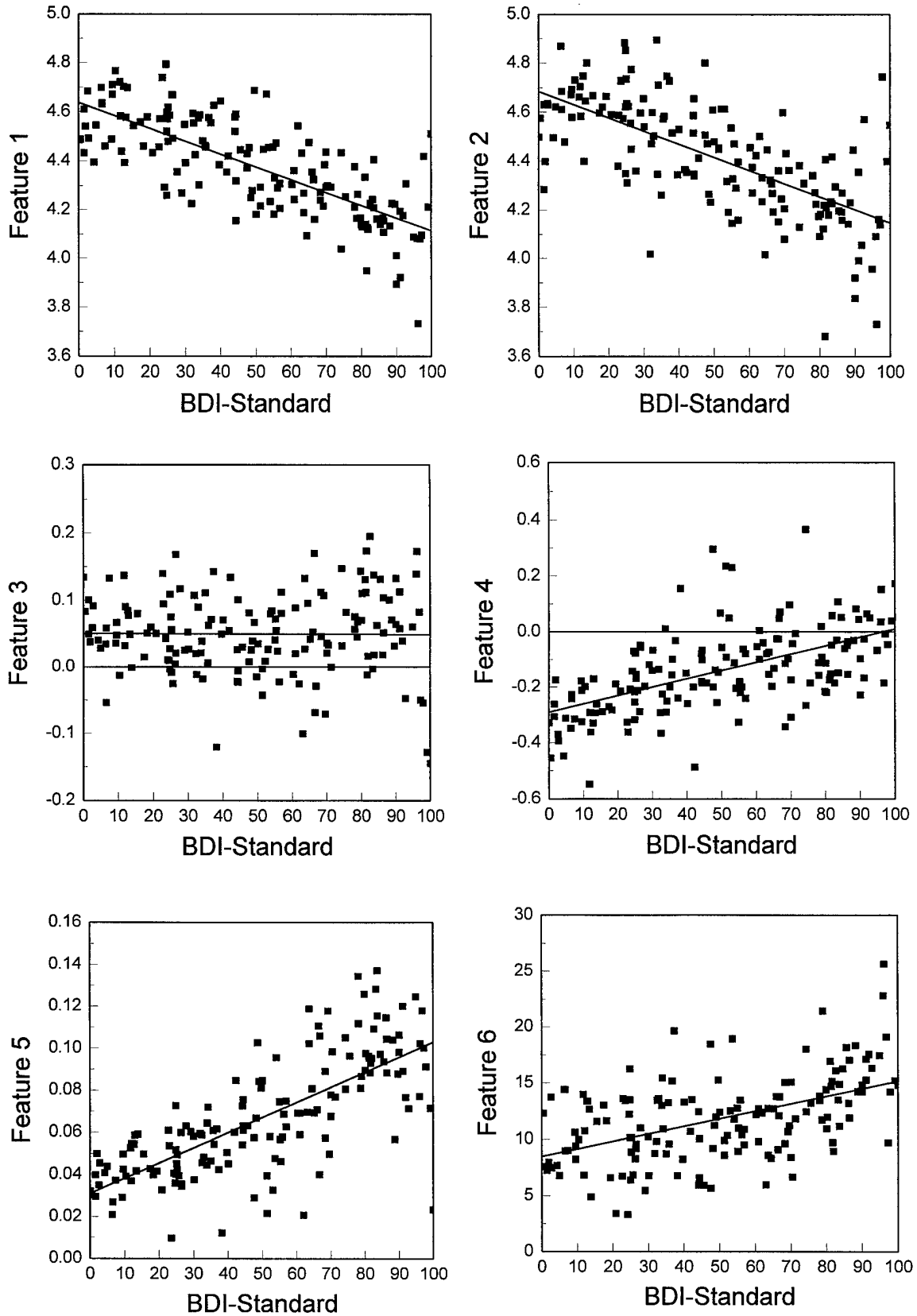
Fig 3. The six parameters are plotted as a function of the *BDI* standard. None of the individual correlations shown exceed $r = 0.74$. The parameters and their respective correlation coefficients are: Parameter 1: FD_TH_75 ($r = -0.756$), Parameter 2: FD_TH_85 ($r = -0.664$), Parameter 3: FD_Sigma ($r = -0.00827$), Parameter 4: CD_Yint ($r = 0.572$), Parameter 5: CD_Slope ($r = 0.733$), Parameter 6: HZ_Proj ($r = 0.502$).

A

Correlation Coefficient (r)

Straightforward Split Analysis

training performance

testing performance

Fraction of data used for training (%)

B

Shrinkage (%)

Straightforward Split Analysis
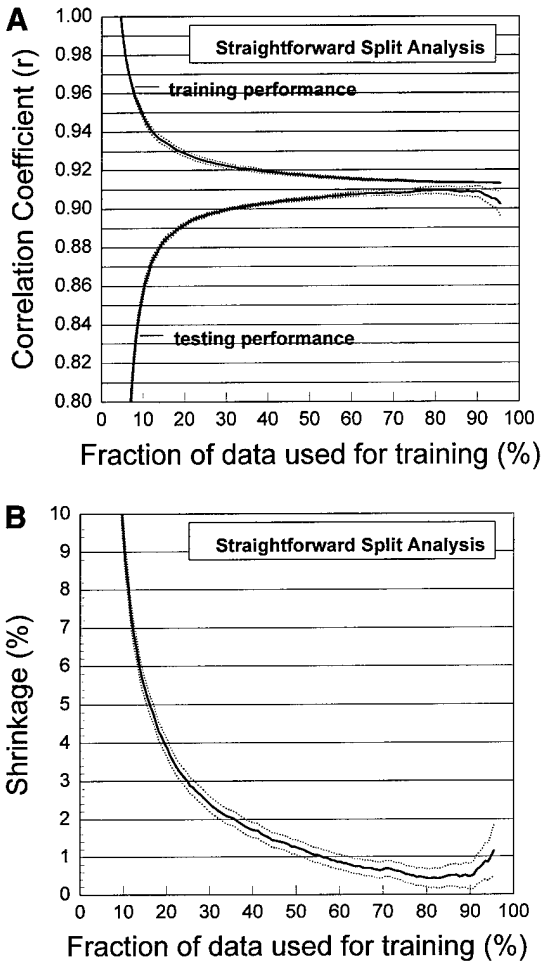
Fraction of data used for training (%)

Fig 4. (A) This graph demonstrates both the training and the testing correlation coefficient (r) for the straightforward split paradigm, as a function of the fraction of the 153 cases used in training set. At 10%, $N_{train} = 15$ and $N_{test} = 146$, at 50%, $N_{train} = 76$ and $N_{test} = 77$, and at 90% $N_{train} = 146$ and $N_{test} = 15$. As the number of cases in the training set increases, the multiple regression fit needs to accomodate a more diverse group and r_{train} drops with increasing N_{train}. The performance of the fit parameters on the testing group increases as N_{train} increases (and N_{test} decreases), since using more cases in training usually increases the generalizability of the coefficients. The error bars shown are $\pm 2\sigma$. At each point along the abscissa, 1000 different random drawings from the 153 cases were used to assign cases to the training and testing sets at each pair of (N_{train}, N_{test}). The mean r of these 1000 samples (solid lines) with the $\pm 2\sigma$ error bars (dotted lines) are shown for each point. (B) The shrinkage is shown for the straightforward split analysis. For these data, shrinkage is seen to be near a minimum at and abscissa value of 85%, where $N_{train} = 130$ and $N_{test} = 23$. The mean shrinkage at this distribution between the training and testing sets was 0.52%, indicating that the multiple linear regression equation was capable of robust generalization.

example at the 10% value on the abscissa, 15 images were used for the training and the remaining 138 images were used for testing. Because only a small number of cases were used in training, the

multiple linear regression algorithm was able to fit the data points quite well $(r = 0.949 \pm 0.0020)$. However, because the relatively few cases used in training were not representative of the wide array of variations in the testing data set, the c-BDI was not able to generalize well, and the testing performance at this point (abscissa = 10%) was relatively low $(r = 0.855 \pm 0.0035)$. The error bars shown in this and all related figures show the 95% confidence limits $(\pm 2\sigma)$, based on 1000 different case distributions. Looking towards the right of Fig 4A, for example where the abscissa value is 80% $(N_{train} = 122, N_{test} = 31)$, the training correlation coefficient is lower $(r_{train} = 0.914 \pm 0.0004)$ compared with $r_{train} = 0.949$ at the 10% point on the abscissa, because there were more points in the training set and a wider case variation was seen. However, with this relatively large number of points used in training, the c-BDI embodied a wider variation in data, and its ability to generalize was better as demonstrated by a higher correlation coefficient for testing $(r = 0.910 \pm 0.0019)$. Towards the right of the 80% point, the number of test cases becomes too few and the occasional bad fit in the testing set is not counterbalanced by the mostly good fits, and so the testing correlation value suffers.

Shrinkage, defined previously, is a measure of how well the c-BDI may be expected to generalize. As the testing performance approaches the training performance, the shrinkage is reduced and the applicability of the technique to the "general" case improves. The shrinkage for the straightforward split paradigm is shown in Fig 4B, along with the $\pm 2\sigma$ error bars. At the 80% point on the abscissa, shrinkage is near a minimum at 0.43%. This indicates that the 80% training-20% testing case mix may be near optimal for this experiment, and that may be an interesting methodological observation to some. More importantly, the low 0.4% shrinkage indicates that the results demonstrated for the c-BDI technique may be representative of a broader patient population.

A second paradigm for distributing training and testing cases is the jackknife method. The training and testing performance using the jackknife approach is illustrated in Fig 5A. In this graph, the abscissa represents the number of cases used in total for the entire training and testing procedure. At an abscissa value of 20, this means that only 20 cases were used for both training and testing. The
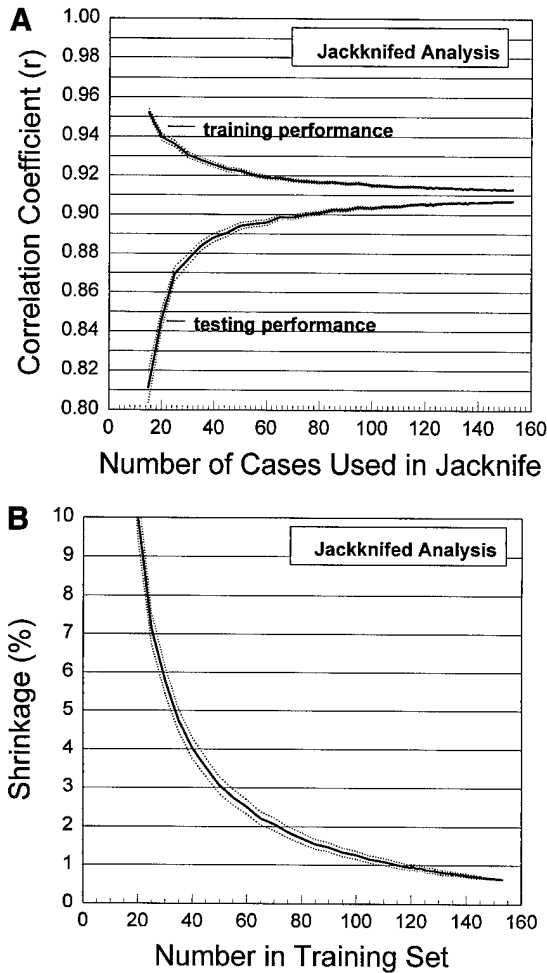
Fig 5. (A) This figure is analogous to the data shown in Fig 6A, except here the results for the jackknifed analysis paradigm are shown. Here, the number on the abscissa is equal to the total number of cases used at each point, $N_{jackknife} = N_{train} + N_{test}$. One case is set aside, and the multiple linear regression technique is run $N_{jackknife}$ times. The mean r from the $N_{jackknife}$ training sessions, and the testing performance is the correlation coefficient calculated from fitting the $N_{jackknife}$ test cases results. At each point along the abscissa corresponding to a specific value of $N_{jackknife}$, 1000 different random samplings from the 153 total cases available were used. The mean (solid line) and 95% confidence limits ($\pm 2\sigma$) were calculated from the 1000 sessions run at each point along the abscissa. As $N_{jackknife}$ approaches N_{cases} towards the right side of this graph, the actual diversity achieved in the different random samplings decreases, to the point where when $N_{jackknife} = N_{cases}$ (the right-most data point), the exact same set of 153 cases was used 1000 times. This is why the error bars approach zero towards the right of the graph. (B) The shrinkage is shown as a function of $N_{jackknife}$ in this figure, demonstrating that for the jackknifed analysis, the shrinkage is at a minimum when $N_{jackknife} = N_{cases}$. It is seen in this figure that the minimum shrinkage value is 0.6%, and that the curve appears to be approaching zero assymtoptically.

error bars were calculated by randomly varying the case mix (from the pool of 153 cases) in these 20 cases, 1000 times. The point of this analysis is to demonstrate the convergence between the training and testing performance as the number of jackknife cases increases.

Figure 5B illustrates the shrinkage for the jackknife analysis. As the number of jackknifed cases increases, the number of cases used in training also increases and the shrinkage is seen to decrease. For the case where all 153 available cases were used in jackknifed approach, the measured shrinkage was 0.65%.

Figure 6 demonstrates the c-BDI as a function of the s-BDI for the jackknife approach. The Pearson correlation coefficient is $r = 0.9069$, meaning that 82.2% (100% $\times r^2$) of the variance of the c-BDI seen in Fig 6 is attributable to its relationship with s-BDI. This implies that 17.7% of the fluctuation seen in the figure is unaccounted for. The excellent reproducibility (ie, precision) and correlation of results between radiologists as seen in Fig 2A-2C gives substantial credibility to the consistency and the quality of their ranking. How much of the 17.7% fluctuation in Fig 6 can be attributed to radiologist imprecision? Recalling the radiologist results shown in Figs 2A-2C, the percent of variance attributable to radiologist imprecision was 4.35% ($100 \times [1 - r^2]$) in the best case (the CC_1 versus CC_2 for RAD_1), 7.8% in the worst case
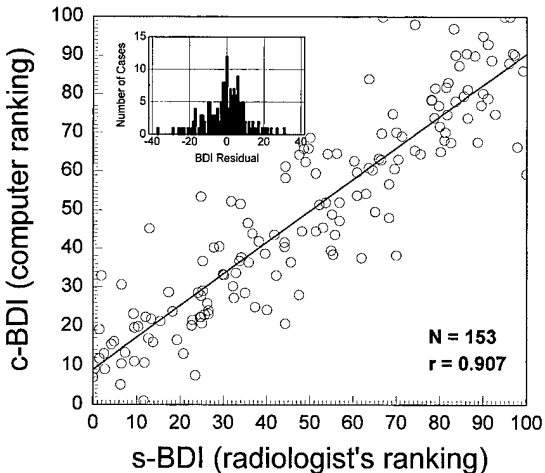

Fig 6. The c-BDI results are shown plotted as a function of the s-BDI. While the computer was not able to achieve the same level of agreement (based on the correlation coefficient) with the radiologists as the radiologists achieved, good performance is nevertheless shown. It is noted that the computer calculated BDI has a reproducability with $r = 1.000$.

(RAD_1, CC_1 versus MLO_1), and 6.3% in the intermediate case (RAD_1 CC_1 versus RAD_2 CC_1), for these ordinal rankings. Averaging these values, we approximate that about 6% to 7% of the fluctuations seen in Fig 6 are attributable to variation in the s-BDI (radiologist scoring). Therefore, the remaining 10% to 11% of the variance must lay with the *inaccuracy* of the computer to replicate the decisions made by the radiologists in determining breast density (this is not due to computer imprecision, since the c-BDI is utterly reproducible).

The breast density index presented in this study was chosen over a continuous scale ranging from 0 to 100, however this does not imply that it is practical or desirable to define 100 different categories for breast density. For comparison, the Wolfe grade methodology and the current American College of Radiology recommendations make use of 4 different categories of breast density. The number of categories that breast density can be meaningfully assigned into is related to the precision that one can actually determine breast density. To evaluate this, an analysis was performed whereby two classification schemes were compared to see what fraction of the cases would be assigned to the same classification category. The number of categories was varied between 2 and 50 in the analysis. Figure 7A shows the percentage of cases that were assigned to the exact same category, plotted as a function of the number of categories used for assignment. For example, for 2 categories the assignment is either "dense" or "not dense," and the percentage of cases that were correctly tabulated into these categories is relatively high. As the number of categories increases, the number of divisions between categories increases, and a smaller percentage of cases end up being classified into the same category. The open circles compare intra-radiologist (comparing the CC_1 and CC_2 sessions of Rad_1) ordinal classification performance. The crosses show inter-radiologist ordinal performance (Rad_2 CC_1 versus s-BDI, which was an average of Rad_1 CC_1, CC_2 and MLO_1 sessions). The filled squares show the comparison between the cardinal scores, the computer c-BDI and the radiologist's s-BDI. The open diamonds show the comparison between the freehand BDI assignment of Rad_1 (CC_3) and the freehand assignment of Rad_2 (CC_3). In Figure 7A, only cases that were assigned into exactly the same category were tallied as "correct," whereas in Fig 7B cases that were assigned

into the exact same or the next adjacent categories (on either side) were counted as "correct." This relaxation of the definition of "correct" improves performance as is apparent in Fig 7B. The definition of "correct" is relaxed to include the surrounding 2 categories in Fig 7C, and categorization performance improves even further.

DISCUSSION

There have been previous efforts to develop numerical estimates of breast density reported in the literature, most notably by Wolfe.[1] The BI-RADs classification schema has been adopted by the American College of Radiology as a standard for breast density characterization. Other investigators have reported using computerized techniques employing planimetry[33,34] and computer-derived image features.[28,35]

In one reported study,[33] radiologists ranked mammograms into 6 discrete categories depending on their estimate of the "proportion of breast volume occupied by the radiological signs of 'ductal prominence' or "mammographic dysplasia."[33] A planimeter was used which required human input (about one minute per film), and essentially used the computer to calculate the fractional area of the breast which was dense, based on hand traced areas of the dense breast regions and the total breast area. The focus of that study was primarily to evaluate the reproducibility of human estimates versus human-planimeter estimates of breast density. As such, the computer was not used to identify mammographic features per se, but only to integrate the radiologist-traced areas. For the 6 category scale used in the study, the investigators found 52.4% exact agreement between radiologist and planimeter estimates of densities. In the study of Saftlas et al,[34] planimetry was used essentially as above and showed 77% agreement based on a 5 category scale of density.

Caldwell et al[28] pioneered the use of the fractal dimension as a feature which correlates well to breast density, as defined by the 4-category Wolfe grade classification scheme (N1, P1, P2, and DY). In terms of categorization reliability, inter-radiologist agreement (3 radiologists compared) in the 4 category scale ranged between 66% and 74% for exact agreement. The computerized assignments to the density categories agreed exactly with the radiologists between 57% and 67%. The computer assignments demonstrated had minor disagreement

(plus exact agreement) in 88% of the 70 cases studied.

The technique of rank-ordering of mammograms used in this study is fundamentally different than assigning breast density using a small number of categories. The rank order data can be retrospectively divided up into a large number of different categories. Rebinning our results to the 4 breast density classification categories used by Caldwell,[28] the computer and radiologist agreed (exactly) 67% of the time, in excellent agreement with Caldwell's 57% to 67%. The intraradiologist exact agreement

for 4 categories observed in this study was calculated (circles on Fig 8A) as 84%, which compares well with Caldwell's interradiologist agreement levels of 66% to 74%. The computer-derived c-BDI compared with the gold standard radiologist s-BDI scoring agreed in 99% of the cases when minor disagreements are disregarded (ie, when assignment in just-adjacent categories are considered as "agreement"), compared to Caldwell's 88% agreement. This improvement of the c-BDI technique over Caldwell's results may be explained by the fact that the c-BDI technique presented in this study used 6 features derived from the μx-mammograms, as opposed to 2 features used by Caldwell et al. Furthermore, while Caldwell et al briefly explored the role that the screen-film characteristic curve played on their computer derived classification parameters, their results quoted above did not include corrections for the characteristic curve or exposure levels that our results include. This may be another factor contributing to the slightly better
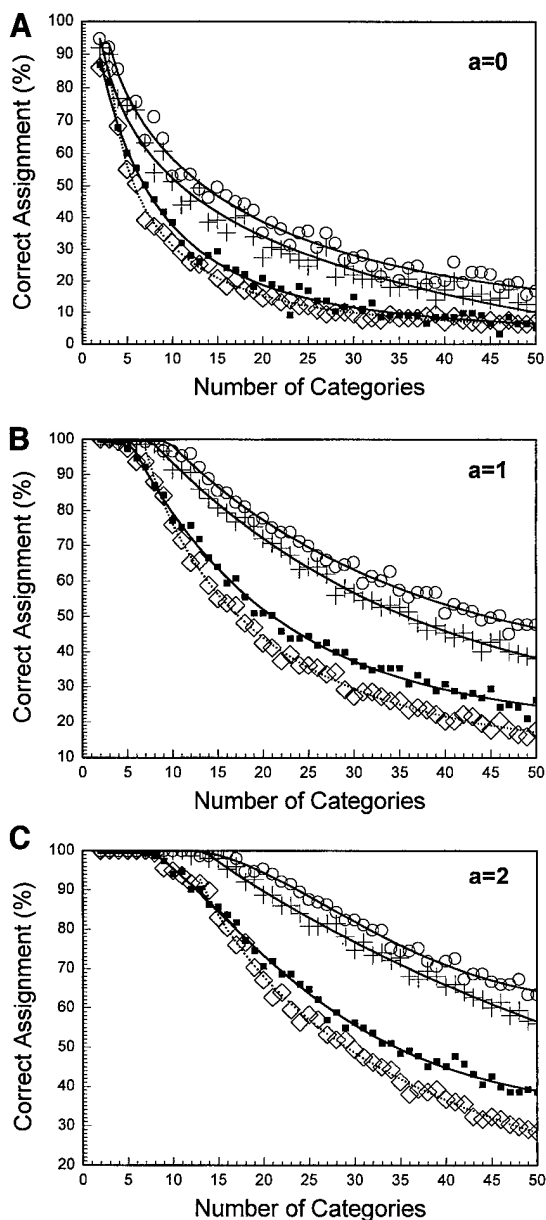

Fig 7. (A) The precision with which breast images can be ranked in order of breast density relates to the number of meaningful categories that breasts can be classified into. In comparing the ranking between two approaches, this graph shows the percentage of assignments into the same categories between the two approaches, as a function of the number of categories. The open circles show the comparison between ordinal ranking sessions RAD_1 CC_1 and RAD_1 CC_2 (intraradiologist). The crosses show comparisons of the ordinal rankings between radiologists (Rad_1's s-BDI and Rad_2 CC_1). The solid squares are the (cardinal) c-BDI results compared with the cardinalized s-BDI, and the open diamonds show the (cardinal) freehand sessions (CC_3) between radiologists (Rad_1 versus Rad_2). (B) This plot is the same as Fig 7A, except that the definition of correct is relaxed to include both the exact and the next adjacent category assignments. This relaxation of the agreement increases the meaningful number of breast density categories that could be used. The open circles show the comparison between ordinal ranking sessions RAD_1 CC_1 and RAD_1 CC_2 (intraradiologist). The crosses show comparisons of the ordinal rankings between radiologists (Rad_1's s-BDI and Rad_2 CC_1). The solid squares are the (cardinal) c-BDI results compared with the cardinalized s-BDI, and the open diamonds show the (cardinal) freehand sessions (CC_3) between radiologists (Rad_1 versus Rad_2). (C) In this plot, mammograms that were reproducably assigned within ± 2 categories were counted as correct. This easing of the constraint further increases the number of meaningful categories that mammograms could be assigned to in terms of breast density. The open circles show the comparison between ordinal ranking sessions RAD_1 CC_1 and RAD_1 CC_2 (intraradiologist). The crosses show comparisons of the ordinal rankings between radiologists (Rad_1's s-BDI and Rad_2 CC_1). The solid squares are the (cardinal) c-BDI results compared with the cardinalized s-BDI, and the open diamonds show the (cardinal) freehand sessions (CC_3) between radiologists (Rad_1 versus Rad_2).

performance of the *c-BDI* in the minor disagreement category.

Figures 7A-7C demonstrate that rank-ordering a large series of mammograms results in greater precision than that achievable by assigning cardinal *BDI* values. For example, focusing on Figure 7B (where minor disagreement by plus or minus one category is considered "agreement") using 90% correct assignment as a threshold requirement, intraradiologist ordinal ranking could achieve 13 meaningful categories, and interradiologist ordinal ranking could achieve 11 meaningful categories of breast density. Cardinal ranking techniques proved less precise. For the computer results (*c-BDI*) compared against the *s-BDI*, it was found that 7 meaningful breast categories could be distinguished. Interradiologist cardinal scoring could also produce about 7 meaningful categories. These results suggest that radiologist organizations considering future modifications to the BIRADs breast density scale may want to consider increasing the number of categories from 4 to 7. It is conceivable that if radiologists were to make use of an atlas showing a series of mammograms covering the full range of breast densities (thus using an ordinal scale), a higher level of precision may be achievable. This technique would be similar to the use of the Greulich and Pyle atlas for skeletal age determination.[36] Alternately, when digital mammography becomes the norm, algorithms such as that reported for the *c-BDI* here could be used to calculate breast density.

CONCLUSION

The link between breast density and the risk of breast cancer that was first made by Wolfe[1,2,16-18,37] has begun to be appreciated by the medical community as a whole.[3,34,38-45] Quantification of a patient's breast density using the *BDI* developed in this study would allow for more precise evaluation of breast cancer risk, which may influence the optimal choice of screening strategy for each patient. For example, patients with moderate breast densities might be evaluated more frequently using mammography, but those with very high *BDIs* might be screened routinely using modalities in addition to mammography, such as ultrasound or MRI.[6,7,46-48] Furthermore, the efficacy of using alternate modalities such as ultrasound or MRI could be studied in terms of the proposed continuous scale for breast density. A more precise metric for quantifying breast density would also allow closer monitoring of changes in breast density due to menopause or hormone replacement therapy.[49-52] In addition, a continuous *BDI* scale may permit better technique optimization for serial mammography screening, even with automatically adjusting mammography systems such as the DMR (General Electric; Milwaukee, WI). A priori knowledge of a precise BDI value would allow an automatic technique system to initiate the technique closer to the optimum level, possibly minimizing exposure total time and reducing motion unsharpness in the mammogram. Finally, the availability of a standardized breast density index such as that proposed here may permit the a priori application of different sets of algorithms for computer aided diagnosis, each set optimized for a specific range of breast density.

ACKNOWLEDGMENT

APPENDIX

In this section, a description is given as to how each of the features listed in Table 1 was calculated. In all cases, the features were only calculated on regions of the μx-mammograms where actual breast parenchyma was imaged; the image background was excluded from the calculation using a "mask." The image served as its own mask, since all background and cropped areas on the images were set to a gray scale value of 0, and all the areas on the image where breast parenchyma was present the gray scale values were > 500.

Feature 1: FD_Th_75

The fractal dimension has been recognized for some time to be a good indicator of breast density.[28] The first step in calculating fractal properties was to produce a series of N_k images with formats decreasing by factors of 2. For example, if the original μx-mammogram was N_x pixels wide by N_y pixels tall, for k = 1 the image is still $N_x \times N_y$, for k = 2 the image is reduced to $N_x/2 \times N_y/2$ in size, for k = 3, the image size is $N_x/4 \times N_y/4$, and for k = 4, the image size is $N_x/8 \times N_y/8$. The images are reduced to smaller formats by averaging gray scale values.

The next step that was applied was to *trinarize* the μx-mammograms. Background pixels in the image were kept zero, pixels that were in the breast but were below a certain gray scale value were set to 1, and pixels in the breast above the threshold value were set to 2. The threshold value was calculated based on a percentile of the range of gray scale in the μx-mammogram. The histogram of the image was calculated, and the gray scale value corresponding to the 75th percentile was chosen as the threshold value for feature 1, FD_Th_75 (for comparison, the median gray scale would correspond to the 50th percentile).

The next step in calculating the fractal features is to calculate the feature of interest, and here the integrated gradient was

calculated using:

$$\text{Gradient}_k = \sum_x \sum_y \sum_{x'=x-1}^{x'=x+1} \sum_{y'=y-1}^{y'=y+1} [\text{IM}(x,y) - \text{IM}(x',y')] \quad [\text{A-1}]$$

All pixels having gray scale values of zero were excluded from the above summation. This operation was performed on 4 images ($N_k = 4$). For images $k = 1, 2, 3$ and 4 (which were increasingly smaller), pairs of (x, y) values were calculated as: ($\text{LOG}_{10}(\frac{1}{2} k), \text{LOG}_{10}(\text{gradient}_k)$). This set of 4 (x, y) points was then fit to a straight line using linear regression, and the value of the feature was calculated as: FD_Th_75 = 2 − slope. Feature 1 is referred to as the fractal dimension of the image thresholded at 75%, abbreviated as FD_Th__75.

Feature 2: FD_Th_85

Feature 2 was calculated exactly as described above for feature 1, except that the image was thresholded at the 85% level instead of the 75% level.

Feature 3: FD_Sigma

Feature 3 was calculated exactly as described above for feature 1, except that the root mean square (RMS) standard deviation was used as the feature calculated. In this case the image was not trinarized. Linear regression was performed as described above, and the slope of the straight line fit was determined. The feature value was calculated again as $F_3 =$ (2-slope).

Feature 4: CD_Yint

Each image was high-pass filtered with a series of 5 different filters, producing 5 different filtered images. The high-pass filtering was performed using so-called blurred mask subtrac-

tion, where a square convolution kernel (all elements of the kernel equal to S^{-2}) of $S \times S$ pixels was convolved with the original image, smoothing it. The smoothed image was then subtracted pixel-by-pixel from the original, and an offset of 2000 was added to the image. For the five different images ($k = 1, 2, 3, 4, 5$), the side length S of the convolution kernel was 5, 9, 13, 17, 21 (ie, S = 4k + 1).

The integrated gradient for each high-pass filtered image was calculated using Equation A-1. Pairs of points (LOG[k], LOG-[gradient_k]) were produced from $k = 1$ to $k = 5$ and these 5 pairs of points were submitted to linear regression analysis. The fit was to a straight line, $Y = \alpha + \beta X$. The fit parameter α is the y-intercept of the line, and this continuous dimension y-intercept was used as feature 5, CD_Yint.

Feature 5: CD_Slope

Feature 5 was calculated as described for Feature 4, except the slope (the β in $Y = \alpha + \beta X$) of the linear fit was used instead of the y-intercept. This feature was the continuous dimension slope, CD_Slope.

Feature 6: HZ_Proj

All of the images in the data set were oriented and displayed with the nipple-to-chest wall axis running horizontal, with the nipple on the left. The gray scale values on the µx-mammograms along horizontal lines in the image (or pixel rows, running in the x dimension) were summed, producing a profile (or vector) $Z(i = 1, N_y)$ which has as many elements as the image is tall (N_y). Only rows containing more than 10 non-zero pixels (those with breast parenchyma) were summed, all others were set to 0. The Root Mean Square (RMS) standard deviation of all non-zero projection values was calculated, and used for the horizontal projection feature, HZ_Proj.

REFERENCES

1. Wolfe JN: Breast patterns as an index of risk for developing breast cancer. AJR Am J Roentgenol 126:1130-1137, 1976

2. Wolfe JN: Risk for breast cancer development determined by mammographic parenchymal pattern. Cancer 37:2486-2492, 1976

3. Boyd NF, Byng JW, Jong RA, et al: Quantitative classification of mammographic densities and breast cancer risk: results from the Canadian National Breast Screening Study. J Natl Cancer Inst 87:670-675, 1995

4. Feig SA, Yaffe MJ: Digital mammography, computer-aided diagnosis, and telemammography. Radiol Clin North Am 33:1205-1230, 1995

5. Yaffe MJ: Direct digital mammography using a scanned-slot CCD imaging system. Med Prog Technol 19:13-21, 1993

6. Feig SA: The role of ultrasound in a breast imaging center. Semin Ultrasound CT MR 10:90-105, 1989

7. Guyer PB, Dewbury KC: Ultrasound of the breast in the symptomatic and X-ray dense breast. Clin Radiol 36:69-76, 1985

8. Graham SJ, Bronskill MJ, Byng JW, et al: Quantitative correlation of breast tissue parameters using magnetic resonance and X-ray mammography. Br J Cancer 73:162-168, 1996

9. Dash N, Lupetin AR, Daffner RH, et al: Magnetic resonance imaging in the diagnosis of breast disease. AJR Am J Roentgenol 146:119-125, 1986

10. Turner DA, Alcorn FS, and Adler YT: Nuclear magnetic resonance in the diagnosis of breast cancer. Radiol Clin North Am 26:673-687, 1988

11. Jansson T, Westlin JE, Ahlstrom H, et al: Positron emission tomography studies in patients with locally advanced and/or metastatic breast cancer: A method for early therapy evaluation? J Clin Oncol 13:1470-1477, 1995

12. Wahl RL, Zasadny K, Helvie M, et al: Metabolic monitoring of breast cancer chemohormonotherapy using positron emission tomography: Initial evaluation. J Clin Oncol 11:2101-2111, 1993

13. Rambaldi PF, Mansi L, Procaccini E, et al: Breast cancer detection with Tc-99m tetrofosmin. Clin Nucl Med 20:703-705, 1995

14. Takahashi T, Moriya E, Miyamoto Y, et al: The usefulness of 201T1C1 scintigraphy for the diagnosis of breast tumor. Nippon Igaku Hoshasen Gakkai Zasshi 54:644-649, 1994

15. Wolfe JN: Developments in mammography. Am J Obstet Gynecol 124:312-323, 1976

16. Wolfe JN, Albert S, Belle S, et al: Breast parenchymal patterns: Analysis of 332 incident breast carcinomas. AJR Am J Roentgenol 138:113-118, 1982

17. Wolfe JN, Albert S, Belle S, et al: Breast parenchymal patterns and their relationship to risk for having or developing carcinoma. Radiol Clin North Am 21:127-136, 1983

18. Wolfe JN, Saftlas AF, Salane M: Mammographic parenchymal patterns and quantitative evaluation of mammographic densities: a case-control study. AJR Am J Roentgenol 148:1087-1092, 1987

19. Rockette HE, Gur D, Metz CE: The use of continuous and discrete confidence judgments in receiver operating characteristic studies of diagnostic imaging techniques. Invest Radiol 27:169-172, 1992

20. Press WH, Flannery BP, Teukolsky SA, et al: Numerical Recipes in C: The Art of Scientific Computing. Cambridge, Cambridge University Press, 1988

21. Astion ML, Wilding P: The application of backpropagation neural networks to problems in pathology and laboratory medicine. Arch Pathol Lab Med 116:995-1001, 1992

22. Gurney JW: Neural networks at the crossroads: Caution ahead. Radiology 193:27-28, 1994

23. Wu Y, Giger ML, Doi K, et al: Artificial neural networks in mammography: Application to decision making in the diagnosis of breast cancer. Radiology 187:81-87, 1993

24. Floyd CE, Tourassi GD: An artificial neural network for lesion detection on single-photon emission computed tomographic images. Invest Radiol 27:667-672, 1992

25. Asada N, Doi K, MacMahon H, et al: Potential usefulness of an artificial neural network for differential diagnosis of interstitial lung diseases: Pilot study. Radiology 177:857-860, 1990

26. Tourassi GD, Floyd CE, Sostman HD, et al: Artificial neural network for diagnosis of acute pulmonary embolism: Effect of case and observer selection. Radiology 194:889-893, 1995

27. Morin RL: Monte Carlo Simulation in the Radiological Sciences. Boca Raton, FL, CRC Press, 1988

28. Caldwell CB, Stapleton SJ, Holdsworth DW, et al: Characterisation of mammographic parenchymal pattern by fractal dimension. Phys Med Biol 35:235-247, 1990

29. Dorfman DD, Berbaum KS, Metz CE: Receiver operating characteristic rating analysis. Generalization to the population of readers and patients with the jackknife method. Invest Radiol 27:723-731, 1992

30. Boone JM: Neural networks at the crossroads. Radiology 189:357-359, 1993

31. Boone JM: Sidetracked at the crossroads. Radiology 193:28-30, 1994

32. Glantz SA: Primer of Biostatistics (3rd ed). New York, NY, McGraw Hill, 1992

33. Lee-Han H, Cooke G, Boyd NF: Quantitative evaluation of mammographic densities: A comparison of methods of assessment. Eur J Cancer Prev 4:285-292, 1995

34. Saftlas AF, Hoover RN, Brinton LA, et al: Mammographic densities and risk of breast cancer. Cancer 67:2833-2838, 1991

35. Taylor P, Hajnal S, Dilhuydy MH, et al: Measuring image texture to separate "difficult" from "easy" mammograms. Br J Radiol 67:456-463, 1994

36. Greulich WW, Pyle SI: Radiographic atlas of the skeletal development of the hand and wrist (2nd ed). Stanford, CA, Stanford University Press, 1959

37. Wolfe JN: Risk of developing breast cancer determined by mammography. Prog Clin Biol Res 12:223-238, 1977

38. Boyd NF, Jensen HM, Cooke G, et al: Relationship between mammographic and histological risk factors for breast cancer. J Natl Cancer Inst 84:1170-1179, 1992

39. Byrne C, Schairer C, Wolfe J, et al: Mammographic features and breast cancer risk: Effects with time, age, and menopause status. J Natl Cancer Inst 87:1622-1629, 1995

40. Ciatto S, Zappa M: A prospective study of the value of mammographic patterns as indicators of breast cancer risk in a screening experience. Eur J Radiol 17:122-125, 1993

41. Beisang AA, Geise RA, Ersek RA: Radiolucent prosthetic gel. Plast Reconstr Surg 87:885-892, 1991

42. Kato I, Beinart C, Bleich A, et al: A nested case-control study of mammographic patterns, breast volume. Cancer Causes and Control 6:431-438, 1995

43. Brisson J, Morrison AS, Khalid N: Mammographic parenchymal features and breast cancer in the breast cancer detection demonstration project. J Natl Cancer Inst 80:1534-1540, 1988

44. Saftlas AF, Wolfe JN, Hoover RN, et al: Mammographic parenchymal patterns as indicators of breast cancer risk. Am J Epidemiol 129:518-526, 1989

45. Vogel VG: High-risk populations as targets for breast cancer prevention trials. Prev Med 20:86-100, 1991

46. Feig SA: Breast masses. Mammographic and sonographic evaluation. Radiol Clin North Am 30:67-92, 1992

47. Fornage BD, Toubas O, Morel M: Clinical, mammographic, and sonographic determination of preoperative breast cancer size. Cancer 60:765-771, 1987

48. Liem SJ: Target ultrasonic mammography. An additional diagnostic tool for the detection of breast cancer. Diagn Imaging Clin Med 54:192-201, 1985

49. Stomper PC, van Voorhis BJ, Ravnikar VA, et al: Mammographic changes associated with postmenopausal hormone replacement therapy: A longitudinal study. Radiology 174:487-490, 1990

50. van Gils CH, Otten JD, Verbeek AL, et al: Short communication: breast parenchymal patterns and their changes with age. Br J Radiol 68:1133-1135, 1995

51. Feig SA: Hormonal reduction of mammographic densities: Potential effects on breast cancer risk and performance of diagnostic and screening mammography. J Natl Cancer Inst 86:408-409, 1994

52. Flook D, Gilhome RW, Harman J, et al: Changes in Wolfe mammographic patterns with aging. Br J Radiol 60:455-456, 1987